

Computational electrocatalysis: methods and fundamental applications on CO2 reduction and formic acid oxidation Granda Marulanda, L.P.

Citation

Granda Marulanda, L. P. (2021, October 19). Computational electrocatalysis: methods and fundamental applications on CO2 reduction and formic acid oxidation. Retrieved from https://hdl.handle.net/1887/3217519

Version: Publisher's Version

Licence agreement concerning inclusion of doctoral thesis License:

in the Institutional Repository of the University of Leiden

Downloaded from: https://hdl.handle.net/1887/3217519

Note: To cite this publication please use the final published version (if applicable).

COMPUTATIONAL ELECTROCATALYSIS: METHODS AND FUNDAMENTAL APPLICATIONS ON CO₂ REDUCTION AND FORMIC ACID OXIDATION

Proefschrift

ter verkrijging van de graad van Doctor aan de Universiteit Leiden, op gezag van Rector Magnificus Prof.dr.ir. H. Bijl, volgens besluit van het College voor Promoties te verdedigen op dinsdag 19 oktober 2021 klokke 13:45uur

door

Laura Patricia Granda Marulanda geboren op 9 juni 1988 te Cali, Colombia

Promotiecommissie:

Promotor: Prof. dr. M. T. M. Koper

Co-promotor: dr. F. Calle-Vallejo (Universitat de Barcelona)

Co-promotor: dr. I. McCrum (Clarkson Univeristy, USA)

Overige commissieleden:

Dr. K. Doblhoff-Dier (Leiden University)

Prof. dr. G. J. Kroes (Leiden University)

Prof. dr. N. López (Institute of Chemical Research

of Catalonia)

Prof. dr. E. J. Meijer (University of Amsterdam)

This PhD Thesis received financial support from A-Leaf H2020-FETPROACT Grant Agreement No. 732840 and partial support from HPC-EUROPA3 (INFRAIA-2016-1-730897) founded under H2020-EU.1.4.

To my parents: Ana Libia Marulanda Pérez y Nelson Jesús Granda Paz

Proverbios y Cantares de Campos de Castilla, 1912 Antonio Machado

Caminante no hay Camino

Caminante, son tus huellas el camino y nada más;
Caminante, no hay camino, se hace camino al andar.
Al andar se hace el camino, y al volver la vista atrás se ve la senda que nunca se ha de volver a pisar.
Caminante no hay camino sino estelas en la mar.

"Wayfarer, there is no path"

Wayfarer, the only way
Is your footprints and no other.
Wayfarer, there is no way.
Make your way by going farther.
By going farther, make your way
Till looking back at where you've wandered,
You look back on that path you may
Not set foot on from now onward.
Wayfarer, there is no way;
Only wake-trails on the waters.

Translated by Rafael Rolón-Muñiz, 2014

Table of Contents

GENERAL INTRODUCTION	1
1.1 THEORETICAL BACKGROUND	2
1.1.1 DENSITY FUNCTIONAL THEORY (DFT)	3
1.1.2 Free energies and adsorption potentials	6
1.2 APPLICATIONS – ELECTROCHEMICAL FORMIC ACID OXIDATION AND CO	O_2
REDUCTION REACTIONS	9
1.2.1 PRACTICAL MOTIVATION	9
1.2.2 SCIENTIFIC MOTIVATION	13
1.3 SCOPE AND OUTLINE OF THIS PHD THESIS	14
1.4 REFERENCES	16
INFLUENCE OF MAN DED MAN CONTEDACTIONS ON THE COLUMN TON ENERG	15C OF
INFLUENCE OF VAN DER WAALS INTERACTIONS ON THE SOLVATION ENERGI	
ADSORBATES AT PT-BASED ELECTROCATALYSTS	
2.1 Introduction	24
2.2 COMPUTATIONAL DETAILS	24
2.3 RESULTS AND DISCUSSION	25
2.4 CONCLUSIONS	31
2.5 References	31
A SIMPLE METHOD TO CALCULATE SOLUTION-PHASE FREE ENERGIES OF CHA	ARGED
SPECIES IN COMPUTATIONAL ELECTROCATALYSIS	
3.1 Introduction	38
3.2 Methods	40
3.2.1 COMPUTATIONAL DETAILS	41
3.2.2 DETERMINATION OF THE FREE ENERGY OF IONS IN SOLUTION	43
3.2.3 HALF-CELL REDOX COUPLE WITH N ELECTRONS TRANSFERRED	44
3.2.4 HALF-CELL REDOX COUPLES WITH UNEQUAL NUMBER OF PROTONS A	4ND
ELECTRONS	45
3 3 FOLIII IRRILIM ADSORPTION ENERGIES AND ADSORPTION POTENTIALS	47

3.4 RESULTS AND DISCUSSION	49
3.5 APPLICATIONS OF THE METHOD IN ELECTROCATALYSIS	49
3.6 CONCLUSIONS	52
3.7 References	53
A SEMIEMPIRICAL METHOD TO DETECT AND CORRECT DFT-BASED GAS-PH.	'ASE
ERRORS AND ITS APPLICATION IN ELECTROCATALYSIS	61
4.1 Introduction	62
4.2 COMPUTATIONAL METHODS	62
4.3 RESULTS AND DISCUSSION	63
4.3.1 PINPOINTING ERRORS	63
4.3.2 IMPLEMENTING ENERGY CORRECTIONS	67
4.3.3 APPLICATIONS IN ELECTROCATALYSIS	71
4.4 CONCLUSIONS	74
4.5 References	
ADSORPTION PROCESSES ON A PD- MONOLAYER-MODIFIED PT(111)	
ELECTRODE	81
5.1 Introduction	82
5.2 EXPERIMENTAL DETAILS	83
5.3 COMPUTATIONAL DETAILS	84
5.4 RESULTS AND DISCUSSION	85
5.4.1 COMPARISON OF THE BLANK VOLTAMMOGRAMS OF PD _{ML} PT(111) A	ND
Рт(111)	85
5.4.2 CATION AND ANION EFFECTS ON THE BLANK VOLTAMMOGRAM OF	
PD _{MI} PT(111)	86
5.4.3 THERMODYNAMICS OF *H, *OH + *H ₂ O, *O, *CLO ₄ , *SO ₄ AND *I	
ADSORPTION	91
5.4.4 Anion adsorption	
5.5 CONCLUSIONS	98
5.6 REFERENCES	

HOW PALLADIUM PROHIBITS CO POISONING DURING ELECTROCATALYTIC	
FORMIC ACID OXIDATION AND CARBON DIOXIDE REDUCTION	105
6.1 Introduction	106
6.2 EXPERIMENTAL RESULTS AND DISCUSSION	107
6.2.1 FORMIC ACID OXIDATION	107
6.2.2 FORMATE ADSORPTION ISOTHERM	109
6.2.3 FORMATE AND CO PRODUCTION FROM CO₂ REDUCTION	111
6.3 DFT RESULTS AND DISCUSSION	113
6.3.1 FORMIC ACID OXIDATION	113
6.3.2 ADSORBED CO FORMATION DURING CO₂ REDUCTION	116
6.4 GENERAL DISCUSSION	
6.4.1 FORMIC ACID OXIDATION	
6.4.2 THE CO ₂ REDUCTION	_
6.5 EXPERIMENTAL SECTION	
6.5.1 ELECTROCHEMICAL MEASUREMENTS	
6.5.2 Preparation of PD monolayers on Pt(111) and Pt(100) sing	
CRYSTALS	
6.5.3 Online High Performance Liquid Chromatography (HPLC).	
6.6 COMPUTATIONAL DETAILS	
6.7 REFERENCES	
0.7 REFERENCES	124
A: Supporting Information for Chapter 2	131
B: Supporting Information for Chapter 3	139
C: SUPPORTING INFORMATION FOR CHAPTER 4	141
D: Supporting Information for Chapter 5	174
E: SUPPORTING INFORMATION FOR CHAPTER 6	187
SUMMARY & FUTURE PERSPECTIVES	203
SAMENVATTING & TOEKOMSTPERSPECTIEVEN	207
LIST OF PUBLICATIONS, CONFERENCES AND AWARDS	211
ACKNOWLEDGEMENTS	213
Curriculum Vitae	215



GENERAL INTRODUCTION

"Inventions grow old and are superseded by other inventions and being the creation of the constructive schemes of mortal men, are themselves mortal. But the laws which the stars and the planets obey and have always obeyed in their paths through the heavens are unchangeable; they never grow old, and therefore they are immortal; they are part of the *eternal truth*."

M. I. Pupin (1923)¹

Michel (Mihajlo) Idvorski Pupin refers to the laws of nature as the *eternal truth*. Perhaps, the reason why we are often in search of more accurate models to represent the operations of the world, is to come closer to its understanding, closer to this *truth*.

In the domain of computational chemistry, accuracy does not always translate to complexity. To understand the how's and why's, simple models of a target system based on the well-founded laws of quantum physics and chemistry- the laws atoms and molecules obey, can lead to scientific revelations the same way as more complex models would do, especially if the model in question is studied by a framework based on those laws. Density Functional Theory (DFT) is one of such frameworks.

In essence, the model of the target system is created by our interpretation and current understanding of the real environment. The beauty of DFT is that it can simulate this model, as if it were simulating the real world. However, sometimes the outcome from DFT does not follow exactly what we expect from chemical concepts or from what we see experimentally. There are two major reasons for this discrepancy. One is that the model is not encapsulating the important interactions, or "something" is not being considered, and this could be because we do not have enough information or knowledge of the real system. The second reason is the limitation of DFT itself, more precisely the overestimations or underestimations of system properties; mostly a fault of the approximate functionals used in DFT. Knowing these limitations is immensely important, as it allows us to discriminate the results, and also encourages us to improve the methods and consequently propose hypotheses to build new knowledge.

In this thesis, we investigate simple computational electrochemical methods, their usability and ways to improve their accuracy (*Chapters 2-4*), and apply them to the study of Formic acid oxidation and production via a collaborative experimental and computational study (*Chapter 5-6*)

1.1 Theoretical Background

It took several decades for quantum-chemical methods to develop into what we have today, all driven by the same ultimate goal: to be able to compute the values of physical properties that describe chemical systems, for instance, energy, bond lengths, bond frequencies, and how such properties change as the system interacts with different environments. In heterogeneous (electro)catalysis, we are interested in the interaction between solids (the electrode), molecules (the reactants or intermediates), and the electrolyte (solvent and ions).

This section gives a summary of the theoretical background behind Quantum Chemistry and DFT gathered from various books and articles. In quantum mechanics, particles are described by the wave function, ψ . This function of state contains all the information about their physical properties. Besides, $|\psi|^2$ is the probability density of finding the particle in a certain region of space, and the value of a physical property is obtained through the action of a corresponding Hermitian operator on the wave function. Here, we focus on the stationary (time-independent) Schrödinger equation (1926).

$$\widehat{H}\psi(r_i) = E\psi(r_i)$$
1.1

Eq.1.1 describes a one-particle system i, with coordinates r_i . $\widehat{\mathbf{H}}$ is the Hamiltonian operator, the energy operator, defined as; $\widehat{H} = \widehat{T} + \widehat{V}$, the sum of the kinetic energy operator, \widehat{T} , and the potential energy operator \widehat{V} . For atoms, the low weight of the electrons compared to the heavy nuclei allows treating the dynamics of electrons and nuclei separately. This allows approximating the full (time dependent) Schrödinger equation by an electronic Schrödinger equation, that is stationary and does not contain the kinetic energy of the ions, and a nuclear Schrödinger equation, that can often be treated classically.

This is the so-called Born-Oppenheimer approximation (B-O, 1927).⁸ Within this approximation the electronic Hamiltonian operator is

$$\widehat{H} = \widehat{T}_e + \widehat{V}_{ee} + \widehat{V}_{en} + \widehat{V}_{ext}$$
 1.2

and it takes into account the kinetic energy of the electrons and their potential energy (arising from electron-electron interactions, \hat{V}_{ee} , attractive electron-nucleus interaction, \hat{V}_{en} , and an external potential, \hat{V}_{ext}). The electron-nucleus interaction is then treated as the attraction between the electron and the field of the fixed nucleus. In Eq.1.1 the eigenfunction ψ corresponding to the lowest energy eigenstate E is the ground state wave function. E is then the corresponding ground state energy of the electronic one-electron wave function at 0K.

However, we are primarily interested in finding the ground-state energy of interacting solids and molecules, that is a system of many atoms, meaning a

system of many electrons, and so the ground state of such system can be determined if we solve the following equation, known as the many-electron Schrödinger equation.

$$\widehat{H}\psi(r_1, r_2, r_3 \dots r_N) = E\psi(r_1, r_2, r_3 \dots r_N)$$

This equation "is the starting point for computational materials science, and the ground-state properties of any system can be determined by solving this equation, if we have a method to solve it."

I. G. Lee⁶

Eq.1.3 depends on 3x N coordinates as the number of N particles increases and, therefore, it becomes too complex to solve, both analytically and numerically, when there are electrons interacting with all the other electrons at the same time. This is where Density Functional Theory (DFT) proposes a simplification that allows the computation of an approximate solution to Eq.1.3.

Before discussing the quantum mechanical framework of Density Functional Theory, we note that other quantum chemical-mechanical frameworks have been developed to solve the many-body Schrödinger equation. One of the mathematical problems is the presence of correlation, that is the electrons interacting with the field created by the other electrons. The Hartree-Fock (HF) method (1930) gives an approximation to this interaction, and although it gives reasonable results for small molecules, it does not do so well for solids. The error in the approximation, arises from replacing the exact electron-electron interaction with a mean-field interaction. Besides the HF method, other methods worth mentioning for solving the many-body Schrödinger equation are: variational methods such as the configuration interaction method (CI), non-variational methods such as the couple cluster method (CC), many-body perturbation Theory (MBPT) and Møller-Plesset approaches.

1.1.1 Density Functional Theory (DFT)

The bases of Density Functional Theory rely on the Hohenberg-Kohn theorems and the equations derived by Kohn and Sham. The first theorem states that the ground-state electronic density, $\rho_0(r)$, contains the same precise information about the system as the ground-state wave function ψ_0 and, therefore, the ground-state wave function can be expressed as a functional of the ground-state electronic density. This allows to write the ground-state expectation value of the Hamiltonian as a functional of ρ_0 . Knowing the molecular Hamiltonian, the many-electron Schrödinger equation can be solved and the ground-state energy of the system and numerous electronic properties of the system can be obtained. Thus, in practice, the first theorem establishes that the ground-state energy of a many-body system, $E_0[\rho]$, is a functional of the ground-state electronic density, which depends on an external potential, $\nu_{ext}(r)$, The total energy functional, $E_{\nu}[\rho]$, can be represented as

$$E_{\nu}[\rho] = F[\rho] + \int \nu_{ext}(r)\rho(r)dr$$
1.4

where $F[\rho] = T[\rho] + V_{ee}[\rho]$, is a universal functional of the density and contains the kinetic energy, $T[\rho]$, and the electron-electron interaction, $V_{ee}[\rho]$, and is independent of $v_{ext}(r)$.

The second theorem (proven with the variational principle⁴) states that there exists an energy functional, $E_{\nu}[\rho]$, that is minimized by the correct or ideal ground-state electron density, ρ_0 , in the external potential, $\nu_{ext}(r)$, and that the minimal value of the energy functional represents the ground-state energy of the system, E_0 .

$$E_{\nu}[\rho] \ge E_{\nu}[\rho_0] = E_0 \tag{1.5}$$

The theorems provide the fundamental principles of DFT but do not allow for its practical use. The practical use of DFT lies within the Kohn-Sham formalism. ¹⁰ In this formalism, the Schrödinger equation is written for a fictitious system of non-interacting particles moving in an effective potential with the same density as a system of interacting particles. The following is a one-electron Schrödinger-like equation, named the Kohn-Sham equation, and can be solved iteratively.

$$\left(-\frac{1}{2}\nabla^2 + \nu_0\right)\varphi_i = \varepsilon_i\varphi_i$$
 1.6

The eigenvalue ϵ_i is the Kohn-Sham energy of the Kohn-Sham orbital φ_i , ν_0 is the effective potential, and the electronic density distribution is calculated by summing all the occupied Kohn-Sham orbitals, φ_i .

$$\rho(r) = \sum_{i}^{N} |\phi_i(r)|^2$$
1.7

The general expression of the total energy of the ground state in this formalism is

$$E[\rho] = v_{ext}(r) + T[\rho] + v_{Coulomb}(\rho) + E_{xc}[\rho]$$
1.8

The first term on the right-hand side is the external potential, the second term is the kinetic energy of the non-interacting electrons (the fictitious Kohn-Sham system), the third term represents the Coulomb repulsion of the electrons, and the fourth term is the exchange and correlation energy, which includes all interactions not accounted for by the other terms (see below). The exchange and correlation energy, $E_{xc}[\rho]$, is the only term in the Kohn-Sham formalism that cannot be computed from first principles. To assess the energy of the real system it is necessary to approximate this unknown term.

Therefore, the usefulness of DFT depends on the ability to find approximations to the exchange and correlation energy functional in a way that they can represent the system of interest in an accurate and time-effective manner.¹¹

The exchange-correlation energy is the sum of the exchange energy, E_x , and the correlation energy, E_c , Eq.1.9.

$$E_{xc} = E_x + E_c$$

The exchange energy results from the anti-symmetry of the electronic wave function, takes into account the repulsive interaction between electrons of the same spin (Pauli exclusion principle), and can be evaluated exactly. The correlation energy results from the tendency of electrons to stay away from each other to decrease the Coulombic interaction. It is more pronounced for electrons of opposite spins as they are more likely to occupy the same orbitals. Exact electronic correlation cannot be calculated analytically. Besides the quantum exchange and correlation effects, the term, E_{xc} , contains the correction to the fictitious non-interacting system's kinetic energy from the real system's kinetic energy ($\Delta T = \text{real}$ -non-real).

Nowadays, various approximations exist for the exchange-correlation energy functional, $E_{XG}[\rho]$. Here are some of them:

- Local density approximation (LDA)¹⁰
 - Commonly used for the description of bulk metals and surfaces, its geometric predictions are usually accurate. However, it has difficulties when describing molecules and ionic systems where the electron density changes rapidly in space. It tends to overestimate binding energies and fails to reproduce ionization potentials.
- Generalized gradient approximation functionals, (GGAs)
 - o Give good results for molecular geometries and ground-state energies. The most commonly used are: PW91, 12 PBE, 13 RPBE 14.
- Hybrid functionals,
 - These are a linear combination of the (exact) exchange calculated with HF and exchange-correlation energies from other approximations. They are widely used for molecules and solids with localized electrons. Common hybrid functionals are PBE0 (25% of exact exchange combined with PBE exchange-correlation),^{15,16} HSE,¹⁷ B3LYP¹⁸ and the Minnesota metahybrids.¹⁹

DFT can be applied to many different systems, to name a few: solids, gases, liquids, polymers, ice, and chemical solutions. Depending on the system that we

want to study, specific basis sets are required. The basis set is a group of functions that expand the Kohn-Sham orbitals, ϕ_i , and their linear combination describes the wave function of the system. The basis set can be local (atom-centered orbitals), non-local (expanded through space) and augmented. Local basis sets are preferable to represent atoms and molecules with orbitals localized around the atoms. A commonly used local basis set is the Gaussian basis set. John Pople, who shared the Noble Prize with Walter Kohn in 1998, named the computational chemistry code "Gaussian" after these orbitals. Due to their local nature, they cannot describe well long-range interactions. Augmented basis sets include additional basis functions to those already present on the atoms, basically adding additional "subshells". Non-local basis sets are based on plane-wave functions, which require the use of periodic-boundary conditions, and are the gold standard for solids.

1.1.2 Free energies and adsorption potentials

The first and main motivation of this thesis is to outline simple computational methods based on first principles calculations using DFT for electrochemical systems. I will focus on affordable methods that can provide a tradeoff between computational expense and accuracy. Specifically focus on solvation effects near the surface of the electrode, the use of thermodynamic cycles to compute solution-phase energies of charged species, and the description of a correction scheme to detect gas-phase errors on the free energies of target molecules important for calculating adsorption processes in electrocatalysis. The second motivation of this thesis is to apply these simple methods to study complex adsorption processes at the $Pd_{ML}Pt(111)$ electrode surface. All the adsorption processes investigated experimentally were performed by Dr. Xiaoting Chen from our group.

Now we zoom out from the quantum chemistry regime and move our focus toward the thermodynamics of the system, which is obtained from the mathematical manipulation of the energies obtained from the DFT calculations. Often, the questions we try to answer do not require intensive computational resources: affordable and accurate simplifications are enough. In the context of electrocatalysis, we are interested in energies of adsorption of species at the interface between the catalyst and the electrolyte. The thermodynamic property that can provide such information is the Gibbs free energy of the reaction, G(T,P) = U + PV - TS, where, T and P are the temperature and pressure, U is the internal energy, P and V are pressure and volume and, in general, we are interested in processes at standard conditions, namely, 1 atm and 298.15 K. To calculate the free energies of adsorption processes, we require the energies of the individual components of the system. As shown in Figure 1.1, we need the energy of the species in the gas phase, the energies of the solution-phase species

(those in the bulk of the solution), the energies of the interacting electrode-

adsorbate system, and finally the energy of the electrode itself.

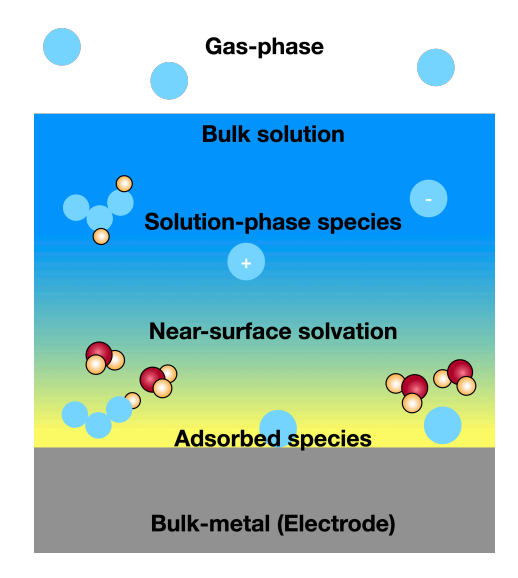


FIGURE 1.1

Illustration of the electrochemical environment and the different levels of abstraction as analyzed with DFT.

The reaction free energies are calculated as the difference of the individual free energies of the reactants and products of the chemical reaction we are investigating.

$$\Delta G^{\circ} = \sum G_{products} - \sum G_{reactants}$$
 1.10

The individual free energies are calculated as,

$$G^{\circ} = E_{DFT} + E_{ZPE} + \int_{T=0}^{T} C_{p} dT - TS$$
 1.11

 E_{DFT} is the relative energy given by the DFT simulation extrapolated to 0 K, E_{ZPE} is the zero-point vibrational energy calculated using statistical mechanics equations within the harmonic oscillator approximation, as shown in Eq.1.12, where h is Planck's constant (4.135667662 × $10^{-15} eV \cdot s$) and v_i are the frequencies of the vibrational modes i, in energy terms expressed as ε_i . T is the temperature (298.15 K) and S is the entropy. For adsorbates, S contains only the vibrational contributions calculated using Eq.1.13, S0 and for gas-phase species, S1 includes all entropy contributions and is taken from standard thermodynamic tables. In Eq. 1.13, S1 is the Boltzmann constant, S2 is the number of modes per atom of the adsorbate, S3 is the energy of the surface slab is approximated as the energy without the contributions from the zero-point energy and entropy.

$$E_{ZPE} = \sum_{i=1}^{n} \frac{1}{2} h \nu_i$$
 1.12

$$S_{vib} = k_B \sum_{i}^{3N} \left[-ln(1 - e^{\beta \varepsilon_i}) + \frac{\beta \varepsilon_i}{e^{(\beta \varepsilon_i - 1)}} \right]$$
 1.13

Note that within this thesis the enthalpic correction term ($\int_{T=0}^{T} C_p \ dT$) in Eq. 1.11, determined from heat capacity data, is neglected unless stated otherwise. When computing reaction energies, this term can often be neglected for systems with no hindered rotations without much loss of accuracy.

For an adsorption reaction like Eq.1.14, $*\,nH_2O$ represents the surface with adsorbed water, $A_{(g)}$ is a gas-phase molecule, $H^+ + e^-$ are a solvated proton and an electron, and $*\,[AH - nH_2O]$ is the co-adsorbed hydrogenated molecule and water system. In *Chapter 4*, we will discuss in detail how to determine the errors associated to the formation energies of gas-phase species and why it is useful to correct them.

$$*nH_2O + A_{(g)} + H^+ + e^- \rightarrow *[AH - nH_2O]$$
 1.14

Within the computational hydrogen electrode approach,²³ the energy corresponding to the proton-electron pair is set equal to $\frac{1}{2}\mu_{H_2}$ – neU, where U is the electrode potential in the reversible hydrogen electrode (RHE) scale, so that the free energy of adsorption of Eq.1.14 is:

$$\Delta G_{ads}^{*[AH-nH_2O]} = G_{*[AH-nH_2O]} - G_{*nH_2O} - G_{A(g)} - \frac{1}{2}\mu_{H_2} + neU$$
 1.15

Using free energies also allows to express the results in terms of potentials²⁴ using the Nernst equation for a reduction reaction:

$$\Delta G^{\circ} = -nFU_{eq}^{\circ}$$
 1.16

n is the number of moles of electrons transferred in the reaction, F is the Faraday constant (96.485 kJ mol⁻¹ V⁻¹ eq⁻¹) and U_{eq}° is the standard equilibrium potential of the cell, referred to the NHE.

For an adsorption process, we can determine the standard equilibrium potential U_{ads}° of reaction 1.16 when the free energy of adsorption in Eq.1.15 is set equal to zero, $\Delta G_{ads} = 0$.

$$U_{ads}^{\circ} = \frac{G_{*[AH-nH_2O]} - G_{*nH_2O} - G_{A(g)} - G_{H^+}}{-n|e|}$$
 1.17

The adsorption energy can be linearly shifted through the value of U, the last term of Eq.1.15.

Thanks to the computational hydrogen electrode (CHE) model²³, we can calculate the energetics of various electrochemical processes with DFT involving a fixed number of proton-electron pairs. The CHE is widespread in the computational electrochemistry community. Other simplifications used to model the electrochemical system are the treatment of the solution-phase environment through the incorporation of a solvation model; implicit solvation, ^{25–35} explicit ^{36–43} solvation or explicit near-surface solvation, also known as micro-solvation. ^{44–46} In the work presented in this PhD thesis, solvation effects are applied through the explicit near-surface solvation model.

Another simple model, which will be discussed in more detail in *Chapter 3*, is the use of tabulated equilibrium standard redox potentials and simple thermodynamic cycles to determine the free energy of a charged species in bulk solution. This allows for the calculation of equilibrium potentials for reactions in which there is not an equal number of proton and electrons. Although this model is not new, we discuss its usefulness and implications in detail.

1.2 Applications – Electrochemical formic acid oxidation and CO₂ reduction reactions

The second motivation of this thesis is to applied the DFT methods discussed in the first part to study fundamental questions pertaining to formic acid oxidation and production on the $Pd_{ML}Pt(111)$ electrode surface. More specifically, we aim to understand the adsorption processes on the bare $Pd_{ML}Pt(111)$ and elucidate the poisoning mechanisms during the oxidation and reduction reactions.

1.2.1 Practical Motivation

One of the quests of major focus toward a sustainable society is that of increasing the usage of renewables as a source of energy and decreasing the usage of fossil fuels. The latter increase greenhouse gas emissions (CH₄, CO₂, N₂O and natural gas), correlated to the increase of global temperature, leading to negative consequences such as global warming and climate change. CO₂ is responsible for more than half of the total emissions.⁴⁷

Renewable energy can be harvested from wind turbines, solar panels, etc. At the moment, we still rely on petroleum and natural gas as our primary source of energy, as shown in Figure 1.2. In principle, we can produce renewable energy and store that energy in chemical bonds with electrochemical cells. In electrolysers, renewable electricity can convert water and CO₂ into fuels such as hydrogen, methanol and formic acid. In fuel cells, hydrogen, methanol, or formic acid, are converted back into electrical energy through spontaneous electrochemical reactions at the two electrodes. Figure 1.3 illustrates a direct

formic acid fuel cell (DFAFC). The corresponding half-cell reactions at the anode and the cathode appear in Table 1.1.

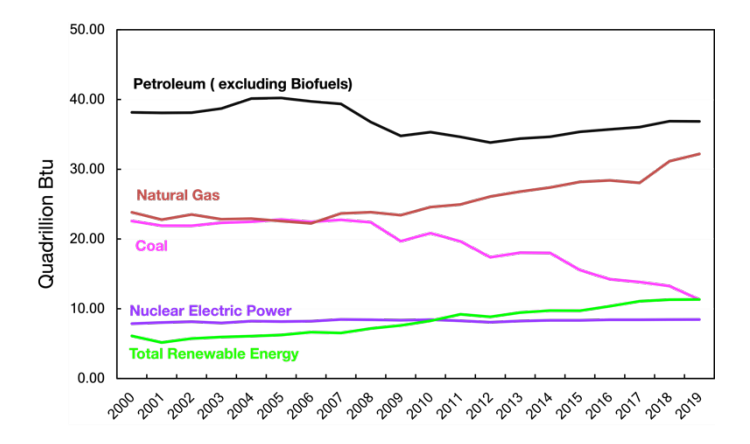


FIGURE 1.2

Energy consumption from different sources between the years 2000-2019. Data source: The U.S Energy Information Administration as per the International Energy Outlook of 2019.48

A fuel cell can offer high energy conversion efficiency and its operation is clean, as long as the fuels are produced from renewable electricity (contrary to combustion processes using fossil resources). Fuel cells contain an ion-conducting electrolyte or membrane, a fuel inlet, an oxidant inlet (oxygen source), an outlet for the reaction products, and two electrodes (anode and cathode). What makes fuel cells lose efficiency in general are the overvoltages required to drive the reactions at the anode and the cathode at a given current density. The further these overvoltages are from the equilibrium potentials of the corresponding half reactions, the less efficient the cell is.

The electrodes in a fuel cell are either the catalyst itself or contain the catalysts dispersed as nanoparticles on a conductive support. The catalyst should be able to enhance the kinetics of the reaction (high activity), and it should also be selective and stable. That is why many research efforts have been devoted to develop catalysts for fuel cells for both anode and cathode, but most importantly for the latter where the sluggish oxygen reduction reaction takes place.

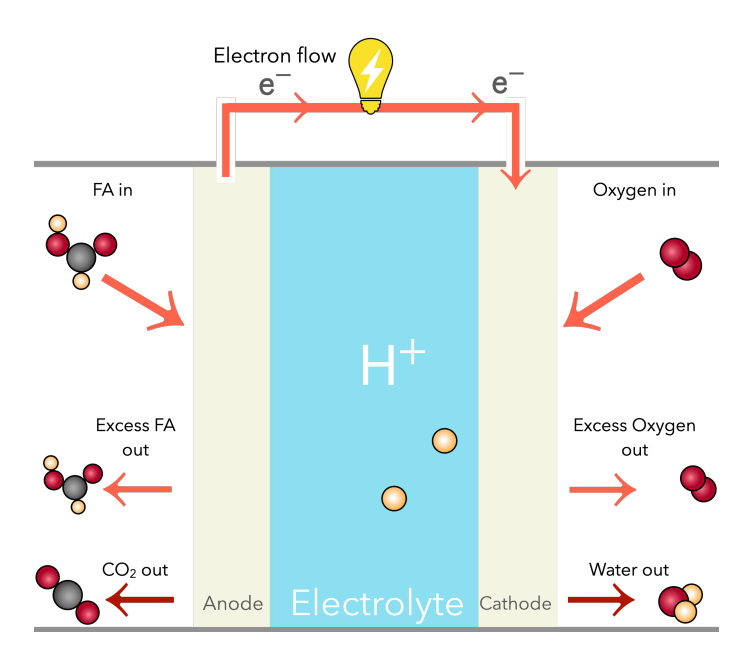


FIGURE 1.3

Illustration of a simplified direct formic acid fuel cell (DFAFC). Hydrogen: light yellow, Oxygen: red, Carbon: dark grey. The fuel, formic acid (FA), is fed to the cell to reach the anode where the oxidation reaction occurs producing CO_2 , protons, and electrons. The electrons flow from the anode to the cathode through an external circuit and the protons pass through the ion conducting-electrolyte to the cathode where they combine with oxygen and electrons to produce water. The fuel and oxidant that do not react, exit the cell as excess reactants.

Figure 1.3 illustrates a (DFAFC).^{49–51} In this cell, formic acid (FA) is the fuel. Since FA, is liquid at room temperature and contains two hydrogen atoms, it is also referred to as "liquid hydrogen" and "hydrogen-carrier".^{52,53} The half-cell anodic (oxidation of formic acid (FA)) and cathodic (oxygen reduction), reactions are shown in Table 1.1. The overall reaction is

$$HCOOH(l) + \frac{1}{2}O_2(g) \rightarrow CO_2(g) + H_2O(l)$$
 1.18

and its cell potential is, $U_{cell} = (1.23 - (-0.11) \text{ V vs SHE})^{54} = 1.34 \text{ V vs SHE}$.

DFAFCs have attracted commercial attention because FA can be stored at standard atmospheric pressures, increasing its appeal in the portable market with respect to hydrogen, which requires high pressure tanks to be stored. Furthermore, the performance with perfluoro sulfonic acid membranes like Nafion® is better than methanol,^{55,56} Alongside the commercial attention, the electrocatalytic oxidation of FA attracts fundamental attention because FA is a simple model molecule to understand the oxidation reaction of other more complex organic molecules.⁵⁷

Scalability and commercialization of DFAFCs at the moment is stagnant due to the deactivation of their commercial Pt-based electrocatalysts. The deactivation is due to poising of the electrocatalysts with CO. Research efforts have been focused on finding alternative catalysts that can tolerate CO poisoning during the oxidation. Pd-based catalysts have shown to be a good alternative, primary because Pd poisons at a slower rate than Pt. However, Pd is still not an ideal catalyst for large-scale production of DFAFCs, due to their poor stability. Alternatives combining Pt- or Pd-based catalysts with other metals have shown improvements, not only on the stability but also toward CO poisoning.⁵⁸⁻⁶⁶ However, the fundamental explanation on why various materials seem to improve their CO tolerance remains elusive, and, therefore, proposes an interesting research question warranting further investigation. In *Chapter 6* we aim to provide insight into this question by studying Pd_{MI} Pt(111), a bimetallic catalyst, made of the two pure metals with the highest activity towards formic acid oxidation. It is also important to note that PdPt catalysts are highly active for the CO₂ reduction reaction. They can achieve CO₂ reduction to HCOOH at low overpotentials, and CO poisoning tolerance during the reduction rection is observed, as well.⁶⁷ Thus, they are appealing as bifunctional electrocatalysts for CO₂ reduction and FA oxidation.

Table 1.1 enumerates different types of fuel cells at different operating temperatures and the corresponding reactions at the anode and the cathode. Each of the half-cell reactions can be catalyzed by different materials that have been developed and optimized for the specific reactions.

TABLE 1.1Fuel cells currently in use and in development, data obtained and adapted from reference⁶⁸ except when specified otherwise.

	Operating		
	Temp. (°C)	Anode	Cathode
AFC			1
(Alkaline)	<100	$H_2 + 20H^- \rightarrow 2$	$H_2O + 2e^ \frac{1}{2}O_2 + H_2O + 2e^- \rightarrow 2OH^-$
PEM		_	
(Polymer			
Electrolyte			1 0 + 211+ + 2 - + 11 0
Membrane)	60-120	$H_2 \rightarrow 2H^+$	$+ 2e^{-}$ $\frac{1}{2}O_2 + 2H^+ + 2e^- \rightarrow H_2O$
DMFC		CH ₃ OH +	$2H_2O$ 3
(Direct Methanol)	60-120	\rightarrow CO ₂ + 6H	$\frac{3}{2}$ 0 ₂ + H ₂ 0 + 2e ⁻ \rightarrow 20H ⁻
DFAFC			
(Direct Formic		HC00	H 1
Acid)	50-8069	\rightarrow CO ₂ + 2H	$\frac{1}{2}O_2 + 2H^+ + 2e^- \rightarrow H_2O$
PAFC			1
(Phosphoric Acid)	160-220	$H_2 \rightarrow 2H^+$	$+2e^{-}$ $\frac{1}{2}O_2 + 2H^+ + 2e^{-} \rightarrow H_2O$
			1 0 + 60 + 2-7
MCF		$H_2 + CC$	$\frac{1}{2}O_2 + CO_2 + 2e^-$
(Molten Carbonate)	600-800	\rightarrow H ₂ O + CO ₂	$_2$ 2 + 2e ⁻ \rightarrow CO ₃ ²⁻
SOFC			1 2 - 2 - 2 -
(Solid Oxide)	800-1000	$H_2 + 0^{2-} \rightarrow H$	$I_2O + 2e^ \frac{1}{2}O_2 + 2e^- \rightarrow O^-$

1.2.2 Scientific Motivation

The fundamental motivation of the second part of this research comes from the need to know why PdPt catalysts show tolerance toward CO poisoning compared to Pt, during both oxidation of formic acid and reduction of CO₂ to formic acid.

To this end, we use well-defined surfaces of Pd and Pt in this research because the atomic-level control they provide can deliver a fundamental understanding of the underlying mechanisms we are interested in, specifically, the tolerance of $Pd_{MI}Pt(111)$ toward CO. Furthermore, there is a vast literature on the topic, particularly on Pt(111), that we can use to shape our understanding of the research questions that motivate us. Also, results obtained on single-crystal surfaces are ideally suitable for comparison to DFT calculations.

The formic acid oxidation reaction involves the transfer of two protons and electrons to form CO₂, as shown below.

$$HCOOH \rightleftharpoons CO_2(g) + 2 H^+ + 2e^-$$

The first mechanism for formic acid oxidation on Pt was proposed by Capon and Parsons,⁷⁰ involving parallel catalytic routes called the direct and indirect pathways. They proposed that formic acid oxidizes to an active intermediate, *COOH, that could either undergo a dehydration (indirect pathway), where a poisoning species seems to form, or a dehydrogenation (direct pathway). In the indirect pathway, the poisoning species, now known as *CO,^{71,72} can be further oxidized to CO₂, while in the direct pathway the intermediate is directly oxidized to CO₂. Later, Cuesta and coworkers⁷³ using attenuated total reflectance-surface-enhanced infrared absorption spectroscopy (ATR-SEIRAS), suggested that the active intermediate for both the indirect and direct paths is adsorbed formate.

The proposal of formate as the active intermediate became controversial when evidence suggested that the faradaic current during the oxidation reaction was observed to increase faster than the formate coverage did,⁷² and also because in this configuration, both oxygens are bound to the surface, and breaking the C-H bond would cost about 1.0 eV.⁷⁴ Therefore, Chen and coworkers⁷² proposed that formate is more a spectator than an active intermediate. Using DFT, Janik⁷⁴ and Schwarz²⁶ proposed that the active intermediate for the direct pathway could be formate with C-H down, as in this configuration the breakage of the C-H bond has a low or no barrier at all.

We can transfer this knowledge to other active catalysts such as Pd. Palladium is highly active for the formic acid oxidation reaction, and for some years CO poisoning was not visible in experiments. Vielstich showed in 1988⁷⁵ that the catalyst could be deactivated by strongly adsorbed species, but evidence of the identity of the species was elusive. Nowadays, we have evidence that the deactivation of the catalysts is caused by CO formation on palladium, although at a much slower rate than on Pt.⁷⁶ In addition, in relevant conditions for fuel cells, the catalyst is deactivated only after long periods of operation.⁷⁷ Therefore, palladium is still an attractive catalyst because it is more tolerant to CO poisoning than Pt during formic acid oxidation. One of the drawbacks, however, is its

difficult preparation and cleaning, especially for single-crystal electrodes, limiting it to fundamental research.

As a result, research on bimetallic catalysts containing Pd and another easy to prepare and clean metal such as Pt, is a promising alternative to understand CO tolerance and increase the catalyst stability. Palladium overlayers grown epitaxially on Pt(hkl) have been investigated by various research groups, namely, those of Kolb, ^{78,79} Feliu, ^{80,81} Markovic ^{82,83} and our group in Leiden. ⁸⁴ These catalysts showed high activity toward formic acid oxidation and clear resistance toward poisoning during the oxidation. ⁷⁸ Furthermore, Kortlever and coworkers ⁸⁵ showed the quasi-reversible behavior of the bimetallic catalyst for both formic acid oxidation and carbon dioxide reduction, as expected for a two-electron transfer reaction. ⁸⁶ This research was followed by work by Chen et al. ⁸⁷ on single crystal catalysts of Pd overlayers on Pt(100), i.e. Pd_{ML}Pt(100), to obtain a more fundamental understanding of the reaction mechanisms.

In the second part of this PhD thesis, we will expand the previous research and focus on comparative studies supported by DFT and experiments performed by Dr. Chen from our group on well-defined surfaces of Pt(111) and Pd_{ML}Pt(111). First, we study in detail the adsorption processes on the bare surface and then we move on to the catalytic reactions, namely, formic acid oxidation and carbon dioxide reduction, with a focus on understanding the absence of CO poisoning observed with the Pd_{ML}Pt(111) catalysts.

1.3 Scope and outline of this PhD thesis

This PhD thesis is organized in two parts: the first part, *Chapters* 2-4, discusses DFT methodologies based on affordable and simple approximations to facilitate the usability of DFT for electrochemical systems, aspiring toward precise, robust and practical procedures. It specifically focuses on near-surface solvation and methods to calculate accurate reference free energies of charged species and gasphase species. In the second part, *Chapters* 5 and 6, these methods are applied to the study of electrocatalytic adsorption processes on Pd_{ML}Pt(111) and its CO tolerance during the formic acid oxidation reaction and carbon dioxide reduction. The simulations are complemented by relevant experimental results, performed by Dr. Xiaoting Chen⁸⁴ from the experimental counterpart of the CASC research group.

In *Chapter 2*, we do a survey of the influence of different functionals, specifically those including and not including long-range interactions, on the near-surface solvation of hydroxide on different Pt near-surface alloys Pt-M-Pt (111). The calculated hydroxide solvation energies allow us to divide the functionals into two groups: over-binding and under-binding functionals. We observe that extrapolating solvation energies is safe when done within the same group of functionals. The difference on average between the solvation energies in these two groups is 0.15 eV. For accurate catalyst design for the oxygen reduction reaction, it is then recommended not to extrapolate energies from one group to the other, as the criteria for catalyst design for this reaction is $\Delta G_{OH} - \Delta G_{OH}^{Pt(111)} \approx 0.1 - 0.15$ eV.

In *Chapter 3*, we review and discuss a method to obtain free energies of charged species in bulk solution, important for electrochemical adsorption processes. This

method uses simple electrochemical thermodynamic cycles to map the energy of a neutral species with that of a charged species using a tabulated half-cell equilibrium reduction potential that contains the charged and the neutral species. With this method we can avoid DFT calculations of the charged species in bulk solution, which is challenging to perform with DFT. The method can be used to calculate equilibrium adsorption potentials involving charged species.

Chapter 4 presents a systematic workflow used to determine errors associated to organic functional groups on 27 different gas-phase molecules. We use this method for CO₂ reduction and CO reduction reactions and show that it is easy to implement and inexpensive, providing a very good match with experimental onset potentials determined for the CO₂ reduction reaction to CO. This method can be used to pinpoint errors of other molecules not studied here and increase the accuracy of DFT results for different exchange correlation functionals.

Chapter 5 discusses a comparative study of the adsorption processes on the well-defined $Pd_{ML}Pt(111)$ and Pt(111) by means of DFT calculations and experiments using cyclic voltammetry. The adsorption of hydroxide, hydrogen, oxygen and water was investigated at different coverages and as a function of applied potential, from which we built surface phase diagrams. We also studied the adsorption of various anions and found that they interact more strongly on $Pd_{ML}Pt(111)$ compared to Pt(111). Our results showed that the "hydrogen" region in the CV of $Pd_{ML}Pt(111)$ can be more accurately described as a "hydrogen-hydroxyl-cation-anion" region.

Chapter 6 extends the investigation from Chapter 5 to the electro-oxidation of formic acid to carbon dioxide, and the reverse reaction, that is the electroreduction of carbon dioxide to formic acid. We show the role of formate during the oxidation reaction as a spectator, the coverage of which prevents *CO poisoning at $Pd_{ML}Pt(111)$ at oxidizing potentials. During the electroreduction, $Pd_{ML}Pt(111)$ is poisoned by *CO at higher negative potentials compared to Pt(111). We show that the activation of the poisoning path is related to the adsorption of *COOH at earlier potentials on Pt than on $Pd_{ML}Pt(111)$.

1.4 References

- (1) Pupin, M. (Mihajlo). *From Immigrant to Inventor*; Charles Scribner's Sons: New York, London, 1923.
- (2) Capelle, K. A Bird's-Eye View of Density-Functional Theory. arXiv:cond-mat/0211443v5 **2006**.
- (3) Ferro-Costas, D.; Pendás, Á. M.; González, L.; Mosquera, R. A. Beyond the Molecular Orbital Conception of Electronically Excited States through the Quantum Theory of Atoms in Molecules. *Phys. Chem. Chem. Phys.* **2014**, *16* (20), 9249-9258.
- (4) Ideas of Quantum Chemistry; Piela, L., Ed.; Elsevier: Amsterdam, 2007.
- (5) Bader, R. F. W. Atoms in Molecules: A Quantum Theory; Clarendon Press: Oxford, 1994.
- (6) Lee, J. G. Computational Materials Science: An Introduction; CRC Press, 2011.
- (7) Schrödinger, E. Quantisierung Als Eigenwertproblem. *Ann. Phys.* **1926**, *385* (13), 437-490.
- (8) Born, M.; Oppenheimer, R. Zur Quantentheorie Der Molekeln. *Ann. Phys.* **1927**, *389*, 457–484.
- (9) Hohenberg, P.; Kohn, W. Inhomogeneous Electron Gas. *Phys. Rev.* **1964**, *136* (3B), B864-B871.
- (10) Kohn, W.; Sham, L. J. Self-Consistent Equations Including Exchange and Correlation Effects. *Phys. Rev.* **1965**, *140* (4A), A1133-A1138.
- (11) Kohn, W. Nobel Lecture: Electronic Structure of Matter---Wave Functions and Density Functionals. *Rev. Mod. Phys.* **1999**, *71* (5), 1253–1266.
- (12) Perdew, J. P.; Burke, K.; Wang, Y. Generalized Gradient Approximation for the Exchange-Correlation Hole of a Many-Electron System. *Phys. Rev. B* **1996**, *54* (23), 16533-16539.
- (13) Perdew, J. P.; Burke, K.; Ernzerhof, M. Generalized Gradient Approximation Made Simple. *Phys. Rev. Lett.* **1996**, 77 (18), 3865-3868.
- (14) Hammer, B.; Hansen, L. B.; Nørskov, J. K. Improved Adsorption Energetics within Density-Functional Theory Using Revised Perdew-Burke-Ernzerhof Functionals. *Phys. Rev. B* **1999**, *59* (11), 7413-7421.
- (15) Perdew, J. P.; Ernzerhof, M.; Burke, K. Rationale for Mixing Exact Exchange with Density Functional Approximations. *J. Chem. Phys.* **1996**, *105* (22), 9982-9985.
- (16) Adamo, C.; Barone, V. Toward Reliable Density Functional Methods without Adjustable Parameters: The PBE0 Model. *J. Chem. Phys.* **1999**, *110* (13), 6158-6170.
- (17) Heyd, J.; Scuseria, G. E.; Ernzerhof, M. Hybrid Functionals Based on a Screened Coulomb Potential. *J. Chem. Phys.* **2003**, *118* (18), 8207-8215.
- (18) Stephens, P. J.; Devlin, F. J.; Chabalowski, C. F.; Frisch, M. J. Ab Initio Calculation of Vibrational Absorption and Circular Dichroism Spectra Using Density Functional Force Fields. *J. Phys. Chem.* **1994**, *98* (45), 11623-11627.

- (19) Zhao, Y.; Truhlar, D. G. The M06 Suite of Density Functionals for Main Group Thermochemistry, Thermochemical Kinetics, Noncovalent Interactions, Excited States, and Transition Elements: Two New Functionals and Systematic Testing of Four M06-Class Functionals and 12 Other Functionals. *Theor Chem Account* 2008, 120 (1), 215-241.
- (20) Fultz, B. Vibrational Thermodynamics of Materials. *Prog. Mater. Sci.* **2010**, *55*, 247–352.
- (21) Chase, Jr., M. W.; Davies, C. A.; Downey, Jr., J. R.; Frurip, D. J.; MacDonald, R. A.; Syverud, A. N. NIST-JANAF Thermochemical Tables. *J. Phys. Chem. Ref. Data* **1985**, *Suppl. 1 to Vol. 14*, 1856.
- (22) Atkins, P. W. *Atkins' Physical Chemistry*, 7th ed.; Paula, J. de, Series Ed.; Physical chemistry; Oxford [etc.]: Oxford University Press, 2002.
- (23) Nørskov, J. K.; Rossmeisl, J.; Logadottir, A.; Lindqvist, L.; Kitchin, J. R.; Bligaard, T.; Jónsson, H. Origin of the Overpotential for Oxygen Reduction at a Fuel-Cell Cathode. *J. Phys. Chem. B* **2004**, *108* (46), 17886-17892.
- (24) Inzelt, G. Crossing the Bridge between Thermodynamics and Electrochemistry. From the Potential of the Cell Reaction to the Electrode Potential. *ChemTexts* **2014**, *1* (1), 2.
- (25) Letchworth-Weaver, K.; Arias, T. A. Joint Density Functional Theory of the Electrode-Electrolyte Interface: Application to Fixed Electrode Potentials, Interfacial Capacitances, and Potentials of Zero Charge. *Phys. Rev. B* **2012**, 86 (7), 075140.
- (26) Schwarz, K. A.; Sundararaman, R.; Moffat, T. P.; Allison, T. C. Formic Acid Oxidation on Platinum: A Simple Mechanistic Study. *Phys. Chem. Chem. Phys.* **2015**, *17* (32), 20805–20813.
- (27) Sundararaman, R.; Schwarz, K. Evaluating Continuum Solvation Models for the Electrode-Electrolyte Interface: Challenges and Strategies for Improvement. *The Journal of Chemical Physics* **2017**, *146* (8), 084111.
- (28) Mathew, K.; Sundararaman, R.; Letchworth-Weaver, K.; Arias, T. A.; Hennig, R. G. Implicit Solvation Model for Density-Functional Study of Nanocrystal Surfaces and Reaction Pathways. *J. Chem. Phys.* **2014**, *140* (8), 084106.
- (29) Mathew, K.; Hennig, R. G. Implicit Self-Consistent Description of Electrolyte in Plane-Wave Density-Functional Theory. *arXiv:1601.03346 [cond-mat]* **2016**.
- (30) Ludwig, T.; Gauthier, J. A.; Brown, K. S.; Ringe, S.; Nørskov, J. K.; Chan, K. Solvent-Adsorbate Interactions and Adsorbate-Specific Solvent Structure in Carbon Dioxide Reduction on a Stepped Cu Surface. *J. Phys. Chem. C* **2019**, *123* (10), 5999-6009.
- (31) Garcia-Ratés, M.; López, N. Multigrid-Based Methodology for Implicit Solvation Models in Periodic DFT. *J. Chem. Theory Comput.* **2016**, *12* (3), 1331-1341.
- (32) Dupont, C.; Andreussi, O.; Marzari, N. Self-Consistent Continuum Solvation (SCCS): The Case of Charged Systems. *J. Chem. Phys.* **2013**, *139* (21), 214110.
- (33) Nishihara, S.; Otani, M. Hybrid Solvation Models for Bulk, Interface, and Membrane: Reference Interaction Site Methods Coupled with Density Functional Theory. *Phys. Rev. B* **2017**, *96* (11), 115429.

- (34) Melander, M. M.; Kuisma, M. J.; Christensen, T. E. K.; Honkala, K. Grand-Canonical Approach to Density Functional Theory of Electrocatalytic Systems: Thermodynamics of Solid-Liquid Interfaces at Constant Ion and Electrode Potentials. J. Chem. Phys. **2018**, 150 (4), 041706.
- (35) Sundararaman, R.; Letchworth-Weaver, K.; Schwarz, K. A. Improving Accuracy of Electrochemical Capacitance and Solvation Energetics in First-Principles Calculations. *J. Chem. Phys.* **2018**, *148* (14), 144105.
- (36) Filhol, J.-S.; Neurock, M. Elucidation of the Electrochemical Activation of Water over Pd by First Principles. *Angew. Chem. Int. Ed.* **2006**, 45 (3), 402-406.
- (37) McCrum, I. T.; Janik, M. J. PH and Alkali Cation Effects on the Pt Cyclic Voltammogram Explained Using Density Functional Theory. *J. Phys. Chem. C* **2016**, *120* (1), 457-471.
- (38) Kolb, M. J.; Wermink, J.; Calle-Vallejo, F.; Juurlink, L. B. F.; Koper, M. T. M. Initial Stages of Water Solvation of Stepped Platinum Surfaces. *Phys. Chem. Chem. Phys.* **2016**, *18* (5), 3416–3422.
- (39) Morais, R. F. de; Kerber, T.; Calle-Vallejo, F.; Sautet, P.; Loffreda, D. Capturing Solvation Effects at a Liquid/Nanoparticle Interface by Ab Initio Molecular Dynamics: Pt201 Immersed in Water. *Small* **2016**, *12* (38), 5312-5319.
- (40) Liu, S.; White, M. G.; Liu, P. Mechanism of Oxygen Reduction Reaction on Pt(111) in Alkaline Solution: Importance of Chemisorbed Water on Surface. *J. Phys. Chem. C* **2016**, *120* (28), 15288-15298.
- (41) Karlberg, G. S. Adsorption Trends for Water, Hydroxyl, Oxygen, and Hydrogen on Transition-Metal and Platinum-Skin Surfaces. *Phys. Rev. B* **2006**, *74* (15), 153414.
- (42) Tripkovic, V.; Skúlason, E.; Siahrostami, S.; K. Nørskov, J.; Rossmeisl, J. The Oxygen Reduction Reaction Mechanism on Pt(111) from Density Functional Theory Calculations. *Electrochim. Acta* **2010**, *55*,(27), 7975–7981.
- (43) Gauthier, J. A.; Dickens, C. F.; Chen, L. D.; Doyle, A. D.; Nørskov, J. K. Solvation Effects for Oxygen Evolution Reaction Catalysis on IrO2(110). *J. Phys. Chem. C* **2017**, *121* (21), 11455–11463.
- (44) Mills, J. N.; McCrum, I. T.; Janik, M. J. Alkali Cation Specific Adsorption onto Fcc(111) Transition Metal Electrodes. *Phys. Chem. Chem. Phys.* **2014**, *16* (27), 13699-13707.
- (45) Calle-Vallejo, F.; F. de Morais, R.; Illas, F.; Loffreda, D.; Sautet, P. Affordable Estimation of Solvation Contributions to the Adsorption Energies of Oxygenates on Metal Nanoparticles. *J. Phys. Chem. C* **2019**, *123* (9), 5578-5582.
- (46) Rendón-Calle, A.; Builes, S.; Calle-Vallejo, F. Substantial Improvement of Electrocatalytic Predictions by Systematic Assessment of Solvent Effects on Adsorption Energies. *Appl. Catal. B* **2020**, *276*, 119147.
- (47) US EPA, O. Inventory of U.S. Greenhouse Gas Emissions and Sinks https://www.epa.gov/ghgemissions/inventory-us-greenhouse-gas-emissions-and-sinks (accessed Mar 23, 2021).
- (48) Capuano, D. L. International Energy Outlook 2020 (IEO2020). 2019, 7.
- (49) Yu, X.; Pickup, P. G. Recent Advances in Direct Formic Acid Fuel Cells (DFAFC). J. Power Sources **2008**, 182 (1), 124-132.

- (50) Fang, Z.; Chen, W. Recent Advances in Formic Acid Electro-Oxidation: From the Fundamental Mechanism to Electrocatalysts. *Nanoscale Adv.* **2021**, *3* (1), 94-105.
- (51) Aslam, N. M.; Masdar, M. S.; Kamarudin, S. K.; Daud, W. R. W. Overview on Direct Formic Acid Fuel Cells (DFAFCs) as an Energy Sources. *APCBEE Procedia* **2012**, 3, 33-39.
- (52) Eppinger, J.; Huang, K.-W. Formic Acid as a Hydrogen Energy Carrier. *ACS Energy Lett.* **2017**, *2* (1), 188–195.
- (53) Grasemann, M.; Laurenczy, G. Formic Acid as a Hydrogen Source Recent Developments and Future Trends. *Energy Environ. Sci.* **2012**, *5* (8), 8171-8181.
- (54) Bratsch, S. G. Standard Electrode Potentials and Temperature Coefficients in Water at 298.15 K. J. Phys. Chem. Ref. Data **1989**, 18 (1), 1-21.
- (55) Rhee, Y.-W.; Ha, S. Y.; Masel, R. I. Crossover of Formic Acid through Nafion® Membranes. *Journal of Power Sources* **2003**, *117* (1), 35–38.
- (56) Kim, H. S.; Morgan, R. D.; Gurau, B.; Masel, R. I. A Miniature Direct Formic Acid Fuel Cell Battery. *Journal of Power Sources* **2009**, *188* (1), 118–121.
- (57) Boronat-González, A.; Herrero, E.; Feliu, J. M. Heterogeneous Electrocatalysis of Formic Acid Oxidation on Platinum Single Crystal Electrodes. *Current Opinion in Electrochemistry* **2017**, *4* (1), 26–31.
- (58) Jiang, K.; Zhang, H.-X.; Zou, S.; Cai, W.-B. Electrocatalysis of Formic Acid on Palladium and Platinum Surfaces: From Fundamental Mechanisms to Fuel Cell Applications. *Phys. Chem. Chem. Phys.* **2014**, *16* (38), 20360-20376.
- (59) Kang, Y. S.; Choi, D.; Cho, J.; Park, H.-Y.; Lee, K.-S.; Ahn, M.; Jang, I.; Park, T.; Ham, H. C.; Yoo, S. J. Highly Active and Durable Ordered Intermetallic PdFe Electrocatalyst for Formic Acid Electrooxidation Reaction. ACS Appl. Energy Mater. 2020, 3 (5), 4226-4237.
- (60) Brandt, K.; Steinhausen, M.; Wandelt, K. Catalytic and Electro-Catalytic Oxidation of Formic Acid on the Pure and Cu-Modified Pd(111)-Surface. *J. Electroanal. Chem.* **2008**, *616* (1), 27–37.
- (61) Ji, Y.; Zhao, R.; Zhang, G.; Chen, Y.; Tang, Y.; Lu, T. Room-Temperature Synthesis and Electrocatalysis of Carbon Nanotubes Supported Palladium-Iron Alloy Nanoparticles. *Electrochimica Acta* **2013**, *111*, 898-902.
- (62) Gojković, S. Lj.; Tripković, A. V.; Stevanović, R. M.; Krstajić, N. V. High Activity of Pt4Mo Alloy for the Electrochemical Oxidation of Formic Acid. *Langmuir* **2007**, 23 (25), 12760-12764.
- (63) Kang, Y.; Qi, L.; Li, M.; Diaz, R. E.; Su, D.; Adzic, R. R.; Stach, E.; Li, J.; Murray, C. B. Highly Active Pt3Pb and Core-Shell Pt3Pb-Pt Electrocatalysts for Formic Acid Oxidation. ACS Nano 2012, 6 (3), 2818-2825.
- (64) Casado-Rivera, E.; Volpe, D. J.; Alden, L.; Lind, C.; Downie, C.; Vázquez-Alvarez, T.; Angelo, A. C. D.; DiSalvo, F. J.; Abruña, H. D. Electrocatalytic Activity of Ordered Intermetallic Phases for Fuel Cell Applications. J. Am. Chem. Soc. 2004, 126 (12), 4043-4049.
- (65) Xu, D.; Bliznakov, S.; Liu, Z.; Fang, J.; Dimitrov, N. Composition-Dependent Electrocatalytic Activity of Pt-Cu Nanocube Catalysts for Formic Acid Oxidation. *Angew. Chem. Int. Ed.* **2010**, *49* (7), 1282-1285.

- (66) Hwang, E.; Kim, H.; Park, H.; Lim, T.; Kim, Y.-T.; Ahn, S. H.; Kim, S.-K. Pd-Sn Alloy Electrocatalysts for Interconversion Between Carbon Dioxide and Formate/Formic Acid. J. Nanosci. Nanotechnol **2017**, 17 (10), 7547–7555.
- (67) Kortlever, R.; Peters, I.; Koper, S.; Koper, M. T. M. Electrochemical CO2 Reduction to Formic Acid at Low Overpotential and with High Faradaic Efficiency on Carbon-Supported Bimetallic Pd-Pt Nanoparticles. *ACS Catal.* **2015**, *5* (7), 3916-3923.
- (68) Carrette, L.; Friedrich, K. A.; Stimming, U. Fuel Cells Fundamentals and Applications. *Fuel Cells* **2001**, *1* (1), 5-39.
- (69) Rees, N. V.; Compton, R. G. Sustainable Energy: A Review of Formic Acid Electrochemical Fuel Cells. *J Solid State Electrochem* **2011**, *15* (10), 2095-2100.
- (70) Capon, A.; Parsons, R. The Oxidation of Formic Acid on Noble Metal Electrodes: II. A Comparison of the Behaviour of Pure Electrodes. *J. Electroanal. Chem. Interf. Electrochem.* **1973**, *44* (2), 239-254.
- (71) Beden, B.; Bewick, A.; Lamy, C. A Study by Electrochemically Modulated Infrared Reflectance Spectroscopy of the Electrosorption of Formic Acid at a Platinum Electrode. *J. Electroanal. Chem. Interf. Electrochem.* **1983**, 148 (1), 147-160.
- (72) Chen, Y.-X.; Heinen, M.; Jusys, Z.; Behm, R. J. Bridge-Bonded Formate: Active Intermediate or Spectator Species in Formic Acid Oxidation on a Pt Film Electrode? *Langmuir* **2006**, *22* (25), 10399-10408.
- (73) Cuesta, A.; Cabello, G.; Gutiérrez, C.; Osawa, M. Adsorbed Formate: The Key Intermediate in the Oxidation of Formic Acid on Platinum Electrodes. *Phys. Chem. Chem. Phys.* **2011**, *13* (45), 20091-20095.
- (74) Neurock, M.; Janik, M.; Wieckowski, A. A First Principles Comparison of the Mechanism and Site Requirements for the Electrocatalytic Oxidation of Methanol and Formic Acid over Pt. *Faraday Discuss.* **2008**, *140* (0), 363-378.
- (75) Solis, V.; Iwasita, T.; Pavese, A.; Vielstich, W. Investigation of Formic Acid Oxidation on Palladium in Acidic Solutions by On-Line Mass Spectroscopy. *J. Electroanal. Chem. Interf. Electrochem.* **1988**, 255 (1), 155-162.
- (76) Miyake, H.; Okada, T.; Samjeské, G.; Osawa, M. Formic Acid Electrooxidation on Pd in Acidic Solutions Studied by Surface-Enhanced Infrared Absorption Spectroscopy. *Phys. Chem. Chem. Phys.* **2008**, *10* (25), 3662-3669.
- (77) Zhang, H.-X.; Wang, S.-H.; Jiang, K.; André, T.; Cai, W.-B. In Situ Spectroscopic Investigation of CO Accumulation and Poisoning on Pd Black Surfaces in Concentrated HCOOH. *J. Power Sources* **2012**, *199*, 165-169.
- (78) Baldauf, M.; Kolb, D. M. Formic Acid Oxidation on Ultrathin Pd Films on Au(Hkl) and Pt(Hkl) Electrodes. *J. Phys. Chem.* **1996**, *100* (27), 11375–11381.
- (79) Hoyer, R.; Kibler, L. A.; Kolb, D. M. The Initial Stages of Palladium Deposition onto Pt(1 1 1). *Electrochim. Acta* **2003**, *49* (1), 63-72.
- (80) Álvarez, B.; Climent, V.; Rodes, A.; M. Feliu, J. Potential of Zero Total Charge of Palladium Modified Pt(111) Electrodes in Perchloric Acid Solutions. *Phys. Chem. Chem. Phys.* **2001**, *3* (16), 3269–3276.
- (81) Souza-Garcia, J.; Berná, A.; Ticianelli, E. A.; Climent, V.; Feliu, J. M. Electrochemical Properties of Palladium Adlayers on Pt(110) Substrates. *J. Electroanal. Chem.* **2011**, *660* (2), 276-284.

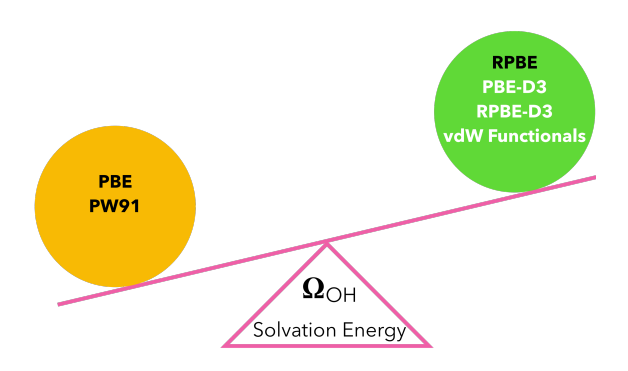
- (82) Marković, N. M.; Lucas, C. A.; Climent, V.; Stamenković, V.; Ross, P. N. Surface Electrochemistry on an Epitaxial Palladium Film on Pt(111): Surface Microstructure and Hydrogen Electrode Kinetics. *Surf. Sci.* **2000**, *465* (1), 103-114.
- (83) Arenz, M.; Stamenkovic, V.; Schmidt, T. J.; Wandelt, K.; Ross, P. N.; Markovic, N. M. The Electro-Oxidation of Formic Acid on Pt-Pd Single Crystal Bimetallic Surfaces. *Phys. Chem. Chem. Phys.* **2003**, *5* (19), 4242-4251.
- (84) Chen, X. Adsorption and Catalysis on Pt and Pd Monolayer-Modified Pt Single Crystal Electrodes, PhD thesis, Leiden University, 2019.
- (85) Kortlever, R.; Balemans, C.; Kwon, Y.; Koper, M. T. M. Electrochemical CO2 Reduction to Formic Acid on a Pd-Based Formic Acid Oxidation Catalyst. *Catal. Today* **2015**, *244*, 58-62.
- (86) Koper, M. T. M. Theory of Multiple Proton-Electron Transfer Reactions and Its Implications for Electrocatalysis. *Chem. Sci.* **2013**, *4* (7), 2710-2723.
- (87) Chen, X.; Koper, M. T. M. Mass-Transport-Limited Oxidation of Formic Acid on a PdMLPt(100) Electrode in Perchloric Acid. *Electrochem. commun.* **2017**, *82*, 155–158.



2

INFLUENCE OF VAN DER WAALS INTERACTIONS ON THE SOLVATION ENERGIES OF ADSORBATES AT PTBASED ELECTROCATALYSTS

Solvation can significantly modify the adsorption energy of species at surfaces, thereby influencing the performance of electrocatalysts and liquid-phase catalysts. Thus, it is important to understand adsorbate solvation at the nanoscale. Here we evaluate the effect of van der Waals (vdW) interactions described by different approaches on the solvation energy of *OH adsorbed on near-surface alloys (NSAs) of Pt. Our results show that the studied functionals can be divided into two groups, each with rather similar average *OH solvation energies: (1) PBE and PW91; and (2) vdW functionals, RPBE, PBE-D3 and RPBE-D3. On average, *OH solvation energies are less negative by ~0.14 eV in group (2) compared to (1), and the values for a given alloy can be extrapolated from one functional to another within the same group. Depending on the desired level of accuracy, these concrete observations and our tabulated values can be used to rapidly incorporate solvation into models for electrocatalysis and liquid-phase catalysis.



This chapter is based on Granda-Marulanda, L. P.; Builes, S.; Koper, M. T. M.; Calle-Vallejo, F. Influence of Van Der Waals Interactions on the Solvation Energies of Adsorbates at Pt-Based Electrocatalysts. ChemPhysChem 2019, 20 (22), 2968–2972

2.1 Introduction

The solvation of adsorbates is becoming a topic of great interest in computational electrocatalysis in view of the current search for more realistic representations of electrode-electrolyte interfaces. Numerous recent experimental works show that solvent and/or electrolyte effects change the activity and selectivity of electrocatalysts for important reactions such as oxygen reduction, 1,2 hydrogen evolution, 3,4 CO₂ reduction, 5,6 and CO reduction. 7,8 In addition, computational works show that solvation and/or cation co-adsorption modify the adsorption energies of reaction intermediates, 9-13 which may not only lead to changes in reaction pathways¹⁴ but also to considerable differences in the calculated activity of electrocatalysts. 10,15 In computational electrocatalysis adsorbate-solvent and adsorbate-electrolyte interactions at the interface can be evaluated implicitly (where the solvent is modelled as a continuum with certain dielectric constant), 13,16-25 explicitly, 26-33 or through combinations of the two. 34,35 Furthermore, less expensive explicit solvation models, sometimes referred as "micro-solvation" or near-surface solvation36-38 have been tailored to save computational resources by using a small number of explicit water molecules to stabilize a given adsorbate.

The role of vdW forces on water clustering, water-metal interactions, and liquid water has been explored by using functionals that account for vdW interactions.³⁹⁻⁴³ In general, dispersion-corrected functionals or those incorporating vdW forces self-consistently tend to increase the adsorption energy of water on metal surfaces. However, the majority of computational electrocatalysis studies carried out within the framework of Density Functional theory (DFT) use common exchange-correlation (xc) functionals that do not account for van der Waals (vdW) interactions. Importantly, those might be necessary for an accurate description of water-water, water-electrode and water-adsorbate interactions.

This *Chapter* presents a study of the role of vdW interactions on the solvation energy of hydroxyl (*OH) adsorbed on near-surface alloys (NSAs) of Pt and late transition metals. Those versatile alloys are salient model catalysts for a variety of electrocatalytic reactions.^{44–47} We observe that: (1) the predictions of *OH solvation at Pt NSAs are comparable for PBE and PW91. (2) The predictions of *OH solvation at Pt NSAs are comparable among RPBE, vdW functionals and GGAs with dispersion corrections. (3) The *OH solvation energies decrease on average by ~0.14 eV from functionals in (2) with respect to those in (1).

2.2 Computational details

The DFT calculations were carried out using the PAW⁴⁸ method in the Vienna Ab initio Simulation Package⁴⁹. We simulated $\sqrt{3} \times \sqrt{3}$ R30° slabs of Pt(111) NSAs with 1 monolayer (ML) of late transition metal atoms in the subsurface (see Figure 2.1) and: (I) 1/3 ML *OH in vacuum, (II) 1/3 ML *OH + 1/3 ML *H₂O, and (III) 2/3 ML *H₂O. The subsurface metals were Co, Ni, Cu, Rh, Pd, Ag, Ir, Pt and Au. The slabs contained four atomic layers: the two uppermost layers and the adsorbates were fully relaxed, while the two bottommost layers were fixed at the converged

interatomic distances of bulk Pt calculated for each exchange-correlation functional. All of the calculated lattice constants appear in Table A8 in the SI. $\rm H_2$ and $\rm H_2O$ were simulated in cubic boxes of 3375 ų. In all simulations, we used 0.01 eV ʹ as convergence criterion for the maximal forces on the atoms, and a plane-wave cutoff of 450 eV.

The k-point samplings were $8\times8\times1$ for the slabs and $1\times1\times1$ for H_2 and H_2O . For the slabs, ~15 Å of vacuum and dipole corrections in the z direction were used to avoid artificial electrostatic interactions between periodic images. The Methfessel-Paxton method⁵⁰ was employed to smear the Fermi level of the slabs with $k_BT = 0.2$ eV, whereas Gaussian smearing was used for H_2 and H_2O with $k_BT = 0.001$ eV. In both cases, all energies were extrapolated to 0 K. We used the computational hydrogen electrode to assess the energetics of solvated protons and electrons.⁵¹ As a first approximation, we made spin-restricted calculations for Ni- and Co-containing NSAs. The free energies were evaluated as: $G = E_{DFT} + ZPE - TS$. The zero-point energy corrections (ZPE) of gases and adsorbates, as well as the adsorbates' vibrational entropies were calculated within the harmonic-oscillator approximation. The $TS_{total}^{298.15K}$ corrections for $H_2(g)$ and $H_2O(1)$ are 0.40 and 0.67 eV.⁵¹ We used the following exchange-correlation functionals: PW91,⁵² PBE,⁵³ RPBE⁵⁴; functionals with semi-empirical corrections, PBE-D3 and RPBE-D3, using the DFT-D3 method,⁵⁵; a functional that evaluates vdW interactions with an optimized version of vdW-DF method,⁵⁶ namely optPBE⁴³; and the BEEF-vdW functional.⁵⁷ Specific energetic and geometric data related to this study appear in the Appeendix A, Figure A3 and Tables A1-A8.

2.3 Results and discussion

Following previous works, 11,37 to obtain the free energy of solvation, (Ω_{OH}) , for *OH on the $\sqrt{3} \times \sqrt{3}$ R30° slab, we determined: (i) the free energy of formation of 1/3 ML *OH coadsorbed with 1/3 ML *H₂O with respect to an ice-like water bilayer with 2/3 ML *H₂O ($\Delta G_{OH}^{H_2O}$), 41,58,59 as shown in Eq. 2.1 and in Figure 2.1a. (ii) The free energy of formation of 1/3ML *OH in vacuum with respect to H₂O(l) (ΔG_{OH}^{vac}) using Eq. 2.2, as depicted in Figure 1b.

$$2 * H_2O \rightarrow *OH + *H_2O + H^+ + e^-$$
 2.1

$$* + H_2O(l) \rightarrow *OH + H^+ + e^-$$
 2.2

where * represents an active site at the surface of the NSAs. Recent works have shown that three *H₂O molecules are required to solvate *OH, as the O atom in *OH can make two hydrogen bonds with surrounding water molecules and the H atom can make one.³⁷ This is also the case for the periodic water bilayers considered here, as shown in Figure 2.1a. The difference between Eq. 2.1 and Eq. 2.2 gives the solvation contribution to the free energy of adsorption (Ω_{OH}):

INFLUENCE OF VAN DER WAALS INTERACTIONS ON THE SOLVATION ENERGIES OF ADSORBATES AT PT-BASED ELECTROCATALYSTS

$$\Omega_{OH} = \Delta G_{OH}^{H_2O} - \Delta G_{OH}^{vac}$$
 2.3

Once Ω_{OH} is known, it can be added to other adsorption energies calculated in vacuum ($\Delta G_{OH}^{vac\#}$) to obtain a first assessment of the adsorption energies in solution ($\Delta G_{OH}^{H_2O\#}$), which are usually burdensome to calculate:³⁷

$$\Delta G_{OH}^{H_2O\#} \approx \Delta G_{OH}^{vac\#} + \Omega_{OH}$$
 2.4

where the superscript # indicates an extrapolation, hence the approximate sign. Previous works concluded that one can extrapolate Ω_{OH} from one facet to another of a given material,³⁷ but that it is not advisable to do so among different materials.⁹⁻¹¹ In the following, we will analyze whether such extrapolations are possible when Ω_{OH} is calculated with a different functional than ΔG_{OH}^{vac} . This is a common situation when using tabulated results from previous works.

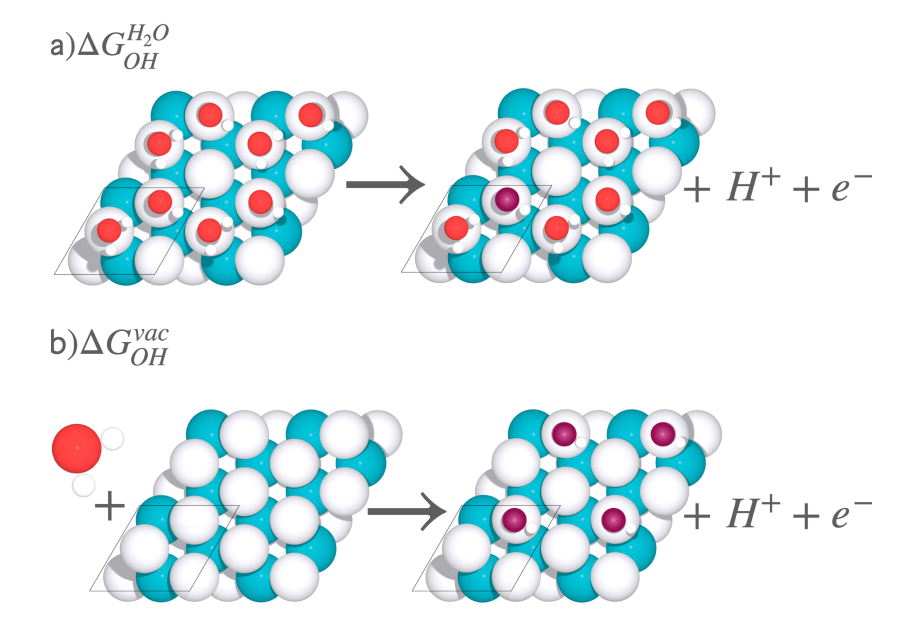


FIGURE 2.1

Schematics of Eq. 2.1 and Eq. 2.2 for the free energies of formation of *OH on Pt NSAs. (a) 1/3 ML *OH coadsorbed with 1/3 ML *H $_2$ O (right side) using as a reference a water bilayer (left side) with one water molecule in the flat configuration and the other one with a hydrogen pointing towards the surface. (b) 1/3 ML *OH in vacuum (right side) using liquid water as a reference (left side). In both cases the slabs are 2×2 repetitions of a (111) $\sqrt{3} \times \sqrt{3}$ R30° supercell as defined by the parallelogram. Each layer in the slab contains 3 metal atoms. Pt: gray, subsurface metal: turquoise, O in H $_2$ O: red, O in OH: purple, H: white. A top and side view of the water adlayer can be seen in Figure A3.

Table 2.1 provides the solvation corrections obtained for *OH with different functionals for nine different Pt NSAs. We have split the functionals into two groups: group 1, formed by PW91 and PBE, and group 2, formed by RPBE, PBE-D3, RPBE-D3, optPBE and BEEF-vdW.

In the following, we explain the creation of two groups and the presence of RPBE (a GGA) in group 2 (with vdW and dispersion-corrected functionals) instead of group 1 (other GGAs).

Although PBÉ and PW91 are not entirely equivalent, ⁶⁰ they do provide similar values for properties such as atomization energies and lattice constants. For example, for the latter property, PW91 gave 3.99 Å and PBE 3.98 Å (see Table A8). Therefore, for adsorption free energies it is expected that the results do not differ significantly. Indeed, we found for Ω_{OH} that the average values for PBE/PW91

are similar (see Table 2.1).

In general, RPBE and PBE/PW91 give different results for properties such as atomization energies for molecules and equilibrium cell volumes for solids.⁶¹ It has been shown that PBE/PW91 over-bind adsorbates to surfaces with respect to experiments, while RPBE under-binds them,⁶² which is presumably connected to RPBE's severe underestimation of surface energies.⁶³

Here we observe something similar: the *OH solvation corrections for NSAs, which are the difference between the adsorption energies of *OH in solution and in vacuum, Eq. 2.3, are on average ~0.15 eV more negative for PBE compared to RPBE (see Table 2.1). This is because on average, ΔG_{OH}^{vac} is 0.11 eV weaker for RPBE vs PBE, whereas $\Delta G_{OH}^{H_2O}$ is weaker by 0.26 eV (see Tables A2 and A3). We note that the trends in Ω_{OH} , $\Delta G_{OH}^{H_2O}$, and ΔG_{OH}^{vac} as a function of the number of valence electrons (see Table 2.1 and Figure A2) are similar for PBE, PW91 and RPBE.

The less negative average solvation energy with respect to PBE/PW91 is also observed for functionals incorporating vdW interactions and dispersion corrections. This is because the adsorbate-metal interactions are more strongly enhanced for ΔG_{OH}^{vac} compared to $\Delta G_{OH}^{H_2O}$, in view of the presence of H₂O in the latter.³⁹ On average, ΔG_{OH}^{vac} is strengthened by 0.17 eV for PBE-D3 with respect to PBE, whereas $\Delta G_{OH}^{H_2O}$ is strengthened only by 0.02 eV (see Tables A2 and A3). We attribute this to the enhanced water-substrate interactions provided by dispersion corrections: the average adsorption energy of the water bilayer is made more negative by 0.22 eV for PBE-D3 with respect to PBE (see Table A4). In fact, it is well known that dispersion corrections increase the binding energy of water adlayers on substrates, ⁴³ which according to Eq. 2.1 and Eq. 2.3 makes the solvation energies less negative.

Altogether, in group 1 we have PBE and PW91, which are over-binding GGAs, while in group 2 we have under-binding GGAs such as RPBE together with vdW functionals and dispersion-corrected functionals. The average solvation energy for the functionals in group 1 is -0.55 eV, while it is -0.40 eV for the functionals in group 2. We emphasize that the division of functionals in groups 1 and 2 is based merely on the results, and a rigorous classification would require data from additional functionals and adsorbates.

Regarding the safe use of Eq. 2.4, there are two important points to be considered: first, for a given functional, the variations among the different alloys are large. The standard deviation for the alloys in groups 1 and 2 is 0.09 and 0.08 eV, respectively. In line with previous works focused on PBE only, our conclusion is that it is unadvisable to use a single solvation correction for all

alloys. Second, for a given alloy one can combine among functionals from either group 1 or group 2, but not between groups. The mean of the standard deviations for the alloys are 0.03 and 0.02 eV for groups 1 and 2, respectively. Essentially, applying PBE-calculated solvation energies to PW91's adsorption energies in vacuum (and vice versa) is possible using Eq. 2.4, as the solvation corrections are similar for both functionals. Ω_{OH} values can also be extrapolated from one functional to another within group 2. However, it is preferable not to extrapolate values of group 1 to group 2 and vice versa, as the differences are on average ~0.15 eV. For instance, the design principle for oxygen reduction catalysts states that optimal catalysts should bind around 0.10-0.15 eV weaker than Pt(111), $\Delta G_{OH} - \Delta G_{OH}^{Pt(111)} \approx 0.1-0.15$ eV, 11,64,65 so it is advisable to avoid intergroup extrapolations. Table 2.1 provides the average values (avg1/avg2) and standard deviations (stdev1/stdev2) for each alloy in each group. Figure A2 shows the energy trends for the two groups. The average and standard deviation for a given alloy across all functionals appear in Table A1.

TABLE 2.1

Free energies of solvation (Ω_{OH}) in eV for 1/3 ML *OH coadsorbed with 1/3 ML *H₂O within a water bilayer using different functionals. avg1 and avg2 are the averages of the solvation energies for group 1 functionals (PBE, PW91) and group 2 functionals (RPBE, vdW functionals: optPBE and BEEF-vdW, and with dispersion corrections: PBE-D3 and RPBE-D3) across the same metal. Stdev1/2 are the corresponding standard deviations of avg1/avg2. MAX and MIN are the maximal and minimal values in the dataset across the same functional. Range is the difference between MAX and MIN.

METAL	PW91	PBE	RPBE	PBE- D3	RPBE- D3	opt- PBE	BEEF- vdW	avg1	avg2	stdev1	stdev2
Со	-0.60	-0.69	-0.50	-0.45	-	-0.52	-0.48	-0.64	-0.49	0.07	0.03
Rh	-0.61	-0.61	-0.45	-0.47	-0.48	-0.47	-0.39	-0.61	-0.45	0.00	0.04
lr	-0.63	-0.63	-0.43	-0.50	-0.50	-0.49	-0.43	-0.63	-0.47	0.00	0.04
Ni	-0.53	-0.52	-0.40	-0.43	-0.45	-0.43	-0.44	-0.53	-0.43	0.01	0.02
Pd	-0.56	-0.56	-0.36	-0.40	-0.41	-0.40	-0.39	-0.56	-0.39	0.00	0.02
Pt	-0.62	-0.62	-0.50	-0.45	-0.57	-0.45	-0.44	-0.62	-0.48	0.00	0.05
Cu	-0.50	-0.42	-0.32	-0.31	-0.27	-0.29	-0.28	-0.46	-0.29	0.06	0.02
Ag	-0.40	-0.38	-0.26	-0.25	-0.27	-0.25	-0.27	-0.39	-0.26	0.02	0.01
Au	-0.49	-0.50	-0.35	-0.35	-0.46	-0.35	-0.33	-0.49	-0.37	0.01	0.05
mean	-0.55	-0.55	-0.39	-0.40	-0.43	-0.41	-0.38				
stdev	0.08	0.10	0.08	0.08	0.11	0.09	0.07				
MAX	-0.40	-0.38	-0.26	-0.25	-0.27	-0.25	-0.27				
MIN	-0.63	-0.69	-0.50	-0.50	-0.57	-0.52	-0.48				
range	0.23	0.32	0.24	0.25	0.30	0.27	0.21				

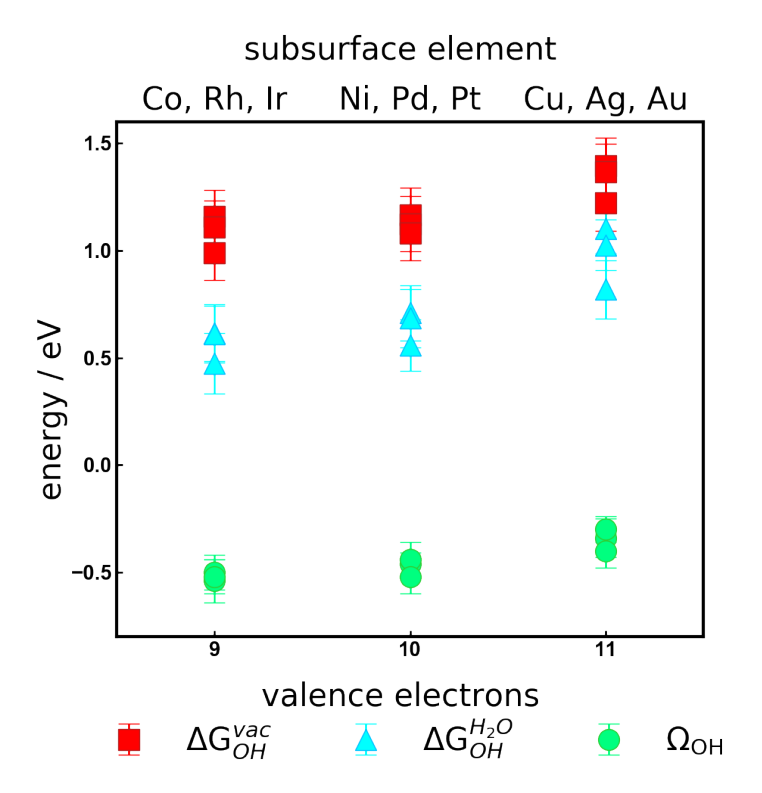


FIGURE 2.2

Adsorption energies of 1/3 ML *OH in vacuum (red, ΔG_{OH}^{vac}), within the water bilayer (blue, $\Delta G_{OH}^{H_2O}$), and in the solvation energy (green, Ω_{OH}), as a function of the number of valence electrons of the subsurface metal atom in the Pt NSAs. The error bars cover the energy range spanned by the different functionals analyzed. The correlation between the number of valence electrons and the d-band centers of the Pt skins is provided in Figure A1.

Figure 2.2 summarizes the trends in adsorption energies in vacuum and in solution together with the *OH solvation energies, as a function of the number of electrons of the metal in the Pt NSAs (see also Figure A1). The data points are the average values for each NSA considering all functionals (avg0) in Tables A2, A3, and A1 for ΔG_{OH}^{vac} , $\Delta G_{OH}^{H_2O}$, and Ω_{OH} , respectively. The error bars correspond to the standard deviation across the metals (stdev0) in Tables A2, A3 and A1, respectively. Importantly, the size of the error bars decreases for Ω_{OH} with respect to ΔG_{OH}^{vac} and $\Delta G_{OH}^{H_2O}$. This shows that: (i) the number of valence electrons of the components can be used to predict solvation corrections, in line with previous works on adsorption-energy trends; 11,66-68 and (ii) because Ω_{OH} results from the difference of ΔG_{OH}^{vac} and $\Delta G_{OH}^{H_2O}$ (Eq. 2.3), its actual values are considerably less functional-dependent than those of the original adsorption energies.

2.4 Conclusions

Using *OH adsorbed on Pt near-surface alloys with transition metals as a case study, we showed that accounting for long-range interactions generally results in a decrease of the strength of solvation contributions to the adsorption energies with respect to GGAs. The decrease is on average ~0.14 eV and is due to the enhancement of water-metal interactions when including long-range interactions. The solvation energies of *OH calculated with PBE are similar to those of PW91 but differ ~0.15 eV from those of RPBE. Solvation energies calculated with RPBE, vdW functionals (optPBE and BEEF-vdW) and dispersion-corrected GGA functionals (PBE-D3 and RPBE-D3) are generally rather similar. Furthermore, solvation corrections can be predicted based on the number of valence electrons of the subsurface metal in the alloy. Depending on the desired level of accuracy, these guidelines can be used to decide whether specific solvation energies need to be calculated or if average values suffice, which can help in making more efficient electrocatalysis and liquid-phase catalysis models.

2.5 References

- (1) Garlyyev, B.; Xue, S.; Pohl, M. D.; Reinisch, D.; Bandarenka, A. S. Oxygen Electroreduction at High-Index Pt Electrodes in Alkaline Electrolytes: A Decisive Role of the Alkali Metal Cations. *ACS Omega* **2018**, *3* (11), 15325–15331.
- (2) Zhao, X.; Gunji, T.; Kaneko, T.; Yoshida, Y.; Takao, S.; Higashi, K.; Uruga, T.; He, W.; Liu, J.; Zou, Z. An Integrated Single-Electrode Method Reveals the Template Roles of Atomic Steps: Disturb Interfacial Water Networks and Thus Affect the Reactivity of Electrocatalysts. *J. Am. Chem. Soc.* **2019**.
- (3) Xue, S.; Garlyyev, B.; Watzele, S.; Liang, Y.; Fichtner, J.; Pohl, M. D.; Bandarenka, A. S. Influence of Alkali Metal Cations on the Hydrogen Evolution Reaction Activity of Pt, Ir, Au, and Ag Electrodes in Alkaline Electrolytes. *ChemElectroChem* **2018**, *5* (17), 2326-2329.
- (4) Ledezma-Yanez, I.; Wallace, W. D. Z.; Sebastián-Pascual, P.; Climent, V.; Feliu, J. M.; Koper, M. T. M. Interfacial Water Reorganization as a PH-Dependent Descriptor of the Hydrogen Evolution Rate on Platinum Electrodes. *Nature Energy* **2017**, *2* (4), nenergy201731.
- (5) Varela, A. S.; Ju, W.; Reier, T.; Strasser, P. Tuning the Catalytic Activity and Selectivity of Cu for CO2 Electroreduction in the Presence of Halides. *ACS Catal.* **2016**, 6 (4), 2136–2144.
- (6) Singh, M. R.; Kwon, Y.; Lum, Y.; Ager, J. W.; Bell, A. T. Hydrolysis of Electrolyte Cations Enhances the Electrochemical Reduction of CO2 over Ag and Cu. *J. Am. Chem. Soc.* **2016**, *138* (39), 13006–13012.
- (7) Murata, A.; Hori, Y. Product Selectivity Affected by Cationic Species in Electrochemical Reduction of CO2 and CO at a Cu Electrode. *Bulletin of The Chemical Society of Japan BULL CHEM SOC JPN* **1991**, 64, 123-127.

- (8) Pérez-Gallent, E.; Marcandalli, G.; Figueiredo, M. C.; Calle-Vallejo, F.; Koper, M. T. M. Structure- and Potential-Dependent Cation Effects on CO Reduction at Copper Single-Crystal Electrodes. *J. Am. Chem. Soc.* **2017**, *139* (45), 16412–16419.
- (9) Tripkovic, V. Thermodynamic Assessment of the Oxygen Reduction Activity in Aqueous Solutions. *Phys. Chem. Chem. Phys.* **2017**, *19* (43), 29381–29388.
- (10) Calle-Vallejo, F.; Krabbe, A.; M. García-Lastra, J. How Covalence Breaks Adsorption-Energy Scaling Relations and Solvation Restores Them. *Chemical Science* **2017**, *8* (1), 124–130.
- (11) He, Z.-D.; Hanselman, S.; Chen, Y.-X.; Koper, M. T. M.; Calle-Vallejo, F. Importance of Solvation for the Accurate Prediction of Oxygen Reduction Activities of Pt-Based Electrocatalysts. *J. Phys. Chem. Lett.* **2017**, *8* (10), 2243–2246.
- (12) Gray, C. M.; Saravanan, K.; Wang, G.; Keith, J. A. Quantifying Solvation Energies at Solid/Liquid Interfaces Using Continuum Solvation Methods. *Molecular Simulation* **2017**, *43* (5-6), 420-427.
- (13) Ludwig, T.; Gauthier, J. A.; Brown, K. S.; Ringe, S.; Nørskov, J. K.; Chan, K. Solvent-Adsorbate Interactions and Adsorbate-Specific Solvent Structure in Carbon Dioxide Reduction on a Stepped Cu Surface. *J. Phys. Chem. C* **2019**, *123* (10), 5999-6009.
- (14) Calle-Vallejo, F.; Koper, M. T. M. Accounting for Bifurcating Pathways in the Screening for CO2 Reduction Catalysts. *ACS Catal.* **2017**, *7* (10), 7346-7351.
- (15) Briquet, L. G. V.; Sarwar, M.; Mugo, J.; Jones, G.; Calle-Vallejo, F. A New Type of Scaling Relations to Assess the Accuracy of Computational Predictions of Catalytic Activities Applied to the Oxygen Evolution Reaction. *ChemCatChem* **2017**, *9* (7), 1261-1268.
- (16) Letchworth-Weaver, K.; Arias, T. A. Joint Density-Functional Theory of the Electrode-Electrolyte Interface: Application to Fixed Electrode Potentials, Interfacial Capacitances, and Potentials of Zero Charge. *Physical Review B* **2012**, *86* (7).
- (17) Schwarz, K. A.; Sundararaman, R.; Moffat, T. P.; Allison, T. C. Formic Acid Oxidation on Platinum: A Simple Mechanistic Study. *Phys. Chem. Chem. Phys.* **2015**, *17* (32), 20805-20813.
- (18) Sundararaman, R.; Schwarz, K. Evaluating Continuum Solvation Models for the Electrode-Electrolyte Interface: Challenges and Strategies for Improvement. *The Journal of Chemical Physics* **2017**, *146* (8), 084111.
- (19) Mathew, K.; Sundararaman, R.; Letchworth-Weaver, K.; Arias, T. A.; Hennig, R. G. Implicit Solvation Model for Density-Functional Study of Nanocrystal Surfaces and Reaction Pathways. *J. Chem. Phys.* **2014**, *140* (8), 084106.
- (20) Mathew, K.; Hennig, R. G. Implicit Self-Consistent Description of Electrolyte in Plane-Wave Density-Functional Theory. *arXiv:1601.03346* [cond-mat] **2016**.
- (21) Garcia-Ratés, M.; López, N. Multigrid-Based Methodology for Implicit Solvation Models in Periodic DFT. *J. Chem. Theory Comput.* **2016**, *12* (3), 1331–1341.
- (22) Dupont, C.; Andreussi, O.; Marzari, N. Self-Consistent Continuum Solvation (SCCS): The Case of Charged Systems. *J. Chem. Phys.* **2013**, *139* (21), 214110.
- (23) Nishihara, S.; Otani, M. Hybrid Solvation Models for Bulk, Interface, and Membrane: Reference Interaction Site Methods Coupled with Density Functional Theory. *Phys. Rev. B* **2017**, *96* (11), 115429.

- (24) Melander, M. M.; Kuisma, M. J.; Christensen, T. E. K.; Honkala, K. Grand-Canonical Approach to Density Functional Theory of Electrocatalytic Systems: Thermodynamics of Solid-Liquid Interfaces at Constant Ion and Electrode Potentials. *J. Chem. Phys.* **2018**, *150* (4), 041706.
- (25) Sundararaman, R.; Letchworth-Weaver, K.; Schwarz, K. A. Improving Accuracy of Electrochemical Capacitance and Solvation Energetics in First-Principles Calculations. *J. Chem. Phys.* **2018**, *148* (14), 144105.
- (26) Filhol, J.-S.; Neurock, M. Elucidation of the Electrochemical Activation of Water over Pd by First Principles. *Angewandte Chemie International Edition* **2006**, 45 (3), 402-406.
- (27) McCrum, I. T.; Janik, M. J. PH and Alkali Cation Effects on the Pt Cyclic Voltammogram Explained Using Density Functional Theory. *J. Phys. Chem. C* **2016**, *120* (1), 457-471.
- (28) Kolb, M. J.; Wermink, J.; Calle-Vallejo, F.; Juurlink, L. B. F.; Koper, M. T. M. Initial Stages of Water Solvation of Stepped Platinum Surfaces. *Phys. Chem. Chem. Phys.* **2016**, *18* (5), 3416-3422.
- (29) Morais, R. F. de; Kerber, T.; Calle-Vallejo, F.; Sautet, P.; Loffreda, D. Capturing Solvation Effects at a Liquid/Nanoparticle Interface by Ab Initio Molecular Dynamics: Pt201 Immersed in Water. *Small* **2016**, *12* (38), 5312-5319.
- (30) Liu, S.; White, M. G.; Liu, P. Mechanism of Oxygen Reduction Reaction on Pt(111) in Alkaline Solution: Importance of Chemisorbed Water on Surface. *J. Phys. Chem. C* **2016**, *120* (28), 15288-15298.
- (31) Karlberg, G. S. Adsorption Trends for Water, Hydroxyl, Oxygen, and Hydrogen on Transition-Metal and Platinum-Skin Surfaces. *Phys. Rev. B* **2006**, *74* (15), 153414.
- (32) Tripkovic, V.; Skúlason, E.; Siahrostami, S.; K. Nørskov, J.; Rossmeisl, J. The Oxygen Reduction Reaction Mechanism on Pt(111) from Density Functional Theory Calculations. *Electrochimica Acta* **2010**, *55*, 7975–7981.
- (33) Gauthier, J. A.; Dickens, C. F.; Chen, L. D.; Doyle, A. D.; Nørskov, J. K. Solvation Effects for Oxygen Evolution Reaction Catalysis on IrO2(110). *J. Phys. Chem. C* **2017**, *121* (21), 11455-11463.
- (34) Kamerlin, S. C. L.; Haranczyk, M.; Warshel, A. Are Mixed Explicit/Implicit Solvation Models Reliable for Studying Phosphate Hydrolysis? A Comparative Study of Continuum, Explicit and Mixed Solvation Models. *ChemPhysChem* **2009**, *10* (7), 1125–1134.
- (35) Sakong, S.; Naderian, M.; Mathew, K.; Hennig, R. G.; Groß, A. Density Functional Theory Study of the Electrochemical Interface between a Pt Electrode and an Aqueous Electrolyte Using an Implicit Solvent Method. *The Journal of Chemical Physics* **2015**, *142* (23), 234107.
- (36) Mills, J. N.; McCrum, I. T.; Janik, M. J. Alkali Cation Specific Adsorption onto Fcc(111) Transition Metal Electrodes. *Phys. Chem. Chem. Phys.* **2014**, *16* (27), 13699-13707.
- (37) Calle-Vallejo, F.; F. de Morais, R.; Illas, F.; Loffreda, D.; Sautet, P. Affordable Estimation of Solvation Contributions to the Adsorption Energies of Oxygenates on Metal Nanoparticles. *J. Phys. Chem. C* **2019**, *123* (9), 5578-5582.

- (38) Rendón-Calle, A.; Builes, S.; Calle-Vallejo, F. Substantial Improvement of Electrocatalytic Predictions by Systematic Assessment of Solvent Effects on Adsorption Energies. *Applied Catalysis B: Environmental* **2020**, 119147.
- (39) Carrasco, J.; Klimeš, J.; Michaelides, A. The Role of van Der Waals Forces in Water Adsorption on Metals. *The Journal of Chemical Physics* **2013**, *138* (2), 024708.
- (40) Michaelides, A.; Ranea, V. A.; de Andres, P. L.; King, D. A. General Model for Water Monomer Adsorption on Close-Packed Transition and Noble Metal Surfaces. *Phys. Rev. Lett.* **2003**, *90* (21), 216102.
- (41) Michaelides, A.; Hu, P. Catalytic Water Formation on Platinum: A First-Principles Study. *J. Am. Chem. Soc.* **2001**, *123* (18), 4235-4242.
- (42) Michaelides, A. Density Functional Theory Simulations of Water-Metal Interfaces: Waltzing Waters, a Novel 2D Ice Phase, and More. *Appl. Phys. A* **2006**, *85* (4), 415-425.
- (43) Klimeš, J.; Bowler, D. R.; Michaelides, A. Chemical Accuracy for the van Der Waals Density Functional. *J. Phys.: Condens. Matter* **2010**, *22* (2), 022201.
- (44) Greeley, J.; Mavrikakis, M. Near-Surface Alloys for Hydrogen Fuel Cell Applications. *Catalysis Today* **2006**, *111* (1), 52–58.
- (45) Calle-Vallejo, F.; Koper, M. T. M.; Bandarenka, A. S. Tailoring the Catalytic Activity of Electrodes with Monolayer Amounts of Foreign Metals. *Chem. Soc. Rev.* **2013**, *42* (12), 5210–5230.
- (46) Tymoczko, J.; Calle-Vallejo, F.; Schuhmann, W.; Bandarenka, A. S. Making the Hydrogen Evolution Reaction in Polymer Electrolyte Membrane Electrolysers Even Faster. *Nature Communications* **2016**, *7*, 10990.
- (47) Zhao, Z.; Lu, G. Computational Screening of Near-Surface Alloys for CO2 Electroreduction. *ACS Catal.* **2018**, *8* (5), 3885–3894.
- (48) Kresse, G.; Joubert, D. From Ultrasoft Pseudopotentials to the Projector Augmented-Wave Method. *Phys. Rev. B* **1999**, *59* (3), 1758-1775.
- (49) Kresse, G.; Furthmüller, J. Efficient Iterative Schemes for Ab Initio Total-Energy Calculations Using a Plane-Wave Basis Set. *Phys. Rev. B* **1996**, *54* (16), 11169–11186.
- (50) Methfessel, M.; Paxton, A. T. High-Precision Sampling for Brillouin-Zone Integration in Metals. *Phys. Rev. B* **1989**, *40* (6), 3616–3621.
- (51) Nørskov, J. K.; Rossmeisl, J.; Logadottir, A.; Lindqvist, L.; Kitchin, J. R.; Bligaard, T.; Jónsson, H. Origin of the Overpotential for Oxygen Reduction at a Fuel-Cell Cathode. *J. Phys. Chem. B* **2004**, *108* (46), 17886-17892.
- (52) Perdew, J. P.; Burke, K.; Wang, Y. Generalized Gradient Approximation for the Exchange-Correlation Hole of a Many-Electron System. *Phys. Rev. B* **1996**, *54* (23), 16533-16539.
- (53) Perdew, J. P.; Burke, K.; Ernzerhof, M. Generalized Gradient Approximation Made Simple. *Phys. Rev. Lett.* **1996**, 77 (18), 3865-3868.
- (54) Hammer, B.; Hansen, L. B.; Nørskov, J. K. Improved Adsorption Energetics within Density-Functional Theory Using Revised Perdew-Burke-Ernzerhof Functionals. *Phys. Rev. B* **1999**, 59 (11), 7413-7421.
- (55) Grimme, S.; Antony, J.; Ehrlich, S.; Krieg, H. A Consistent and Accurate Ab Initio Parametrization of Density Functional Dispersion Correction (DFT-D) for the 94 Elements H-Pu. *J. Chem. Phys.* **2010**, *132* (15), 154104.

- (56) Dion, M.; Rydberg, H.; Schröder, E.; Langreth, D. C.; Lundqvist, B. I. Van Der Waals Density Functional for General Geometries. *Phys. Rev. Lett.* **2004**, *92* (24), 246401.
- (57) Wellendorff, J.; Lundgaard, K. T.; Møgelhøj, A.; Petzold, V.; Landis, D. D.; Nørskov, J. K.; Bligaard, T.; Jacobsen, K. W. Density Functionals for Surface Science: Exchange-Correlation Model Development with Bayesian Error Estimation. *Phys. Rev. B* **2012**, *85* (23), 235149.
- (58) Ogasawara, H.; Brena, B.; Nordlund, D.; Nyberg, M.; Pelmenschikov, A.; Pettersson, L. G. M.; Nilsson, A. Structure and Bonding of Water on Pt(111). *Phys. Rev. Lett.* **2002**, *89* (27), 276102.
- (59) Schnur, S.; Groß, A. Properties of Metal-Water Interfaces Studied from First Principles. *New J. Phys.* **2009**, *11* (12), 125003.
- (60) Mattsson, A. E.; Armiento, R.; Schultz, P. A.; Mattsson, T. K. R. Nonequivalence of the Generalized Gradient Approximations PBE and PW91; 2006.
- (61) Kurth, S.; Perdew, J. P.; Blaha, P. Molecular and Solid-State Tests of Density Functional Approximations: LSD, GGAs, and Meta-GGAs. *International Journal of Quantum Chemistry* **1999**, 75 (4–5), 889–909.
- (62) Díaz, C.; Pijper, E.; Olsen, R. A.; Busnengo, H. F.; Auerbach, D. J.; Kroes, G. J. Chemically Accurate Simulation of a Prototypical Surface Reaction: H2 Dissociation on Cu(111). *Science* **2009**, *326* (5954), 832–834.
- (63) Janthon, P.; Kozlov, S. M.; Viñes, F.; Limtrakul, J.; Illas, F. Establishing the Accuracy of Broadly Used Density Functionals in Describing Bulk Properties of Transition Metals. *J. Chem. Theory Comput.* **2013**, *9* (3), 1631-1640.
- (64) Stephens, I. E. L.; Bondarenko, A. S.; Grønbjerg, U.; Rossmeisl, J.; Chorkendorff, I. Understanding the Electrocatalysis of Oxygen Reduction on Platinum and Its Alloys. *Energy Environ. Sci.* **2012**, *5* (5), 6744-6762.
- (65) Calle-Vallejo, F.; Bandarenka, A. S. Enabling Generalized Coordination Numbers to Describe Strain Effects. *ChemSusChem* **2018**, *11* (11), 1824–1828.
- (66) Calle-Vallejo, F.; Martínez, J. I.; García-Lastra, J. M.; Rossmeisl, J.; Koper, M. T. M. Physical and Chemical Nature of the Scaling Relations between Adsorption Energies of Atoms on Metal Surfaces. *Phys. Rev. Lett.* **2012**, *108* (11), 116103.
- (67) Calle-Vallejo, F.; Inoglu, N. G.; Su, H.-Y.; Martínez, J. I.; Man, I. C.; Koper, M. T. M.; Kitchin, J. R.; Rossmeisl, J. Number of Outer Electrons as Descriptor for Adsorption Processes on Transition Metals and Their Oxides. *Chem. Sci.* **2013**, *4* (3), 1245–1249.
- (68) Su, H.-Y.; Sun, K.; Wang, W.-Q.; Zeng, Z.; Calle-Vallejo, F.; Li, W.-X. Establishing and Understanding Adsorption-Energy Scaling Relations with Negative Slopes. *J. Phys. Chem. Lett.* **2016**, *7* (24), 5302–5306.



3

A SIMPLE METHOD TO CALCULATE SOLUTION-PHASE FREE ENERGIES OF CHARGED SPECIES IN COMPUTATIONAL ELECTROCATALYSIS

Calculating the adsorption potentials of ions with density functional theory and comparing across various ions requires an accurate reference energy of the ion in solution and electrons at the same electrochemical scale. Here we highlight a previously used method for determining the reference free energy of solution phase ions using a simple electrochemical thermodynamic cycle, which allows this free energy to be calculated from that of a neutral gas-phase or solid species and an experimentally measured equilibrium potential, avoiding the need to model solvent around the solution phase ion in the electronic structure calculations. While this method is not new, we describe its use and utility in detail and show that this same method can be used to find the free energy of any ion from any reaction, as long as the half-cell equilibrium potential is known, even for reactions that do not transfer the same number of protons and electrons. To illustrate its usage, we compare the adsorption potentials obtained with DFT of I*, Br*, Cl*, and SO_4 * on Pt(111) and Au(111), and OH* and Ag* on Pt(111) with those measured experimentally and find that this simple and computationally affordable method reproduces the experimental trends.

This chapter is based on Granda-Marulanda, L. P.; McCrum, I. T.; Koper, M. T. M. A Simple Method to Calculate Solution-Phase Free Energies of Charged Species in Computational Electrocatalysis. J. Phys.: Condens. Matter **2021**, 33 (20), 204001.

3.1 Introduction

Elucidation and understanding of the complex structure at the electrochemical interface, between electrolyte, adsorbates, and electrode, is one of the main fundamental problems in electrochemistry/electrocatalysis. The advancement of in situ spectroscopic and imaging techniques has allowed fundamental information at the atomic and molecular level to be obtained.¹⁻⁹ In addition, the increase of computational power has allowed computational tools based on the generalized gradient approximation (GGA) Density Functional Theory (DFT) to provide predictions complementary to experimental results, based on the computed adsorption energetics, thermodynamics, and kinetics of processes at the electrochemical interface.¹⁰⁻¹⁵

Among the main computational challenges that first-principles DFT simulations face at present are (i) the description of the potential dependence of the electrochemical processes and (ii) the description of the solvated species (protons and charged species) in the bulk solution phase and the description of these same species at the metal-electrode interface. In the first case, the biggest limitation is that the methods available to simulate variations of the electrode potential dependence are computationally more expensive than the traditional simulations, due to the necessity of changing the charge during the simulation to keep the potential constant. ¹⁶⁻¹⁸

In periodic simulations, where plane-wave basis sets are used, calculating negatively charged species by adding charges to a small supercell can lead to unphysical energies. This is due to the so-called "charge leakage", which are non-wanted interactions with the next periodic representation of the system, and also because of the unphysical distribution of the charge in the cell due to improper screening.¹⁹

To address this, periodic DFT models have been devised to simulate charged systems, by adding a background charge to make the system charge neutral but with the extra requirement of an energy correction afterwards.^{20–22} Similarly, it has also been proposed to add background charge with a dielectric continuum to prevent charge transfer.²³ Recently, Tölle et al.,²⁴ suggested a method to calculate ionization potentials of liquid water in periodic systems, where the finite charge subsystem is embedded and surrounded by an extended subsystem, obtaining comparable results of the ionization potential with experimental data and continuum dielectric models.

The other difficulty faced by DFT simulations is the description of solvated species. The calculated energies within the DFT framework represent systems in the gas phase (or vacuum) at 0 K, instead of systems in solution phase as they are in an electrochemical environment. In general, models that are meant to capture solvation effects in electrochemistry, including explicit solvation, 25–32 implicit solvation^{33–38} or a combination of the two, 99–41 add significant computational expense to the calculation due to the long length and time scales of the solvation structure and dynamics. Explicit solvation is modelled by adding solvent molecules in the simulation cell, where the solvent structure can be based on periodic electronic-structure calculations using GGA-DFT, ab initio molecular dynamics (AIMD), or classical molecular dynamics. 42–44 Implicit solvation is modelled as a dielectric continuum as described by the experimentally measured bulk dielectric constant and is a model that is in active development and

improvement.^{45–47} These solvation models can be applied to both solvation in the bulk solution and at the electrode-adsorbate-electrolyte interface. Even though much effort has been devoted to accurately compute solvation energies of protons and ions in solution,^{48–54} by combining thermodynamic cycles with implicit continuum models,^{53,55,56} or by calculating the solvation energy of charged species, either with implicit or explicit solvation, the subject remains a challenging part of computational electrochemistry.^{57,58}

Fortunately, for ions in bulk solution, thermodynamic cycles can be very practical because they provide free energies of charged species in solution by relating the exact free energy of a solution-phase ion to that of a readily and accurately calculated neutral gas-phase or solid-state species, for instance by using experimental redox potentials. Such thermodynamic cycles allow solution-phase free energies to be calculated without the need to model the solvent.

One such thermodynamic cycle which has gained standard, widespread use in computational electrochemistry is the "computational hydrogen electrode" (CHE),⁵⁹ in which the free energy of a proton-electron pair is related to that of hydrogen gas, $H_{(aq)}^+ + e^- \rightleftharpoons \frac{1}{2} H_{2(g)}$, by the definition of the equilibrium potential of the standard or reversible hydrogen electrode (RHE). At a potential of 0 V vs RHE and standard conditions of 1 bar, and 298.15 K, the proton-electron pair ($H^+ + e^-$) is in equilibrium with hydrogen gas $H_{2(g)}$, allowing the free energy of the proton-electron pair to be calculated from neutral $\frac{1}{2} H_{2(g)}$. This method allows for the thermodynamics of reactions involving coupled proton-electron transfers to be calculated easily and accurately using DFT.

Many similar thermodynamic cycles have been used to calculate the free energy of solution-phase ions other than protons. Calle-Vallejo et al. used experimentally measured formation energies of liquid nitric acid and the aqueous nitrate anion and the DFT calculated free energy of nitric acid in the gas phase to calculate the free energy of the nitrate anion in aqueous solution to examine its adsorption thermodynamics. ⁶⁰ In a recent study, McCrum et al. ⁶¹ used two different methods to calculate the free energy of halide anions in solution, so that the thermodynamics of their adsorption to an electrode surface could be determined. In the first method, the energy of the halide anion in vacuum was calculated using DFT, then it was corrected to the aqueous electrolyte by adding on an experimentally measured solvation energy, similar to the method used by Yeh et al.⁶² To then convert the energy of the ion-electron couple from an absolute scale to the normal hydrogen electrode scale, a second experimental value is needed, the absolute (vacuum) potential of the hydrogen electrode at standard state (4.4 V).63 In the second method, the authors used an approach similar to that of the computational hydrogen electrode, relating the free energy of the aqueous halide anions to that of the gas-phase halogens using their experimentally measured standard reduction potentials. This latter method is also described by Hansen et al.64 to study chlorine evolution and Gossenberger et al.65 to construct phase diagrams of halides co-adsorbed with hydrogen on platinum.

In another investigation to determine the likelihood of co-adsorption of ClO_4^* and Cl^* with OH^* on Pt(111), 66 the authors used the same method to calculate the free energy of ClO_4^- (aq) and Cl^- (aq). In this latter method, the half-cell equilibrium potentials of the redox couples of $(Cl_2(g)/Cl^-$ (aq)) and $(ClO_4^-$ (aq), $H^+/Cl_2(g)$), and the calculated free energies of $Cl_2(g)$ and $H_2O(l)$ are needed. The final solution-phase free energy of the anions, ClO_4^- (aq) and Cl^- (aq) is then corrected to their initial experimental concentrations, using the Nernst equation, also similar to the

work described by Gossenberger et al. 67 Additionally, various studies have discussed the relevance of thermodynamic cycles often combined with an implicit continuum model to determine solvation energies to calculate pKa's and reduction potentials. $^{68,55,53,56,69-71}$

Therefore, using standard redox potentials to obtain solvation energies or vice versa through thermodynamic cycles is well known, and while many thermodynamic cycles can and have been defined, there is a need to re-visit and illustrate the potential of this conceptually simple, computationally efficient, and transferable method to calculate the reference free energy of any solution-phase ion, in bulk electrolyte, far from the electrode surface. Resources containing thousands of redox reactions, such as the standard thermodynamic tables of equilibrium potentials,^{72,73} are available, and so it is very likely that the species of interest are tabulated there.

In this *Chapter*, we describe how the free energy of any solvated ion can be calculated from that of a neutral gas-phase or solid-state species and an experimentally measured equilibrium potential, eliminating the need to model solvation for the bulk solution-phase species with DFT. We show that, in combination with the computational hydrogen electrode, this method works even for half-cell reactions which involve an unequal number of protons and electrons.⁷⁴ This is of fundamental importance because achieving robust predictions with computational modelling depends on the choice of the reference state. A solution phase reference state is necessary, for example, for the computation of specific adsorption potentials of ions on electrodes.^{61,64-66} The interactions between adsorbed ions, the solvent, and reaction intermediates, are of significant importance in catalysis and electrocatalysis, as they can modify bond breaking/formation, adsorption energies, and consequently reaction pathways⁷⁵⁻⁸³ important for catalyst design.

Since this method relies on the experimentally measured equilibrium potential, we could argue that it is less "ab initio" than the CHE, thus we are limited to the availability of suitable experimental data and need to be aware of the accuracy of the experimentally measured potentials. However, the advantages are (i) that it facilitates the calculation of the free energies of various ions at the same potential scale, which is the scale at which the equilibrium potential sits, and (ii) similar to the CHE, there is no increase in the computational intensity of the calculations, as the calculations rely on neutral gas-phase species. We show examples of how to calculate solution free energies of ions in the context of computational electrocatalysis, and finally demonstrate how this method can be used by using DFT to examine the thermodynamics of adsorption of I*, Br*, Cl*, and SO₄* on Pt(111) and Au(111), and OH* and Ag* on Pt(111) and comparing with those measured experimentally.

3.2 Methods

In this section, we first describe the method for calculating the free energy of an ion in solution, and then apply this method to calculate the adsorption free energy of Cl^* , Br^* , I^* , and SO_4^* on Pt(111) and Au(111), and OH^* and Ag^* on Pt(111).

3.2.1 Computational Details

The Vienna Ab Initio Simulation Package (VASP)84-86 was used to perform the DFT calculations, using a plane-wave basis set and the Projector Augmented Wave approach.^{87,88} The cut-off energy for the basis set was 450 eV. The Perdew-Burke-Ernzerhof, (PBE), exchange-correlation functional was used. 89,90 Both the Pt(111) and Au(111) surfaces were modeled as a 4 layer slab (or 5 layer slab, in the case of SO₄* on Au(111) and Pt(111)), with the bottom 2 layers frozen at the experimentally measured lattice constants of 3.92 Å and 4.08 Å (as a first approximation), respectively, 91 in a 3×3 unit cell. A Monkhorst-Pack mesh kspace sampling grid⁹² of 5×5×1 and 8×8×1 were used for Pt(111) and Au(111), respectively. To simulate the surfaces, a vacuum spacing larger than 14 Å between the slabs was set. Dipole corrections were included in the surfacenormal direction.93 Structural optimization was performed until the forces on each atom were below 0.02 eV Å-1. The adsorption thermodynamics for each adsorbate were evaluated at 1/9 monolayer (ML) coverage. OH* and SO₄* were additionally simulated with co-adsorbed explicit water molecules to approximate the near-surface solvation effect on the adsorption energy.

For sulfate adsorption, see Eq. 3.1, a 6H₂O* water bilayer was used as the reactant state and two water molecules were displaced upon SO₄* adsorption, giving a product state with 4 water molecules co-adsorbed with SO₄*. For OH*, see Eq. 3.2, the reference state was three hydrogen-bonded water molecules adsorbed on the surface (3H₂O*), one proton was then removed to create the product state, which was two water molecules co-adsorbed with OH*. While the water adsorbed on the surface in the initial state, and the water remaining on the surface, co-adsorbed with the adsorbate in the product state, were static, and only vibrational entropy changes were considered, the adsorption reaction does include the entropy change associated with the adsorbate displacing adsorbed water molecules into bulk solution (2 water molecules displaced for SO₄*, 1 for OH*). Additional entropy changes of the solvent near the surface are not considered. This method of modeling the effects of near-surface solvent therefore only approximates the change in entropy upon adsorption. This method also captures only the most local solvating enthalpic interactions, such as hydrogen bonding to the adsorbate and static dipole screening, approximating what could be considered part of the first "solvation shell" around the adsorbate and surface.

$$6H_2O * +SO_{4(aq)}^{2-} \rightarrow [SO_4 + 4H_2O] * +2H_2O_{(aq)} + 2e^-$$
 3.1

$$3H_2O * \rightarrow [OH + 2H_2O] * + H^+ + e^-$$
 3.2

Silver adsorption on Pt(111) was examined at a coverage of 1 and 2 ML, in a 1×1 Pt(111) unit cell, with a $9\times9\times1$ k-space grid. Single gas-phase molecules are calculated in a large box of (15 Å × 15 Å × 15 Å), with a k-point grid of $1\times1\times1$. The 0 K DFT energy of metallic silver is calculated using a slab model, instead of a 3-d bulk structure. We varied the slab thickness (above the thickness where the energy of the slab is converged) of a Ag(111) 1×1 unit cell, where the slope of a

line fit to the energy versus slab thickness represents the energy of bulk silver, per bulk atom. This slab method allows for a greater cancellation of errors than with a 3-d bulk structure. 94 The slabs were symmetric, with the middle two layers frozen at the experimentally measured lattice constant.

All free energies of the gas-phase species are calculated following Eq. 3.3 given further below, at 298.15 K and 1 atm of pressure, except for liquid water, which is calculated at its experimentally measured partial pressure at 298.15 K, where basically its gas-phase entropy is corrected by -0.0887 eV.^{59,95} SO₂ (aq) was taken as the free energy of SO₂(g) as correction by its solvation energy (-0.005 eV)⁹⁶ does not significantly changes the energy. The work function was determined as the difference between the Fermi energy and the one electron potential in vacuum, $\Phi = V - E_{fermi}$. The partial charges where determined with the AIM Bader analysis, ^{97,98} using the Bader program from Henkelman's group. ⁹⁹

The free energy of the solution (aqueous) phase anion is calculated following the method we describe in the following section. Briefly, we use a tabulated value of the experimentally measured equilibrium potential connecting a neutral gasphase (see Figure 3.1) or solid-state species, with the aqueous-phase ion of interest from which the adsorption energies or potentials are calculated. For I, Br, and Cl, this reaction was the reduction from solid I₂ and gas-phase Br₂ and Cl₂, which at standard state have equilibrium potentials of 0.620, 1.094, and 1.36 V vs SHE.⁷² The free energy of solid-phase iodine was calculated as that of gasphase iodine at a partial pressure equal to its vapor pressure at room temperature. 100 For SO₄2-, this reaction was that of sulfur dioxide reduction, see Eq. 3.9, with an equilibrium potential at standard state of 0.158 V vs SHE.⁷² For Ag⁺, the free energy of the aqueous silver cation was calculated from that of metallic silver, with an equilibrium potential of 0.799 V vs SHE .72 For each reaction, the experimentally measured equilibrium potential at standard state was obtained from the data in "Standard Electrode Potentials and Temperature Coefficients in Water at 298.15K". 72 Lastly, for OH*, the free energy of adsorption was calculated relative to hydrogen gas and water, following the computational hydrogen electrode method, CHE, 59 with a standard equilibrium potential of exactly 0 V vs SHE.

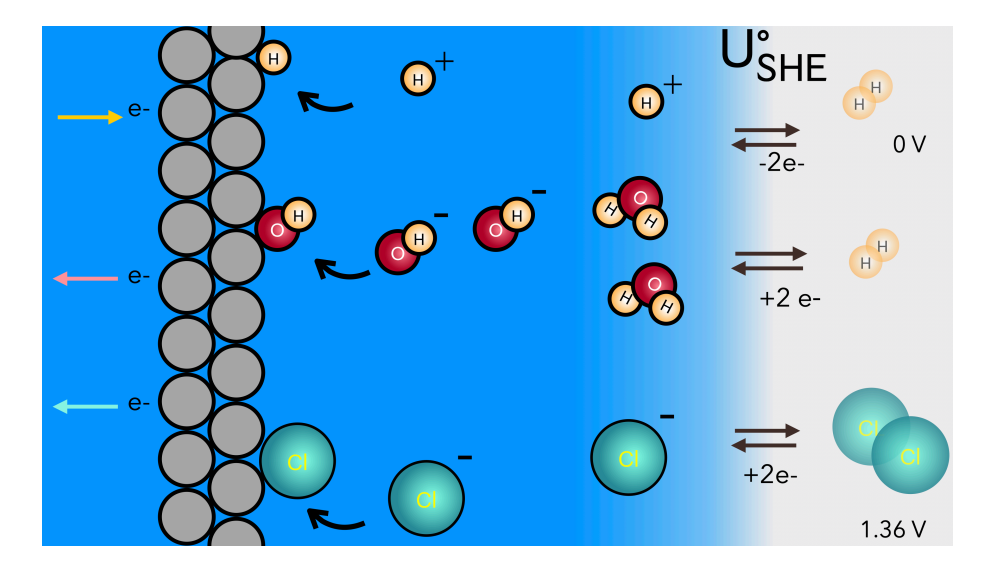


FIGURE 3.1

Representation of ions (Cl⁻, OH⁻, H⁺), in solution phase in equilibrium with gas-phase species at their experimentally measured equilibrium potentials, except for $OH^{-,72}$ (right), and same ions adsorbed on a generic electrode with 111 facet (left). The reference neutral species for adsorbed OH* are $H_2O(I)$ and $H_2(g)$ using the CHE at 0 V vs SHE.

3.2.2 Determination of the free energy of ions in solution

The accuracy of the energy of the solution-phase ion using thermodynamic cycles depends on how well DFT can represent the neutral species. Therefore, it is crucial to include gas-phase corrections or solid-phase corrections to the neutral species from which the ion solution free energy will be calculated. For instance, if one is interested in the solution-phase free energy of oxalic acid, although a neutral species, its solution-phase free energy can be calculated from $CO_2(g)$ and its equilibrium redox potential $2CO_2(g) + 2H^+ + 2e^- \rightarrow H_2C_2O_4$, $CO_2(g)$, $H^+/H_2C_2O_4$, $U_{SHE}^c = -0.432 \text{ V}$. In this case, the calculated DFT energy of $CO_2(g)$ will require a gas-phase correction that is functional dependent.

The free energy of the gas-phase species X(g) can then be determined with DFT and statistical mechanics following Eq. 3.3

$$G_{X_{(g)}} = E_{DFT} + ZPE + E_{int} - TS + PV$$
 3.3

where ZPE is the zero-point vibrational energy, E_{int} includes the vibrational, rotational, and translational contributions (above 0 K) to the internal energy, and S is the entropy of the gas-phase molecule. The internal energy is calculated using statistical mechanics for vibrational, rotational, and translational energy, while

the entropy, in this *Chapter*, is taken from standard thermodynamic tables, ⁷³ PV is the pressure-volume contribution to the free energy, obtained as $PV = Nk_BT$ where N = 1 mole, k_B is the Boltzmann constant and T is the temperature.

In this *Chapter*, for the solid-state species, the 0 K DFT energy is taken as an approximation of the free energy of the solid at room temperature. In the following, we show how to obtain the free energy of solution-phase ions from gas-phase species. The first step is to identify a reaction that links the charged species we are interested in with a neutral species that is ideally in the gas phase or in the solid phase, and has a known (experimentally measured) equilibrium potential (which can be found, for example, in the electrochemical series, tabulated for many ions). 72,73 For example, if we want to determine the aqueous free energy of $Cl_{(aq)}^{-}$, we can use its standard half-cell reduction reaction, $\frac{1}{2}Cl_{2(g)}^{+}$ $e^- \rightleftharpoons Cl_{(aq)}^-$, with equilibrium potential $U_{SHE}^\circ = 1.36 \text{ V}$. This reaction links an easy to calculate neutral gas-phase species, $Cl_{2(g)}$, with the charged, difficult to model, $Cl_{(aq)}^{-}$, allowing for the calculation of the free energy of the anion from that of the gas-phase species. 61,64,65 The CHE model⁵⁹ is an example of such an electrochemical thermodynamic cycle, but it is a special case where the equilibrium potential is defined to be exactly 0 V vs SHE at pH = 0, or 0 V vs RHE at all pH). In the method described here, we will show how to use such a cycle to determine the solution-phase free energy of ions using half-cell redox reactions that do not transfer the same number of protons and electrons.

A general representation of how to determine the free energy of solution-phase of charged species will be shown in the next sections, where we use reactions with a known experimental equilibrium potential, in two scenarios. The first is for reactions transferring electrons (with no proton transferred with the electrons), for instance, the Cl_2 (g)/Cl half-cell redox reaction, and the second for reactions transferring different numbers of protons and electrons, for instance the $SO_{4\,(aq)}^{2-}$, $\text{H}^+/\text{SO}_2(\text{aq})$, half-cell redox reaction, where a different number of protons (4 H⁺) and electrons (2 e⁻) participate in the reaction.

3.2.3 Half-cell redox couple with n electrons transferred

The following method has been described in the literature to calculate the free energy of an ion in solution to then construct adsorbate phase diagrams and determine adsorption potentials. ^{64,65} For the following generic reaction:

$$\frac{1}{2}A_{2(g)} + ne^{-} \rightleftharpoons A_{(aq)}^{n-}$$
 3.4

the change in free energy on a given potential scale is:

$$\Delta G = G_{A_{(aq)}}^{n-} - \frac{1}{2}G_{A_{2(g)}} + n|e_0|U$$
3.5

At standard conditions and in the SHE scale, the free energy change is:

$$\Delta G^{\circ} = G_{A_{(aq)}}^{\circ} - \frac{1}{2} G_{A_{2(g)}}^{\circ} + n |e_{0}| U_{SHE}^{\circ}$$
3.6

where $G_{A(aq)}^{\circ}$, is the standard solution-phase free energy of the anion, $A_{(aq)}^{n-}$. $G_{A_{2(g)}}^{\circ}$, is the standard gas-phase free energy of the neutral species, $A_{2(g)}$. The last term of Eq. 3.5, $-n|e_0|U$, is the free energy of the electrons participating in the reaction at an arbitrary potential scale, n is the number of electrons, and $|e_0|$ is the elementary charge taken as positive. Eq. 3.6 is the free energy at standard conditions, and U_{SHE}° , is the electrode potential of the half-cell redox reaction on the SHE scale. Therefore, the free energy of the electrons at standard conditions is $-n|e_0|U_{SHE}^{\circ}$.

Note that at equilibrium, the change in the standard reaction free energy is equal to zero, $\Delta G^{\circ} = 0$, and the standard solution-phase free energy of the anion, $G_{A(aq)}^{\circ}$, can be obtained from the standard gas-phase free energy, $G_{A_2(g)}^{\circ}$, and the experimentally measured equilibrium potential, U_{SHE}° , taken from the standard electrode potential tables, ^{72,73} as shown in Eq. 3.7

$$G_{A(aq)}^{\circ} = \frac{1}{2} G_{A_{2(g)}}^{\circ} - n|e_0|U_{SHE}^{\circ}$$
3.7

At a different initial concentration of the anion, we can use the Nernst equation to obtain the anion solution-phase free energy at any concentration, important when comparing with experimental observations performed at non-standard state conditions, as done in reference 66 to determine the solution phase free energy of Cl⁻ (aq) and ClO₄⁻ (aq). The described approach can also be used to calculate the free energy of an aqueous cation, as shown by Akhade et al. 78

3.2.4 Half-cell redox couples with unequal number of protons and electrons

Many electrochemical reactions involve the transfer of both protons and electrons, sometimes in unequal numbers, to or from charged species. Since we can treat the free energy of ions and the energy of electrons independently, we can use the described method twice to calculate the free energy of an ion in a reaction involving protons (or for any other number of ions). The first calculation relates the free energy of protons to hydrogen gas at equilibrium, equivalent to the CHE approach, and the second calculation computes the free energy of the ion of interest, as described above. This procedure can be repeated for any number of dissimilar ions in a given reaction. We can use this method with any reaction with (unequal) number of protons and electrons. Of course, the method works because at every calculation, we make use of an experimentally known equilibrium potential, as such avoiding the complicated and inaccurate calculation of the ion solvation energy.

In this method, the free energy of protons is described similarly as expressed in Eq. 3.7 for the generic redox couple (A_2/A^{n-}) . In the particular case of the hydrogen half-redox reaction, $(H^+/H_2(g))$, the equilibrium potential is defined to be 0 V vs SHE and, therefore, the second term in Eq. 3.7 is zero, allowing us to

substitute the free energy of the protons for that of the DFT-calculated free energy of $H_2(g)$, as shown in Eq. 3.8, in a similar way as within the CHE framework.⁵⁹

$$\frac{1}{2} G_{H_2(g)}^{\circ} = G_{H_{(aq)}}^{\circ}$$
 3.8

As an example, we will show in a stepwise manner how to obtain the solutionphase free energy of $SO_{4(aq)}^{2-}$ using a half-cell redox reaction that combines a neutral species $SO_2(aq)$ with the charged $SO_{4(aq)}^{2-}$ species, see Eq. 3.9. Note that the number of electrons and protons are different. The redox equation with its equilibrium potential⁷² and the standard free energy are shown below:

$$SO_{4\,(aq)}^{2-} + 4H^+ + 2e^- \rightleftharpoons SO_{2\,(aq)} + 2\,H_2O\,(l),$$
 $U_{SHE}^{\circ} = 0.158\,V$ 3.9

$$\Delta G^{\circ} = G_{SO_{2(aq)}}^{\circ} + 2G_{H_{2}O(l)}^{\circ} - G_{SO_{4(aq)}}^{\circ} - 4G_{H^{+}}^{\circ} + 2|e_{0}|(U_{SHE}^{\circ})$$
3.10

Eq. 3.10 is equal to zero, $\Delta G^{\circ} = 0$, when U is equal to U_{SHE}° . By using Eq.3.8, and evaluating $-n|e_0U_{SHE}^{\circ} = -2|e_0|(0.158)V$ as shown in Eq. 3.11, we can calculate the standard solution-phase free energy of $SO_{4(aq)}^{2-}$ in the SHE scale, $G_{SO_{4(aq)}^{2-}}^{\circ}$ as shown in Eq. 3.12

$$\Delta G^{\circ} = G^{\circ}_{SO_{2(aq)}} + 2G^{\circ}_{H_{2}O(l)} - G^{\circ}_{SO^{2-}_{4(aq)}} - 2G^{\circ}_{H_{2(g)}} + 2e_{0}(0.158V) = 0$$
3.11

$$G_{SO_{4(aq)}^{2-}}^{\circ} = G_{SO_{2(aq)}}^{\circ} + 2G_{H_2O(l)}^{\circ} - 2G_{H_2(g)}^{\circ} + 2e_0(0.158V)$$
 3.12

Now, the solution-phase free energy of the anion can be calculated from the free energy of neutral species, those of $SO_2(g)$, $H_2(g)$ and $H_2O(g)$. The free energy of water is obtained from that of $H_2O(g)$ and corrected to that of liquid water. For $SO_2(aq)$, we did not include the correction and use the energy in the gas phase as the difference between the aqueous and gas-phase energies, based on experimental results, is almost zero (-0.005 eV) and does not significantly change the energy (see the computational methods section).

Similarly, other redox couple reactions could be used to obtain the solution-phase free energy of $SO_{4~(aq)}^{2-}$, as shown in Figure 3.2 . For instance, the free energy of $SO_{4~(aq)}^{2-}$, can also be determined from the equilibrium potentials of $(S_2O_6^{2-}(aq), H^+/SO_2~(aq), U_{SHE}^\circ = 0.37~V)$ to determine the energy of $S_2O_6^{2-}$ (aq) and then followed by $(SO_{4~(aq)}^{2-})$, $H^+/S_2O_6^{2-}$ (aq), $U_{SHE}^\circ = -0.05~V$) to then determine the solution-phase free energy of SO_4^{2-} (aq).⁷²

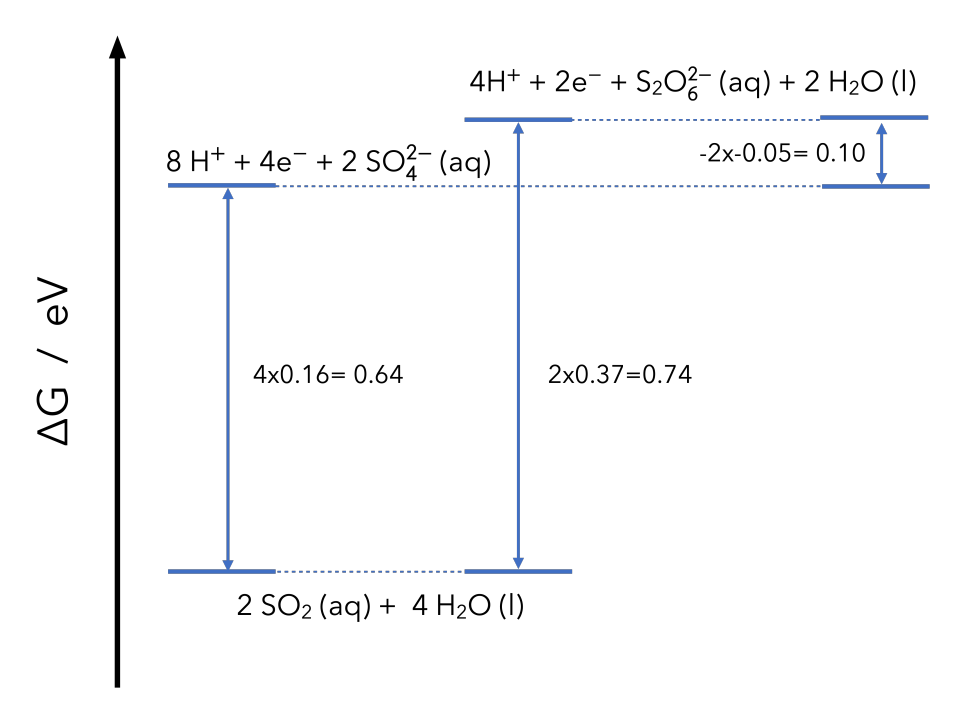


FIGURE 3.2

Illustration of electrochemical thermodynamic cycles that can be used to determine the solution-phase free energy of $SO_4^{2-}(aq)$ using the standard equilibrium potentials for $[SO_4^{2-}(aq), H^+ / SO_2(aq), U_{SHE}^{\circ}=0.158 \text{ V}],^{72}$ or by combining $[S_2O_6^{2-}(aq), H^+ / SO_2(aq), U_{SHE}^{\circ}=0.37 \text{ V}],^{72}$ and $[SO_4^{2-}(aq), H^+ / S_2O_6^{2-}(aq), U_{SHE}^{\circ}=-0.05 \text{ V}],^{72}$

3.3 Equilibrium adsorption energies and adsorption potentials

The solution-phase free energy of an ion is important in many areas of research and is particularly important for surface electrochemistry and (electro)catalysis, as the solution-phase free energy of an ion can be used to calculate adsorption thermodynamics and is necessary for comparing the adsorption strength between different species/adsorbates. These adsorption thermodynamics can be calculated relative to a neutral, gas-phase species such as $\text{Cl}_2(g)$ instead of $\text{Cl}^-(aq)$ (as described above), but this prohibits comparing adsorption strength from solution between different adsorbates (for example, Cl^* to Br^*) as this comparison will require a correction of the gas-phase dissociation energy, ionization energy, and solvation energy for each adsorbate. It is important to be able to compare the adsorption strength between adsorbates as it allows the state, structure, and composition of the surface to be determined, for instance through a surface phase diagram.

In this section, we will show how to calculate the adsorption energy of an anion on any given surface site using the solution-phase free energy obtained using the method described here. The adsorption thermodynamics is calculated following the reaction given in Eq. 3.13, where $A_{(aq)}^{n-}$ represents a generic anion, (*) a bare surface site, and A* the adsorbed anion.

$$A_{(aq)}^{n-} + * \rightarrow A^* + ne^-$$
 3.13

A similar reaction can be written for cation adsorption, with the electron written as a reactant instead of a product. Based on Eq. 3.13, we can write the change in free energy upon adsorption, shown in Eq. 3.14 (again, a similar equation can be written for cation adsorption):

$$\Delta G^{ads} = G_{A^*} - G_* - G_{A_{(aq)}^{n-}} - n|e_0|U_{SHE}$$
3.14

where G_{A^*} is the free energy of the adsorbed species, G_* the free energy of the bare surface, $G_{A^{n-}_{(aq)}}$ the free energy of the solution phase anion, and $-n|e_0|U_{SHE}$ the free energy of the electrons transferred in the reaction at potential U_{SHE} , and the final adsorption energy can be shifted linearly with this term at an applied bias of interest to build, for instance, energy vs potential diagrams. Combining the CHE⁵⁹ approach with this method, we can add a term to Eq. 3.14 to consider the change in dipole moment induced by the adsorption of the charged species (*A) on the surface (*), $\Delta \mu^{ads} = (\mu_{*A} - \mu_*)$, and an additional term, $(U_{SHE} - U_{PZC}/d)$, to account for the dipole interaction with the electrode-electrolyte electric field. Based on the Helmholtz approximation of the double layer, ⁵⁹ d is ~3.0 Å and we get Eq. 3.15

$$\Delta G_{*A}^{ads} = G_{A^*} - G_* - G_{A_{(aq)}^{n-}} - n|e_0|U_{SHE} + \Delta \mu^{ads} \frac{(U_{SHE} - U_{PZC})}{d}$$
 3.15

The potential of zero charge, U_{PZC} , is taken as the experimentally measured in the SHE scale.¹⁰⁵ Approximating the U_{PZC} to 0 V vs SHE does not significantly change the absolute adsorption potentials, see Table B3. This equation can then be solved for the equilibrium adsorption potential, $U_{ads,SHE}^{\circ}$, which represents the potential where adsorption becomes favorable (when $\Delta G^{ads} = 0$), shown in Eq.3.16

$$U_{ads,SHE}^{\circ} = \frac{G_{*A} - G_{A^{-}}(aq) - G_{*} - \frac{\Delta \mu^{ads}}{d} U_{PZC}}{n|e_{0}| - \frac{\Delta \mu^{ads}}{d}}$$
3.16

The potential scale on which this equilibrium adsorption potential sits depends on the methodology used to calculate the free energy of the ion in solution. Here, the standard hydrogen electrode scale is used. The free energy of the adsorbed species G_{A^*} , is calculated following Eq. 3.17:

$$G_{A^*} = E_{DFT} + ZPE - TS_{vib}$$
3.17

where E_{DFT} is the 0 K DFT energy of the adsorbate on the surface, the ZPE is the zero-point vibrational energy, and S_{vib} is the vibrational entropy of the adsorbate. The free energy of the bare surface, G_* , is taken simply as the DFT energy at 0 K,

given that the vibrational energy/entropy of the surface is not significantly perturbed by the adsorbate.

3.4 Results and Discussion

3.5 Applications of the method in electrocatalysis

To illustrate the use of this method in calculating relative adsorption strengths, we calculated the adsorption free energy at low coverage (1/9 ML) of iodide, bromide, chloride, and sulfate on Pt(111) and Au(111) and hydroxide on Pt(111). For comparison, we also calculated the adsorption free energy of Ag on Pt(111). From these adsorption free energies, we have calculated the equilibrium adsorption potential, the potential at which adsorption (at this coverage) becomes favorable, and plotted this against the experimentally measured adsorption potential. This is shown in Figure 3.3a, b).

From Figure 3.3a , b), it is clear that we can capture the relative trend in adsorption strength between each of these species, with the trend between the anions following I* > Br* > Cl* > SO₄* > OH* across both surfaces. It is also apparent that all of the adsorbates bind less strongly on Au(111) than on Pt(111). This can be understood in terms of a more repulsive interaction between the adsorbates outer p-shells and the expanded d band of Au(111), compared to Pt(111), due to relativistic effects being more predominant on Au(111). Furthermore, the d-band of Au(111) is more occupied than Pt(111). This repulsive interaction also results in a longer bond length between the ions and the surface for ions adsorbed on Au(111) than on Pt(111), see Table B1. Of course, these trends were already known from experiment, 110,111 and agree well with prior computational calculations. 107

We also examined the change in work function and the partial charges on the adsorbates with a Bader charge analysis, summarized in Table B1. We note that the analysis which includes solvation (SO₄*-sol) considers only the change in work function associated with the single adsorbed water structures considered for the reactant (6H₂O*) and product (SO₄*+4H₂O*) states. Our calculations follow the general trends found previously with DFT, see Groß et. al., ¹¹²⁻¹¹⁴ Pašti et al., ^{109,115,116} and Illas et al. ¹⁰⁷ For Pt(111), we find a decrease in work function induced by the adsorption of Cl, Br, and I, and an increase induced by the adsorption of SO₄. In the case of Au(111), we see an increase in work function induced by the adsorption of Cl, Br and SO₄ and a decrease induced by the adsorption of I.

Based on the Bader charge analysis, the adsorbates which retain more negative charge also induce a larger dipole moment (Table B1), and therefore they would benefit from solvation near the electrode surface to stabilize their energy. The general trend for induced dipole moment on both Pt(111) and Au(111) follows SO₄>Cl>Br>I. The work function of Au(111) is smaller than that of Pt(111). The higher the work function the less charge transfer, therefore the electronegative adsorbates on Au(111) will retain more negative charge than when adsorbed on Pt(111). The character of the halide bond on both Pt(111) and Au(111) has been conceptualized to be covalent in nature; 118,114 however, we can say that between the two, the bonding on Au(111) is slightly more ionic than on Pt(111), especially

for Cl, Br and SO_4 . In general, adsorbates that show higher charge separation tend to be more ionic in character, ¹¹⁹ but that is not always the case (as for instance Cl on $Cu(111)^{120}$). Additional studies of electronic structure would be necessary to further investigate this.

The important result from Figure 3.3a , b) is that by using the method of determining the free energy of each ion in solution phase, at the same potential scale, we can reproduce the trends in adsorption potentials from DFT. We can now be confident in applying this method to understand more complex phenomena.

In general, we see good agreement between DFT and experiment when we include near-surface solvation for not only the trend in adsorption strength between adsorbates, but also the absolute value of the adsorption potentials. We can use Figure 3.3a, b) to make a few important points about this accuracy.

First, we note that we expect the calculated adsorption potential to be exchange-correlation functional dependent; the exact magnitude of the adsorption energy will vary with functional. If there is a significant difference in the van der Waals contribution to binding for these adsorbates between Pt(111) and Au(111), this could cause an additional dependence on functional, as traditional functionals poorly capture van der Waals interactions. However, we expect the trend between the adsorbates, differences between adsorption on Au(111) and Pt(111) (assuming the van der Waals contribution to binding is small), and the effect of near-surface solvation, to be less dependent on the chosen functional.

Second, it is interesting to see that by including only a few explicit water molecules hydrogen-bonded to the adsorbate, the adsorption potentials for SO₄* on both Pt(111) and Au(111) as well as for OH* on Pt(111) are brought much closer to those measured experimentally (Figure 3.3a, b)) The mean and maximum absolute errors (MAE, MAX) are MAE = 0.19 eV and MAX = 0.48 eV , compared to Figure 3.3a , b), where they are without solvation and the MAE =0.33 eV and MAX= 0.76 eV and, therefore, far from the experimental results. This suggests that the influence of the rest of the water in the electrochemical environment, the second and third solvation shells of the adsorbate, might not further influence the stabilization of the adsorbate, as we already see a significant decrease in the MAE of about ~0.14 eV. Prior work by Calle-Vallejo et al. 121,122 and Janik et al., 123 suggests that for many adsorbates, there is a threshold of number of explicit water molecules that will stabilize the energy of the adsorbate, and above that number, there is no significant impact. A wide variety of other methods for solvating the surface (implicit solvation, explicit solvation with classical or *ab-initio* molecular dynamics; for example) can be used in combination with the method we describe here to calculate the free energy of ions in solution, to further probe the effects of near-surface solvation on the adsorption energetics.

Third, it appears that the adsorption potentials on Au(111) are consistently underpredicted relative to experiment (at least for I*, Br*, and Cl*), whereas this is not the case for Pt(111). Table B1 shows that the anions retain more negative charge (and create a larger change in surface-normal dipole moment on adsorption) on Au(111) than on Pt(111). We have included the dipole correction to the adsorption potential as calculated in Eq. 3.16, but this does not lead to a significant change in adsorption potential (Table B3), and so this alone cannot explain the difference in "accuracy" between Au(111) and Pt(111). We might expect, however, that the effect of near-surface solvation depends, at least in part, on the magnitude of the surface-normal dipole moment. As the halides retain more charge and generate a more positive surface normal dipole moment upon

adsorption on Au(111) than on Pt(111), we expect the effect of near-surface solvation on the adsorption of the halides, which we did not consider, to be larger on Au(111) than on Pt(111). In support of this idea, we can see that Figure 3.3a, b), where near-surface solvation is neglected (for all adsorbates), the calculated adsorption potential is equally far from the parity line for both Pt(111) and Au(111) for adsorbates which generate a more positive surface-normal dipole moment (Cl*, SO_4 *). Additionally, we find the magnitude of the effect of solvation on the adsorption of SO_4 * (shifts adsorption potential by -0.27 V on Pt(111) and -0.68 V on Au(111)) proportional to the change in surface-normal dipole moment (0.47 eÅ on Pt(111), 0.82 eÅ on Au(111)).

We note that additional differences between Pt(111) and Au(111) could be due to a difference in the contribution of van der Waals interactions, which traditional exchange-correlation functionals poorly describe, as well as experimental factors; the experimentally measured potentials for anion adsorption on Au(111) were measured relative to the saturated calomel electrode (SCE), its potential on an SHE scale had to be assumed to shift these potentials to the same scale as those measured on Pt(111).

Lastly, the adsorption of some of the ions competes with that of other species (for example, I* on Pt(111) with H*, and Ag* on Pt(111) with SO_4 *), which would affect the measured adsorption potential; we have not considered this effect. Another factor, might be the use of experimental lattice constants, instead of DFT-converged lattice constants, due to the strained exerted on the slab, although we believe this to be a minor effect, it is good to keep in mind.

The preceding discussion makes it clear that the accuracy of the calculated adsorption potentials depends on a variety of factors including (i) the choice of exchange correlation functional (which influences both the energy of the reference gas-phase molecule to calculate the free energy of the ion in solution and the adsorption energy), (ii) the inclusion of near-surface solvation effects, (iii) co-adsorption, and (iv) the accuracy of the experimentally measured adsorption potential (including the choice and stability of the reference electrode). We mention these points here as they are important to understand how to model ion adsorption in the electrochemical environment, but each requires further study. Therefore, this *Chapter* is not intended as an evaluation of the accuracy of the method we have described here for calculating the free energy of solution-phase ions, only an example of its usefulness and simplicity.

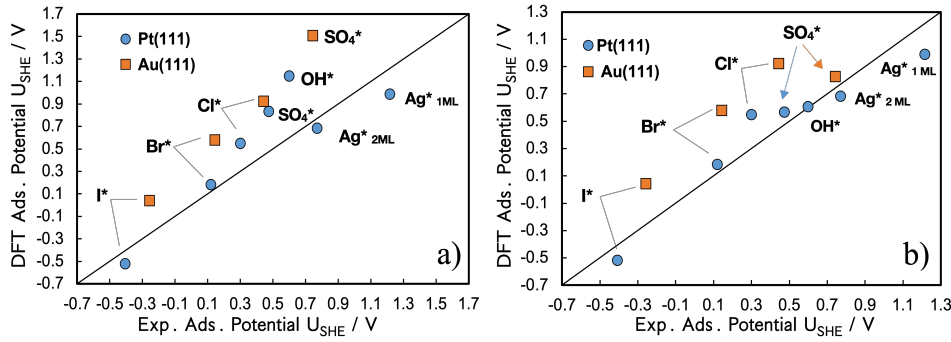


FIGURE 3.3A, B)

DFT simulated and experimentally measured equilibrium adsorption potential 110,111,124 of I*, Br*, CI*, and SO₄* on Pt(111) and Au(111) as well as OH* and the first and second monolayers of Ag* on Pt(111). All potentials are simulated/measured at low coverage (1/9 ML), except for Ag* on Pt(111) (for which the coverage is 1 and 2 ML). In (b), the adsorption potentials calculated for OH* on Pt(111) and SO₄* on Pt(111) and Au(111) include the effect of near-surface solvation, approximated by including co-adsorbed water molecules. The mean and maximum absolute errors (MAE and MAX) for (a) are (0.33, 0.76 eV) and for (b) are (0.19, 0.48 eV). Table B2 shows the calculated and experimentally measured adsorption potentials.

3.6 Conclusions

In this *Chapter* we have revised and illustrated a simple method that facilitates the calculation of solution-phase free energies of ions, eliminating the need to model solvation of the ions in bulk solution, and showed its importance by calculating adsorption potentials of different ions on the same potential scale. This is achieved by using an experimentally measured equilibrium potential to calculate the free energy of the ion in solution from a neutral gas-phase or solid-phase species. The method shows how the electrons and protons can be numerically arranged separately allowing to use any half-cell redox reaction.

We apply the method to examine the adsorption of a variety of different ions on Pt(111) and Au(111) and show the trend in adsorption strength matches the experimental trend. Our method is computationally efficient and its accuracy in terms of the energetics of the solution-phase charged species is only limited by how well DFT can model neutral gas-phase species and by the accuracy of the experimentally measured equilibrium potential of the reaction connecting the ion of interest to the neutral gas or solid-phase species. However, the accuracy of the calculated ion adsorption potential not only depends on the previous limitations but also by how well DFT can capture the effects of near-surface solvation, especially for adsorbates which induce a large surface-normal dipole moment, and the effects of a near-surface electric field.

The method used here is not new, however, we hope that by describing the methodology in detail and illustrating its usefulness, it will see more widespread use, such that the thermodynamics and kinetics of electrochemical and electrocatalytic reactions involving ions other than protons, will be more

frequently simulated with density functional theory. Such a method is necessary, for example, to examine the composition of a catalyst surface in electrochemical environments (surface phase diagram), competition in adsorption between species under reaction conditions, and the stability of an electrode or catalyst surface with respect to dissolution or (re)deposition; all examples at the forefront of computational electrocatalysis.

3.7 References

- (1) Hori, Y.; Koga, O.; Yamazaki, H.; Matsuo, T. Infrared Spectroscopy of Adsorbed CO and Intermediate Species in Electrochemical Reduction of CO2 to Hydrocarbons on a Cu Electrode. *Electrochim. Acta* **1995**, *40* (16), 2617-2622.
- (2) Osawa, M. Dynamic Processes in Electrochemical Reactions Studied by Surface-Enhanced Infrared Absorption Spectroscopy (SEIRAS). *BCSJ* **1997**, *70* (12), 2861-2880.
- (3) Heinen, M.; Chen, Y. X.; Jusys, Z.; Behm, R. J. In Situ ATR-FTIRS Coupled with on-Line DEMS under Controlled Mass Transport Conditions—A Novel Tool for Electrocatalytic Reaction Studies. *Electrochim. Acta* **2007**, *52* (18), 5634–5643.
- (4) Neto, A. O.; Nandenha, J.; Assumpção, M. H. M. T.; Linardi, M.; Spinacé, E. V.; de Souza, R. F. B. In Situ Spectroscopy Studies of Ethanol Oxidation Reaction Using a Single Fuel Cell/ATR-FTIR Setup. *International Journal of Hydrogen Energy* 2013, 38 (25), 10585-10591.
- (5) Pander, J. E.; Baruch, M. F.; Bocarsly, A. B. Probing the Mechanism of Aqueous CO2 Reduction on Post-Transition-Metal Electrodes Using ATR-IR Spectroelectrochemistry. *ACS Catal.* **2016**, *6* (11), 7824-7833.
- (6) Wain, A. J.; O'Connell, M. A. Advances in Surface-Enhanced Vibrational Spectroscopy at Electrochemical Interfaces. *ADV PHYS-X* **2017**, *2* (1), 188-209.
- (7) Perales-Rondon, J. V.; Hernandez, S.; Martin-Yerga, D.; Fanjul-Bolado, P.; Heras, A.; Colina, A. Electrochemical Surface Oxidation Enhanced Raman Scattering. *Electrochim. Acta* **2018**, *282*, 377-383.
- (8) Baricuatro, J. H.; Kim, Y.-G.; Korzeniewski, C. L.; Soriaga, M. P. Tracking the Prelude of the Electroreduction of Carbon Monoxide via Its Interaction with Cu(100): Studies by Operando Scanning Tunneling Microscopy and Infrared Spectroscopy. *Catal. Today* 2020, 358, 210-214.
- (9) Zhu, Y.; Wang, J.; Chu, H.; Chu, Y.-C.; Chen, H. M. In Situ/Operando Studies for Designing Next-Generation Electrocatalysts. *ACS Energy Lett.* **2020**, *5* (4), 1281–1291.
- (10) Greeley, J.; Mavrikakis, M. Alloy Catalysts Designed from First Principles. *Nat. Mater.* **2004**, *3* (11), 810–815.
- (11) Greeley, J.; Jaramillo, T. F.; Bonde, J.; Chorkendorff, I.; Nørskov, J. K. Computational High-Throughput Screening of Electrocatalytic Materials for Hydrogen Evolution. *Nat. Mater.* **2006**, *5* (11), 909-913.
- (12) Magnussen, O. M.; Groß, A. Toward an Atomic-Scale Understanding of Electrochemical Interface Structure and Dynamics. *J. Am. Chem. Soc.* **2019**, *141* (12), 4777–4790.
- (13) Xin, H.; Linic, S. Communications: Exceptions to the d-Band Model of Chemisorption on Metal Surfaces: The Dominant Role of Repulsion between Adsorbate States and Metal d-States. J. Chem. Phys. **2010**, 132 (22), 221101.

- (14) Nørskov, J. K.; Abild-Pedersen, F.; Studt, F.; Bligaard, T. Density Functional Theory in Surface Chemistry and Catalysis. *PNAS* **2011**, *108* (3), 937-943.
- (15) Diaz-Morales, O.; Ledezma-Yanez, I.; Koper, M. T. M.; Calle-Vallejo, F. Guidelines for the Rational Design of Ni-Based Double Hydroxide Electrocatalysts for the Oxygen Evolution Reaction. *ACS Catal.* **2015**, *5* (9), 5380-5387.
- (16) Sakong, S.; Groß, A. The Electric Double Layer at Metal-Water Interfaces Revisited Based on a Charge Polarization Scheme. *J. Chem. Phys.* **2018**, *149* (8), 084705.
- (17) Schnur, S.; Groß, A. Challenges in the First-Principles Description of Reactions in Electrocatalysis. *Catal. Today* **2011**, *165* (1), 129-137.
- (18) Rossmeisl, J.; Skúlason, E.; Björketun, M. E.; Tripkovic, V.; Nørskov, J. K. Modeling the Electrified Solid-Liquid Interface. *Chem. Phys. Lett.* **2008**, 466 (1), 68-71.
- (19) Cohen, A. J.; Mori-Sánchez, P.; Yang, W. Insights into Current Limitations of Density Functional Theory. *Science* **2008**, *321* (5890), 792-794.
- (20) Lozovoi, A. Y.; Alavi, A.; Kohanoff, J.; Lynden-Bell, R. M. Ab Initio Simulation of Charged Slabs at Constant Chemical Potential. *J. Chem. Phys.* **2001**, *115* (4), 1661-1669.
- (21) Filhol, J.-S.; Neurock, M. Elucidation of the Electrochemical Activation of Water over Pd by First Principles. *Angew. Chem. Int. Ed.* **2006**, *45* (3), 402-406.
- (22) Taylor, C. D.; Wasileski, S. A.; Filhol, J.-S.; Neurock, M. First Principles Reaction Modeling of the Electrochemical Interface: Consideration and Calculation of a Tunable Surface Potential from Atomic and Electronic Structure. Phys. Rev. B 2006, 73 (16), 165402.
- (23) A. Gauthier, J.; D. Chen, L.; Bajdich, M.; Chan, K. Implications of the Fractional Charge of Hydroxide at the Electrochemical Interface. *Phys. Chem. Chem. Phys.* **2020**, *22* (13), 6964–6969.
- (24) Tölle, J.; Gomes, A. S. P.; Ramos, P.; Pavanello, M. Charged-Cell Periodic DFT Simulations via an Impurity Model Based on Density Embedding: Application to the Ionization Potential of Liquid Water. *Int. J. Quantum Chem.* **2019**, *119* (1), e25801.
- (25) Schnur, S.; Groß, A. Properties of Metal-Water Interfaces Studied from First Principles. *New J. Phys.* **2009**, *11* (12), 125003.
- (26) Desai, S. K.; Pallassana, V.; Neurock, M. A Periodic Density Functional Theory Analysis of the Effect of Water Molecules on Deprotonation of Acetic Acid over Pd(111). *J. Phys. Chem. B* **2001**, *105* (38), 9171–9182.
- (27) Gauthier, J. A.; Dickens, C. F.; Chen, L. D.; Doyle, A. D.; Nørskov, J. K. Solvation Effects for Oxygen Evolution Reaction Catalysis on IrO2(110). *J. Phys. Chem. C* **2017**, *121* (21), 11455–11463.
- (28) Kimmel, G. A.; Matthiesen, J.; Baer, M.; Mundy, C. J.; Petrik, N. G.; Smith, R. S.; Dohnálek, Z.; Kay, B. D. No Confinement Needed: Observation of a Metastable Hydrophobic Wetting Two-Layer Ice on Graphene. *J. Am. Chem. Soc.* **2009**, *131* (35), 12838–12844.
- (29) Gunathunge, C. M.; Ovalle, V. J.; Li, Y.; Janik, M. J.; Waegele, M. M. Existence of an Electrochemically Inert CO Population on Cu Electrodes in Alkaline PH. *ACS Catal.* **2018**, 8 (8), 7507-7516.
- (30) Tripkovic, V. Thermodynamic Assessment of the Oxygen Reduction Activity in Aqueous Solutions. *Phys. Chem. Chem. Phys.* **2017**, *19* (43), 29381-29388.
- (31) Shan, N.; Liu, B. Elucidating Molecular Interactions in Glycerol Adsorption at the Metal-Water Interface with Density Functional Theory. *Langmuir* **2019**, *35* (14), 4791-4805.
- (32) Granda-Marulanda, L. P.; Builes, S.; Koper, M. T. M.; Calle-Vallejo, F. Influence of Van Der Waals Interactions on the Solvation Energies of Adsorbates at Pt-Based Electrocatalysts. *ChemPhysChem* **2019**, *20* (22), 2968-2972.

- (33) Ringe, S.; Oberhofer, H.; Hille, C.; Matera, S.; Reuter, K. Function-Space-Based Solution Scheme for the Size-Modified Poisson-Boltzmann Equation in Full-Potential DFT. *J. Chem. Theory Comput.* **2016**, *12* (8), 4052-4066.
- (34) Mathew, K.; Sundararaman, R.; Letchworth-Weaver, K.; Arias, T. A.; Hennig, R. G. Implicit Solvation Model for Density-Functional Study of Nanocrystal Surfaces and Reaction Pathways. *J. Chem. Phys.* **2014**, *140* (8), 084106.
- (35) Schwarz, K. A.; Sundararaman, R.; Moffat, T. P.; Allison, T. C. Formic Acid Oxidation on Platinum: A Simple Mechanistic Study. *Phys. Chem. Chem. Phys.* **2015**, *17* (32), 20805–20813.
- (36) Sakong, S.; Groß, A. The Importance of the Electrochemical Environment in the Electro-Oxidation of Methanol on Pt(111). ACS Catal. **2016**, 6 (8), 5575-5586.
- (37) Weitzner, S. E.; Akhade, S. A.; Varley, J. B.; Wood, B. C.; Otani, M.; Baker, S. E.; Duoss, E. B. Toward Engineering of Solution Microenvironments for the CO2 Reduction Reaction: Unraveling PH and Voltage Effects from a Combined Density-Functional-Continuum Theory. J. Phys. Chem. Lett. 2020, 11 (10), 4113-4118.
- (38) Qiao, C.; Zhang, J.; Jiang, P.; Zhao, S.; Song, X.; Yu, J. A Molecular Approach for Predicting Phase Diagrams of Ternary Aqueous Saline Solutions. *Chem. Eng. Sci.* **2020**, *211*, 115278.
- (39) Brancato, G.; Rega, N.; Barone, V. A Hybrid Explicit/Implicit Solvation Method for First-Principle Molecular Dynamics Simulations. *J. Chem. Phys.* **2008**, *128* (14), 144501.
- (40) Sakong, S.; Naderian, M.; Mathew, K.; Hennig, R. G.; Groß, A. Density Functional Theory Study of the Electrochemical Interface between a Pt Electrode and an Aqueous Electrolyte Using an Implicit Solvent Method. *The Journal of Chemical Physics* 2015, 142 (23), 234107.
- (41) Ge, X.; Wang, J.; Zhang, Z.; Wang, X.; Chen, M. Thermodynamic Modeling of Electrolyte Solutions by a Hybrid Ion-Interaction and Solvation (HIS) Model. Calphad 2015, 48, 79-88
- (42) Spohr, E. Computer Simulation of the Water/Platinum Interface. J. Phys. Chem. **1989**, 93 (16), 6171-6180.
- (43) Li, X.; Ågren, H. Molecular Dynamics Simulations Using a Capacitance-Polarizability Force Field. *J. Phys. Chem. C* **2015**, *119* (33), 19430-19437.
- (44) Steinmann, S. N.; Ferreira De Morais, R.; Götz, A. W.; Fleurat-Lessard, P.; Iannuzzi, M.; Sautet, P.; Michel, C. Force Field for Water over Pt(111): Development, Assessment, and Comparison. *J. Chem. Theory Comput.* **2018**, *14* (6), 3238-3251.
- (45) Sundararaman, R.; Schwarz, K. Evaluating Continuum Solvation Models for the Electrode-Electrolyte Interface: Challenges and Strategies for Improvement. *The Journal of Chemical Physics* **2017**, *146* (8), 084111.
- (46) N. Steinmann, S.; Sautet, P.; Michel, C. Solvation Free Energies for Periodic Surfaces: Comparison of Implicit and Explicit Solvation Models. *Phys. Chem. Chem. Phys.* **2016**, *18* (46), 31850-31861.
- (47) Gauthier, J. A.; Ringe, S.; Dickens, C. F.; Garza, A. J.; Bell, A. T.; Head-Gordon, M.; Nørskov, J. K.; Chan, K. Challenges in Modeling Electrochemical Reaction Energetics with Polarizable Continuum Models. ACS Catal. 2019, 9 (2), 920-931.
- (48) Marenich, A. V.; Cramer, C. J.; Truhlar, D. G. Universal Solvation Model Based on Solute Electron Density and on a Continuum Model of the Solvent Defined by the Bulk Dielectric Constant and Atomic Surface Tensions. *J. Phys. Chem. B* **2009**, *113* (18), 6378-6396.

- (49) Kelly, C. P.; Cramer, C. J.; Truhlar, D. G. Aqueous Solvation Free Energies of Ions and Ion–Water Clusters Based on an Accurate Value for the Absolute Aqueous Solvation Free Energy of the Proton. J. Phys. Chem. B 2006, 110 (32), 16066-16081.
- (50) Marković, Z.; Tošović, J.; Milenković, D.; Marković, S. Revisiting the Solvation Enthalpies and Free Energies of the Proton and Electron in Various Solvents. *Comput. Theor. Chem.* **2016**, *1077*, 11-17.
- (51) Malloum, A.; Fifen, J. J.; Conradie, J. Solvation Energies of the Proton in Methanol Revisited and Temperature Effects. *Phys. Chem. Chem. Phys.* **2018**, *20* (46), 29184-29206.
- (52) Zhan, C.-G.; Dixon, D. A. First-Principles Determination of the Absolute Hydration Free Energy of the Hydroxide Ion. *J. Phys. Chem. A* **2002**, *106* (42), 9737-9744.
- (53) Bryantsev, V. S.; Diallo, M. S.; Goddard III, W. A. Calculation of Solvation Free Energies of Charged Solutes Using Mixed Cluster/Continuum Models. J. Phys. Chem. B 2008, 112 (32), 9709–9719.
- (54) Dupont, C.; Andreussi, O.; Marzari, N. Self-Consistent Continuum Solvation (SCCS): The Case of Charged Systems. J. Chem. Phys. 2013, 139 (21), 214110.
- (55) Pliego, J. R. Thermodynamic Cycles and the Calculation of PKa. *Chem. Phys. Lett.* **2003**, *367* (1), 145–149.
- (56) Ho, J. Are Thermodynamic Cycles Necessary for Continuum Solvent Calculation of PKas and Reduction Potentials? *Phys. Chem. Chem. Phys.* **2014**, *17* (4), 2859-2868.
- (57) Wang, C.; Ren, P.; Luo, R. Ionic Solution: What Goes Right and Wrong with Continuum Solvation Modeling. *J. Phys. Chem. B* **2017**, *121* (49), 11169-11179.
- (58) Stein, C. J.; Herbert, J. M.; Head-Gordon, M. The Poisson-Boltzmann Model for Implicit Solvation of Electrolyte Solutions: Quantum Chemical Implementation and Assessment via Sechenov Coefficients. *J. Chem. Phys.* **2019**, *151* (22), 224111.
- (59) Nørskov, J. K.; Rossmeisl, J.; Logadottir, A.; Lindqvist, L.; Kitchin, J. R.; Bligaard, T.; Jónsson, H. Origin of the Overpotential for Oxygen Reduction at a Fuel-Cell Cathode. J. Phys. Chem. B 2004, 108 (46), 17886-17892.
- (60) Calle-Vallejo, F.; Huang, M.; Henry, J. B.; Koper, M. T. M.; Bandarenka, A. S. Theoretical Design and Experimental Implementation of Ag/Au Electrodes for the Electrochemical Reduction of Nitrate. *Phys. Chem. Chem. Phys.* **2013**, *15* (9), 3196-3202.
- (61) McCrum, I. T.; Akhade, S. A.; Janik, M. J. Electrochemical Specific Adsorption of Halides on Cu 111, 100, and 211: A Density Functional Theory Study. *Electrochim. Acta* 2015, 173, 302-309.
- (62) Yeh, K.-Y.; Restaino, N. A.; Esopi, M. R.; Maranas, J. K.; Janik, M. J. The Adsorption of Bisulfate and Sulfate Anions over a Pt(111) Electrode: A First Principle Study of Adsorption Configurations, Vibrational Frequencies and Linear Sweep Voltammogram Simulations. Catal. Today 2013, 202, 20-35.
- (63) Trasatti, S. The Absolute Electrode Potential: An Explanatory Note (Recommendations 1986). *Pure Appl. Chem.* **1986**, *58* (7), 955-966.
- (64) Hansen, H. A.; Man, I. C.; Studt, F.; Abild-Pedersen, F.; Bligaard, T.; Rossmeisl, J. Electrochemical Chlorine Evolution at Rutile Oxide (110) Surfaces. *Phys. Chem. Chem. Phys.* **2009**, *12* (1), 283–290.
- (65) Gossenberger, F.; Roman, T.; Groß, A. Hydrogen and Halide Co-Adsorption on Pt(111) in an Electrochemical Environment: A Computational Perspective. *Electrochim. Acta* **2016**, 216, 152-159.
- (66) Bondarenko, A. S.; Stephens, I. E. L.; Hansen, H. A.; Pérez-Alonso, F. J.; Tripkovic, V.; Johansson, T. P.; Rossmeisl, J.; Nørskov, J. K.; Chorkendorff, I. The Pt(111)/Electrolyte

- Interface under Oxygen Reduction Reaction Conditions: An Electrochemical Impedance Spectroscopy Study. *Langmuir* **2011**, *27* (5), 2058-2066.
- (67) Gossenberger, F.; Juarez, F.; Groß, A. Sulfate, Bisulfate, and Hydrogen Co-Adsorption on Pt(111) and Au(111) in an Electrochemical Environment. *Front. Chem.* **2020**, 8.
- (68) Harima, Y. Standard Potential and Chemical Solvation Energy of an Electron in Ethylenediamine. *J. Electroanal. Chem. Interf. Electrochem.* **1988**, 252 (1), 53-60.
- (69) Marenich, A. V.; Ho, J.; Coote, M. L.; Cramer, C. J.; Truhlar, D. G. Computational Electrochemistry: Prediction of Liquid-Phase Reduction Potentials. *Phys. Chem. Chem. Phys.* **2014**, *16* (29), 15068-15106.
- (70) J. Göttle, A.; M. Koper, M. T. Proton-Coupled Electron Transfer in the Electrocatalysis of CO 2 Reduction: Prediction of Sequential vs. Concerted Pathways Using DFT. Chem. Sci. 2017, 8 (1), 458-465.
- (71) Kepp, K. P. Thermochemically Consistent Free Energies of Hydration for Di- and Trivalent Metal Ions. J. Phys. Chem. A **2018**, 122 (37), 7464-7471.
- (72) Bratsch, S. G. Standard Electrode Potentials and Temperature Coefficients in Water at 298.15 K. J. Phys. Chem. Ref. Data **1989**, *18* (1), 1-21.
- (73) Lide, D. R. CRC Handbook of Chemistry and Physics, 85th Edition; CRC Press, 2004.
- (74) Seitz, L. C.; Dickens, C. F.; Nishio, K.; Hikita, Y.; Montoya, J.; Doyle, A.; Kirk, C.; Vojvodic, A.; Hwang, H. Y.; Norskov, J. K.; Jaramillo, T. F. A Highly Active and Stable IrOx/SrlrO3 Catalyst for the Oxygen Evolution Reaction. *Science* **2016**, *353* (6303), 1011–1014.
- (75) Strmcnik, D.; Kodama, K.; Vliet, D. van der; Greeley, J.; Stamenkovic, V. R.; Marković, N. M. The Role of Non-Covalent Interactions in Electrocatalytic Fuel-Cell Reactions on Platinum. *Nature Chem* **2009**, *1* (6), 466-472.
- (76) Stoffelsma, C.; Rodriguez, P.; Garcia, G.; Garcia-Araez, N.; Strmcnik, D.; Marković, N. M.; Koper, M. T. M. Promotion of the Oxidation of Carbon Monoxide at Stepped Platinum Single-Crystal Electrodes in Alkaline Media by Lithium and Beryllium Cations. *J. Am. Chem. Soc.* 2010, 132 (45), 16127-16133.
- (77) Colic, V.; Pohl, M. D.; Scieszka, D.; Bandarenka, A. S. Influence of the Electrolyte Composition on the Activity and Selectivity of Electrocatalytic Centers. *Catal. Today* **2016**, *262*, 24–35.
- (78) Akhade, S. A.; McCrum, I. T.; Janik, M. J. The Impact of Specifically Adsorbed Ions on the Copper-Catalyzed Electroreduction of CO2. *J. Electrochem. Soc.* **2016**, *163* (6), F477.
- (79) McCrum, I. T.; Janik, M. J. First Principles Simulations of Cyclic Voltammograms on Stepped Pt(553) and Pt(533) Electrode Surfaces. *ChemElectroChem* **2016**, *3* (10), 1609-1617.
- (80) Ringe, S.; Clark, E. L.; Resasco, J.; Walton, A.; Seger, B.; Bell, A. T.; Chan, K. Understanding Cation Effects in Electrochemical CO2 Reduction. *Energy Environ. Sci.* **2019**, *12* (10), 3001–3014.
- (81) Waegele, M. M.; Gunathunge, C. M.; Li, J.; Li, X. How Cations Affect the Electric Double Layer and the Rates and Selectivity of Electrocatalytic Processes. *J. Chem. Phys.* **2019**, *151* (16), 160902.
- (82) Gauthier, J. A.; Fields, M.; Bajdich, M.; Chen, L. D.; Sandberg, R. B.; Chan, K.; Nørskov, J. K. Facile Electron Transfer to CO2 during Adsorption at the Metal|Solution Interface. *J. Phys. Chem. C* **2019**, *123* (48), 29278-29283.
- (83) Kristoffersen, H. H.; Chan, K.; Vegge, T.; Hansen, H. A. Energy-Entropy Competition in Cation-Hydroxyl Interactions at the Liquid Water-Pt(111) Interface. *Chem. Commun.* **2020**, 56 (3), 427-430.
- (84) Kresse, G.; Furthmüller, J. Efficient Iterative Schemes for Ab Initio Total-Energy Calculations Using a Plane-Wave Basis Set. *Phys. Rev. B* **1996**, *54* (16), 11169-11186.

- (85) Kresse, G.; Furthmüller, J. Efficiency of Ab-Initio Total Energy Calculations for Metals and Semiconductors Using a Plane-Wave Basis Set. *Comput. Mater. Sci.* **1996**, *6* (1), 15–50.
- (86) Kresse, G. Ab Initio Molecular Dynamics for Liquid Metals. J. Non-Cryst. Solids 1995, 192-193, 222-229.
- (87) Blöchl, P. E. Projector Augmented-Wave Method. Phys. Rev. B 1994, 50 (24), 17953-17979.
- (88) Kresse, G.; Joubert, D. From Ultrasoft Pseudopotentials to the Projector Augmented-Wave Method. *Phys. Rev. B* **1999**, *59* (3), 1758-1775.
- (89) Perdew, J. P.; Burke, K.; Ernzerhof, M. Generalized Gradient Approximation Made Simple. *Phys. Rev. Lett.* **1996**, *77* (18), 3865–3868.
- (90) Perdew, J. P.; Burke, K.; Ernzerhof, M. Perdew, Burke, and Ernzerhof Reply: *Phys. Rev. Lett.* **1998**, *80* (4), 891–891.
- (91) Charles Kittel. Introduction to Solid State Physics, 7th Edition | Wiley; 2004.
- (92) Monkhorst, H. J.; Pack, J. D. Special Points for Brillouin-Zone Integrations. *Phys. Rev. B* **1976**, 13 (12), 5188-5192.
- (93) Bengtsson, L. Dipole Correction for Surface Supercell Calculations. *Phys. Rev. B* **1999**, *59* (19), 12301-12304.
- (94) Singh-Miller, N. E.; Marzari, N. Surface Energies, Work Functions, and Surface Relaxations of Low-Index Metallic Surfaces from First Principles. Phys. Rev. B 2009, 80 (23), 235407.
- (95) Calle-Vallejo, F.; Koper, M. T. M. First-Principles Computational Electrochemistry: Achievements and Challenges. *Electrochim. Acta* **2012**, *84*, 3-11.
- (96) Goldberg, R. N.; Parker, V. B. Thermodynamics of Solution of SO/Sub 2/(g) in Water and of Aqueous Sulfur Dioxide Solutions; PB-86-166808/XAB; National Bureau of Standards, Washington, DC (USA), 1985.
- (97) Bader, R. F. W. Atoms in Molecules: A Quantum Theory; Clarendon Press: Oxford, 1994.
- (98) Bader, R. F. W. Atoms in Molecules. Acc. Chem. Res. 1985, 18 (1), 9-15.
- (99) Henkelman, G.; Arnaldsson, A.; Jónsson, H. A Fast and Robust Algorithm for Bader Decomposition of Charge Density. *Ojha, K* **2006**, *36* (3), 354-360.
- (100) Baxter, G. P.; Hickey, C. H.; Holmes, W. C. THE VAPOR PRESSURE OF IODINE. J. Am. Chem. Soc. **1907**, *29* (2), 127-136.
- (101) Peterson, A. A.; Abild-Pedersen, F.; Studt, F.; Rossmeisl, J.; Nørskov, J. K. How Copper Catalyzes the Electroreduction of Carbon Dioxide into Hydrocarbon Fuels. *Energy Environ. Sci.* **2010**, *3* (9), 1311-1315.
- (102) Christensen, R.; Hansen, H. A.; Vegge, T. Identifying Systematic DFT Errors in Catalytic Reactions. Catal. Sci. Technol. 2015, 5 (11), 4946-4949.
- (103) Granda-Marulanda, L. P.; Rendón-Calle, A.; Builes, S.; Illas, F.; Koper, M. T. M.; Calle-Vallejo, F. A Semiempirical Method to Detect and Correct DFT-Based Gas-Phase Errors and Its Application in Electrocatalysis. ACS Catal. 2020, 10 (12), 6900-6907.
- (104) Persson, K. A.; Waldwick, B.; Lazic, P.; Ceder, G. Prediction of Solid-Aqueous Equilibria: Scheme to Combine First-Principles Calculations of Solids with Experimental Aqueous States. *Phys. Rev. B* **2012**, *85* (23), 235438.
- (105) Ojha, K.; Arulmozhi, N.; Aranzales, D.; Koper, M. T. M. Double Layer at the Pt(111)-Aqueous Electrolyte Interface: Potential of Zero Charge and Anomalous Gouy-Chapman Screening. *Angew. Chem. Int. Ed.* **2020**, *59* (2), 711-715.
- (106) Autschbach, J. Perspective: Relativistic Effects. J. Chem. Phys. 2012, 136 (15), 150902.
- (107) Migani, A.; Illas, F. A Systematic Study of the Structure and Bonding of Halogens on Low-Index Transition Metal Surfaces. *J. Phys. Chem. B* **2006**, *110* (24), 11894–11906.

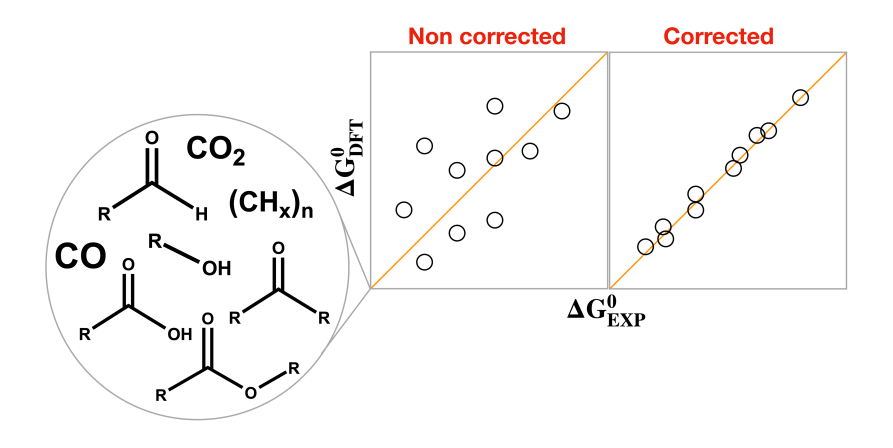
- (108) Hammer, B.; Norskov, J. K. Why Gold Is the Noblest of All the Metals. *Nature* **1995**, *376* (6537), 238-240.
- (109) Pašti, I. A.; Mentus, S. V. Halogen Adsorption on Crystallographic (111) Planes of Pt, Pd, Cu and Au, and on Pd-Monolayer Catalyst Surfaces: First-Principles Study. *Electrochim. Acta* **2010**, 55 (6), 1995–2003.
- (110) Garcia-Araez, N.; Climent, V.; Herrero, E.; Feliu, J.; Lipkowski, J. Thermodynamic Studies of Bromide Adsorption at the Pt(111) Electrode Surface Perchloric Acid Solutions: Comparison with Other Anions. J. Electroanal. Chem. 2006, 591 (2), 149-158.
- (111) Lipkowski, J.; Shi, Z.; Chen, A.; Pettinger, B.; Bilger, C. Ionic Adsorption at the Au(111) Electrode. *Electrochim. Acta* **1998**, *43* (19), 2875-2888.
- (112) Roman, T.; Groß, A. Periodic Density-Functional Calculations on Work-Function Change Induced by Adsorption of Halogens on Cu(111). *Phys. Rev. Lett.* **2013**, *110* (15), 156804.
- (113) Gossenberger, F.; Roman, T.; Forster-Tonigold, K.; Groß, A. Change of the Work Function of Platinum Electrodes Induced by Halide Adsorption. *Beilstein J Nanotechnol* **2014**, *5*, 152–161.
- (114) Roman, T.; Gossenberger, F.; Forster-Tonigold, K.; Groß, A. Halide Adsorption on Close-Packed Metal Electrodes. *Phys. Chem. Chem. Phys.* **2014**, *16* (27), 13630-13634.
- (115) Pasti, I.; Gavrilov, N.; Mentus, S. Fluorine Adsorption on Transition Metal Surfaces: A DFT Study. J. Serbian Chem. Soc. **2013**, 78 (11), 1763-1773.
- (116) Pašti, I. A.; Gavrilov, N. M.; Mentus, S. V. DFT Study of Chlorine Adsorption on Bimetallic Surfaces Case Study of Pd3M and Pt3M Alloy Surfaces. *Electrochim. Acta* **2014**, *130*, 453-463.
- (117) Derry, G. N.; Kern, M. E.; Worth, E. H. Recommended Values of Clean Metal Surface Work Functions. J. Vac. Sci. Technol. A 2015, 33 (6), 060801.
- (118) Baker, T. A.; Friend, C. M.; Kaxiras, E. Nature of Cl Bonding on the Au(111) Surface: Evidence of a Mainly Covalent Interaction. J. Am. Chem. Soc. 2008, 130 (12), 3720-3721.
- (119) Oliveira, V.; Cremer, D. Transition from Metal-Ligand Bonding to Halogen Bonding Involving a Metal as Halogen Acceptor a Study of Cu, Ag, Au, Pt, and Hg Complexes. *Chem. Phys. Lett.* **2017**, *681*, 56-63.
- (120) Peljhan, S.; Kokalj, A. Adsorption of Chlorine on Cu(111): A Density-Functional Theory Study. J. Phys. Chem. C 2009, 113 (32), 14363–14376.
- (121) Calle-Vallejo, F.; F. de Morais, R.; Illas, F.; Loffreda, D.; Sautet, P. Affordable Estimation of Solvation Contributions to the Adsorption Energies of Oxygenates on Metal Nanoparticles. *J. Phys. Chem. C* **2019**, *123* (9), 5578-5582.
- (122) Rendón-Calle, A.; Builes, S.; Calle-Vallejo, F. Substantial Improvement of Electrocatalytic Predictions by Systematic Assessment of Solvent Effects on Adsorption Energies. *Appl. Catal. B* **2020**, *276*, 119147.
- (123) Mills, J. N.; McCrum, I. T.; Janik, M. J. Alkali Cation Specific Adsorption onto Fcc(111) Transition Metal Electrodes. Phys. Chem. Chem. Phys. 2014, 16 (27), 13699-13707.
- (124) Hachiya, T.; Itaya, K. In Situ Scanning Tunneling Microscopy of Underpotential Deposition in Aqueous Solution III. Silver Adlayers on Au(111). *Ultramicroscopy* **1992**, *42-44*, 445-452.



4

A SEMIEMPIRICAL METHOD TO DETECT AND CORRECT DFT-BASED GAS-PHASE ERRORS AND ITS APPLICATION IN ELECTROCATALYSIS

Computational models of adsorption at metal surfaces are often based on DFT and make use of the generalized gradient approximation. This likely implies the presence of sizable errors in the gas-phase energetics. Here, we take a step closer toward chemical accuracy with a semiempirical method to correct the gas-phase energetics of PBE, PW91, RPBE, and BEEF-vdW exchange-correlation functionals. The proposed two-step method is tested on a data set of 27 gas-phase molecules belonging to the carbon cycle: first, the errors are pinpointed based on formation energies, and second, the respective corrections are sequentially applied to ensure the progressive lowering of the data set's mean and maximum errors. We illustrate the benefits of the method in electrocatalysis by a substantial improvement of the calculated equilibrium and onset potentials for CO₂ reduction to CO on Au, Ag, and Cu electrodes. This suggests that fast and systematic gas-phase corrections can be devised to augment the predictive power of computational catalysis models.



This chapter is based on Granda-Marulanda, L. P.; Rendón-Calle, A.; Builes, S.; Illas, F.; Koper, M. T. M.; Calle-Vallejo, F. A Semiempirical Method to Detect and Correct DFT-Based Gas-Phase Errors and Its Application in Electrocatalysis. ACS Catal. 2020, 10 (12), 6900–6907

4.1 Introduction

For decades, considerable effort has been devoted to increasing the accuracy of density functional theory (DFT). This has been done by developing more accurate exchange-correlation functionals at the generalized gradient approximation (GGA) level,¹⁻³ hybrid functionals,⁴⁻⁶ and range-separated functionals.⁷⁻⁹ In addition, different correction schemes have been developed to account for electron localization¹⁰ or dispersion interactions.¹¹⁻¹³ Lately, machine learning schemes¹⁴ have also been proposed to bypass Kohn-Sham equations. In general, these efforts include careful computational benchmarking and comparison to experiments.¹⁵⁻¹⁷

Ån agreement has been reached in the scientific community about the level of theory required to simulate certain materials with a good tradeoff between computational time and accuracy. For instance, hybrid functionals are advisable for molecules and solids with localized electrons, while GGAs usually suffice for bulk and surface metals. However, the choice is not trivial when dealing with systems where metals and molecules are involved and ought to be simulated at the same level of theory. In such a case, the accuracy may be improved by using GGA functionals and adding semiempirical corrections to the DFT energies of molecules, as done for thermochemical reaction energies of interest in catalysis, 18,19 formation and decomposition energies of solids, 20,21 and catalytic kinetic barriers. 22,23

In this *Chapter*, we provide a simple and fast procedure for detecting gas-phase errors based on the formation energies of reactants and products calculated with DFT. Improving the description of the gas-phase is shown to enhance catalytic predictive power by analyzing the electrocatalytic CO₂ reduction reaction to CO on Au, Ag, and Cu electrodes. The reduction of CO₂ and CO (hereafter denoted as CO₂RR and CORR, respectively) are of great importance in catalysis science and technology, as they lead to valuable feedstocks and fuels such as methane, ethylene, ethanol, and formic acid while helping in balancing the carbon cycle.²⁴⁻²⁶ Although DFT has been used to predict enhanced catalysts for other electrocatalytic reactions,²⁷⁻²⁹ it has been so far challenging to elaborate robust design routines for CO₂RR and CORR to hydrocarbons and oxygenates.³⁰ Thus, the method presented in this *Chapter* may help boost materials design via screening for those paramount reactions.

4.2 Computational Methods

All calculations were performed using the Vienna Ab initio Simulation Package. Dissimilar gas-phase errors have been pointed out in previous studies for the total energy of CO(g) and $CO_2(g)^{18,19,32}$ using PBE and RPBE. In addition, others suggested a correction for the total energy of $H_2(g)$ to be applied only when using BEEF-vdW. Thus, we made a functional-dependent analysis including four different xc functionals habitually used in catalysis, namely PBE, PW91, RPBE, and BEEF-vdW.

The gas-phase molecules were relaxed with the conjugate gradient algorithm in boxes of ~3375 Å³, considering only the Γ point. The effect of the cores on the valence electron density are incorporated using the projector-augmented wave

(PAW) method.³⁷ To compute the formation energies of the molecules, graphite was represented by graphene. Approximating graphene as the standard state of carbon is based on the weak interlayer cohesive energy of graphite (0.031 - 0.064 eV/atom)^{38–43} (see Section C6 in Appendix C). The optimized interatomic distances of graphene are 1.43 (PBE and RPBE) and 1.42 Å (PW91 and BEEF-vdW).

The convergence criterion for the maximal forces on the atoms for all simulations was 0.01 eV Å⁻¹, and the plane wave cutoff was set to 400 eV. Convergence tests for the free energy of reaction of $CO_2(g) + H_2(g) \rightarrow CO(g) + H_2O(g)$ with plane-wave cutoffs in the range of 300 – 1000 eV within PBE showed that 400 eV is enough to achieve accurate reaction energies with an average difference of ~5 meV (see Table C1). None of the species analyzed has unpaired electrons, so spin unrestricted calculations were not required. Gaussian smearing with $k_BT = 0.001$ eV was used. In all cases, the energies were extrapolated to 0 K.

The reaction free energies were obtained as $\Delta G^0 = \Delta E_{DFT} + \Delta ZPE - T\Delta S^0$, where ZPE is the zero-point energy contribution calculated from the vibrational frequencies obtained using the harmonic-oscillator approximation. The standard total entropies (S^0) and the experimental standard free energies ($\Delta G_{\rm exp}^0$) were obtained from thermodynamic tables 44-46 at T=298.15 K. In cases where $\Delta G_{\rm exp}^0$ was not tabulated, it was evaluated by combining entropy and enthalpy values: $\Delta G_{\rm exp}^0 = \Delta H_{\rm exp}^0 - T\Delta S_{\rm exp}^0$. We did not include heat capacity effects as recent studies showed that formation energies are not significantly modified by them from 0 to 298.15 K.²¹

Electrocatalytic CO₂ reduction to CO was modeled based on the free energy scheme described in previous reports,⁴⁷ making use of the computational hydrogen electrode⁴⁸ for the description of proton-electron transfers. The reaction pathway proceeds via CO₂ hydrogenation (step 1: $CO_2 + H^+ + e^- + * \rightarrow *COOH$), followed by *CO formation (step 2: $*COOH + H^+ + e^- \rightarrow *CO + H_2O_{(1)}$), and desorption

(step 3: ${}^*CO \rightarrow {}^*+CO$). In this approach, the onset potential is numerically equivalent to the additive inverse of the largest positive reaction energy considering steps 1 and 2 only ($U_{onset} = -\max(\Delta G_1, \Delta G_2)/e^-$) as step 3 is not electrochemical. We note that alternative pathways for CO₂RR to CO in the experimental literature suggest that CO₂ may be activated by an electron transfer prior to its adsorption, and the adsorbed species is stabilized by a hydrated cation close to the surface. ^{49–53} Since the modeling of decoupled proton-electron transfers is challenging from a plane-wave DFT standpoint, here we limit ourselves to the standard mechanism ⁴⁷ using corrected gas-phase energies.

4.3 Results and Discussion

4.3.1 Pinpointing Errors

The data set used to determine the errors (data set A) consists of 27 molecules involved in the CO₂RR and CORR, in which we include at least one representative molecule of the following functional groups: hydrocarbons, alcohols, carboxylic acids, esters, ethers, aldehydes, and ketones. We included

compounds with one to five carbon atoms in the structure (see the full list of compounds in Table C2). Data set A contains the DFT-calculated standard free energy of formation (ΔG_{DFT}^0) of the target molecules (γ) using C(s), O₂(g), and H₂(g) as a reference:

$$aC + bO_2 + cH_2 \rightarrow \gamma$$
 4.1

For instance, for acetaldehyde, Eq. 4.1 is $2C + \frac{1}{2}O_2 + 2H_2 \rightarrow C_2H_4O$. The total errors in the formation energy of each molecule in data set A (\mathcal{E}_T), represent the discrepancy between ΔG^0_{DFT} and $\Delta G^0_{\mathrm{exp}}$:

$$\varepsilon_T = \Delta G_{DFT}^0 - \Delta G_{\exp}^0$$
 4.2

It is worth noting that \mathcal{E}_T can either be positive or negative (or zero, in case there is a perfect energetic description). As a first approximation, we consider a group-additivity type of scheme⁵⁴ where a given molecule with different functional groups may have different errors present in its ΔG^{0}_{DFT} . Thus, the total error (\mathcal{E}_T) can be decoupled in the separate contributions of the functional groups present in the molecule (\mathcal{E}_i). In mathematical terms this is expressed as: $\mathcal{E}_T \approx \sum_{i=1}^n \mathcal{E}_i$, so that

the total error with respect to experiments for a given molecule (ε_T) is approximately the sum of the errors inherited from the n functional groups present in the molecule (ε_i). As shown in Table C2, data set A is formed by CO, CO₂, and molecules containing CH_x, hydroxyl, carbonyl, carboxyl, ether, and ester functional groups.

A second data set (data set B) consists of calculated free energies of reaction for the CO_2RR and CORR to produce the molecules in data set A (see Tables C3-C4). We use data set B to verify whether the corrections implemented in data set A are appropriate. This is the case when there is a decrease in the mean absolute error (MAE) and maximum absolute error (MAX) in data set B as the corrections are successively applied. The free energies of reaction in data set B are grouped in two: firstly, reactions with CO as a reactant and γ as a product, as shown in Eq. 4.3 (see Table C4).

$$gCO + kH_2 \rightarrow \gamma + mH_2O$$
 4.3

For instance, for acetaldehyde, Eq. 4.3 is: $2CO+3H_2 \rightarrow C_2H_4O$. Particular cases are the formation of CO₂ and HCOOH from CO, which follow Eq. 4.4.

$$CO + H_2O \rightarrow \gamma + rH_2 \tag{4.4}$$

Secondly, data set B contains reactions with CO_2 as a reactant and γ as a product, as shown in Eq. 4.5 (see Table C3).

$$xCO_2 + yH_2 \rightarrow \gamma + zH_2O$$
 4.5

Eq. 4.5 applied to acetaldehyde is: $2CO_2 + 5H_2 \rightarrow C_2H_4O + 3H_2O$. In these equations, water is considered to be in gas phase (H₂O(g); see Section C3 in the Appendix C). We categorized the errors for each functional based on organic functional groups (-CH_x, hydroxyl, carbonyl, carboxyl, ether, and ester functional groups) and molecules (in particular, CO and CO₂), as shown in Table 4.1. For example, acetaldehyde has one -CH_x (-CH₃) group and one carbonyl (-CHO) group. Table C5 contains the corrections added per exchange-correlation functional and organic functional group.

The errors in the standard free energies (hereafter referred to simply as errors) in Table 4.1 are xc-functional-dependent, so that the signs and magnitude change in each case, in line with previous studies. This dependence can be expected because exchange-correlation functionals are fitted for certain applications using different data sets. The following, we will explain how the errors in Table 4.1 were determined, taking PBE as an example. Note in passing that the analysis is similar for the other functionals included in this study, and all values are tabulated in Section C4 of the Appendix C.

To pinpoint the errors, we first determined all deviations (\mathcal{E}_T) in the calculated free energies of formation of the molecules in data set A relative to the experimental ones using Eq. 4.2. We paid special attention to CO₂ and CO as they are the reactants of CO₂RR and CORR, respectively (all reactions in data set B). For PBE, the error in CO₂ is $\mathcal{E}_T^{cO_2} = -0.19 \, \mathrm{eV}$, whereas that of CO is $\mathcal{E}_T^{cO} = 0.24 \, \mathrm{eV}$. Thus, the magnitudes of the two errors are comparable but the signs are opposite. The CO₂ error appears in similar molecules such as HCOOH ($\mathcal{E}_T^{HCOOH} = -0.19 \, \mathrm{eV}$) and is commonly referred to as the OCO backbone error in the literature. ^{18,19,32,34} Previous studies reported corrections of -0.45 eV for RPBE ^{19,32} and -0.59 eV for BEEF-vdW, ³² which agree well with our values of -0.46 and -0.56 eV, respectively. The small correction of -0.07 eV for CO_(g) in RPBE is likely a reflection of RPBE's original fit against CO adsorption energies. ³³ We note in passing that simultaneous OCO/H₂ corrections are also available in the literature for BEEF-vdW of 0.33/0.09, ³² 0.41/0.09, ³⁴ and 0.29/0.10 eV. ¹⁸

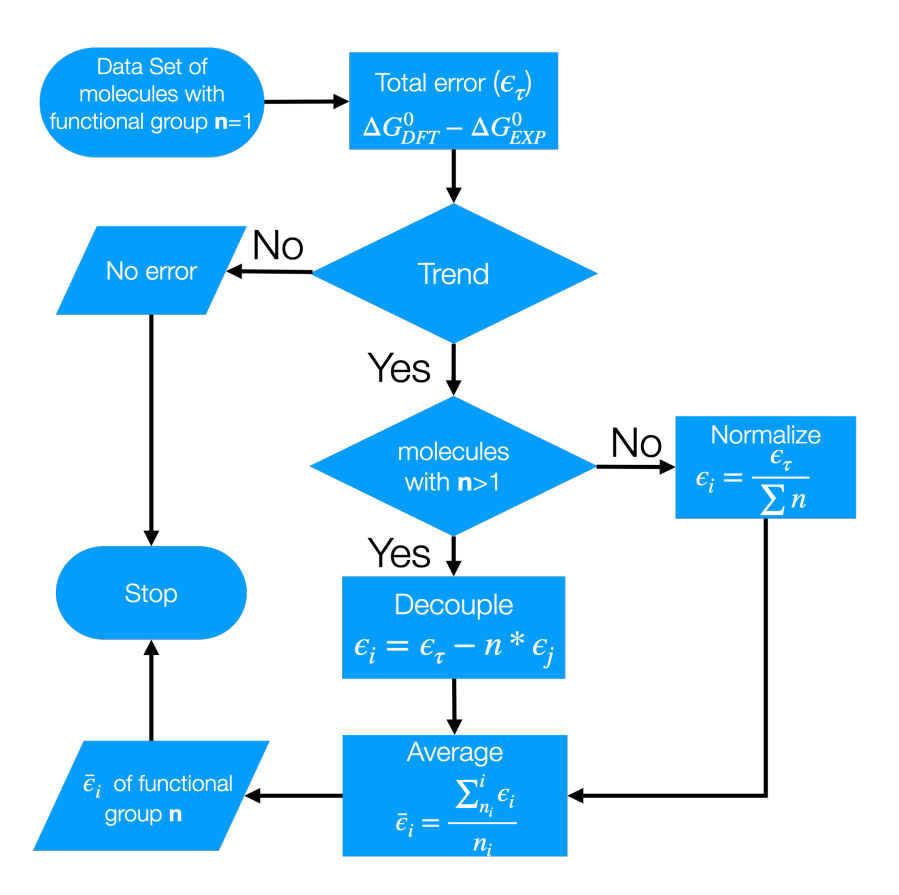
We continued the correction procedure, summarized in scheme 4.1, with the simplest molecules in the list, namely, alkanes (only C-H and single C-C bonds) and observed an increasingly positive error depending on the number of hydrocarbon units (-CH_x) (see Table C6). For PBE, that error is on average $\varepsilon_{CH_x} \approx 0.03 \, \mathrm{eV}/CH_x$. Although small, such an error is cumulative, and therefore, for a molecule with 5 -CH_x units it becomes $\varepsilon_{CH_x} \approx 0.03 \, \frac{\mathrm{eV}}{CH_x} \times 5 \, \mathrm{CH}_x \approx 0.15 \, \mathrm{eV}$. Note that

we obtained \mathcal{E}_{CH_x} by dividing the error in the formation energy of each alkane by the number of -CH_x units in it and averaging the results for all alkanes in data set A.

Beyond alkanes, one can increase the complexity of the molecules with additional functional groups. For example, we noted that the error for aldehydes and ketones decreased proportionally to the length of the chain. Therefore, to decouple the error associated to carbonyl groups from that of $-CH_x$ groups, we subtracted from the total error of the molecules the error provided by their $-CH_x$

units (see for instance Table C7). In mathematical terms, for a molecule with the formula $R_1C=OR_2$ (where R_1 and R_2 are either -H or -CH_x units): $\varepsilon_T \approx n_C \cdot \varepsilon_{CH} + \varepsilon_{C=Q-1}$, where n_C is the number of -CH_x units.

To illustrate the use of the formula, consider the total error ($\mathcal{E}_T^{C_2H_4O}$) for acetaldehyde of -0.09 eV, and the -CH_x error (\mathcal{E}_{CH_x}) of 0.03 eV. The carbonylassociated error is $\mathcal{E}_{-c-o-}^{C_2H_4O} \approx \mathcal{E}_T^{C_2H_4O} - n_C \cdot \mathcal{E}_{CH_x} = -0.11 \, \text{eV}$. Averaging over all the aldehydes and ketones in this study, we obtained $\mathcal{E}_{-C=O-} = -0.10 \, \text{eV}$ for PBE. Table 4.1 shows the CO and CO₂ errors as well as the average errors determined for the following organic functional groups: -C=O- (aldehydes and ketones), -CH_x (alkanes), -(C=O)O- (carboxylic acids and esters) and -OH (alcohols). Note that the error for -(C=O)O- in PBE is identical to that of CO₂, whereas for PW91, RPBE, and BEEF-vdW, that is not the case, as the errors have the same signs but sizably different magnitudes.



SCHEME 4.1

Workflow to determine functional-dependent errors in energies related to functional groups.

The error in the -OH group for PBE and PW91 is not large enough to warrant correction for simple alcohols. However, this correction may be needed for polyalcohols and in studies focused specifically on methanol and ethanol (see Appendix C, Section C4.1.4 for more details). Before closing this subsection, we stress that a detailed description of the assessment of all errors for every xcfunctional can be found in Section C4 in Appendix C. We note that ethylene, acetylene, ethylene oxide and dimethyl ether are present in data set A. Since a larger sample of molecules would be necessary to determine the errors corresponding to their respective functional groups (alkenes, alkynes, and (cyclic) ethers), here the corrections for those molecules are limited to the corrections in the reactants only (CO and CO₂).

TABLE 4.1 Gas-Phase error corrections for the standard free energy of CO_2 , CO, and molecules containing -C=O- (Carbonyl Groups in Aldehydes and Ketones), -CHx (Alkanes), and -(C=O)O- (carboxyl groups in carboxylic acids and esters) as per xc functional.^a

Error	PBE	PW91	RPBE	BEEF-vdW
CO ₂	-0.19	-0.15	-0.46	-0.56
СО	0.24	0.25	-0.07	-0.18
-C=O-	-0.10	-0.10	-0.21	-0.27
-CHx	0.03	-0.01	0.08	0.21
-(C=O)O-	-0.19	-0.19	-0.27	-0.34 (-0.44)
-OH	-0.04	-0.04	-0.01	-0.14

^a The two values reported for -(C=O)O- when using BEEF-vdW are for carboxylic acids and esters (the latter in parentheses). All values are in eV.

4.3.2 Implementing Energy Corrections

Data set A was used not only to determine total errors in the formation energies of molecules (\mathcal{E}_T), but also to assess the organic group contributions to such errors (\mathcal{E}_i). In principle, one can use those errors to correct the formation energies of molecules, the combination of which should lead to accurate reaction energies. In this order of ideas, corrected reaction energies ($\Delta G_{DFT, corr}^0$) can be calculated as:

$$\Delta G_{DFT, corr}^{0} = \Delta G_{DFT}^{0} - \left(\sum \varepsilon_{T}^{P} - \sum \varepsilon_{T}^{R}\right)$$
 4.6

where the sums collect all the errors associated to the reactants (\mathcal{E}_T^R) and products (\mathcal{E}_T^P), taking into account the stoichiometric coefficients. For example, consider the reduction of CO₂ to acetic acid: $2CO_2 + 4H_2 \rightarrow CH_3COOH + 2H_2O$. We find with

RPBE that $\Delta G_{DFT}^0 = 0.32 \, \mathrm{eV}$, whereas $\Delta G_{\mathrm{exp}}^0 = -0.44 \, \mathrm{eV}$, which corresponds to a large total error $\varepsilon_T^{CH_3COOH} = 0.76 \, \mathrm{eV}$. According to Table 4.1, RPBE has errors associated to the description of CO₂, the -COOH group and the -CH₃ moiety in CH₃COOH. If the errors pinpointed using data set A are contributing to the large total error, suitably correcting CO₂ and CH₃COOH should lead to a sizable reduction of the total error. This is what we find, as $\sum_{\varepsilon_T^P} = 2\varepsilon_{C^{O_2}}^{co_2} = -0.92 \, \mathrm{eV}$ and $\sum_{\varepsilon_T^P} = \varepsilon_{CH_2} + \varepsilon_{-C=OO^-} = -0.19 \, \mathrm{eV}$, so that $\Delta G_{DFT,corr}^0 = -0.41 \, \mathrm{eV}$, which differs from the experimental value ($\Delta G_{\mathrm{exp}}^0 = -0.44 \, \mathrm{eV}$) by 0.03 eV only.

To verify that the errors in the reaction energies of data set B are systematically reduced upon applying the corrections in Table 4.1, we followed a stepwise procedure. First, we applied corrections to data set B only related to reactants (namely CO₂ and CO). Next, we applied corrections related to products. Figure 4.1 and Figure 4.2 show the calculated free energies of reaction versus the experimental free energies for the four functionals studied (PBE, PW91, RPBE, BEEF-vdW). Figure 4.1 provides parity plots for CO-based reactions (Eqs. 4.3 and 4.4) and Figure 4.2 does so for CO₂-based reactions (Eq. 4.5). From the three columns in each figure, the first one corresponds to the non-corrected DFT data, the plots in the second column contain the data upon correcting for reactant-related errors (namely CO or CO₂), and the third column contains the data upon correcting for reactant- and product-related errors altogether.

More molecules can be added to data set A so as to include more organic functional groups and molecules with several groups in their structure. Molecules with alkene, alkyne, epoxy, and ether functional groups as well as aromatic compounds are necessary in data set A to determine their corresponding errors. Here, the free energies of production from CO or CO₂ of ethylene, acetylene, dimethyl ether, and ethylene oxide were corrected for the errors in the reactants only, and no product-related corrections were made (see Table C5).

The gray-shaded areas in Figure 4.1 and Figure 4.2 cover an area around the parity line of \pm MAE, and the purple-shaded area extends over \pm 0.15 eV around the parity line. For CO reduction reactions and PBE calculations, the MAE is initially 0.61 eV (left column) and is lowered to 0.10 eV after applying the CO correction (central column) and to 0.04 eV after applying both CO and product-related corrections (right column). Similarly, the MAXs go from 1.04 to 0.20 and then to 0.17 eV. For the CO₂ reduction reactions and PBE, the MAE is successively reduced from 0.43 to 0.10 and then to 0.04 eV. Likewise, the MAXs decrease from 1.10 to 0.24 and finally to 0.17 eV. Further details can be found in Table C24, where the MAEs after the first and second correction for all the xc-functionals are provided. We conclude from those values that the errors in data set B are lowered by one order of magnitude once the correction scheme is applied to the species in data set A.

We have included an alternative analysis where data set A is divided into a training set and an extrapolation set in Section C7 of Appendix C. From this analysis we find approximately the same functional-related errors as in Table 4.1 (within ± 0.01 eV on average). The MAEs in the extrapolation set after the corrections are comparable to those in Figure 4.1 and Figure 4.2, illustrating the predictive power of the method and its statistical reliability.

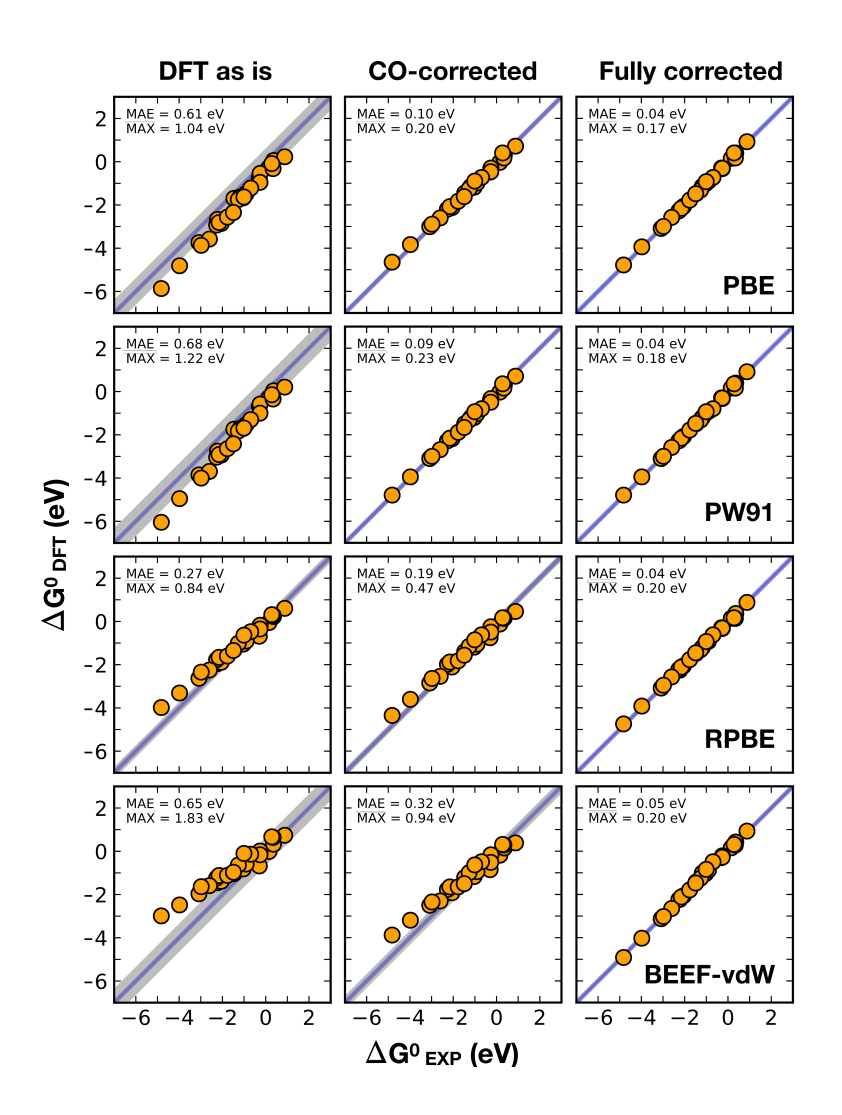


FIGURE 4.1

Parity plots for the experimental and DFT-calculated free energies of production of 27 different compounds from CO and H_2 using PBE, PW91, RPBE and BEEF-vdW. The left column shows the data calculated with DFT without any correction. The center column shows the data upon the first correction (errors in CO), and the right column shows the data after correcting for errors in CO and the products. The mean and maximum absolute errors (MAE and MAX) are shown in each case. The shaded gray area is \pm MAE in each case. The blue shaded area around the parity line covers an area of \pm 0.15 eV.

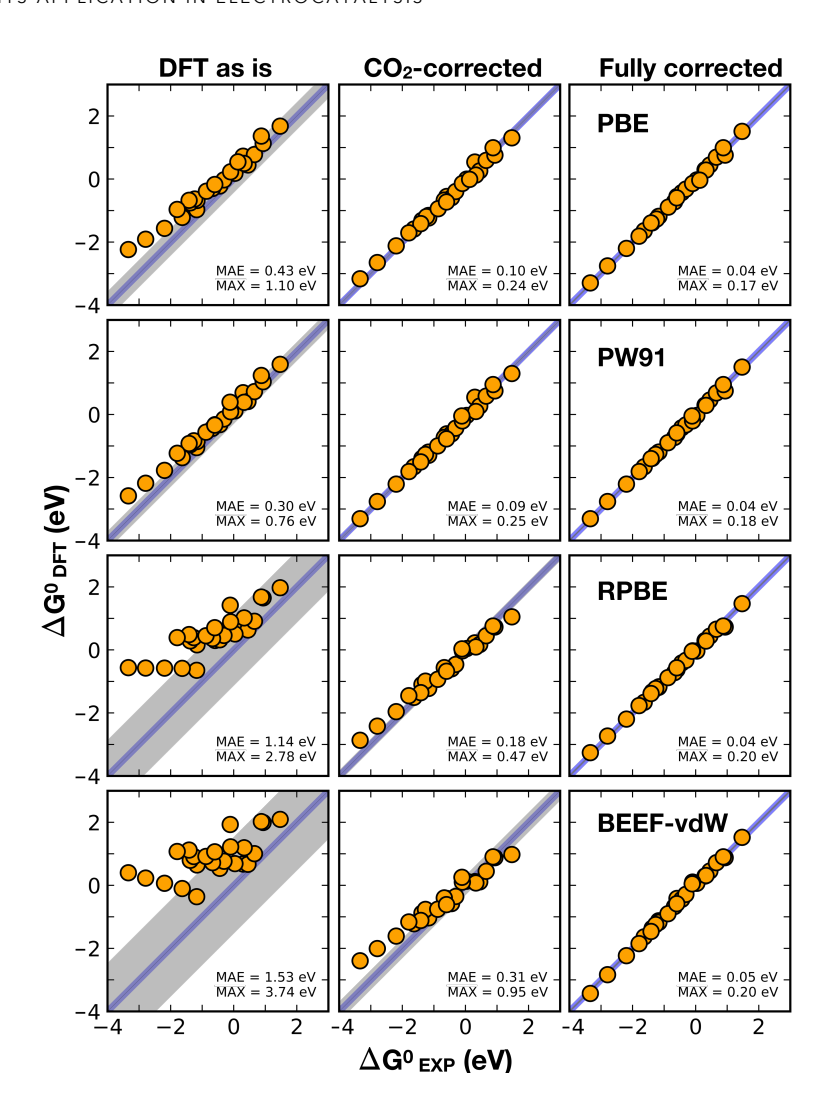


FIGURE 4.2

Parity plot for the experimental and DFT-calculated free energies of production of 27 different products from CO_2 and H_2 using PBE, PW91, RPBE and BEEF-vdW. The left column shows the data calculated with DFT without any correction. The center column shows the data upon the first correction (errors in CO_2), and the right column shows the data after correcting for errors in CO_2 and the products. The mean and maximum absolute errors (MAE and MAX) are shown in each case. The shaded gray area is \pm MAE in each case. The blue shaded area around the parity line covers an area of \pm 0.15 eV.

4.3.3 Applications in Electrocatalysis

Table 4.2 reveals an important commonality among the xc functionals under study: although the CO and CO_2 errors change from one functional to the next, their difference is nearly constant and equal to ~0.4 eV, on average. This constant energetic separation poses a fundamental limitation for the modeling of catalytic reactions wherein those two compounds are involved, one as a reactant and the other as a product. To show the reaches of this finding, let us consider the example of CO_2 electrocatalytic reduction (CO_2RR) to CO

$$CO_2 + 2(H^+ + e^-) \rightarrow CO + H_2O_{(I)}$$
 4.7

The backward reaction is known as CO oxidation and is also an important electrocatalytic reaction involved in direct ethanol and methanol fuel cells.⁵⁶ Moreover, Eq. 4.7 can also be catalyzed in the gas phase using H₂ in a process called reverse water-gas shift, and the backward reaction is the industrial process known as the water-gas shift.⁵⁷ In brief, DFT-based models of this seemingly simple process with numerous applications in electrocatalysis and heterogeneous catalysis may have large gas-phase associated errors.

TABLE 4.2 CO₂ and CO errors and their nearly constant difference ($\varepsilon_T^{co} - \varepsilon_T^{co_2}$) across xc-functionals.^a

Error	PBE	PW91	RPBE	BEEF-vdW
СО	0.24	0.25	-0.07	-0.18
CO_2	-0.19	-0.15	-0.46	-0.56
$oldsymbol{arepsilon}_{T}^{CO} - oldsymbol{arepsilon}_{T}^{CO_{2}}$	0.43	0.40	0.39	0.38
Average	0.40			
Standard deviation	0.02			

^aAll values are in eV.

Figure 4.3 compares CO_2RR to CO on Au(111) single-crystal electrodes using PBE with (Figure 4.3b) and without (Figure 4.3a) gas-phase corrections applied to CO_2 and CO. Likewise, Figures CS and CG in Appendix C, section CS, provide data for Au(100) and Au(110). In Figure 4.3a, where DFT data appear as is, the reaction energy of Eq. 4.7 is 0.63 eV. Conversely, it is 0.20 eV in Figure 4.3b, where the energies of CO_2 and CO have been corrected. For comparison, such difference is 0.20 eV in experiments²⁵ (it is 0.30 eV in Table CS). The difference stems from the liquid state of water in Eq. 4.7). In terms of the equilibrium potential of the reaction, this all means that PBE predicts it to be at -0.32 V vs RHE, whereas both the correction method and experiments set it at -0.10 V vs RHE. The difference is substantial and amounts to ~220 mV. Note in passing that there are no changes in the energy differences between *COOH and *CO, as the corrections are only

applied to the gas phase. Corrections for adsorbates have been proposed before¹⁸ but have escaped the subject and scope of this study.

Within the context of CO₂RR modeling with the computational hydrogen electrode, 47,48 the onset potential is given by the largest-positive consecutive difference in Figure 4.3 ($U_{onset} = -\max(\Delta G_1, \Delta G_2)/e^-$; see the Computational Methods section). In Figure 4.3a, such difference is 0.90 eV, whereas in Figure 4.3b it is 0.71 eV, so that the predicted onset potentials are -0.90 and -0.71 V vs RHE, respectively. As the experimental value of the onset potential is -0.66 V vs RHE, the deviations from experiments are ~0.24 (as is) and 0.05 V (corrected).

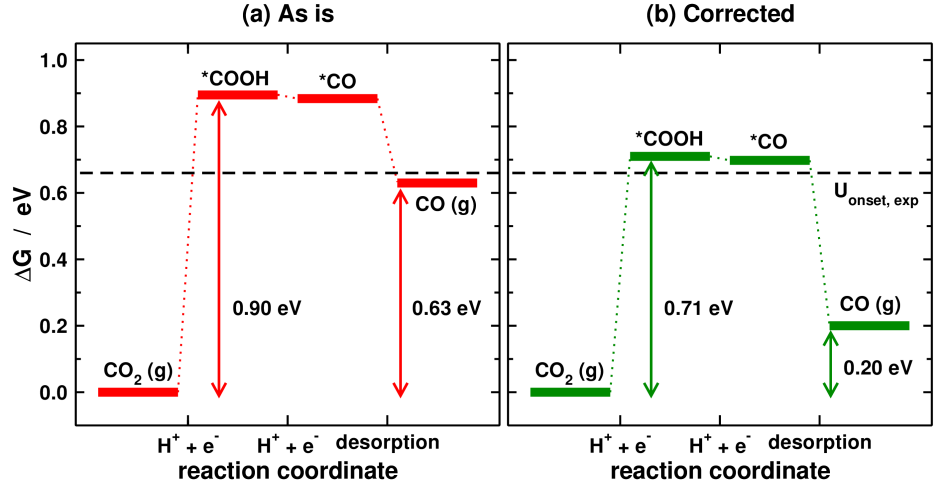


FIGURE 4.3

Free energy diagrams for CO_2 reduction to CO using Au(111) single-crystal electrodes. (a) Using DFT-PBE data as is, and (b) correcting CO_2 and CO for their gas-phase errors. The black dashed line at 0.66 eV marks the free energy corresponding to the experimental onset potential of -0.66 V vs RHE.⁵⁸

We note that the sizable lowering of the error from 0.24 to 0.05 V is a direct result of correcting gas-phase energetics. To assess whether this is a particularity of Au(111) electrodes or part of a more general trend, we also compared the calculated and experimental onset potentials for Au(100), Au(110), Au_{poly}, Ag(111), Ag_{poly}, and Cu_{poly}. The results in Figure 4.4a show that DFT data are systematically deviated from the parity line, which results in a MAE of 0.20 V and a MAX of 0.27 V. Conversely, the CO₂-and-CO corrected data in Figure 4.4b are located around the parity line with MAE = 0.06 V and MAX = 0.09 V. Substantial improvements are also observed for Au(111) and Au(100) using gasphase corrections with RPBE, see Figures C7-C8. Thus, we conclude that models

for CO_2RR to CO may in general benefit from the gas-phase corrections found in this work.

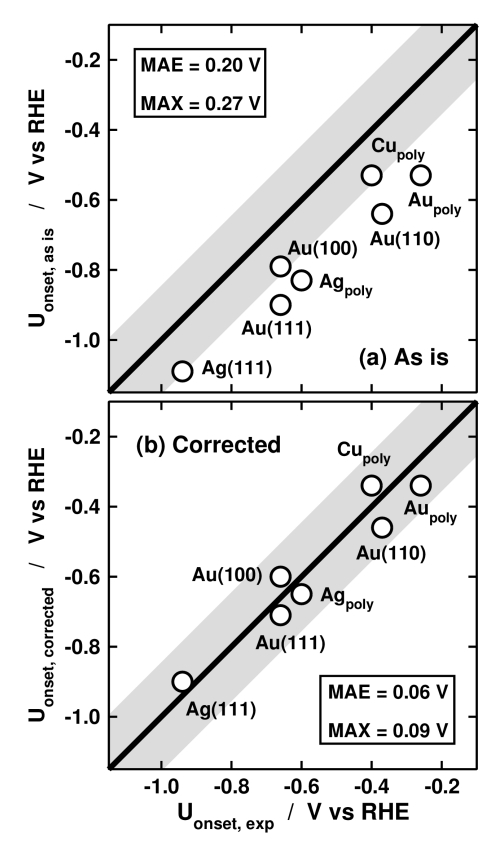


FIGURE 4.4

Parity plots comparing the onset potentials for electrochemical CO_2 reduction to CO using different metals. (a) Using DFT-PBE data as is, and (b) correcting CO_2 and CO for their gas-phase errors. The mean and maximum absolute errors (MAE and MAX) are shown in each case. The gray areas around the parity line cover an area of \pm 0.15 V around it. The experimental data were taken from references 58–61 (see details in Table C25).

4.4 Conclusions

When interfaces between metals and fluids are simulated at the GGA level, sizable errors may appear in the description of the gas-phase molecules energetics. Here, we proposed a two-step semiempirical method to determine gas-phase errors, based on the formation energies of 27 different molecules. Furthermore, implementing the corresponding corrections allows for predictions in the analyzed data set of CO₂RR and CORR reaction energies that lower by 1 order of magnitude the average and maximum errors with respect to experiments.

The method also shows that the errors for CO_2 and CO differ by ~0.4 eV for all the examined exchange-correlation functionals. Thus, an intrinsic limitation of DFT exists for the accurate description of reaction energies containing these two molecules, as is the case for CO_2 reduction to CO or CO0 oxidation to CO2, etc. Such limited description leads to inaccurate predictions of equilibrium and onset potentials, which may hinder the rational catalyst design.

Conversely, using our correction scheme on various Au, Ag and Cu electrodes decreased the average error in the predicted onset potentials from 0.21 to 0.06 V with respect to experiments. Therefore, in addition to pinpointing and lowering gas-phase errors, the method also helps in providing more accurate electrocatalytic models.

While the present corrections have been applied for electrochemical reactions, the procedure is general enough to be applied to correct the thermochemistry of heterogeneously catalyzed reactions where reactants and products are in the gas phase but the intermediate steps take place at the catalyst surface. Finally, the correction protocol can be enriched by adding more gas-phase molecules to the data set, 62 and using machine learning algorithms to detect and predict errors in structurally more complex substances.

4.5 References

- (1) Perdew, J. P. Workhorse Semilocal Density Functional for Condensed Matter Physics and Quantum Chemistry. *Phys. Rev. Lett.* **2009**, *103* (2), 026403.
- (2) Cancio, A.; Chen, G. P.; Krull, B. T.; Burke, K. Fitting a Round Peg into a Round Hole: Asymptotically Correcting the Generalized Gradient Approximation for Correlation. *J. Chem. Phys.* **2018**, *149* (8), 084116.
- (3) Sun, J.; Ruzsinszky, A.; Perdew, J. P. Strongly Constrained and Appropriately Normed Semilocal Density Functional. *Phys. Rev. Lett.* **2015**, *115* (3), 036402.
- (4) Becke, A. D. A New Mixing of Hartree-Fock and Local Density-functional Theories. *J. Chem. Phys.* **1993**, 98 (2), 1372-1377.

- (5) Xu, X.; Goddard, W. A. The X3LYP Extended Density Functional for Accurate Descriptions of Nonbond Interactions, Spin States, and Thermochemical Properties. *Proc. Natl. Acad. Sci.* **2004**, *101* (9), 2673-2677.
- (6) Maier, T. M.; Arbuznikov, A. V.; Kaupp, M. Local Hybrid Functionals: Theory, Implementation, and Performance of an Emerging New Tool in Quantum Chemistry and Beyond. *Wiley Interdiscip. Rev. Comput. Mol. Sci.* **2019**, *9* (1), e1378.
- (7) Dion, M.; Rydberg, H.; Schröder, E.; Langreth, D. C.; Lundqvist, B. I. Van Der Waals Density Functional for General Geometries. *Phys. Rev. Lett.* **2004**, *92* (24), 246401.
- (8) Román-Pérez, G.; Soler, J. M. Efficient Implementation of a van Der Waals Density Functional: Application to Double-Wall Carbon Nanotubes. *Phys. Rev. Lett.* **2009**, *103* (9), 096102.
- (9) Wellendorff, J.; Lundgaard, K. T.; Møgelhøj, A.; Petzold, V.; Landis, D. D.; Nørskov, J. K.; Bligaard, T.; Jacobsen, K. W. Density Functionals for Surface Science: Exchange-Correlation Model Development with Bayesian Error Estimation. *Phys. Rev. B* **2012**, *85* (23), 235149.
- (10) Dudarev, S. L.; Botton, G. A.; Savrasov, S. Y.; Humphreys, C. J.; Sutton, A. P. Electron-Energy-Loss Spectra and the Structural Stability of Nickel Oxide: An LSDA+U Study. *Phys. Rev. B* **1998**, *57* (3), 1505-1509.
- (11) Grimme, S.; Antony, J.; Ehrlich, S.; Krieg, H. A Consistent and Accurate Ab Initio Parametrization of Density Functional Dispersion Correction (DFT-D) for the 94 Elements H-Pu. *J. Chem. Phys.* **2010**, *132* (15), 154104.
- (12) Caldeweyher, E.; Bannwarth, C.; Grimme, S. Extension of the D3 Dispersion Coefficient Model. *J. Chem. Phys.* **2017**, *147* (3), 034112.
- (13) Janthon, P.; Luo, S. (Andy); Kozlov, S. M.; Viñes, F.; Limtrakul, J.; Truhlar, D. G.; Illas, F. Bulk Properties of Transition Metals: A Challenge for the Design of Universal Density Functionals. *J. Chem. Theory Comput.* **2014**, *10* (9), 3832-3839.
- (14) Brockherde, F.; Vogt, L.; Li, L.; Tuckerman, M. E.; Burke, K.; Müller, K.-R. Bypassing the Kohn-Sham Equations with Machine Learning. *Nat. Commun.* **2017**, *8* (1), 1–10.
- (15) Lejaeghere, K.; Bihlmayer, G.; Björkman, T.; Blaha, P.; Blügel, S.; Blum, V.; Caliste, D.; Castelli, I. E.; Clark, S. J.; Corso, A. D.; Gironcoli, S. de; Deutsch, T.; Dewhurst, J. K.; Marco, I. D.; Draxl, C.; Dułak, M.; Eriksson, O.; Flores-Livas, J. A.; Garrity, K. F.; Genovese, L.; Giannozzi, P.; Giantomassi, M.; Goedecker, S.; Gonze, X.; Grånäs, O.; Gross, E. K. U.; Gulans, A.; Gygi, F.; Hamann, D. R.; Hasnip, P. J.; Holzwarth, N. a. W.; Iuşan, D.; Jochym, D. B.; Jollet, F.; Jones, D.; Kresse, G.; Koepernik, K.; Küçükbenli, E.; Kvashnin, Y. O.; Locht, I. L. M.; Lubeck, S.; Marsman, M.; Marzari, N.; Nitzsche, U.; Nordström, L.; Ozaki, T.; Paulatto, L.; Pickard, C. J.; Poelmans, W.; Probert, M. I. J.; Refson, K.; Richter, M.; Rignanese, G.-M.; Saha, S.; Scheffler, M.; Schlipf, M.; Schwarz, K.; Sharma, S.; Tavazza, F.; Thunström, P.; Tkatchenko, A.; Torrent, M.; Vanderbilt, D.; Setten, M. J. van; Speybroeck, V. V.; Wills, J. M.; Yates, J. R.; Zhang, G.-X.; Cottenier, S. Reproducibility in Density Functional Theory Calculations of Solids. Science 2016, 351 (6280), aad3000.

- (16) Kurth, S.; Perdew, J. P.; Blaha, P. Molecular and Solid-State Tests of Density Functional Approximations: LSD, GGAs, and Meta-GGAs. *Int. J. Quantum Chem.* **1999**, *75* (4-5), 889-909.
- (17) Briquet, L. G. V.; Sarwar, M.; Mugo, J.; Jones, G.; Calle-Vallejo, F. A New Type of Scaling Relations to Assess the Accuracy of Computational Predictions of Catalytic Activities Applied to the Oxygen Evolution Reaction. *ChemCatChem* **2017**, *9* (7), 1261–1268.
- (18) Christensen, R.; Hansen, H. A.; Vegge, T. Identifying Systematic DFT Errors in Catalytic Reactions. *Catal. Sci. Technol.* **2015**, *5* (11), 4946-4949.
- (19) Peterson, A. A.; Abild-Pedersen, F.; Studt, F.; Rossmeisl, J.; Nørskov, J. K. How Copper Catalyzes the Electroreduction of Carbon Dioxide into Hydrocarbon Fuels. *Energy Environ. Sci.* **2010**, *3* (9), 1311-1315.
- (20) Calle-Vallejo, F.; Martínez, J. I.; García-Lastra, J. M.; Mogensen, M.; Rossmeisl, J. Trends in Stability of Perovskite Oxides. *Angew. Chem. Int. Ed.* **2010**, *49* (42), 7699-7701.
- (21) Bartel, C. J.; Weimer, A. W.; Lany, S.; Musgrave, C. B.; Holder, A. M. The Role of Decomposition Reactions in Assessing First-Principles Predictions of Solid Stability. *Npj Comput. Mater.* **2019**, *5* (1), 1-9.
- (22) Tameh, M. S.; Dearden, A. K.; Huang, C. Accuracy of Density Functional Theory for Predicting Kinetics of Methanol Synthesis from CO and CO2 Hydrogenation on Copper. J. Phys. Chem. C 2018, 122 (31), 17942-17953.
- (23) Blaylock, D. W.; Ogura, T.; Green, W. H.; Beran, G. J. O. Computational Investigation of Thermochemistry and Kinetics of Steam Methane Reforming on Ni(111) under Realistic Conditions. *J. Phys. Chem. C* **2009**, *113* (12), 4898-4908.
- (24) Bushuyev, O. S.; Luna, P. D.; Dinh, C. T.; Tao, L.; Saur, G.; Lagemaat, J. van de; Kelley, S. O.; Sargent, E. H. What Should We Make with CO2 and How Can We Make It? *Joule* **2018**, *2* (5), 825-832.
- (25) Nitopi, S.; Bertheussen, E.; Scott, S. B.; Liu, X.; Engstfeld, A. K.; Horch, S.; Seger, B.; Stephens, I. E. L.; Chan, K.; Hahn, C.; Nørskov, J. K.; Jaramillo, T. F.; Chorkendorff, I. Progress and Perspectives of Electrochemical CO2 Reduction on Copper in Aqueous Electrolyte. *Chem. Rev.* **2019**, *119* (12), 7610-7672.
- (26) Birdja, Y. Y.; Pérez-Gallent, E.; Figueiredo, M. C.; Göttle, A. J.; Calle-Vallejo, F.; Koper, M. T. M. Advances and Challenges in Understanding the Electrocatalytic Conversion of Carbon Dioxide to Fuels. *Nat. Energy* **2019**, *4* (9), 732-745.
- (27) Calle-Vallejo, F.; Tymoczko, J.; Colic, V.; Vu, Q. H.; Pohl, M. D.; Morgenstern, K.; Loffreda, D.; Sautet, P.; Schuhmann, W.; Bandarenka, A. S. Finding Optimal Surface Sites on Heterogeneous Catalysts by Counting Nearest Neighbors. *Science* **2015**, *350* (6257), 185–189.
- (28) Seh, Z. W.; Kibsgaard, J.; Dickens, C. F.; Chorkendorff, I.; Nørskov, J. K.; Jaramillo, T. F. Combining Theory and Experiment in Electrocatalysis: Insights into Materials Design. *Science* **2017**, *355* (6321), eaad4998.

- (29) Garlyyev, B.; Fichtner, J.; Piqué, O.; Schneider, O.; Bandarenka, A. S.; Calle-Vallejo, F. Revealing the Nature of Active Sites in Electrocatalysis. *Chem. Sci.* **2019**, *10* (35), 8060-8075.
- (30) Jovanov, Z. P.; Hansen, H. A.; Varela, A. S.; Malacrida, P.; Peterson, A. A.; Nørskov, J. K.; Stephens, I. E. L.; Chorkendorff, I. Opportunities and Challenges in the Electrocatalysis of CO2 and CO Reduction Using Bifunctional Surfaces: A Theoretical and Experimental Study of Au-Cd Alloys. J. Catal. 2016, 343, 215-231.
- (31) Kresse, G.; Furthmüller, J. Efficient Iterative Schemes for Ab Initio Total-Energy Calculations Using a Plane-Wave Basis Set. *Phys. Rev. B* **1996**, *54* (16), 11169-11186.
- (32) Studt, F.; Abild-Pedersen, F.; Varley, J. B.; Nørskov, J. K. CO and CO2 Hydrogenation to Methanol Calculated Using the BEEF-VdW Functional. *Catal. Lett.* **2013**, *143* (1), 71-73.
- (33) Hammer, B.; Hansen, L. B.; Nørskov, J. K. Improved Adsorption Energetics within Density-Functional Theory Using Revised Perdew-Burke-Ernzerhof Functionals. *Phys. Rev. B* **1999**, *59* (11), 7413-7421.
- (34) Studt, F.; Behrens, M.; Kunkes, E. L.; Thomas, N.; Zander, S.; Tarasov, A.; Schumann, J.; Frei, E.; Varley, J. B.; Abild-Pedersen, F.; Nørskov, J. K.; Schlögl, R. The Mechanism of CO and CO2 Hydrogenation to Methanol over Cu-Based Catalysts. *ChemCatChem* **2015**, *7* (7), 1105–1111.
- (35) Perdew, J. P.; Burke, K.; Ernzerhof, M. Generalized Gradient Approximation Made Simple. *Phys. Rev. Lett.* **1996**, *77* (18), 3865-3868.
- (36) Perdew, J. P.; Burke, K.; Wang, Y. Generalized Gradient Approximation for the Exchange-Correlation Hole of a Many-Electron System. *Phys. Rev. B* **1996**, *54* (23), 16533–16539.
- (37) Kresse, G.; Joubert, D. From Ultrasoft Pseudopotentials to the Projector Augmented-Wave Method. *Phys. Rev. B* **1999**, *59* (3), 1758–1775.
- (38) Wang, W.; Dai, S.; Li, X.; Yang, J.; Srolovitz, D. J.; Zheng, Q. Measurement of the Cleavage Energy of Graphite. *Nat. Commun.* **2015**, *6* (1), 1–7.
- (39) Girifalco, L. A.; Lad, R. A. Energy of Cohesion, Compressibility, and the Potential Energy Functions of the Graphite System. *J. Chem. Phys.* **1956**, *25* (4), 693-697.
- (40) Zacharia, R.; Ulbricht, H.; Hertel, T. Interlayer Cohesive Energy of Graphite from Thermal Desorption of Polyaromatic Hydrocarbons. *Phys. Rev. B* **2004**, *69* (15), 155406.
- (41) Benedict, L. X.; Chopra, N. G.; Cohen, M. L.; Zettl, A.; Louie, S. G.; Crespi, V. H. Microscopic Determination of the Interlayer Binding Energy in Graphite. *Chem. Phys. Lett.* **1998**, *286* (5), 490-496.
- (42) Xia, M.; Liang, C.; Cheng, Z.; Hu, R.; Liu, S. The Adhesion Energy Measured by a Stress Accumulation-Peeling Mechanism in the Exfoliation of Graphite. *Phys. Chem. Chem. Phys.* **2019**, *21* (3), 1217-1223.
- (43) Liu, Z.; Liu, J. Z.; Cheng, Y.; Li, Z.; Wang, L.; Zheng, Q. Interlayer Binding Energy of Graphite: A Mesoscopic Determination from Deformation. *Phys. Rev. B* **2012**, 85 (20), 205418.

- (44) Lide, D. R. CRC Handbook of Chemistry and Physics, 85th Edition; CRC Press, 2004.
- (45) Chase, Jr., M. W.; Davies, C. A.; Downey, Jr., J. R.; Frurip, D. J.; MacDonald, R. A.; Syverud, A. N. NIST-JANAF Thermochemical Tables. *J. Phys. Chem. Ref. Data* **1985**, *Suppl. 1 to Vol. 14*, 1856.
- (46) Informatics, N. O. of D. and. NIST Chemistry WebBook https://webbook.nist.gov/chemistry/ (accessed Oct 18, 2019).
- (47) Hansen, H. A.; Varley, J. B.; Peterson, A. A.; Nørskov, J. K. Understanding Trends in the Electrocatalytic Activity of Metals and Enzymes for CO2 Reduction to CO. *J. Phys. Chem. Lett.* **2013**, *4* (3), 388-392.
- (48) Nørskov, J. K.; Rossmeisl, J.; Logadottir, A.; Lindqvist, L.; Kitchin, J. R.; Bligaard, T.; Jónsson, H. Origin of the Overpotential for Oxygen Reduction at a Fuel-Cell Cathode. *J. Phys. Chem. B* **2004**, *108* (46), 17886-17892.
- (49) Akhade, S. A.; McCrum, I. T.; Janik, M. J. The Impact of Specifically Adsorbed Ions on the Copper-Catalyzed Electroreduction of CO2. *J. Electrochem. Soc.* **2016**, *163* (6), F477.
- (50) Pérez-Gallent, E.; Marcandalli, G.; Figueiredo, M. C.; Calle-Vallejo, F.; Koper, M. T. M. Structure- and Potential-Dependent Cation Effects on CO Reduction at Copper Single-Crystal Electrodes. J. Am. Chem. Soc. 2017, 139 (45), 16412-16419.
- (51) Ringe, S.; Clark, E. L.; Resasco, J.; Walton, A.; Seger, B.; Bell, A. T.; Chan, K. Understanding Cation Effects in Electrochemical CO2 Reduction. *Energy Environ. Sci.* **2019**, *12* (10), 3001–3014.
- (52) Singh, M. R.; Kwon, Y.; Lum, Y.; Ager, J. W.; Bell, A. T. Hydrolysis of Electrolyte Cations Enhances the Electrochemical Reduction of CO2 over Ag and Cu. *J. Am. Chem. Soc.* **2016**, *138* (39), 13006-13012.
- (53) Resasco, J.; Chen, L. D.; Clark, E.; Tsai, C.; Hahn, C.; Jaramillo, T. F.; Chan, K.; Bell, A. T. Promoter Effects of Alkali Metal Cations on the Electrochemical Reduction of Carbon Dioxide. *J. Am. Chem. Soc.* **2017**, *139* (32), 11277-11287.
- (54) Benson, S. W.; Buss, J. H. Additivity Rules for the Estimation of Molecular Properties. Thermodynamic Properties. *J. Chem. Phys.* **1958**, *29* (3), 546–572.
- (55) Teng, B.-T.; Wen, X.-D.; Fan, M.; Wu, F.-M.; Zhang, Y. Choosing a Proper Exchange–Correlation Functional for the Computational Catalysis on Surface. *Phys. Chem. Chem. Phys.* **2014**, *16* (34), 18563–18569.
- (56) Lamy, C.; Lima, A.; LeRhun, V.; Delime, F.; Coutanceau, C.; Léger, J.-M. Recent Advances in the Development of Direct Alcohol Fuel Cells (DAFC). *J. Power Sources* **2002**, *105* (2), 283-296.
- (57) Ratnasamy, C.; Wagner, J. P. Water Gas Shift Catalysis. Catal. Rev. 2009, 51 (3), 325-440.
- (58) Todoroki, N.; Tei, H.; Tsurumaki, H.; Miyakawa, T.; Inoue, T.; Wadayama, T. Surface Atomic Arrangement Dependence of Electrochemical CO2 Reduction on Gold: Online Electrochemical Mass Spectrometric Study on Low-Index Au(Hkl) Surfaces. ACS Catal. **2019**, *9* (2), 1383–1388.
- (59) Kuhl, K. P.; Hatsukade, T.; Cave, E. R.; Abram, D. N.; Kibsgaard, J.; Jaramillo, T. F. Electrocatalytic Conversion of Carbon Dioxide to Methane and Methanol on Transition Metal Surfaces. *J. Am. Chem. Soc.* **2014**, *136* (40), 14107-14113.

- (60) Hoshi, N.; Kato, M.; Hori, Y. Electrochemical Reduction of CO2 on Single Crystal Electrodes of Silver Ag(111), Ag(100) and Ag(110). *J. Electroanal. Chem.* **1997**, 440 (1), 283-286.
- (61) Ma, M.; Trześniewski, B. J.; Xie, J.; Smith, W. A. Selective and Efficient Reduction of Carbon Dioxide to Carbon Monoxide on Oxide-Derived Nanostructured Silver Electrocatalysts. *Angew. Chem. Int. Ed.* **2016**, *55* (33), 9748-9752.
- (62) Urrego-Ortiz, R.; Builes, S.; Calle-Vallejo, F. Fast Correction of Errors in the DFT-Calculated Energies of Gaseous Nitrogen-Containing Species. *ChemCatChem* **2021**. doi.org/10.1002/cctc.202100125



ADSORPTION PROCESSES ON A PD-MONOLAYER-MODIFIED PT(111) ELECTRODE

Specific adsorption of anions is an important aspect in surface electrochemistry in view of its influence on reaction kinetics as either a promoter or an inhibitor. Perchloric acid is typically considered as an ideal electrolyte for investigating electrocatalytic reactions due to the lack of specific adsorption of the perchlorate anion on several metal electrodes. In this work, cyclic voltammetry and computational methods are combined to investigate the interfacial processes on a Pd monolayer deposited on Pt(111) single crystal electrodes in perchloric acid solution. The "hydrogen region" of this $Pd_{ML}Pt(111)$ surface exhibits two voltammetric peaks: the first "hydrogen peak" at 0.246 V vs RHE involves the replacement of hydrogen by hydroxyl, and the second "hydrogen peak" H_{II} at 0.306 V vs RHE appears to be the replacement of adsorbed hydroxyl by specific perchlorate adsorption. The two peaks merge into a single peak when a more strongly adsorbed anion, such as sulfate, is involved. Our density functional theory calculations qualitatively support the peak assignment and show that anions generally bind more strongly to the Pd_{ML}Pt(111) surface than to Pt(111).

This chapter is based on Chen, X.; Granda-Marulanda, L. P.; McCrum, I. T.; Koper, M. T. M. Adsorption Processes on a Pd Monolayer-Modified Pt(111) Electrode. Chem. Sci. 2020, 11 (6), 1703-1713. Also published in Chen, X. Adsorption and Catalysis on Pt and Pd Monolayer-Modified Pt Single Crystal Electrodes, PhD thesis, Leiden University, 2019- Chapter 4

All experiments were performed by Xiaoting Chen.

5.1 Introduction

Improved understanding of electrocatalytic reactions taking place in various energy storage and energy conversion devices becomes increasingly crucial with the advent of electrochemical fuel production and fuel-cell technologies. For many relevant electrocatalytic reactions, such as the hydrogen oxidation reaction (HOR), the oxygen reduction reaction (ORR), the formic acid oxidation, and the CO₂ reduction reaction, not only the surface structure but also the adsorption of anions/cations from the supporting electrolyte influence the reactivity through different interactions of these co-adsorbates with key reaction intermediates. For instance, hydrogen (*H) and hydroxyl (*OH) are important surface-bonded intermediates during the aforementioned reactions. In previous works, we showed that cations co-adsorb with hydroxyl species on the step sites of Pt electrodes at low potentials, and that the corresponding cation-hydroxyl interaction is responsible for the non-Nernstian pH shift, a shift due to the weakened adsorption of *OH by the cation on the surface, of the step-related voltammetric peak.^{4,5}

Platinum is one of the most important catalysts due to its widespread application in heterogeneous catalysis and electrochemistry. There have been plenty of studies on single-crystal platinum electrodes since the preparation method of clean platinum surfaces introduced by Clavilier.⁶ Palladium is a platinum-group metal and similar to Pt in many chemical and physical properties. Interestingly, Pd surfaces show a higher activity toward formic acid oxidation than Pt, but the most remarkable difference with Pt is the absence of CO poisoning during formic acid oxidation on Pd.⁷⁻⁹ Moreover, Pd electrodes have attracted increasing attention as catalysts for the CO₂ electroreduction reaction, as they selectively reduce CO₂ to formic acid with low overpotential, ^{10,11} implying that Pd is an (almost) reversible catalyst for the conversion of formic acid to carbon dioxide and vice versa.¹²

To better understand the special reactivity of palladium, detailed investigations on atomically well-defined Pd surfaces are highly desirable. However, the electrochemistry of well-defined Pd surfaces is not as well studied as for Pt surfaces, which arises partially from the difficulty to prepare Pd single crystals as well as from the effect that palladium absorbs substantial amounts of hydrogen below 0.2 V vs RHE, masking other reactions taking place on its surface. Epitaxially grown Pd layers on a foreign metal are a promising alternative and have attracted considerable attention, particularly Pt(111) surfaces modified by a Pd monolayer. The lattice parameters of both metals are close, 3.89 Å for Pd and 3.92 Å for Pt, and it has been pointed out that the reactivity of the Pd monolayer system is comparable to that of the corresponding Pd single crystal. Epitaxial Pd. 18,19

To understand the fundamental aspects of the electrode activity, we need to consider the adsorption behavior on single-crystal electrodes in acid electrolyte solutions. Particularly interesting are perchloric and sulfuric acid solutions, especially in relation to specific anion adsorption. In sulfuric acid, the $Pd_{ML}Pt(111)$ electrode has been studied by spectroelectrochemical experiments, showing that the majority of species on the surface are hydrogen at low potential and (bi)sulfate²⁰ at high potential. Remarkably, a reversible double peak adsorption state appears in the hydrogen region of the voltammogram of a $Pd_{ML}Pt(111)$ in

0.1 M HClO₄. Previous studies in a low potential window (0.05-0.35 V vs RHE) have ascribed these peaks to hydrogen underpotential deposition (H_{upd}) because a hydrogen coverage of 1 H_{upd} per Pd corresponds very well to the total charge under these two peaks (240 μ C cm⁻²).^{21,22} However, the double-peak nature of this "hydrogen region" of Pd_{ML}Pt(111) remains unresolved.

In this *Chapter*, we use a combination of experimental and computational methods for the elucidation of the surface species formed on the well-defined $Pd_{ML}Pt(111)$ surface in the so-called "hydrogen region". We argue that in perchloric acid solution, the "hydrogen region" on the $Pd_{ML}Pt(111)$ surface is rather a "hydrogen-hydroxyl-cation-anion region". We show the existence of cation and anion effects on the peaks in the "hydrogen region", showing that OH and anions interact much more strongly with the $Pd_{ML}Pt(111)$ surface than with the Pt(111) surface.

These results improve our fundamental understanding of anion, cation and OH adsorption on well-defined, single-crystal palladium surfaces, which will be important for interpreting and tuning the catalytic activity of palladium-based electrochemical interfaces.

5.2 Experimental Details

Cyclic voltammetry measurements were carried out in standard electrochemical cells using a three-electrode assembly at room temperature. Experiments were performed in a fluorinated ethylene propylene (PEP, Nalgene) electrochemical cell for hydrofluoric acid, whereas a glass cell was used for the other electrolytes. All glassware was cleaned in an acidic solution of potassium permanganate overnight, followed by rinsing with an acidic solution of hydrogen peroxide and repetitive rinsing and boiling with ultrapure water. A Pt(111) bead-type electrode, with a diameter of 2.27 mm, was used as working electrode. Prior to each experiment, the working electrode was prepared according to the Clavilier method.⁶ A platinum wire was used as counter electrode and a reversible hydrogen electrode (RHE) was employed as the reference electrode, in a separate compartment filled with the same electrolyte, at the same pH as the electrolyte in the electrochemical cell. All potentials are reported versus the RHE. The electrochemical measurements were performed with the single-crystal electrode in the hanging meniscus configuration. The potential was controlled with an Autolab PGSTAT302N potentiostat. The current density shown in the manuscript represents the measured current normalized to the geometric area of the working electrode.

The Pd monolayer in this study was prepared using a method similar to the one reported before. ^{17,20} The freshly prepared Pt(111) electrode was immersed into the Pd²⁺ containing solution at 0.85 V vs RHE, where no Pd deposition occurred, and the potential was continuously cycled between 0.07 and 0.85 V vs RHE at 50 mV s⁻¹. The amount of palladium on the surface was monitored by following the evolution of the voltammetric peak at 0.23 V vs RHE (as shown in Figure D1), characteristic of the presence of Pd adatoms, the charge (and current density) of which depend on the palladium coverage. ^{17,23} Scanning tunnelling microscopy (STM) images have revealed that monoatomic high Pd islands nucleate on the Pt(111) surface with no noticeable preference for nucleation sites, and that a full Pd monolayer without detectable holes is formed after deposition. ²⁴ STM also

shows the presence of an ordered sulphate adlayer with a $\sqrt{3} \times \sqrt{9}$)R19.1° structure on the Pd monolayer, as is also the case for the Pd(111) surface.²⁵ After Pd modification, the Pd_{ML}Pt(111) electrode was taken from the cell and thoroughly rinsed with ultrapure water before performing further electrochemistry tests. Further insight into the nature of the adsorbed species on the electrode was obtained by means of charge displacement experiments using CO (Linde 6.0) as a neutral probe. The procedure to perform CO displacement measurements is similar to the one reported before.²⁶ Briefly, a gaseous CO stream was dosed at a fixed potential and a transient current was recorded until the Pd_{ML}Pt(111) surface was covered by a monolayer of CO.

Electrolytes were made from ultrapure water (Milli-Q, 18.2 M Ω cm), high purity reagents HClO₄ (70%), H₂SO₄(96%), NaClO₄ (99.99%), CH₃SO₃H (>99.0%) and HF (40%) from Merck Suprapur and HCl, PdSO₄ (99.99%), LiClO₄ (99.99%) from Aldrich Ultrapure. Before each experiment, the electrolytes were first purged with argon (Air Products, 5.7) for at least 30 min to remove air from the solution.

5.3 Computational Details

To better understand adsorption phenomena on the Pd_{ML}Pt(111) electrode, we have evaluated the free energies of adsorption of hydrogen, oxygen, hydroxide, and different anions on Pt(111), and Pd_{ML}Pt(111) using Density Functional Theory (DFT) calculations. The potential-dependent free energies of adsorption of hydrogen, oxygen, hydroxide were calculated at different surface coverages using the computational hydrogen electrode.²⁷ By calculating the free energies of adsorption at different coverages we can determine the composition of the electrode surface in the electrochemical environment, which is useful for fundamental studies of electrocatalysis.^{19,28,29}

Additionally, we calculated the potential-dependent free energies of adsorption of other anions, namely, perchlorate, sulfate and bisulfate using an alternative computational reference method as outlined in detail in *Chapter 3*. The relative binding strength of bicarbonate and fluoride at a coverage of 1/9 ML was also calculated to compare the interaction of different anions on both surfaces. Plotting the adsorption free energy as a function of coverage and electrochemical potential allows for direct comparison with experimentally measured cyclic voltammograms, providing information on the identity and the relevant coverage of the species adsorbed on the surface at a particular potential (where peaks in current in the experimental CV correspond to changes in adsorbate coverage and/or identity). Further information on the DFT methods employed in this *Chapter* can be found in Appendix D.

5.4 Results and discussion

5.4.1 Comparison of the blank voltammograms of Pd_{ML}Pt(111) and Pt(111)

The cyclic voltammogram of $Pd_{MI}Pt(111)$ in $0.1~M~H_2SO_4$ shows the presence of a sharp pair of peaks (Figure 5.1a), slightly irreversible, with a peak potential of 0.23 V vs RHE in the positive-going scan and of 0.21 V vs RHE in the negative-going scan. The sharpness of the peak suggests the replacement of adsorbed species, i.e. hydrogen and (bi)sulphate, as a function of potential. Note that on Pt(111), hydrogen adsorption/desorption and (bi)sulphate adsorption/desorption give rise to separate voltammetric signals (between 0.05 and 0.30 V vs RHE and between 0.30 and 0.55 V vs RHE, respectively). This single sharp peak observed on the $Pd_{ML}Pt(111)$ surface can be explained by the replacement of adsorbed hydrogen at potentials below 0.22 V vs RHE by adsorbed (bi)sulphate at potentials above 0.22 V vs RHE, caused by the stronger (bi)sulphate adsorption on $Pd_{ML}Pt(111)$ compared to Pt(111).

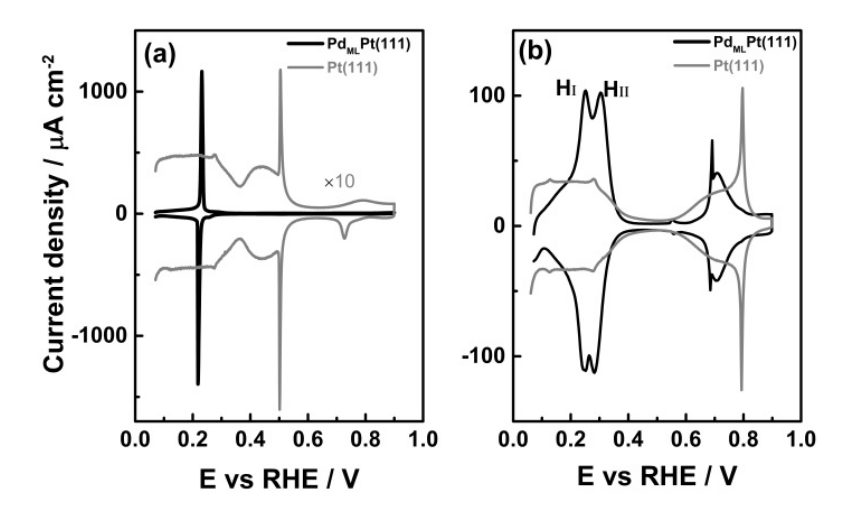


FIGURE 5.1

Cyclic voltammograms of $Pd_{ML}Pt(111)$ in (a) 0.1 M H_2SO_4 and (b) 0.1 M $HCIO_4$ recorded at 50 mV s⁻¹. The blank voltammograms for Pt(111) recorded under identical conditions are shown for comparison.

Figure 5.1b shows the cyclic voltammogram of $Pd_{ML}Pt(111)$ in 0.1 M HClO₄ electrolyte, compared to Pt(111). The $Pd_{ML}Pt(111)$ electrode exhibits characteristic windows in the same potential regions of 0.05-0.35 V vs RHE, 0.35-0.60 V vs RHE and 0.60-0.90 V vs RHE as Pt(111). This led previous authors to conclude that the voltammetric peaks between 0.05-0.35 V vs RHE correspond to hydrogen adsorption, that the 0.35-0.60 V vs RHE is the double layer region, and that OH adsorbs in the 0.60-0.90 V vs RHE window. However, there are some important differences. The first effect of the Pd ML is an increase of the overall charge

between 0.05-0.35 V vs RHE from 160 μ C cm⁻² for bare Pt(111) to 240 μ C cm⁻² for a full monolayer of Pd decorating the Pt(111). The groups of Feliu²¹ and Markovic²² ascribed the higher charge of the reversible peak in the low potential window to H_{upd} on Pd monolayer due to a stronger H_{upd}-Pd_{ML}Pt(111) interaction compared to the H_{upd}-Pt(111) interaction, and to the excellent correspondence to a full monolayer of hydrogen (1 ML of one monovalent adsorbate adsorbed per surface atom, or 1.5×10^{15} atoms cm⁻², is exactly 240 μ C cm⁻²). Secondly, the "hydrogen region" features two sharp peaks, indicated as the "first hydrogen peak" $H_{\rm I}$ and "second hydrogen peak" $H_{\rm II}$ (at 0.25 and 0.30 V vs RHE, respectively), which is in contrast with the characteristic behavior of hydrogen adsorption on wide Pt(111) terraces, namely a broad and plateau-like peak. In the "double layer region" between 0.35 and 0.60 V vs RHE, a small peak is observed at 0.55 V vs RHE in the positive-going scan and 0.56 V vs RHE in the reversed scan (note the unexpected higher potential of the cathodic peak), as already reported by Feliu et al.²¹ As the potential increases from 0.60 to 0.90 V vs RHÉ, there is a sharp peak at 0.69 V vs RHE followed by a broader feature (with the corresponding reversible features in the negative-going scan). This sharp peak has been ascribed to OH adsorption and is observed only for a Pd monolayer covering a Pt(111) substrate with very low step density, i.e. it requires wide (111) terraces.²¹ The combination of a sharp and broad peak is very typical for a disorder-order transition in the adlayer,³² but the sequence (sharp peak at low coverage, broad peak at higher coverage) is unexpected.

5.4.2 Cation and anion effects on the blank voltammogram of Pd_{ML}Pt(111)

Figure 5.2a shows cyclic voltammograms for the Pd_{ML}Pt(111) electrode in 0.1 M $HClO_4$ (pH = 1), 0.01 M $HClO_4$ (pH = 2) and 0.001 M $HClO_4$ (pH = 3) electrolytes. On the reversible hydrogen electrode (RHE) scale, the H_I peak is observed to be independent of pH, perchlorate concentration and the ionic strength of the electrolyte solution, in acidic electrolyte (pH = 1 - 3) in the absence of alkali metal cations. As the pH lowers, or rather as the perchlorate concentration increases, peaks H_I and H_{II} start overlapping more and more as shown in Figure 5.2b. Figure 5.2c and d illustrate that the effect of cations on the H_I peak of the Pd_{MI} Pt(111) electrode becomes apparent when voltammograms are recorded in 0.001 M HClO₄ (pH = 3) with different amounts of alkali perchlorate salts. With increasing concentration of alkali metal cation, the H_I peak shifts to more positive potential in comparison with the peak potential (0.246 V vs RHE) in 0.001 M HClO₄ without alkali cations. The shift is more pronounced for larger cations: for 0.01 M Li⁺ (Figure 5.2c) and 0.01 M Na⁺ (Figure 5.2d) containing electrolytes, the H_I peak is shifted to 0.262 and 0.272 V vs RHE, respectively. This effect of the cation on the peak potential is identical to the effect that we observed previously for the steprelated "hydrogen" peaks on stepped Pt electrodes. 4,5

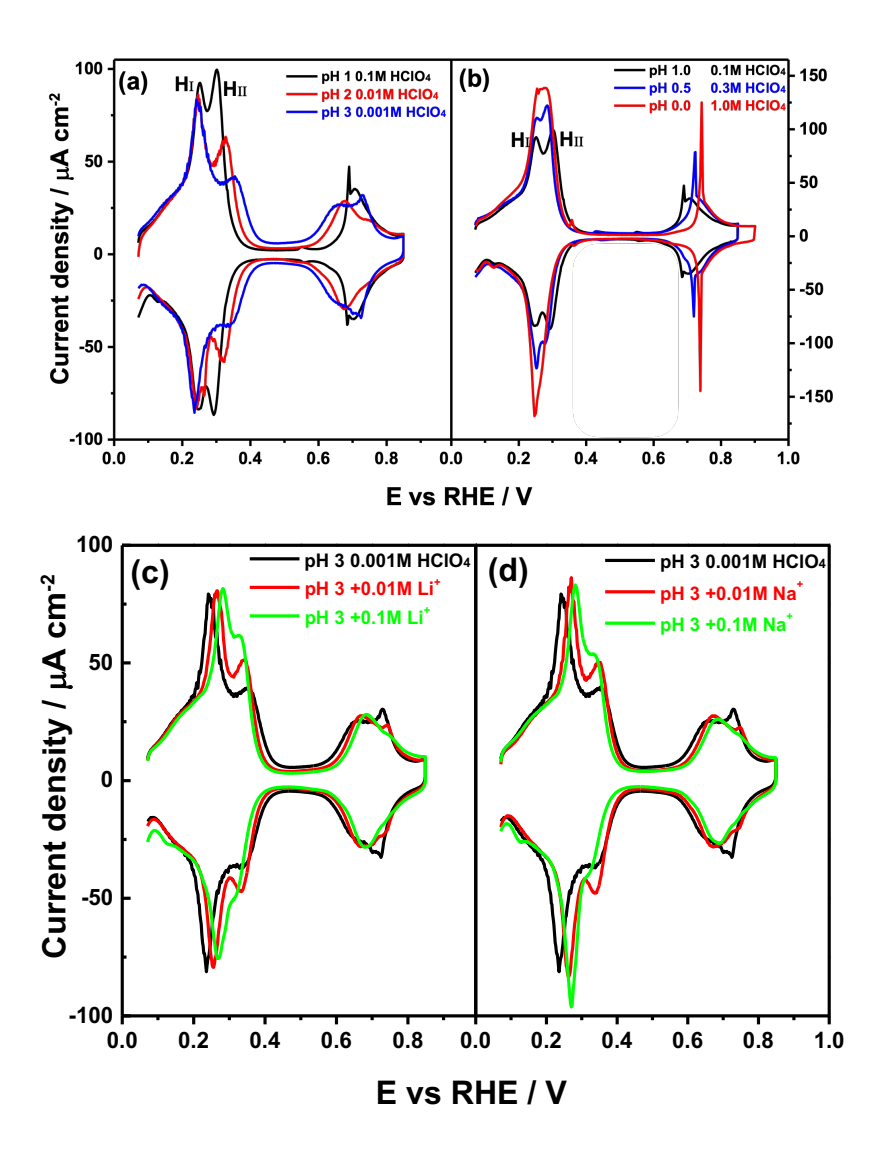


FIGURE 5.2

Cyclic voltammograms of $Pd_{ML}Pt(111)$ in (a) 0.1 M HClO₄ (pH = 1), 0.01 M HClO₄ (pH = 2) and 0.001 M HClO₄ (pH = 3) solutions and (b) 0.1 M HClO₄ (pH = 1), 0.5 M HClO₄ (pH = 0.3) and 1.0 M HClO₄ (pH = 0) solutions. (c) and (d) 0.001 M HClO₄ (pH = 3) solution without and with MeClO₄, where Me is Li and Na, as indicated. Scan rate: 50 mV s⁻¹.

Therefore, we conclude that, similarly to the stepped Pt electrodes, the $H_{\rm I}$ peak involves the replacement of $H_{\rm ads}$ by $OH_{\rm ads}$ and this adsorbate replacement reaction is driven to more positive potentials due to the destabilizing effect of the co-adsorbed alkali cation on hydroxyl adsorption.^{4,5,33} At constant pH, the adsorption of alkali cations on the $Pd_{\rm ML}$ Pt(111) surface becomes more favorable

with increasing cation concentration, resulting in a greater shift of the $H_{\rm I}$ peak, as shown in Figure 5.2c and d. A reaction equation of the $H_{\rm I}$ reduction/oxidation peak on $Pd_{\rm ML}Pt(111)$ can thus be formally written as:

$$x(OH_{ads} - cation_{ads}) + (1+x)H^{+} + (1+x)e^{-} \rightleftharpoons H_{ads} + xH_{2}O + x(cation_{sol})$$
 5.1

Remarkably, Figure 5.2 shows that the H_{II} peak does not show the same cation effect as the H_I peak. By contrast, the H_{II} peak is sensitive to anion concentration (and identity, as shown in Figure 5.3) and the pH of the electrolyte. Figures 2a and b show that the H_{II} peak becomes sharper and shifts to lower potential with increasing HClO₄ concentration. For clarity, we show representative voltammograms of Pd_{ML}Pt(111) in Figure 5.2b; results obtained in electrolytes with detailed wider range of pH values are shown in Figure D2 in Appendix D. Figure 5.2c and d (and Figure D2) show that the shift in the H_{II} peak seems to be at least partially due to different perchlorate concentration, as at constant pH the H_{II} peak grows with increasing perchlorate concentration and also shows a negative potential shift. Another important observation from Figure 5.2 is that the voltammetric feature between 0.60 to 0.90 V vs RHE is sensitive to the HClO₄ concentration. This feature shifts to a higher potential in the presence of a higher concentration of perchlorate, suggesting that the formation of the adsorbate in this potential window is inhibited by the presence of perchlorate. A consistent explanation for this effect of perchlorate, which will be considered for the remainder of this *Chapter*, is that the H_{II} peak involves either the specific adsorption of perchlorate, or a strong interaction of perchlorate with the other adsorbates. If OH_{ads} is formed in the H_I peak (Eq. 5.1), then a reaction equation describing the H_{II} peak could formally read as:

$$x(0H_{ads} - cation_{ads}) + x(H^+ + e^-) + y(anion_{sol}) \rightleftharpoons xH_2O + y(anion_{ads}) + x(cation_{sol})$$
5.2

In this equation, the extent of anion adsorption is influenced by the anion concentration, but also by the pH, as the potential of zero charge (E_{pzc}) shifts to higher potential on the RHE scale with increasing pH, enhancing perchlorate adsorption at a given potential on the RHE scale.

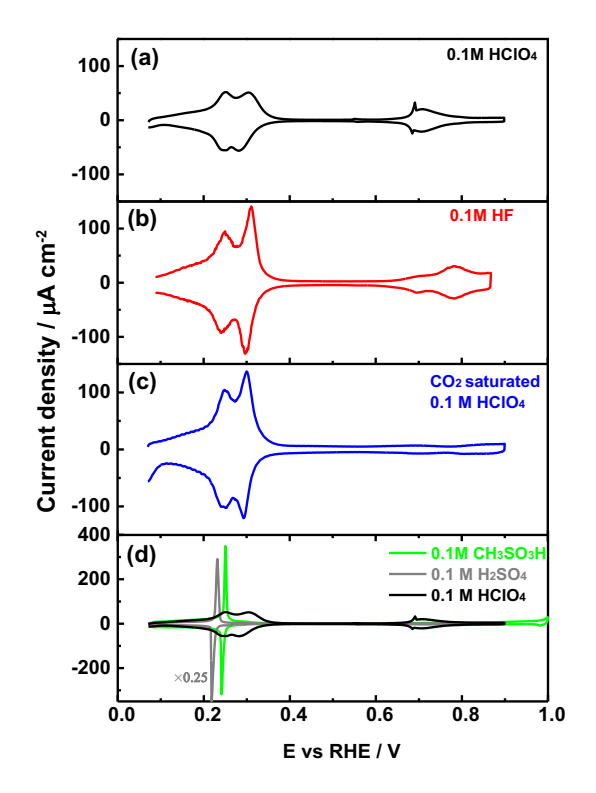


FIGURE 5.3 Cyclic voltammogram of $Pd_{ML}Pt(111)$ recorded in (a) 0.1 M HClO₄, (b) 0.1 M HF, (c) CO₂ saturated 0.1 M HClO₄ solution, and (d) 0.1 M CH₃SO₃H. Scan rate: 50 mV s⁻¹.

To explore the anion effect on the H_{II} peak further, Figure 5.3 shows the voltammetry for different anions. In agreement with Figure 5.2, there is no impact of the anion on the H₁ peak in the presence of F (Figure 5.3b) and HCO₃ (Figure 5.3c), which suggests that anion adsorption or interaction is insufficient to perturb the OH_{ads} in this potential window. On the other hand, the H_{II} peak is observed to increase in sharpness in 0.1 M hydrofluoric acid (HF) (Figure 5.3b) and in CO₂ saturated (Figure 5.3c) perchloric acid compared to 0.1 M HClO₄ solution, suggesting that F and HCO₃ anion affect the shape of the H_{II} peak. The role of anion adsorption is also reflected in the marked competitive adsorption with the adsorption states between 0.60 and 0.90 V vs RHE: in 0.1 M HF, these states are suppressed compared to 0.1 M HClO₄ solution, whereas in CO₂ saturated 0.1 M HClO₄ solution these states are blocked completely by adsorbed bicarbonate, just as in sulfuric acid (as shown in Figure 5.1a). Spectroelectrochemical experiments have shown that the bands corresponding to adsorbed bicarbonate on Pd_{ML}Pt(111) surface appear at 0.40 V vs RHE, i.e. in the beginning of the "double-layer" window.34

The voltammograms of Pt(111) in 0.1 M CH₃SO₃H and HClO₄ electrolytes have been observed to be very similar, showing that both are non-specifically adsorbing electrolytes on Pt(111),³⁵ see also Figure D3. Surprisingly, the cyclic voltammogram shown in Figure 5.3d strongly suggests the methanesulfonate

anion from the CH_3SO_3H electrolyte behaves similar to the $0.1~M~H_2SO_4$ solution, and, therefore, methanesulfonate must be strongly adsorbed on the $Pd_{ML}Pt(111)$ electrode surface at low potentials. These results suggest that the SO_3 from (bi)sulphate/ CH_3SO_3H adsorbs more strongly on the Pd surface than on Pt. For such strong anion adsorption, reactions 1 and 2 are replaced by:

$$H_{ads} + y (anion) \rightleftharpoons H^+ + e^- + y (anion_{ads})$$
 5.3

It may be that a small concentration of Cl $^{-}$ preexists as a trace impurity in HClO₄ and/or is generated by the reduction of perchlorate ions catalyzed by palladium. 22 In order to eliminate the possibility of chloride present in HClO₄ being responsible for the $H_{\rm II}$ peak, small amounts (10^{-6} and 10^{-5} M) of Cl $^{-}$ were intentionally added to 0.1 M HClO₄ (pH = 1) and 0.001 M HClO₄ (pH = 3) solutions, respectively. Figure D4 in Appendix D shows the change caused by Cl $^{-}$: the $H_{\rm I}$ and $H_{\rm II}$ peaks exhibit some asymmetry, in contrast to the symmetric peaks observed in solutions containing only HClO₄. This observation makes it highly unlikely that the $H_{\rm II}$ peak is related to the presence of chloride anions.

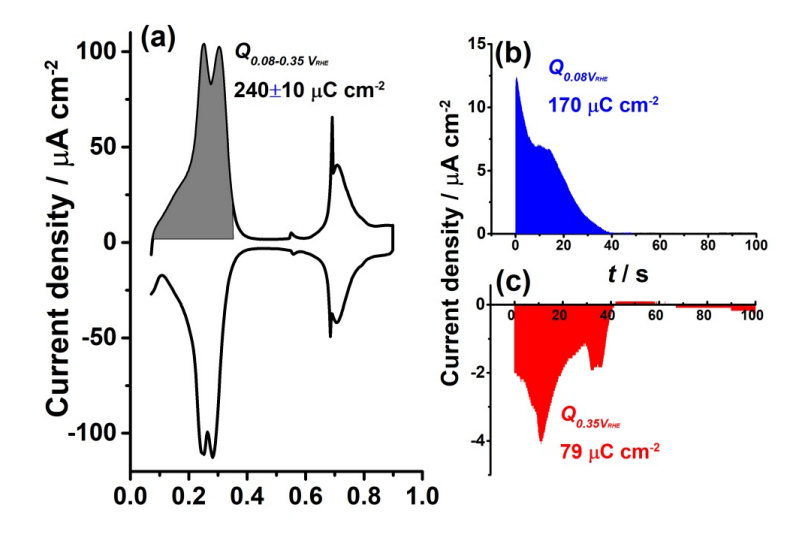


FIGURE 5.4

(a) Cyclic voltammogram of $Pd_{ML}Pt(111)$ recorded in (a) 0.1 M HClO₄; current-time transients recorded during CO adsorption/displacement at (b) 0.08 V vs RHE and (c) 0.35 V vs RHE in 0.1 M HClO₄.

To further elucidate the nature of the adsorption-desorption process in the hydrogen region at the $Pd_{ML}Pt(111)/e$ lectrolyte interface in perchloric acid, CO displacement experiments were performed. For the CO displacement experiment, CO was added to the solution and its adsorption at the electrode surface at fixed potential leads to a current transient related to the displacement of species adsorbed on the surface in the absence of CO. The total surface charge

at a chosen potential can be determined by integrating the transients. At the threshold of hydrogen evolution, i.e. at ca. 0.08 V vs RHE, the maximum charge density corresponding to the displacement of adsorbed hydrogen is obtained. As can be seen from Figure 5.4b, the transient current is positive which points to the oxidative desorption of H_{upd} :

$$H_{upd} - Pd_{ML}Pt(111) + CO \rightarrow CO - Pd_{ML}Pt(111) + H^{+} + e^{-}$$
 5.4

The H_{upd} coverage at 0.08 V vs RHE is then estimated to be $170/250 \approx 0.68$ ML. Correspondingly, at 0.35 V vs RHE negatively charged anions A are reductively displaced by CO following the reaction equation:

$$A - Pd_{ML}Pt(111) + CO + e^- \rightarrow CO - Pd_{ML}Pt(111) + A^-$$
 5.5

The result shows good agreement between the charge density values obtained from the integration of the transient current response (249 μ C cm $^{-2}$) and of the voltammetric profile characteristic (240±10 μ C cm $^{-2}$) of the Pd_{ML}Pt(111) interface. The reductive desorption of anions (as shown in Figure 5.4c) indeed indicates that adsorbed anions are involved in the H_{II} peak and the calculated $\Theta_{\rm A}$ on Pd_{ML}Pt(111) at the low potential region in 0.1 M HClO₄ is around 0.33 ML, according to the coulometric estimation.

5.4.3 Thermodynamics of *H, *OH + * H_2O , *O, *ClO₄, *SO₄ and * HSO_4 adsorption

Figure 5.5a and b show the experimentally measured cyclic voltammograms (upper panel) of Pt(111) and Pd_{ML}Pt(111) in 0.1 M HClO₄ along with the DFT-calculated free energies of adsorption of hydrogen, hydroxide, oxygen, and perchlorate as a function of potential vs RHE (lower panel). The lower panel shows the most stable coverages at any given potential (for more details, see Appendix D). The coverages investigated with DFT are: hydroxide from 2/9 to 2/3 ML for Pt(111) and from 1/9 to 2/3 ML for Pd_{ML}Pt(111), hydrogen from 1/9 to 1 ML for both Pt(111) and Pd_{ML}Pt(111), from 1/9 to 2/3 ML for oxygen on both Pt(111) and Pd_{ML}Pt(111), and 1/9 ML of perchlorate on both surfaces. The black horizontal line at 0 eV represents the reference state of the bare surface and the red line represents the adsorption of perchlorate.

It is important to consider the adsorption of water onto the electrode surface, as its adsorption could compete with that of hydrogen and hydroxide. However, given that the adsorption of water depends strongly on van der Waals (vdW) interactions, and these interactions are poorly captured with DFT-GGAs,³⁷ an accurate calculation of the adsorption energy of water is difficult. This is important not only for considering water adsorption, but also for the effects of co-adsorbed water on hydroxide adsorption. We therefore used three methods to evaluate the adsorption of water and its effect on our conclusions, primarily on the adsorption thermodynamics of solvated *OH: (1) a combined PBE and empirical vdW correction with PBE-D3^{38,39} only on the adsorption of *OH + *H₂O and *H₂O using solution-phase water as the reference state. (2) Using only PBE with the adsorbed water adlayer as the reference state for hydroxide adsorption

where the error in the adsorption energy of the water bilayer in the reactant state, and that of the partial bilayer in the *OH +*H $_2$ O product state, may partially cancel out. ^{40,41} (3) Using empirical vdW corrections with PBE-D3 for all adsorbates, *H, *H $_2$ O, *OH+*H $_2$ O and *O, and solution-phase water as the reference state.

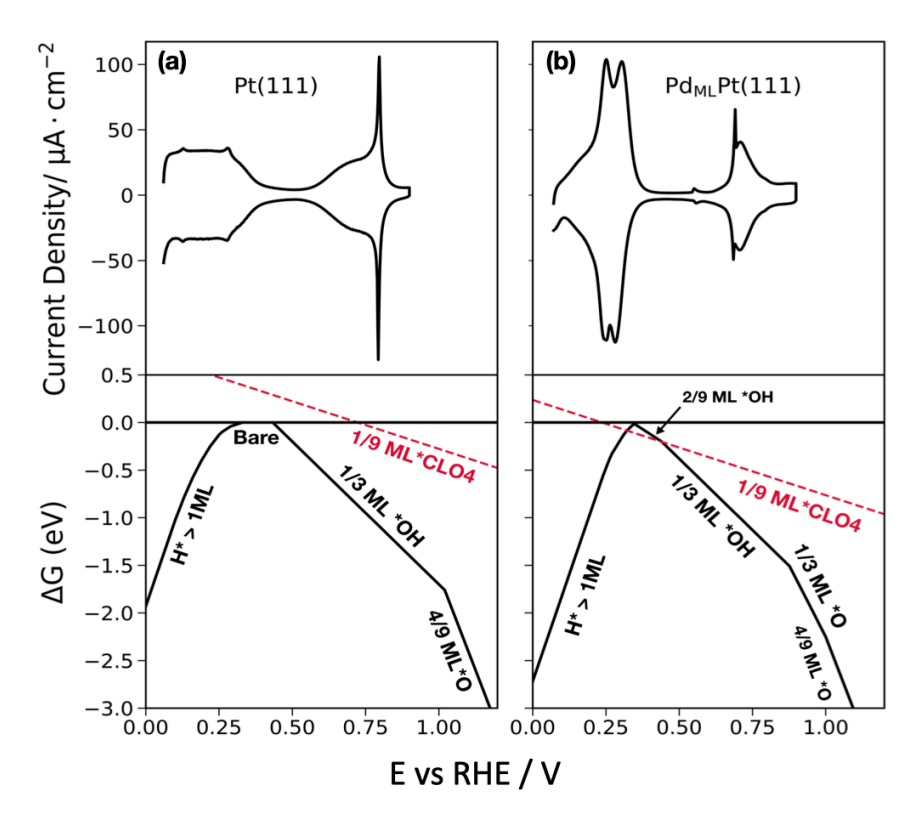


FIGURE 5.5

Upper panels are the cyclic voltammograms of (a) Pt(111) and (b) $Pd_{ML}Pt(111)$) in 0.1 M HClO₄ recorded at 50 mV s⁻¹. Black lines in the lower panels show the most stable adsorption free energies and the most favorable coverages as a function of potential for the adsorption of hydrogen (*H), hydroxide (*OH) and oxygen (*O). Perchlorate adsorption (*ClO₄) is shown in red at a 1/9 ML coverage.

The phase diagrams obtained with the different methods 1, 2 and 3 for $Pd_{ML}Pt(111)$ and Pt(111) are shown in Appendix D, Figures D6 and D7. In general, all the methods show similar trends of *H, *OH + *H₂O and *O adsorption. We have decided to base our conclusion on results derived from method 2 (shown in Figure 5.5) as it is simple and captures well the trends compared to experiment. For Pt(111) and $Pd_{ML}Pt(111)$, the trends obtained with method 2 and 3 are comparable to each other, as the adsorption energies and the overall trend does not significantly change as shown in Figures D6 b, c and D7 b, c. In the case of method 1, the only difference observed is the adsorption of water on $Pd_{ML}Pt(111)$ appearing at a lower potential than that of hydroxide *OH, in contrast to method

2 and 3 where hydrogen adsorption (*H) is followed by the adsorption of hydroxide (*OH). In all cases, the calculated adsorption potential of hydroxide lies around 0.3-0.4 V vs RHE for Pd_{ML}Pt(111) and 0.38-0.40 V vs RHE for Pt(111). Generally, PBE tends to overestimate binding energies, 42,43 which explains why the hydroxide adsorption potentials are more negative than the experimentally measured potentials. A more detailed description of the calculation of the free energies of adsorption of hydroxide can be found as "Adsorption Free energies of *OH, *H and *O" in Figure D5 in Appendix D.

Taking Pt(111) as a reference case (for which the adsorption thermodynamics of hydrogen, hydroxide, and oxygen are known), the surface composition as a function of potential (Figure 5.5a, lower panel) matches semi-quantitatively the experiments (Figure 5.5a, upper panel). DFT results show that the broad peak at low potentials corresponds with hydrogen adsorption at full monolayer coverage below 0.33 V vs RHE followed by the double layer region (where water is adsorbed), followed by 1/3 ML hydroxide adsorption at 0.43 V vs RHE and, finally, oxygen adsorption at 4/9 ML coverage at 1.02 V vs RHE. The results shown in Figure 5.5a for Pt(111) agree with previously calculated energy diagrams of Pt(111)¹⁹ with small differences in absolute values due to the different functional used. Including configurational entropy for the adsorbed species would probably bring the computational results in closer agreement with experiment. This is shown for hydrogen adsorption on Pt(111) and Pt(100) where a comparison of the slopes and intercept given by the relationship between the adsorption free energy as a function of coverage, including configurational entropy resulted in adsorption potentials closer to those obtained experimentally.³³ Furthermore, Karlberg et al. show how including lateral interaction of hydrogen adsorbed species and configurational entropies is important for simulating cyclic voltammograms of the hydrogen adsorption and desorption process.44

Figure 5.5b shows the calculated phase diagram of Pd_{MI}Pt(111) (lower panel). At potentials below 0.34 V vs RHE, hydrogen is adsorbed on the surface at 1ML coverage; hydroxide adsorption happens at 0.35 V vs RHE at 2/9 ML coverage followed by 1/3 ML hydroxide adsorption at 0.44 V vs RHE. At higher potentials oxygen adsorption becomes favorable at 0.88 V vs RHE at 1/3 ML coverage and at 1.0 V vs RHE at 4/9 ML coverage. Compared to Pt(111), oxygen adsorbates bind stronger on the Pd_{MI} Pt(111) surface. As will be discussed in the following sections, the DFT results support the conclusion from the previous section that the low potential peaks (H_I + H_{II}) correspond to an exchange between adsorbed hydrogen and adsorbed anions (*OH + *H₂O, *ClO₄). From the DFT modelling alone, it is unclear what species is adsorbed in the high potential peak (0.65-0.8 V vs RHE) observed in experiment, because oxygen adsorption is predicted to occur at potentials more positive of this peak. Therefore, if oxygen adsorption does not occur in that region, backed up by experimental results, that leaves the species present in the high potential peak as *ClO₄, *OH or a mixed adlayer of the two. The charge in this high potential peak is then most likely due to either an increase in the adsorbed hydroxide coverage (within a mixed perchlorate/hydroxide adlayer) or a replacement of perchlorate with a higher coverage of adsorbed hydroxide, as we expect adsorbed perchlorate to keep some of its charge (as seen for adsorbed (bi)sulfate, for example) and exhibit repulsive interactions.

5.4.4 Anion adsorption

To further understand the anion effect on the H_I and H_{II} region observed in the experiments, we investigated the adsorption thermodynamics of various anions, *ClO_4 , *HSO_4 , *SO_4 , *F , and *HCO_3 on Pt(111) and $Pd_{ML}Pt(111)$. Adsorption of these anions was considered only at low coverage of 1/9 ML and explicitly solvated with 1 water molecule for each of the anions except for *F where 2 water molecules were used and for *OH where a partially dissociated water bilayer $(1/3^*OH-1/3^*H_2O)$ solvation was used. We will first discuss the main results obtained for *ClO_4 , *HSO_4 and *SO_4 and then we will show a comparison between the binding strength of *ClO_4 , *HSO_4 , *SO_4 , *F , and *HCO_3 anions on $Pd_{ML}Pt(111)$ compared to that of Pt(111).

Obtaining an accurate adsorption potential for anions such as ClO₄, SO₄² and HSO₄⁻ depends on how accurate their solution-phase free energy is determined. There are many methods which could be used to calculate the solution-phase free energy, including thermodynamic cycles which avoid the need to correctly capture the solvation energy of the anion with traditional DFT techniques, which is a difficult task because of the long length and time scales of important solvation dynamics. However, to take those into account molecular dynamics simulations are preferred. 45,46 Here, the solution-phase free energy of perchlorate, sulfate and bisulfate was calculated as described in *Chapter 3*. Briefly, the free energy of the aqueous anion is determined by using the calculated DFT energy of a neutral species (typically in the gas phase), that upon reduction produces the target anion, and by using the half-redox equilibrium potential at which this reduction reaction occurs, we can easily calculate the free energy of the solution-phase anion. This method is analogous to the computational hydrogen electrode method (CHE)²⁷ for calculating the free energy of protons in solution, but in the case of hydrogen/protons, the equilibrium potential is defined to be exactly 0 V vs SHE and is not experimentally measured. 47-49 For more detailed and robust methods to determine solution-phase free energies and simulate CVs see ref.^{50,51}

Our DFT results show that the adsorption potential at which perchlorate binds on the Pd_{ML}Pt(111) at 1/9 ML coverage overlaps with that of low coverages of hydrogen *H at 0.32 V vs RHE and with *OH at 0.44 V vs RHE V, as shown by the red line in Figure 5.5b (lower panel). The adsorption potential of perchlorate on Pt(111) lies at more positive potentials around 0.72 V vs RHE than the calculated adsorption of 1/3 ML hydroxide *OH, which occurs at around 0.43 V vs RHE. This suggests that perchlorate adsorbs more strongly on Pd_{ML}Pt(111) than on Pt(111), and could outcompete hydroxyl adsorption and even low-coverage hydrogen adsorption on Pd_{ML}Pt(111). Conversely, on Pt(111) hydroxyl outcompetes perchlorate adsorption. Furthermore, at higher potentials, after ~0.55 V vs RHE, a perchlorate-hydroxyl mixed adlayer could form, and as the potential is increased this mixed adlayer can either (i) co-adsorb higher *OH coverages with *ClO₄, or (ii) higher coverages of *OH displace *ClO₄ from the mixed adlayer leaving an adlayer of just high-coverage *OH. This is in good agreement with our interpretation of the experimental voltammetry.

However, as we are unsure of the absolute accuracy of our calculated perchlorate adsorption potentials (in contrast to hydroxyl, for example, where we know at which potentials it adsorbs on Pt(111) from experiment), it is difficult to know if we should expect perchlorate adsorption before hydroxyl adsorption on the Pd_{ML}Pt(111) from our DFT calculations alone. Taking again Pt(111) as a benchmark, there is some experimental spectroscopic evidence interpreted to

show both that perchlorate affects hydroxyl adsorption on Pt(111)⁵² and/or even specifically adsorbs in the double layer/hydroxide/oxide regions (~0.4-0.8 V vs RHE).⁵³ More recent studies by Attard et al.⁵⁴ show the double layer and hydroxyl adsorption regions of cyclic voltammograms measured on Pt(111) are sensitive to the perchlorate concentration, suggesting that perchlorate strongly interacts with the surface.

Therefore, considering only our DFT results, there is computational support that the low potential peak in the CV measured on $Pd_{ML}Pt(111)$ (comprising both H_I and H_{II} in Figure 5.1b) corresponds to an exchange between *H / *OH+* H_2O and *ClO₄ as seen in Figure 5.2b and Figure 5.5b (lower panel), and is, therefore, not solely due to hydrogen adsorption, consistent with the conclusions from the experimental voltammograms, CO displacement measurements, and cation/anion/pH effects. The total coverage of hydrogen and anion (*OH) adsorption matches that measured by *CO displacement (Figure 5.4b and c). However, we have calculated a *H coverage of 1 ML adsorbed at low potentials (at the lower potential limit of the CV), and CO displacement gives an *H coverage of ~0.71 ML. This discrepancy could be due to the omission of configurational entropy for the calculation of the free energy, which would make

high-coverage *H adsorption less favorable than calculated here.

Additionally, we compared the calculated adsorption potentials of *SO₄ with the CV of Pt(111) and the adsorption potential of *\$O₄ and *HSO₄ with the CV of Pd_{ML}Pt(111) as measured in 0.1 M H₂SO₄, see Figure 5.6. The calculated adsorption potential of sulfate on Pt(111) is 0.57 V vs RHE, falling in the high potential region of the CV where sulfate/bisulfate adsorption is known to occur on Pt(111).55-59 Significant debate has centered on which anion (bisulfate vs. sulfate) corresponds to this adsorption peak in the cyclic voltammogram; given our limited investigation of the coverage dependence and the effect of solvation near the electrode surface, we do not intend to answer this question here, and take this result to be indicative of (bi)sulfate adsorption. For Pd_{ML}Pt(111), the calculated bisulfate and sulfate adsorption potentials are 0.47 V vs RHE and 0.45 V vs RHE respectively, in both cases falling in the region where (bi)sulfate is adsorbed on the surface fully blocking active sites. Similar to Pt(111), this peak has been assigned to bisulfate/sulfate anions based on the spectroscopic data obtained by in situ FTIR experiments.²¹ It is important to note that with our DFT model employed here we cannot specify which anion adsorbs more preferably in the bisulfate sulfate region on both surfaces. This model could be improved by examining additional coverages of (bi)sulfate/sulfate, water solvation and also by specifying a more accurate solution-phase reference state for the anions. 60,61

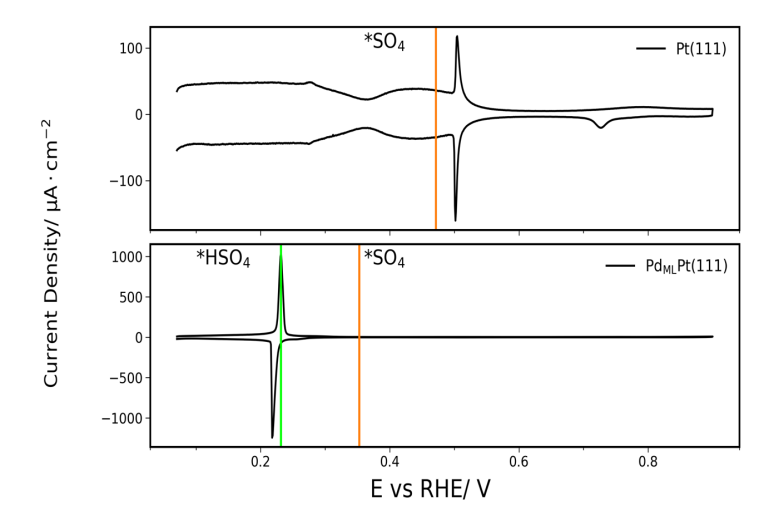


FIGURE 5.6

Cyclic voltammograms of Pt(111) and $Pd_{ML}Pt(111)$ in 0.1M H_2SO_4 recorded at 50 mV s⁻¹ along with the DFT calculated adsorption potentials for * SO_4 in orange and * HSO_4 in green.

We found that in general, anions bind more strongly to the Pd_{ML}Pt(111) surface than on Pt(111). This is shown in Figure 5.7, where the DFT-calculated relative free energies of adsorption with respect to Pt(111) are shown. Such a comparison of adsorption strength between Pd_{MI}Pt(111) and Pt(111) is not dependent on the energy of the solution-phase anion. For all the adsorbates studied, with the exception of *OH in vacuum, the binding energy is stronger on Pd_{MI}Pt(111). The bars in orange represent the adsorbed anion without solvation and the bars in blue represent the adsorbed anion with water solvation. We use one explicit water molecule for all adsorbates, except for *OH which is solvated as a 1/3*OH-1/3 *H₂O bilayer, and for fluoride which is solvated by two water molecules. It is interesting to note that for most of the adsorbates the solvation effect is more predominant on Pd_{ML}Pt(111), as noted by the more negative energy for the anion solvated with respect to that in vacuum. However, for bisulfate in the bidentate configuration, *HŜO₄ bid., bicarbonate *HCO₃, and fluoride *F the solvation effect is slightly more predominant on Pt(111), by ~0.04 eV, ~0.05 eV and ~0.04 eV, respectively, as observed by the less negative energy difference of the solvated anion compared to the conditions in vacuum.

Interestingly, we also find that water binds more strongly to $Pd_{ML}Pt(111)$ than to Pt(111). A single water molecule (at 1/9 ML coverage) binds ~ 0.15 eV stronger and within a 2/3 ML water adlayer the binding strength per water molecule is ~ 0.03 eV stronger on the $Pd_{ML}Pt(111)$ compared to Pt(111). This suggests that the typically stronger adsorption seen for the anions on $Pd_{ML}Pt(111)$ with solvation vs. without solvation may be simply due to a stronger adsorption of water on the $Pd_{ML}Pt(111)$ surface.

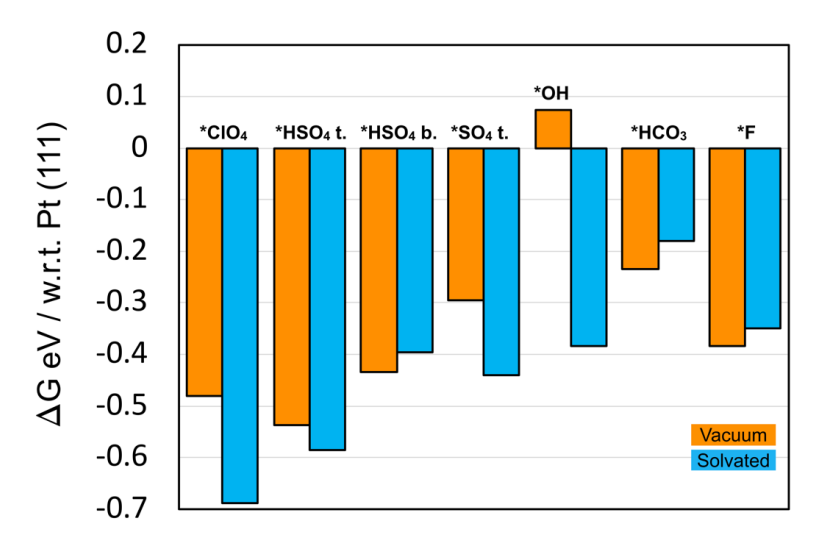


FIGURE 5.7

Relative DFT-calculated free energies on $Pd_{ML}Pt(111)$ calculated with respect to (w.r.t.) Pt(111) for perchlorate *ClO₄, bisulfate in tridentate configuration *HSO₄ t., bisulfate in bidentate configuration *HSO₄ b., sulfate in tridentate configuration *SO₄ t., hydroxyl *OH, bicarbonate *HCO₃ and fluoride *F. The orange bars represent the free energies in vacuum and the blue bars represent the solvated free energies.

While with DFT alone we cannot differentiate the phenomena in $H_{\rm I}$ and $H_{\rm II}$ separately, in conjunction with the experimentally observed pH, cation, and anion effects, we conclude that (i) the first feature in the low-potential peak on the $Pd_{\rm ML}$ Pt(111), the region of $H_{\rm I}$ and $H_{\rm II}$, is comprised of an exchange between adsorbed *H and *OH + * $H_{\rm 2}$ O adlayer matching the location, total charge, and ratio of *H/anion charge displaced as measured by experiment, and (ii) that this region ($H_{\rm I}$ and $H_{\rm II}$) is affected by the specific adsorption of perchlorate. Additional DFT studies should be performed to further investigate the effects of perchlorate coverage, and near-surface solvation, as well as methods to accurately and reliably define the free energy of solution-phase anions, so that the competition between adsorbed hydroxide and adsorbed perchlorate can be confidently quantified.

We have also shown that our DFT model gives a good estimate of the adsorption potentials of *SO_4 and *HSO_4 on Pt(111) and Pd_{ML}Pt(111), matching qualitatively those obtained experimentally, giving further semi-quantitative confidence in the perchlorate results. Lastly, in agreement with the experimental results, DFT also supports stronger anion binding on Pd_{ML}Pt(111) compared to Pt(111).

Hydroxyl adsorption plays an important role in catalytic reactions such as the oxygen reduction reaction, and its adsorption trends have helped explain non-Nernstian pH dependence shifts on Pt(110) and Pt(100). Such shifts are a result of a weaker binding of *OH on the surface, due to an effect of alkali metal cations in alkaline solutions. Therefore, studying *OH adsorption on the $Pd_{ML}Pt(111)$, allows us to explain CV features and can provide further information for mechanistic studies where binding of *OH species serve as descriptor for catalytic

activity such as oxygen reduction. Similarly, anion adsorption is important for catalytic reactions such as formic acid oxidation, where it has been shown that the presence of pre-adsorbed sulfate induces a lower onset potential on Pt(111).⁶² On Pd thin films, formic acid oxidation is suppressed by sulfate/bisulfate anions and CO formation is enhanced.⁶³ Beyond catalytic reactions, specific adsorption of anions are of particular interest in studies of surface structure.^{64,65}

5.5 Conclusions

In this *Chapter*, we identified the adsorption processes taking place in the various peaks of the blank voltammogram of the well-defined Pd_{MI}Pt(111) surface in perchloric acid by means of experimental and computational studies. We showed that:

(i) The "first hydrogen peak" H_I at 0.246 V vs RHE is not due to just adsorption and desorption of hydrogen, but actually involves the replacement of hydrogen by hydroxyl. The hydroxyl adsorption is sensitive to the nature of the electrolyte cation, in agreement with our previous work on stepped Pt electrodes.

(ii) The "second hydrogen peak" $H_{\rm II}$ at 0.306 V vs RHE involves the exchange of *H/*OH to adsorbed perchlorate *ClO₄. The coverage of the adsorbed perchlorate, can be assumed to be 1/3 ML on $Pd_{\rm ML}Pt(111)$ at the positive end of the $H_{\rm II}$ peak. If more strongly adsorbed anions are added to the electrolyte, the $H_{\rm I}$ and $H_{\rm II}$ peaks merge, and the high potential adsorption states are blocked; that is, strongly adsorbed anions suppress OH/O adsorption at both lower and higher potentials. In strong contrast to Pt(111), we have not identified any anion that we can safely assume to be not adsorbed specifically on $Pd_{\rm ML}Pt(111)$.

We believe that these detailed insights will be very important in correctly interpreting and understanding the catalytic properties of palladium and palladium-modified electrodes.

5.6 References

- (1) Strmcnik, D.; Kodama, K.; Vliet, D. van der; Greeley, J.; Stamenkovic, V. R.; Marković, N. M. The Role of Non-Covalent Interactions in Electrocatalytic Fuel-Cell Reactions on Platinum.

 Nature Chem 2009, 1 (6), 466-472.
- (2) Magnussen, O. M. Ordered Anion Adlayers on Metal Electrode Surfaces. *Chem. Rev.* **2002**, 102 (3), 679-726.
- (3) Tripkovic, D. V.; Strmcnik, D.; van der Vliet, D.; Stamenkovic, V.; Markovic, N. M. The Role of Anions in Surface Electrochemistry. *Faraday Discuss.* **2009**, *140* (0), 25–40.
- (4) Chen, X.; McCrum, I. T.; Schwarz, K. A.; Janik, M. J.; Koper, M. T. M. Co-Adsorption of Cations as the Cause of the Apparent PH Dependence of Hydrogen Adsorption on a Stepped Platinum Single-Crystal Electrode. *Angew. Chem. Int. Ed* **2017**, *56* (47), 15025-15029.
- (5) McCrum, I. T.; Chen, X.; Schwarz, K. A.; Janik, M. J.; Koper, M. T. M. Effect of Step Density and Orientation on the Apparent PH Dependence of Hydrogen and Hydroxide Adsorption on Stepped Platinum Surfaces. *J. Phys. Chem. C* **2018**, *122* (29), 16756-16764.
- (6) Clavilier, J.; Armand, D.; Sun, S. G.; Petit, M. Electrochemical Adsorption Behaviour of Platinum Stepped Surfaces in Sulphuric Acid Solutions. *J. Electroanal. Chem. Interf. Electrochem.* **1986**, 205 (1), 267–277.
- (7) Chen, X.; Koper, M. T. M. Mass-Transport-Limited Oxidation of Formic Acid on a PdMLPt(100) Electrode in Perchloric Acid. *Electrochem. commun.* **2017**, *82*, 155–158.
- (8) Arenz, M.; Schmidt, T. J.; Wandelt, K.; Ross, P. N.; Markovic, N. M. The Oxygen Reduction Reaction on Thin Palladium Films Supported on a Pt(111) Electrode. *J. Phys. Chem. B* **2003**, *107* (36), 9813-9819.
- (9) Arenz, M.; Stamenkovic, V.; Ross, P. N.; Markovic, N. M. Surface (Electro-)Chemistry on Pt(111) Modified by a Pseudomorphic Pd Monolayer. *Surf. Sci.* **2004**, *573* (1), 57-66.
- (10) Kortlever, R.; Balemans, C.; Kwon, Y.; Koper, M. T. M. Electrochemical CO2 Reduction to Formic Acid on a Pd-Based Formic Acid Oxidation Catalyst. *Catal. Today* **2015**, *244*, 58-62.
- (11) Min, X.; Kanan, M. W. Pd-Catalyzed Electrohydrogenation of Carbon Dioxide to Formate: High Mass Activity at Low Overpotential and Identification of the Deactivation Pathway. *J. Am. Chem. Soc.* **2015**, *137* (14), 4701-4708.
- (12) Armstrong, F. A.; Hirst, J. Reversibility and Efficiency in Electrocatalytic Energy Conversion and Lessons from Enzymes. *Proc Natl Acad Sci USA* **2011**, *108* (34), 14049.
- (13) Cuesta, A.; Kibler, L. A.; Kolb, D. M. A Method to Prepare Single Crystal Electrodes of Reactive Metals: Application to Pd(Hkl). J. Electroanal. Chem. 1999, 466 (2), 165-168.
- (14) Baldauf, M.; Kolb, D. M. Formic Acid Oxidation on Ultrathin Pd Films on Au(Hkl) and Pt(Hkl) Electrodes. J. Phys. Chem. **1996**, 100 (27), 11375–11381.
- (15) Kibler, L. A.; El-Aziz, A. M.; Hoyer, R.; Kolb, D. M. Tuning Reaction Rates by Lateral Strain in a Palladium Monolayer. *Angew. Chem. Int. Ed.* **2005**, *44* (14), 2080-2084.
- (16) El-Aziz, A. M.; Hoyer, R.; Kibler, L. A.; Kolb, D. M. Potential of Zero Free Charge of Pd Overlayers on Pt(111). Electrochim. Acta 2006, 51 (12), 2518-2522.
- (17) Thin Films: Preparation, Characterization, Applications; Soriaga, M. P., Stickney, J., Bottomley, L. A., Kim, Y.-G., Eds.; Springer US, 2002.
- (18) Attard, G. A.; Price, R.; Al-Akl, A. Palladium Adsorption on Pt(111): A Combined Electrochemical and Ultra-High Vacuum Study. *Electrochim. Acta* **1994**, *39* (11), 1525–1530.

- (19) McCrum, I. T.; Hickner, M. A.; Janik, M. J. First-Principles Calculation of Pt Surface Energies in an Electrochemical Environment: Thermodynamic Driving Forces for Surface Faceting and Nanoparticle Reconstruction. *Langmuir* **2017**, *33* (28), 7043–7052.
- (20) Álvarez, B.; Climent, V.; Rodes, A.; Feliu, J. M. Anion Adsorption on Pd-Pt(111) Electrodes in Sulphuric Acid Solution. *J. Electroanal. Chem.* **2001**, *497* (1), 125-138.
- (21) Alvarez, B.; Feliu, J. M.; Clavilier, J. Long-Range Effects on Palladium Deposited on Pt(111). *Electrochem. Commun.* **2002**, *4* (5), 379–383.
- (22) Arenz, M.; Stamenkovic, V.; Schmidt, T. J.; Wandelt, K.; Ross, P. N.; Markovic, N. M. The Effect of Specific Chloride Adsorption on the Electrochemical Behavior of Ultrathin Pd Films Deposited on Pt(111) in Acid Solution. *Surf. Sci.* **2003**, *523* (1), 199–209.
- (23) Llorca, M. J.; Feliu, J. M.; Aldaz, A.; Clavilier, J. Electrochemical Structure-Sensitive Behaviour of Irreversibly Adsorbed Palladium on Pt(100), Pt(111) and Pt(110) in an Acidic Medium. *J. Electroanal. Chem.* **1993**, *351* (1), 299–319.
- (24) Hoyer, R.; Kibler, L. A.; Kolb, D. M. The Initial Stages of Palladium Deposition onto Pt(1 1 1). *Electrochim. Acta* **2003**, *49* (1), 63–72.
- (25) Okada, J.; Inukai, J.; Itaya, K. Underpotential and Bulk Deposition of Copper on Pd(111) in Sulfuric Acid Solution Studied by in Situ Scanning Tunneling Microscopy. *Phys. Chem. Chem. Phys.* **2001**, *3* (16), 3297–3302.
- (26) Clavilier, J.; Albalat, R.; Gomez, R.; Orts, J. M.; Feliu, J. M.; Aldaz, A. Study of the Charge Displacement at Constant Potential during CO Adsorption on Pt(110) and Pt(111) Electrodes in Contact with a Perchloric Acid Solution. *J. Electroanal. Chem.* 1992, 330 (1), 489-497.
- (27) Nørskov, J. K.; Rossmeisl, J.; Logadottir, A.; Lindqvist, L.; Kitchin, J. R.; Bligaard, T.; Jónsson, H. Origin of the Overpotential for Oxygen Reduction at a Fuel-Cell Cathode. *J. Phys. Chem. B* **2004**, *108* (46), 17886-17892.
- (28) Sakong, S.; Naderian, M.; Mathew, K.; Hennig, R. G.; Groß, A. Density Functional Theory Study of the Electrochemical Interface between a Pt Electrode and an Aqueous Electrolyte Using an Implicit Solvent Method. *The Journal of Chemical Physics* **2015**, *142* (23), 234107.
- (29) Sakong, S.; Groß, A. Methanol Oxidation on Pt(111) from First-Principles in Heterogeneous and Electrocatalysis. *Electrocatalysis* **2017**, *8* (6), 577–586.
- (30) Garcia-Araez, N.; Lukkien, J. J.; Koper, M. T. M.; Feliu, J. M. Competitive Adsorption of Hydrogen and Bromide on Pt(100): Mean-Field Approximation vs. Monte Carlo Simulations. *J. Electroanal. Chem.* **2006**, 588 (1), 1-14.
- (31) Garcia-Araez, N.; Koper, M. T. M. A Sublattice-Model Isotherm for the Competitive Coadsorption of Hydrogen and Bromide on a Pt(100) Electrode. *Phys. Chem. Chem. Phys.* **2010**, *12* (1), 143-148.
- (32) Koper, M. T. M.; Lukkien, J. J. Modeling the Butterfly: Influence of Lateral Interactions and Adsorption Geometry on the Voltammetry at (111) and (100) Electrodes. *Surf. Sci.* **2002**, 498 (1), 105-115.
- (33) McCrum, I. T.; Janik, M. J. PH and Alkali Cation Effects on the Pt Cyclic Voltammogram Explained Using Density Functional Theory. *J. Phys. Chem. C* **2016**, *120* (1), 457–471.
- (34) Berná, A.; Rodes, A.; Feliu, J. M.; Illas, F.; Gil, A.; Clotet, A.; Ricart, J. M. Structural and Spectroelectrochemical Study of Carbonate and Bicarbonate Adsorbed on Pt(111) and Pd/Pt(111) Electrodes. J. Phys. Chem. B **2004**, 108 (46), 17928-17939.
- (35) Sandoval-Rojas, A. P.; Gómez-Marín, A. M.; Suárez-Herrera, M. F.; Climent, V.; Feliu, J. M. Role of the Interfacial Water Structure on Electrocatalysis: Oxygen Reduction on Pt(111) in Methanesulfonic Acid. *Catal. Today* **2016**, *262*, 95-99.

- (36) Orts, J. M.; Gómez, R.; Feliu, J. M.; Aldaz, A.; Clavilier, J. Potentiostatic Charge Displacement by Exchanging Adsorbed Species on Pt(111) Electrodes—Acidic Electrolytes with Specific Anion Adsorption. *Electrochim. Acta* **1994**, *39* (11), 1519–1524.
- (37) Carrasco, J.; Klimeš, J.; Michaelides, A. The Role of van Der Waals Forces in Water Adsorption on Metals. *J. Chem. Phys.* **2013**, *138* (2), 024708.
- (38) Grimme, S.; Antony, J.; Ehrlich, S.; Krieg, H. A Consistent and Accurate Ab Initio Parametrization of Density Functional Dispersion Correction (DFT-D) for the 94 Elements H-Pu. J. Chem. Phys. **2010**, 132 (15), 154104.
- (39) Grimme, S.; Ehrlich, S.; Goerigk, L. Effect of the Damping Function in Dispersion Corrected Density Functional Theory. *J. Comput. Chem.* **2011**, *32* (7), 1456-1465.
- (40) Granda-Marulanda, L. P.; Builes, S.; Koper, M. T. M.; Calle-Vallejo, F. Influence of Van Der Waals Interactions on the Solvation Energies of Adsorbates at Pt-Based Electrocatalysts. *ChemPhysChem* **2019**, *20* (22), 2968-2972.
- (41) He, Z.-D.; Hanselman, S.; Chen, Y.-X.; Koper, M. T. M.; Calle-Vallejo, F. Importance of Solvation for the Accurate Prediction of Oxygen Reduction Activities of Pt-Based Electrocatalysts. *J. Phys. Chem. Lett.* **2017**, *8* (10), 2243–2246.
- (42) Janthon, P.; Kozlov, S. M.; Viñes, F.; Limtrakul, J.; Illas, F. Establishing the Accuracy of Broadly Used Density Functionals in Describing Bulk Properties of Transition Metals. *J. Chem. Theory Comput.* **2013**, *9* (3), 1631-1640.
- (43) Sun, J.; Remsing, R. C.; Zhang, Y.; Sun, Z.; Ruzsinszky, A.; Peng, H.; Yang, Z.; Paul, A.; Waghmare, U.; Wu, X.; Klein, M. L.; Perdew, J. P. Accurate First-Principles Structures and Energies of Diversely Bonded Systems from an Efficient Density Functional. *Nat. Chem.* **2016**, *8* (9), 831-836.
- (44) Karlberg, G. S.; Jaramillo, T. F.; Skúlason, E.; Rossmeisl, J.; Bligaard, T.; Nørskov, J. K. Cyclic Voltammograms for H on Pt(111) and Pt(100) from First Principles. *Phys. Rev. Lett.* **2007**, 99 (12), 126101.
- (45) Schnur, S.; Groß, A. Properties of Metal-Water Interfaces Studied from First Principles. *New J. Phys.* **2009**, *11* (12), 125003.
- (46) Magnussen, O. M.; Groß, A. Toward an Atomic-Scale Understanding of Electrochemical Interface Structure and Dynamics. *J. Am. Chem. Soc.* **2019**, *141* (12), 4777-4790.
- (47) McCrum, I. T.; Akhade, S. A.; Janik, M. J. Electrochemical Specific Adsorption of Halides on Cu 111, 100, and 211: A Density Functional Theory Study. *Electrochim. Acta* **2015**, *173*, 302–309.
- (48) Gossenberger, F.; Roman, T.; Groß, A. Hydrogen and Halide Co-Adsorption on Pt(111) in an Electrochemical Environment: A Computational Perspective. *Electrochim. Acta* **2016**, *216*, 152-159.
- (49) Hansen, H. A.; Man, I. C.; Studt, F.; Abild-Pedersen, F.; Bligaard, T.; Rossmeisl, J. Electrochemical Chlorine Evolution at Rutile Oxide (110) Surfaces. *Phys. Chem. Chem. Phys.* **2010**, *12* (1), 283–290.
- (50) Li, Y.; Janik, M. J. Recent Progress on First-Principles Simulations of Voltammograms. *Curr. Opin. Electrochem.* **2019**, *14*, 124-132.
- (51) Bagger, A.; Arán-Ais, R. M.; Stenlid, J. H.; Santos, E. C. dos; Arnarson, L.; Jensen, K. D.; Escudero-Escribano, M.; Cuenya, B. R.; Rossmeisl, J. Ab Initio Cyclic Voltammetry on Cu(111), Cu(100) and Cu(110) in Acidic, Neutral and Alkaline Solutions. *ChemPhysChem* **2019**, *20* (22), 3096-3105.

- (52) Huang, Y.-F.; Kooyman, P. J.; Koper, M. T. M. Intermediate Stages of Electrochemical Oxidation of Single-Crystalline Platinum Revealed by in Situ Raman Spectroscopy. *Nat. Commun.* **2016**, *7* (1), 12440.
- (53) Sawatari, Y.; Inukai, J.; Ito, M. The Structure of Bisulfate and Perchlorate on a Pt(111) Electrode Surface Studied by Infrared Spectroscopy and Ab-Initio Molecular Orbital Calculation. *J. Electron Spectrosc. Relat. Phenom.* **1993**, 64-65, 515-522.
- (54) Attard, G. A.; Brew, A.; Hunter, K.; Sharman, J.; Wright, E. Specific Adsorption of Perchlorate Anions on Pt{hkl} Single Crystal Electrodes. *Phys. Chem. Chem. Phys.* **2014**, *16* (27), 13689-13698.
- (55) Braunschweig, B.; Daum, W. Superstructures and Order–Disorder Transition of Sulfate Adlayers on Pt(111) in Sulfuric Acid Solution. *Langmuir* **2009**, *25* (18), 11112–11120.
- (56) Funtikov, A. M.; Stimming, U.; Vogel, R. Anion Adsorption from Sulfuric Acid Solutions on Pt(111) Single Crystal Electrodes. J. Electroanal. Chem. 1997, 428 (1), 147-153.
- (57) Kunimatsu, K.; Samant, M. G.; Seki, H.; Philpott, M. R. A Study of HSO4– and SO42– Co-Adsorption on a Platinum Electrode in Sulfuric Acid by in-Situ Ft-Ir Reflection Absorption Spectroscopy. *J. Electroanal. Chem. Interf. Electrochem.* **1988**, *243* (1), 203-208.
- (58) Faguy, P. W.; Markovic, N.; Adzic, R. R.; Fierro, C. A.; Yeager, E. B. A Study of Bisulfate Adsorption on Pt(111) Single Crystal Electrodes Using in Situ Fourier Transform Infrared Spectroscopy. *J. Electroanal. Chem. Interf. Electrochem.* **1990**, *289* (1), 245-262.
- (59) Clavilier, J. The Role of Anion on the Electrochemical Behaviour of a {111} Platinum Surface; an Unusual Splitting of the Voltammogram in the Hydrogen Region. *J. Electroanal. Chem. Interf. Electrochem.* **1980**, 107 (1), 211–216.
- (60) Santana, J. A.; Cabrera, C. R.; Ishikawa, Y. A Density-Functional Theory Study of Electrochemical Adsorption of Sulfuric Acid Anions on Pt(111). *Phys. Chem. Chem. Phys.* **2010**, *12* (32), 9526-9534.
- (61) Yeh, K.-Y.; Restaino, N. A.; Esopi, M. R.; Maranas, J. K.; Janik, M. J. The Adsorption of Bisulfate and Sulfate Anions over a Pt(111) Electrode: A First Principle Study of Adsorption Configurations, Vibrational Frequencies and Linear Sweep Voltammogram Simulations. Catal. Today 2013, 202, 20-35.
- (62) Perales-Rondón, J. V.; Herrero, E.; Feliu, J. M. Effects of the Anion Adsorption and PH on the Formic Acid Oxidation Reaction on Pt(111) Electrodes. *Electrochim. Acta* 2014, 140, 511-517.
- (63) Miyake, H.; Okada, T.; Samjeské, G.; Osawa, M. Formic Acid Electrooxidation on Pd in Acidic Solutions Studied by Surface-Enhanced Infrared Absorption Spectroscopy. *Phys. Chem. Chem. Phys.* **2008**, *10* (25), 3662-3669.
- (64) Vasiljevic, N.; Wood, M.; Heard, P. J.; Schwarzacher, W. The Influence of Specific Anion Adsorption on the Surface Roughness of Electrodeposited Polycrystalline Cu Films. *J. Electrochem. Soc.* **2010**, *157* (4), D193-D198.
- (65) Zei, M. S.; Qiao, G.; Lehmpfuhl, G.; Kolb, D. M. The Influence of Anions on the Structure of Underpotentially Deposited Cu on Au(111): A LEED, RHEED and AES Study. Ber. Bunsenges. Phys. Chem. 1987, 91 (4), 349-353.





6

HOW PALLADIUM PROHIBITS CO POISONING DURING ELECTROCATALYTIC FORMIC ACID OXIDATION AND CARBON DIOXIDE REDUCTION

Here, we elucidate the atomistic details of how a palladium electrocatalyst avoids CO poisoning during both formic acid oxidation to carbon dioxide and carbon dioxide reduction to formic acid. To this end, we compare results obtained with a Pt(111) single-crystal electrode modified with and without a single monolayer of palladium. We apply (high-scan-rate) cyclic voltammetry together with density functional theory in a comparative fashion to explain the absence of CO poisoning on the palladium electrode. We show how the high formate coverage on $Pd_{ML}Pt(111)$ protects the surface from poisoning during formic acid oxidation, and why the adsorption of CO precursor dictates the delayed poisoning of $Pd_{ML}Pt(111)$ during CO_2 reduction. We show that the nature of the hydrogen adsorbed on $Pd_{ML}Pt(111)$ is considerably different from Pt(111), supporting a model to explain the reversibility of this reaction. Our results can help in design catalysts for which CO poisoning needs to be avoided.

This chapter is based on Chen, X.; Granda-Marulanda, L. P.; McCrum, I. T.; Koper, M. T. M How Palladium prohibits CO poisoning during electrocatalytic Formic Acid oxidation and CO2 reduction. <u>Submitted</u>
Also published in, Chen, X. Adsorption and Catalysis on Pt and Pd Monolayer-Modified Pt Single Crystal Electrodes, PhD thesis, Leiden University, 2019- Chapter 5

All experiments were performed by Xiaoting Chen.

6.1 Introduction

Low-temperature fuel cells consuming organic molecules as fuel have been regarded as a prospective solution to reduce our dependence on traditional fossil fuels.^{1,2} Formic acid is one of the fuel candidates to be employed in a so-called direct formic acid fuel cell (DFAFC).^{2,3} The electrocatalytic formic acid oxidation reaction has also been considered as a model reaction for the oxidation of more complex organic molecules. Of all pure metal electrodes, platinum and palladium show the highest formic acid oxidation activity. Formic acid oxidation on Pt surfaces has been studied extensively and the dual-pathway mechanism⁵ has been well established by the community.² This mechanism assumes that there are two parallel pathways in the reaction scheme. One pathway leads to the desired final product CO₂ at relatively low potentials through a reactive intermediate (presumably some form of adsorbed formate⁶), and another pathway includes a chemical dehydration step leading to adsorbed CO, which acts as a poison blocking the surface and impedes further oxidation of formic acid. The identification of CO as the poisoning intermediate and its role in the oxidation mechanism has been widely accepted,7 but the nature of the reactive intermediate in the direct pathway is still under strong debate. The prominence of the CO poisoning pathway on Pt electrodes renders Pt an unsuitable catalyst for direct formic acid fuel cells and also not ideal for the study of the direct pathway.8,9

Recent advances in catalyst development have led to the synthesis of Pd-based metal nanoparticles with excellent catalytic properties towards formic acid oxidation. Pd-based catalysts for the electrochemical formic acid oxidation generally display high activity and, remarkably, the absence of CO poison formation. Therefore, Pd model electrodes can be used to study the mechanism of the direct pathway without the interference of CO poisoning, and, perhaps more importantly, to understand how CO poisoning can be avoided. However, Pd single crystals are difficult to prepare. Epitaxially grown Pd layers on a foreign metal are an interesting alternative, particularly Pt single-crystal surfaces modified by a Pd monolayer. Pd 10,11,16-20 The lattice parameters of both metals are close and it has been pointed out that the reactivity of Pd monolayer system is comparable to that of the corresponding Pd single crystal. Pd.

Palladium-based materials have also emerged as the best catalysts for the reverse reaction, i.e. carbon dioxide electroreduction to formic acid. 22-26 Theoretically, for a two-electron transfer reaction such as the conversion between formic acid and CO₂, reversible catalysts with very low overpotential must exist, 27 and palladium-based electrocatalysts seem to approach this ideal situation closely.

This opens up the possibility of using palladium-based catalysts for application in unitized regenerative fuel cells based on carbon dioxide and formic acid. Recent efforts from our group have verified that Pd overlayers deposited on polycrystalline Pt, reduce CO₂ to formic acid and may perform as reversible catalysts.²² Furthermore, Pd_xPt_{1-x} nanoparticles were

applied as bifunctional electrocatalysts for both the CO₂ reduction and formic acid oxidation and showed improved tolerance to CO poisoning and lower overpotentials.²⁸

In this *Chapter*, we perform systematic electrochemical studies of formic acid oxidation and carbon dioxide reduction on Pd monolayer decorated Pt single crystals and explore the important role played by the involved formate anions on the direct formic acid oxidation pathway. We also study both reactions in comparison to unmodified Pt single crystals. In combination with first-principles density functional theory calculations, our studies reveal the crucial role of adsorbed formate anions in inhibiting CO poisoning during the formic acid oxidation. On the other hand, CO poisoning does occur during CO₂ reduction, but only at relatively high overpotential. Our DFT calculations indicate that the faster poisoning of Pt(111) during CO₂ reduction is related to the much stronger binding of the key *COOH intermediate on Pt(111) compared to palladium.

6.2 Experimental Results and Discussion

6.2.1 Formic acid oxidation

Figure 6.1 a shows the blank voltammogram of Pd_{ML}Pt(111) in 0.1 M HClO₄, compared to Pt(111). The Pd_{ML}Pt(111) electrode exhibits the same characteristic regions as Pt(111). For Pt(111), these windows correspond to the H adsorption-desorption feature (0.05<E<0.35 V_{RHE}), the double layer region (0.35<E<0.60 V_{RHE}), and the adsorption-desorption process for OH_{ads} (0.60<E<0.90 V_{RHE}).²⁹ However, as we have shown recently and in *Chapter* 5, for the Pd_{ML}Pt(111) electrode, these regions correspond to different reactions.³⁰ The two peaks in the "hydrogen region" of Pd_{ML}Pt(111) involve the replacement of adsorbed H by adsorbed OH (peak at E=0.21 V_{RHE}) and the replacement of adsorbed OH by adsorbed ClO₄" (peak at E=0.31 V_{RHE}). At higher potential (>0.65 V_{RHE}), the adsorbed perchlorate is replaced by a higher coverage of OH_{ads} or by adsorbed O. The primary reason for the strong difference between Pd_{ML}Pt(111) and Pt(111) surface is the significantly stronger anion and OH adsorption on the Pd_{ML}Pt(111) surface.

In Figure 6.1 b, the voltammograms for the oxidation of formic acid on $Pd_{ML}Pt(111)$ and Pt(111) in 0.1 M HClO₄ containing 50 mM HCOOH are shown. In perchloric acid, the effect of anion adsorption should be minimal, though we do note that we assume specific perchlorate adsorption on $Pd_{ML}Pt(111)$ above 0.30 V_{RHE} (see previous paragraph). As shown in Figure 6.1b, on the Pt(111) electrode formic acid oxidation starts from 0.35 V_{RHE} along with a peak current of 2.2 mA cm⁻² during the positive-going scan, with a slightly higher peak current density at 0.6 V during the negative-going scan because the CO poisoning intermediate has been oxidatively stripped at potentials above 0.70 V_{RHE} (as shown in Figure 6.1c).

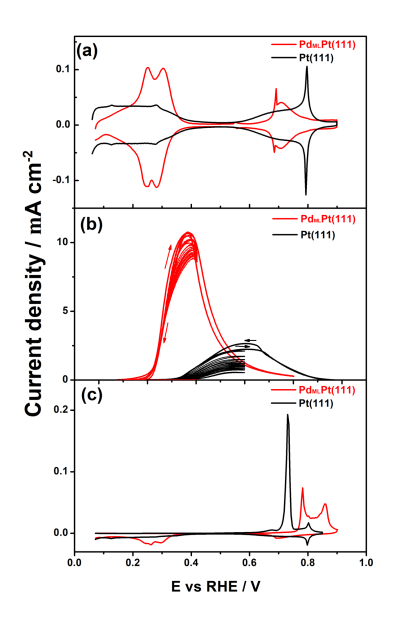


FIGURE 6.1

(a) Cyclic voltammogram of $Pd_{ML}Pt(111)$ electrode (red) and Pt(111) (black) in 0.1 M HClO₄. (b) Voltammograms for the oxidation of formic acid on $Pd_{ML}Pt(111)$ electrode (red) and Pt(111) (black) in 0.1 M HClO₄ + 50 mM HCOOH. The evolution of 12 cycles on a rotating $Pd_{ML}Pt(111)$ (red) and Pt(111) (black) electrode at 1600 rpm with continuous cycling to two lower vertex potentials: one to the potential of the oxidation peak where no oxidative stripping of adsorbed CO takes place (see Figure 6.1c), and one to a higher potential at which adsorbed CO is oxidatively stripped off. Scan rate: 50 mV s⁻¹. (c) CO stripping voltammogram for $Pd_{ML}Pt(111)$ electrode (red curve) and Pt(111) (black curve) in 0.1 M HClO₄. Scan rate: 10 mV s⁻¹.

Figure 6.1b also shows the fast deactivation of the formic acid oxidation on Pt(111) due to the accumulation of the surface adsorbed CO generated if we cycle to a vertex potential of 0.6 V_{RHE} at which the adsorbed CO is not oxidatively stripped. The formic acid oxidation current decreases fourfold after 12 cycles. These results are consistent with previous results for Pt(111), namely there exists two parallel pathways (direct and CO formation pathway) during the positive-going scan, while the negative-going scan after CO has been oxidatively stripped at high potential is usually chosen as representative for the formic acid oxidation through the direct pathway only.³¹

For the $Pd_{ML}Pt(111)$ electrode, a peak current density of 11.0 mA cm⁻² at 0.38 V_{RHE} (ca. four times higher current than on Pt(111), at a 0.2 V lower potential) is observed together with a low onset potential at around 0.20 V_{RHE} . The remarkable observation in Figure 6.1b is that there is hardly any hysteresis for the oxidation current in the positive- and negative-going scan

of $Pd_{ML}Pt(111)$ electrode between 0.05 and 0.40 V_{RHE} , suggesting the absence of CO poisoning. Therefore, only the formic acid oxidation direct pathway occurs, in agreement with previous studies. ^{10,18} Figure 6.1c shows that surface-adsorbed CO on the $Pd_{ML}Pt(111)$ electrode cannot be oxidatively stripped until the positive-going scan reaches 0.90 V_{RHE} . Comparison of the blank voltammograms of $Pd_{ML}Pt(111)$ and Pt(111) in Figure 6.1a with the formic acid oxidation curves in Figure 6.1b indicates that the onset of formic acid oxidation appears to coincide with hydrogen desorption at 0.20 V_{RHE} , suggesting that the adsorbed hydrogen inhibits the formic acid oxidation at low potential.

Figure 6.1c shows the CO stripping voltammograms of Pd_{ML}Pt(111) and Pt(111) surfaces in 0.1 M HClO₄, resp. Very low currents are measured on both Pd_{ML}Pt(111) and Pt(111) electrodes during the positive-going scan until 0.6 V_{RHE}, implying that both surfaces are completely blocked by adsorbed CO at low potential. From this observation we conclude that CO binds strongly and irreversibly to both surfaces. For Pt(111), the oxidative stripping peak for adsorbed CO is located at about 0.72 V_{RHE} and the subsequent scan shows the well-known butterfly feature of Pt(111) in 0.1 M HClO₄. By comparing to Pt(111), the CO stripping peak of Pd_{ML}Pt(111) electrode is shifted to more positive potentials, between 0.80 and 0.90 V_{RHE} , suggesting slower CO oxidation kinetics on Pd_{ML}Pt(111) compared to Pt(111) under identical experiment conditions, in agreement with a previous report.³² The charge corresponding to the CO stripping peak is related to the CO coverage, from which we estimate the coverages of CO on Pt(111) and Pd_{ML}Pt(111) electrode to be 0.69 and 0.75 ML, respectively, consistent with previous reports for Pt(111)^{33,34} and Pd(111).³⁵ From these observations, we infer that we cannot ascribe the lack of CO poisoning during formic acid oxidation on Pd_{ML}Pt(111) to a lower CO adsorption strength; if anything, the stripping results show that CO binds stronger to $Pd_{MI}Pt(111)$ than to Pt(111).

6.2.2 Formate adsorption isotherm

Given the important role of adsorbed formate in the oxidation mechanism, we want to compare the adsorbed formate coverages for Pt(111) and $Pd_{ML}Pt(111)$ as a function of potential. At normal scan rates, the electrochemical signal corresponding to formate adsorption is masked by the formic acid oxidation currents; however, by employing higher scan rates, it is possible to detect adsorbed formate.³¹ The current for the reversible formate adsorption/desorption process is proportional to the scan rate, whereas the current for the oxidation of formic acid is independent of the scan rate as this is a process which is purely controlled by the kinetics of the reaction.

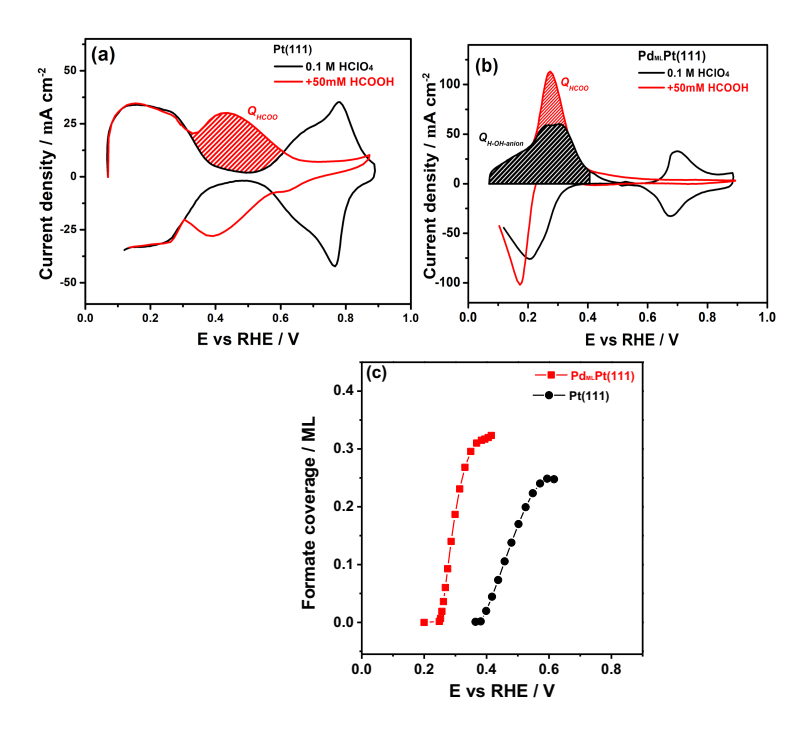


FIGURE 6.2

Voltammograms of (a) Pt(111) and (b) Pd_{ML}Pt(111) electrode in 0.1 M HClO₄ (black line) and 0.1 M HClO₄ + 50 mM HCOOH (red line) solution at a high scan rate of 50 V s⁻¹. (c) Comparison between the coverage of adsorbed formate as a function of potential on the Pd_{ML}Pt(111) and Pt(111) electrode.

Thus, by selecting fast enough scan rates, the current corresponding to the adsorption process will be much larger than the current corresponding to the oxidation of the intermediate so that this latter contribution can be considered negligible.

Figure E2 a and b in the Appendix E show the blank voltammograms of Pt(111) and Pd_{ML}Pt(111) in 0.1 M HClO₄ solution recorded at 0.05 and 50 V s⁻¹, resp. As can be seen, the currents associated to the typical H_{upd} region, the double layer region and the OH adsorption region of the Pt(111) electrode in perchloric acid media recorded at 50 V s⁻¹ have increased 3 orders of magnitude in comparison to that of 0.05 V s⁻¹, as expected. Although there appears to be a change in shape in the low potential region (0.05<E<0.40 V_{RHE}) of Pd_{ML}Pt(111) recorded at 50 V s⁻¹ compared to the blank at 0.05 V s⁻¹, the charge associated to the H_{upd} and anion adsorption has the same value of 240 μ C cm⁻². The OH adsorption profile of the Pd_{ML}Pt(111) electrode, between 0.65 and 0.80 V_{RHE}, recorded at 50 V s⁻¹ also increases 3 orders of magnitude compared to that recorded at 0.05 V s⁻¹. In the presence of formic acid, as shown in Figure 6.2a, the high-scan-rate voltammogram of Pt(111) is practically symmetric through the j=0 axis,

which indicates that currents are mainly due to adsorption processes and that the contribution from the continuous formic acid oxidation process can be neglected.

The characteristic H adsorption-desorption feature between 0.05 and 0.35 V_{RHE} is similar to what is found in 0.1 M HClO₄, the signal corresponding to formate adsorption is observed between 0.38 and 0.70 V_{RHE} , whereas the OH adsorption feature has diminished due to the blocking effect of adsorbed formate, in agreement with previous fast voltammetry results.³¹ The potential region of adsorbed formate agrees with that observed by ATR-FTIR on polycrystalline Pt electrodes.³⁶ Figure 6.2b shows the highscan-rate voltammogram of Pd_{MI} Pt(111) in 0.1 M HClO₄ + 50 mM HCOOH. The characteristic H-OH-anion feature between 0.05 and 0.40 V_{RHE} overlaps with the signal corresponding to formate adsorption, whereas the OH/O adsorption feature has diminished due to the formate blocking effect. To determine the charge corresponding to the adsorption of formate (Q_{HCOO}) on the Pd_{ML}Pt(111) electrode, we calculate the charge corresponding to the adsorption states in the presence of formate, and subtract the charge corresponding to the feature H-OH-anion ($Q_{H, anions}$) in the absence of formic acid (see Figure 6.2b).

If the double layer capacity of Pt(111) is the same in the absence and presence of formic acid, we can obtain the experimental isotherms for formate absorption on both surfaces from high scan-rate voltammetry, assuming an electrosorption valency equal to -1. According to the spectroscopic studies, the adsorbed formate (HCOO) on the Pt ^{6,37} and Pd ^{38,39} surface is bidentate formate. It is now generally agreed that the adsorbed bidentate formate species exist stably on the surface and does not desorb oxidatively as CO₂.^{7,40,41} Therefore, the bidentate formate should be considered as a spectator species in the formic acid oxidation pathway. A fully saturated layer of bidentate formate has a coverage of 0.5 ML per Pt surface atom.

Comparing the bidentate formate coverage-electrode potential curves in Figure 6.2c on Pt(111) and Pd_{ML}Pt(111) electrode, the bidentate formate adsorbate reaches a higher coverage of 1/3 ML on Pd_{ML}Pt(111) compared to that of 1/4 ML on Pt(111). Also, formate binds at ca. 0.20 V lower potential on Pd_{ML}Pt(111), implying stronger adsorption of formate on the palladium-modified surface.

6.2.3 Formate and CO production from CO₂ reduction

Next, we turn our attention to a comparison of CO_2 electroreduction on $Pd_{ML}Pt(111)$ and Pt(111). Figure 6.3a and b show the production of formic acid and (adsorbed) CO from the reduction of CO_2 on $Pd_{ML}Pt(111)$ (Figure 6.3a) and Pt(111) (Figure 6.3b) electrode as a function of potential. The formic acid production was followed with online HPLC as introduced in the Experimental Section. Figure 6.3a shows the production of formic acid on the $Pd_{ML}Pt(111)$ electrode starts at a potential of -0.29 V_{RHE} and

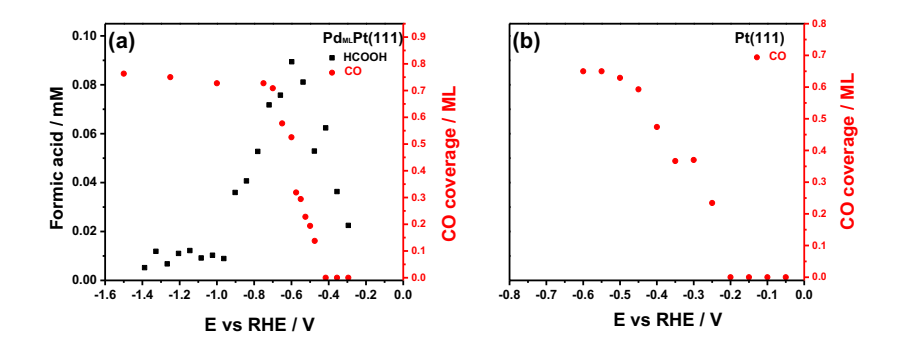


FIGURE 6.3

Formation of formic acid detected with online HPLC and the CO coverage calculated from stripping voltammograms on (c) $Pd_{ML}Pt(111)$ and (d) Pt(111) electrode under the same experimental condition.

approaches a peak production around -0.60 V_{RHE} , and the trend here is similar to our previous results of $Pd_xPt_{(1-x)}$ nanoparticles.²² Recently reported Pd catalysts also demonstrate formate formation at low overpotential and high efficiency.²³ On the other hand, Pt(111) does not produce any measurable amounts of formic acid. Previous studies have shown both Pt(111)⁴² and Pd(111)⁴³ single crystal electrodes to be inefficient CO_2 electroreduction catalysts as they convert CO_2 to adsorbed CO_3 as the major product.

To investigate the formation of CO during CO_2 reduction on the $Pd_{ML}Pt(111)$ and Pt(111) electrode, experiments were carried out by stripping off adsorbed CO by going to positive potentials. We first scanned the potential to different negative vertex potentials performing CO_2 reduction at 1 mV s^{-1} following the same process as with online HPLC. Next, the electrode was scanned to positive potentials at 10 mV/s, in the same cell immediately after finishing CO_2 reduction to avoid any contamination/exposure to air during electrode transfer. The corresponding cyclic voltammograms are shown in the Appendix E (Figure E4 a and b). From the CO stripping charges, we can determine the CO surface coverage generated during the CO_2 reduction; these CO coverages are shown as red data points in Figure 6.3.

Figure 6.3 shows that on the $Pd_{ML}Pt(111)$ electrode CO_2 reduction starts producing adsorbed CO at potentials more negative than -0.475 V_{RHE} , whereas on Pt(111) adsorbed CO is formed at potentials more negative than -0.25 V_{RHE} . On $Pd_{ML}Pt(111)$, the CO coverage saturates at ca. -0.70 V_{RHE} . Comparing to the production of formic acid in Figure 6.3a, it is also clear that the formation of formic acid drops as the $Pd_{ML}Pt(111)$ electrode becomes saturated with adsorbed CO. This is thus a clear indication that the $Pd_{ML}Pt(111)$ electrode is able to reduce CO_2 to formic acid at low overpotential window but becomes passivated due to the formation of a CO adlayer when the potential is more negative.

6.3 DFT Results and Discussion

To better understand the experimental observations during formic acid oxidation and electrochemical $\mathrm{CO_2}$ reduction on $\mathrm{Pd_{ML}Pt}(111)$ compared to Pt(111), we used DFT to calculate the free energies of formation of the adsorbed species involved in the reactions, *H, *OCHO, *COOH, and *CO. We will focus on explaining the absence of *CO poisoning on $\mathrm{Pd_{ML}Pt}(111)$ during formic acid oxidation at low potentials, in comparison to the rapid poisoning on Pt(111) (see Figure 6.2), based on the adsorption characteristics of formate *OCHO. In the case of the $\mathrm{CO_2}$ reduction reaction, we will provide a thermodynamic explanation of the rapid CO poisoning of Pt(111) vs $\mathrm{Pd_{ML}Pt}(111)$ based on the adsorption energetics of *COOH, the precursor of *CO, on both surfaces.

6.3.1 Formic acid oxidation

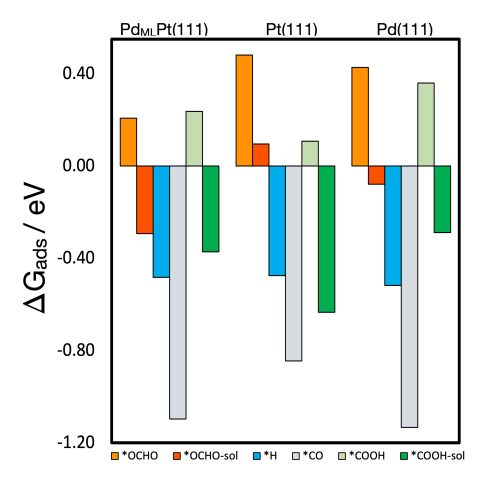


FIGURE 6.4

Formation energies of adsorbed *OCHO, *H, *COOH, and *CO at 1/9 ML coverage at 0 V vs. RHE on $Pd_{ML}Pt(111)$, Pt(111) and Pd(111) from formic acid in solution. *OCOH in bright orange is non solvated and in dark orange/red it is solvated, *OCHO-sol. *COOH in light green is non solvated and in dark green it is solvated, *COOH-sol.

Figure 6.4 shows the free energies of formation of *H, *CO, *OCHO, *COOH at 1/9 ML coverage at 0 V vs RHE. The free energy of *COOH in the absence of solvation is in light green and with solvation *COOH-sol, in dark green, and for *OCHO, bright orange is without solvation and dark orange/red is with solvation. The energies shown in Figure 6.4 are calculated from formic acid in the solution phase. For solvated *COOH, we

used *COOH with two water molecules, one of which is hydrogen bonded to the OH in *COOH, and for solvated formate we used 1 H₂O molecule; for more details about solvation, see the Appendix E. The most favorable adsorption sites on all electrode surfaces for *H and *CO were the highly coordinated fcc hollow sites. Note that for Pt(111) we used *CO atop configuration instead, as experimentally this is known to be the preferred site. The difference in energy between atop and fcc for *CO on Pt(111) at 1/3 ML coverage is ~ 0.1 eV. We found that the most favorable configuration of formate, *OCHO, is bound to the surface of the electrode through the oxygen atoms with each oxygen adsorbed atop a surface atom. The adsorption trend on Pd_{MI} Pt(111) and Pd(111) is *OCHO-sol < *COOHsol < *H <*CO, and on Pt(111) surface, hydrogen has a weaker adsorption than *COOH-sol, and the trend is *OCHO-sol < *H < *COOH-sol < *CO. However, at higher coverages of 1/4 ML, the adsorption energy of *H is more favorable than that of *COOH-sol. Also, formate adsorption is significantly more favorable on $Pd_{ML}Pt(111)$ than on Pt(111) and Pd(111), while *COOH-sol adsorption is more favorable on Pt(111) than on Pd_{ML}Pt(111) and Pd(111), and this trend holds for both coverages, 0.11 ML and 0.25 ML. Bader charge analysis shows more negative charge retained on the adsorbates adsorbed on Pd_{ML}Pt(111) and Pd(111) than on Pt(111). (See Table S4 in the Appendix E). We can conceptually explain this formate adsorption and charge trend in terms of the different work functions of the catalysts, where the surface with the lower work function is expected to have a higher affinity for anion adsorption (and hence also a corresponding lower potential of zero charge). The trend in work function follows $Pd_{ML}Pt(111)$ (5.14 eV)< Pd(111) (5.29 eV) < Pt(111) (5.74 eV).

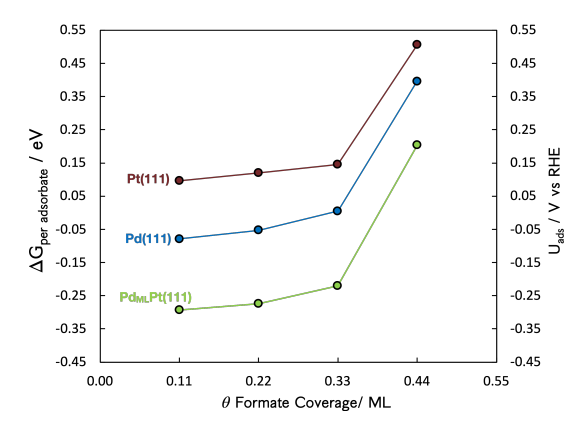


FIGURE 6.5

Formation energies (left y axis) and corresponding adsorption potentials (right y axis) for adsorbed formate from formic acid in solution as a function of coverage, on Pd_{ML}Pt(111) (green), Pd(111) (blue), and Pt(111) (red).

We further investigated formate adsorption on each surface, by calculating the formate adsorption energy as a function of coverage, see Figure 6.5. We find that formate adsorbs significantly more strongly on $Pd_{ML}Pt(111)$ than Pt(111) and Pd(111) at all investigated coverages, in agreement with the experimental results in Figure 6.2. At high coverages, beyond 0.33ML, formate anions can no longer adsorb in a bidentate configuration, and adsorption is significantly less favorable on all three surfaces than adsorption at low coverages. In the potential region where formic acid oxidation occurs, above 0.2 and 0.4 V for $Pd_{ML}Pt(111)$ and Pt(111), resp. (see Figure 6.1), formate can favorably adsorb up to relatively high coverages of 0.33 ML, where 2/3 of the surface atoms are blocked. Therefore, we have investigated the effect of this adsorbed formate, from 0.11ML to 0.33ML, on the formation of the adsorbed reaction intermediates, *H, *CO, *COOH-sol from formic acid. The results are shown in Figure 6.6.

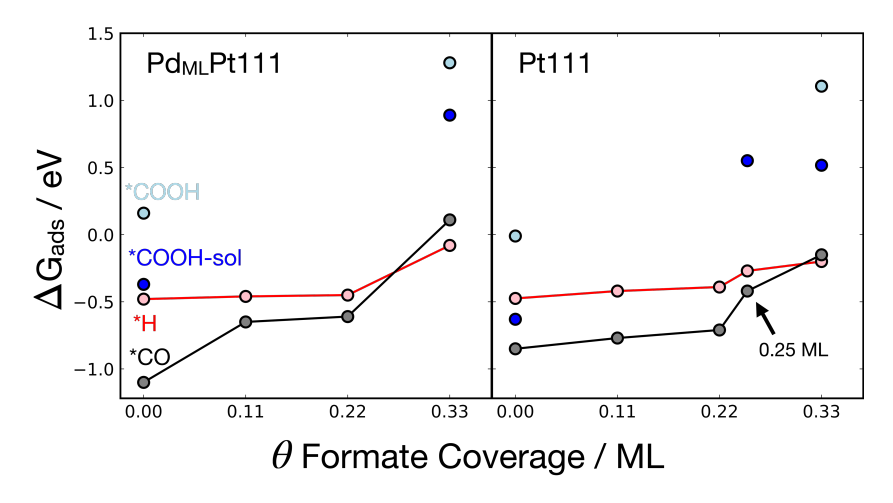


FIGURE 6.6

Free energies of formation of adsorbed *H, *CO, and *COOH at 1/9 ML at 0 V vs RHE, for $Pd_{ML}Pt(111)$ and Pt(111), as a function of different coverages of coadsorbed formate from 0.11ML to 0.33ML also including 0.25 ML for Pt(111) as specified with the arrow, because this is the experimentally observed maximum coverage on Pt(111). Only the low and higher coverages for *COOH are shown (0.11ML and 0.33ML), where *COOH-sol (blue) is with solvation and *COOH (light blue) is without. Connecting lines are only intended as a guide for the eye.

Figure 6.6 shows the formation free energies of adsorbed *H, *CO, and *COOH-sol co-adsorbed with formate at coverages from 0.11ML to 0.33ML on $Pd_{ML}Pt(111)$ (left) and Pt(111) (right). The free energy of the solvated *COOH-sol with 0.33ML of *OCHO, contains an upper bound estimate of the solvation effect on *COOH, as the solvation energy calculated for the non-co-adsorbed system is added to the free energy of the co-adsorbed one.

This is less computationally intensive than modelling explicit solvation for the high-coverage co-adsorbed system (see Appendix E for more details).

For Pd_{ML}Pt(111) the adsorption strength of *H is not significantly altered when co-adsorbed with 0.11ML to 0.22ML of formate, and its adsorption energy is more positive (less favorable) than that of *CO at the same conditions. However, because the adsorption strength of *CO is more strongly affected by the presence of co-adsorbed formate, at formate coverages of 0.33 ML, the trend is reversed and *CO is clearly less favorably adsorbed than *H by ~ 0.20 eV. Thus, at 0.33 ML formate coverage, it is more favorable for *H to be co-adsorbed with formate than *CO. Furthermore, adsorbed formate at 0.33ML weakens *COOH-sol adsorption, as seen in Figure 6.6, and consequently hinders its further dissociation to *CO, providing a further reason why CO poisoning is not observed during formic acid oxidation in the experiments on Pd_{ML}Pt(111).

For Pt(111), the presence of formate also weakens *H and *CO adsorption but not as significantly as on $Pd_{ML}Pt(111)$, meaning that the effect of formate on their adsorption strength is smaller on Pt(111). The effect of co-adsorbed formate on the difference in the formation energy of *CO and *H is also smaller on this surface than on Pd_{ML}Pt(111). At formate coverages of 0.33 ML, the difference in *H, and *CO adsorption strength is only 0.05 eV. Furthermore, as formate adsorption is weaker on Pt(111) than on Pd_{ML}Pt(111), its adsorption potential is more positive (see Figure 6.5), and in general a lower coverage of formate will be adsorbed on Pt(111) than on Pd_{ML}Pt(111) at the onset of formic acid oxidation. At a formate coverage of 0.25 ML, the Pt(111) surface is only 50% covered, leaving active sites available for *CO formation from its precursor *COOH-sol, given its favorable formation energy even in the presence of this co-adsorbed formate. This results in *CO poisoning of Pt(111) during formic acid oxidation. Thus, formate adsorption is important for formic acid oxidation in both Pd_{ML}Pt(111) and Pt(111), not as an active intermediate, but more as a self-protector against CO poisoning, and this is more significant on $Pd_{ML}Pt(111)$ than on Pt(111).

6.3.2 Adsorbed CO formation during CO₂ reduction

Figure 6.7 shows the formation free energies of adsorbed *OCHO, *COOH, *CO and *H, on $Pd_{ML}Pt(111)$, Pt(111) and Pd(111) calculated relative to CO_2 (g), electrons and protons. The adsorption energy trend at 1/9 ML coverage on $Pd_{ML}Pt(111)$ and Pd(111) follows *OCHO-sol < *COOH-sol<*H <*CO whereas on Pt it is *OCHO-sol <*H <*COOH-sol <*CO. The main difference in the trends is that on Pt(111) the adsorption strength of *COOH-sol is stronger than that of *H at this coverage. *CO and *OCHO-sol are much more strongly adsorbed on $Pd_{ML}Pt(111)$ and Pd(111), but *COOH is much more strongly adsorbed on Pt(111). In the case of hydrogen, its adsorption free energy is similar on all the surfaces.

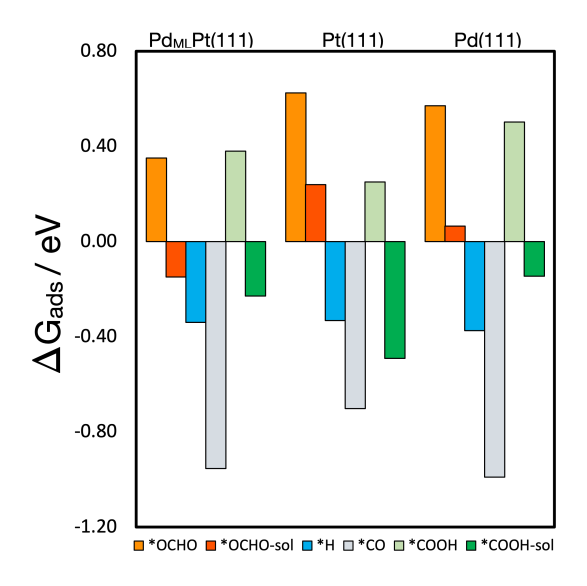


FIGURE 6.7

Formation energies of *OCHO, *H, *COOH, and *CO at 1/9 ML coverage at 0 V vs. RHE on $Pd_{ML}Pt(111)$, Pt(111) and Pd(111) calculated relative to CO_2 (g), protons and electrons and for *H, calculated relative to (H⁺ + e⁻). *OCOH in bright orange is non solvated and in dark orange (red) is solvated, *OCHO-sol.*COOH in light green is non solvated and in dark green is solvated, *COOH-sol.

The first observation we make from Figure 6.7 is that under *H is always more stable than *OCHO. This is basically in agreement with our observation from Figure 6.1 that *H inhibits formate adsorption. Therefore, we consider that *OCHO is not the intermediate in the CO₂ reduction to formic acid/formate. There is growing agreement in the literature that for catalysts that to reduce CO₂ close to the thermodynamic potential, including palladium, the key intermediate is *H, i.e. hydride.^{23,44} Formate is then formed by nucleophilic attack of the *H to the carbon of CO₂. ^{23,44}

It is therefore likely that during the reduction reaction, the surfaces are covered with hydrogen. With this in mind, we investigated the effect of 1/3 and 1 ML hydrogen coverage on the adsorption energetics of *COOH (see Figure E6), and the chemical nature of the adsorbed hydrogen by calculating partial Bader charges (see Table S4) and the corresponding work function (Table S5) for 1/9, 1/3, and 1 ML coverages, which provides a qualitative analysis of our results. From Figure E6 we observe that the *COOH free energy of adsorption becomes less favorable as hydrogen coverage increases due to repulsion interactions, but *COOH remains more favorably adsorbed on Pt(111) than on Pd_{ML}Pt(111) and Pd (111). We note that from experiment (Figure 6.3) *CO formation starts 0.25 V earlier on Pt(111), and in Figure E6, the adsorption energy of *COOH in the presence of 1 ML of H* looks to be roughly 0.25 eV more favorable on Pt(111) than on Pd_{ML}Pt(111).

It is interesting to note that the partial charge of the hydrogen adsorbed on the Pd_{ML}Pt(111) surface is much more negative than that on the Pt(111) surface at all coverages. This creates a different trend in dipole moment/work function on the surfaces: an increase on Pd_{ML}Pt(111) and a decrease on Pt(111) up to 1ML, see Table S4 and Table S5 in the Appendix E. Our DFT results match the trend seen in experimentally measured changes in work function of Pt(111)⁴⁵ and Pd(111) in UHV during the adsorption of hydrogen. Although we do not have direct evidence for the exact mechanism to form formic acid, we hypothesize that the significantly different chemical states of the hydrogen on Pd vs. Pt play an important role. Since hydrogen has a more negative partial charge on Pd_{ML}Pt(111) than on Pt(111), it is expected to act as a reactive hydride species (facilitating a nucleophilic attack to the carbon) to form formic acid. 44,46 On Pd_{MI}Pt(111), the partially negatively charged hydrogen can either be transferred to a non-adsorbed CO₂ molecule that is very close to the surface, or to the carbon of adsorbed *COOH. This nucleophilic attack is less likely to occur on Pt(111) because the surface hydrogen has much less negative partial charge. Also, on Pt(111) the *COOH adsorbs more strongly, leading to the surface becoming covered/poisoned with CO* at a less negative potential, so that the nucleophilic attack by H* on CO₂ cannot occur.

On the basis of Figure 6.7, *COOH-sol adsorption is more favorable on Pt(111) than on $Pd_{ML}Pt(111)$. The limiting potentials for the formation of *COOH-sol on $Pd_{ML}Pt(111)$ and Pt(111) are 0.23 and 0.49 V_{RHE} . Therefore, formation of *CO from its precursor *COOH-sol is likely to occur on Pt(111) at less negative potentials compared to $Pd_{ML}Pt(111)$, in good agreement with the experimental observations (see Figure 6.3). Also note that *COOH-sol needs to replace *H, which is favorable only on Pt(111) (see Figure 6.7). Therefore, *CO formation is more likely to occur on Pt(111) than on $Pd_{ML}Pt(111)$ as the adsorption of its precursor *COOH occurs at earlier potentials than on $Pd_{ML}Pt(111)$. Once the surface is covered with *CO, *H can no longer form and the pathway to forming formic acid/formate is blocked.

6.4 General Discussion

6.4.1 Formic acid oxidation

The experimental results and the DFT calculations indicate that adsorbed formate plays a key role in preventing CO poisoning on the $Pd_{ML}Pt(111)$ electrode during formic acid oxidation. The DFT calculations predict that the effect of co-adsorbed formate towards weakening CO* is larger on $Pd_{ML}Pt(111)$ than on Pt(111), such that at the maximum coverage of formate on $Pd_{ML}Pt(111)$, i.e. 0.33 ML, the formation energy of CO is unfavorable compared to the formation energy of adsorbed H at this conditions, whereas at the maximum coverage of formate on Pt(111), i.e. 0.25 ML, the

formation energy of CO is still more favorable compared to H. Therefore, CO formation from *COOH is suppressed on $Pd_{ML}Pt(111)$, but still happens on Pt(111). There is, however, an additional geometric argument why CO poisoning on $Pd_{ML}Pt(111)$ would be suppressed. It is well known that the formation of CO from formic acid requires an ensemble site of two (or more) neighboring free sites. ^{7,47} The $Pd_{ML}Pt(111)$ shows strong formate adsorption with a high saturation coverage of 0.33 ML. This 1/3 ML formate coverage means that at full coverage, 2/3 of the Pd surface atoms are blocked and the ensemble site of two neighboring Pd sites is not available. Therefore, CO poisoning is inhibited geometrically. On the other hand, the 1/4 ML saturation coverage of formate on Pt(111) is not high enough to block the ensemble site, and hence the Pt(111) surface becomes easily poisoned by CO.

Interestingly, while the formation of *CO is blocked on the 0.33 ML formate-covered Pd_{MI}Pt(111) electrode, formic acid oxidation still takes place with high rate. This can be explained by recent models for formic acid oxidation, which consider adsorbed formate as a "spectator", and which identify the active formate intermediate as a formate species interacting to the surface through the C-H bond. This configuration with the C-H pointing to the 1/3 ML of "free" Pd_{ML}Pt(111) surface sites can react to CO₂ by fast C-H cleavage due to the affinity of the Pd surface to hydrogen. Note that in this picture, adsorbed formate is more than a spectator, as it specifically blocks the surface from CO formation, and thereby protects the surface from poisoning. On Pt(111), the adsorbed formate does not bind strong enough to play the same role. In more chemically intuitive terms, we attribute this ability of palladium to "self-protect" from CO poisoning to the higher affinity of Pd and Pd_{ML}Pt(111) to anions. We relate the higher anion affinity of Pd_{ML}Pt(111) and Pd compared to Pt(111) to their lower work function, and hence a lower potential of zero charge.

Our model for formic acid oxidation and the mechanism of CO poisoning is illustrated in Figure 6.8a. On Pd_{ML}Pt(111), the surface is covered with such a high coverage of formate, that the only remaining interaction of formate with the surface is through the C-H bond. This interaction cleaves the C-H bond and releases CO₂. The pathway to *CO formation is blocked because the ensemble site for CO formation is unavailable and because the binding of CO at such a high formate coverage is highly unfavorable. On Pt(111), the formate coverage is lower. Formate is presumably still activated through cleaving the C-H bond, making the adsorbed formate an inactive spectator species. However, the ensemble site for CO formation is available and the binding of CO at this formate coverage is still reasonably favorable. As a result, the surface will accumulate *CO and becomes poisoned.

We have attempted to test this model for the $Pd_{ML}Pt(100)$ electrode, which shows a mass-transport-limited formic acid oxidation at normal scan rate. Figure E3 shows fast voltammetry results for the formic acid oxidation on $Pd_{ML}Pt(100)$ electrode. Unfortunately, the oxidation of formic acid on $Pd_{ML}Pt(100)$ electrode is still very fast, even in 0.1 M $Pd_{ML}Pt(100)$ at 50 V s⁻¹, so that this electrode is too active

to determine the saturation coverage of adsorbed formate, and hence we cannot confirm that on $Pd_{ML}Pt(100)$, adsorbed formate protects the surface from CO poisoning.

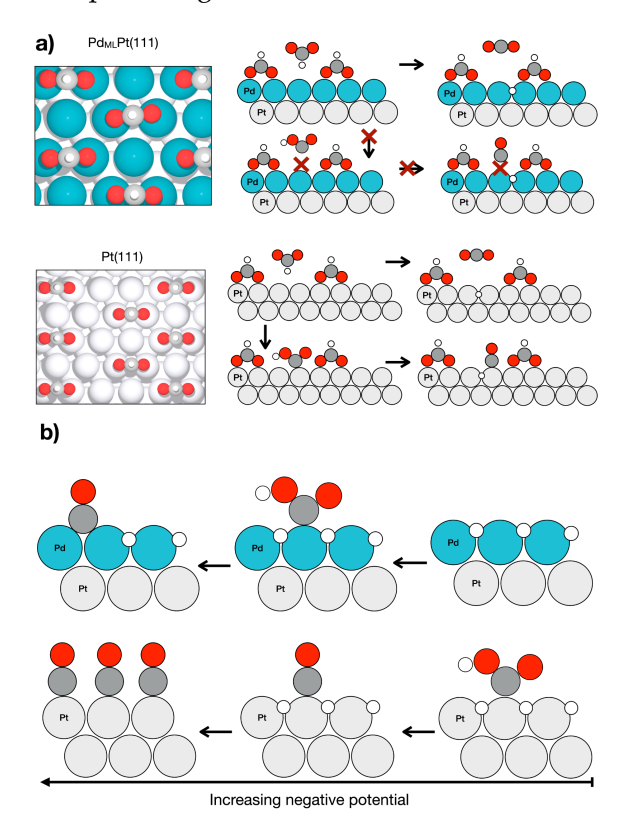


FIGURE 6.8

a) Illustration of the model mechanism for CO poisoning pathway during formic acid oxidation on $Pd_{ML}Pt(111)$ (upper drawing) and Pt(111) (lower drawing) with top views of the surfaces on the left and side views on the right. During formic acid oxidation the coverage on $Pd_{ML}Pt(111)$ is 1/3 ML, and on Pt(111) is 1/4 ML. On Pt(111) the necessary two neighboring surface atoms for *CO formation from *COOH are available, while on $Pd_{ML}Pt(111)$ they are not available. b) Illustration of the model mechanism for CO poisoning pathway during CO_2 reduction reaction, on $Pd_{ML}Pt(111)$ (upper sketch) and Pt(111) (lower sketch). Note that *COOH is adsorbed on Pt(111) at a less negative potential than on $Pd_{ML}Pt(111)$.Oxygen is in red, carbon in grey, hydrogen in white.

6.4.2 The CO₂ reduction

Pd surfaces produce formate at low potential close to the thermodynamic potential of formic acid formation from CO₂ reduction. At more negative potentials, the surface passivates due to the accumulation of CO.^{22,23} The electrochemically generated surface adsorbed hydrogen has been hypothesized to play key role during the electrohydrogenation of CO₂ to formate on the Pd surface.²³ In this case, high-coverage formate adsorption cannot explain the absence of CO poisoning at low overpotential, as formate adsorbs only at potentials positive of hydrogen adsorption (see Figure 6.2). Therefore, we also consider it unlikely that adsorbed formate is the intermediate in the CO₂ reduction on palladium. Supporting the hypothesis of the electrochemically generated adsorbed hydrogen being the reactive species, DFT shows that the nature of this adsorbed hydrogen differs significantly from Pd_{MI} Pt(111) to Pt(111). On Pd_{MI} Pt(111) it is more negatively charged than on Pt(111), and this negatively charged hydrogen ("hydride") can be transferred to a positively charged carbon (on a CO₂ molecule close to the surface (or to an adsorbed *COOH)) through a nucleophilic attack, to form formate. 44,46 Another attractive feature of this model for formate formation is that it is, on the molecular level, the exact how formate is oxidized, namely through formation/cleavage of a C-H bond with the H interacting with the catalyst surface. It is likely that this molecular reversibility is related to the observed kinetic reversibility of this reaction, when carried out on a suitable catalyst.

The DFT calculations suggest that the CO poisoning during CO₂ reduction is related to the stability of the *COOH intermediate. Since *COOH is considerably more stable on Pt(111) compared to Pd_{ML}Pt(111), CO poisoning happens much faster on Pt(111) and formic acid/formate is not produced (see Figure 6.3). Our model for CO poisoning during CO₂ reduction reaction is illustrated in Figure 6.8b. In summary, on Pt(111) *COOH adsorbs at less negative potentials than on Pd_{ML}Pt(111). However, at sufficiently negative potential, *COOH formation becomes favorable on Pd_{ML}Pt(111) as well and therefore we start seeing *CO poisoning also on that surface.

In this *Chapter*, we have used a well-defined epitaxially grown Pd monolayer on Pt(111) in comparison to a Pt(111) single crystal electrode to unveil the detailed relationship between surface structure, adsorbed intermediates, and reactivity for electrocatalytic formic acid oxidation and CO₂ reduction, with the specific aim to understand the ability of Pd catalysts to withstand CO poisoning. The Pd_{ML}Pt(111) surface shows a higher activity for formic acid oxidation than Pt(111). Our fast-scan voltammetry results show a higher coverage of 1/3 ML formate anion adsorption on the Pd_{ML}Pt(111) electrode compared to a saturation coverage of 1/4 ML on Pt(111). Supported by DFT results, we argue that the high binding energy of formate and the resulting higher coverage of formate anions, blocks the ensemble site necessary for CO formation, explaining why palladium does not poison by CO during formic acid oxidation. During CO₂ reduction, the electrochemically generated adsorbed surface

hydrogen is significantly more negatively charged on $Pd_{ML}Pt(111)$ than on Pt(111), and as a result, formation of formate via a nucleophilic attack of the negatively charged hydrogen to a positively charged carbon is more likely. The $Pd_{ML}Pt(111)$ surface produces formate at a low potential of -0.29 V_{RHE} but starts producing adsorbed CO at potentials more negative than -0.475 V_{RHE} , whereas Pt(111) is poisoned at less negative potential and never produces formate. Combined experimental and DFT results suggest that the faster poisoning on Pt(111) compared to $Pd_{ML}Pt(111)$ is due to stronger adsorption of *COOH, the precursor of *CO, at less negative potentials on Pt(111).

6.5 Experimental Section

6.5.1 Electrochemical Measurements

Electrolytes were prepared from ultrapure water (Merck Millipore, 18.2 M Ω cm, TOC<3 ppb) and high-purity reagents (Merck Suprapur, Sigma-Aldrich Trace Select). Before each experiment, the electrolytes were first purged with argon (Air Products, 5.7) for 30 min to remove air from the solution. In the case of CO₂ reduction experiments, the electrolyte was subsequently purged with CO₂ (Linde, 4.5) for at least 30 min to saturate the solution. For CO stripping experiments, the single-crystal electrode was in contact with a CO (Linde 6.0) saturated solution in hanging meniscus configuration at fixed potential of 0.1 V_{RHE} for 30 s, which is sufficient to form a complete monolayer of CO on the electrode. Afterwards, argon was bubbled for 15 min to remove CO from the solution, followed by the CO oxidative stripping experiment.

Cyclic voltammetry measurements were carried out in standard electrochemical cells using a three-electrode assembly at room temperature. All glassware was cleaned in an acidic solution of potassium permanganate overnight, followed by rinsing with an acidic solution of hydrogen peroxide and repetitive rinsing and boiling with ultrapure water. Pt(111) and Pt(100) bead-type electrodes were used as working electrodes (diameter of 2.27 mm and 3.46 mm, resp.) for cyclic voltammetry, and 10 mm disk-type electrodes were used for online high performance liquid chromatography (HPLC) experiments, resp. Prior to each experiment, the working electrodes were prepared according to the Clavilier method. 48 A platinum wire was used as counter electrode and a reversible hydrogen electrode (RHE), in a separate compartment filled with the same electrolyte, at the same pH as the electrolyte in the electrochemical cell, was employed as the reference electrode. The electrochemical measurements were performed with the single-crystal electrode in the hanging meniscus configuration. The potential was controlled with an Autolab PGSTAT302N potentiostat. The fast-scan cyclic voltammetry experiments were performed using a Bio-Logic SP-300 potentiostat. The current density shown here represents the measured current normalized to the geometric area of the working electrode.

6.5.2 Preparation of Pd monolayers on Pt(111) and Pt(100) single crystals

The Pd monolayers were prepared using the method similar to the one reported before. 21,49 The freshly prepared Pt(111) and Pt(100) electrodes were immersed into a Pd²⁺ containing solution at 0.85 V_{RHE}, where no Pd deposition occurred, and the potential was continuously cycled between 0.07 and 0.85 V_{RHE} at 50 mV s⁻¹. The amount of palladium on the Pt(111) surface was monitored by following the evolution of the voltammetric peak at 0.23 V_{RHE} (as shown in Figure E1 a), characteristic of the presence of Pd adatoms, whose charge (and current density) depend on the palladium coverage. Scanning tunnelling microscopy (STM) experiments have revealed the existence of small monoatomic high Pd islands which nucleate on the Pt(111) surface with no noticeable preference of nucleation sites and a full Pd monolayer without detectable holes can be formed after deposition.³² The STM images show the presence of an ordered sulphate adlayer with a $(\sqrt{3}\times\sqrt{9})$ R19.1° structure on the Pd monolayer. ³² After preparation, the Pd_{ML}Pt(111) electrode was taken from the cell and thoroughly rinsed with ultrapure water before electrochemical measurements. For the Pd_{MI}Pt(100) electrode, the single crystal was taken from the cell and then immersed in a nitrite saturated solution at open circuit to generate a layer of nitric oxide (NO) on the surface. Next, the crystal was thoroughly rinsed with ultrapure water to avoid any contamination from the acidic nitrite solution and subsequently was transferred to the electrochemical cell at 0.85 V_{RHE} and the adsorbed NO was reductively stripped. The NO procedure is a kind of electrochemical annealing which leads to a Pt(100) electrode fully covered by a single palladium monolayer.49 The palladium monolayer was monitored by following the evolution of the voltammetric peaks at 0.17, 0.27 and 0.39 V_{RHE} (as shown in Figure E1 b).

6.5.3 Online High Performance Liquid Chromatography (HPLC)

For online detection of products dissolved in the electrolyte during CO_2 reduction as a function of applied potential, online HPLC was used. While the potential was changed from 0.0~V to the required potential, samples were collected with an open tip positioned close ($\sim 10~\mu m$) to the electrode. Sampling was done at a rate of $60~\mu L$ min⁻¹, and each sample had a volume of $60~\mu L$. Since the potential was changed at $1~mV~s^{-1}$, each sample contained the products averaged over a potential change of 60~mV. After voltammetry, these samples were analyzed by HPLC (Prominence HPLC, Shimadzu; Aminex HPX 87-H column, Biorad).

6.6 Computational Details

Density functional theory (DFT) calculations were used to compute the adsorption/formation energies of *H, *CO, *OCHO and *COOH adsorbates involved in the formic acid oxidation and CO2 reduction reactions on Pd_{ML}Pt(111) (Pt(111) covered by one monolayer of Pd), Pt(111) and Pd(111). All calculations were performed using the PAW⁵¹ method in the Vienna Ab initio Simulation Package⁵² using the PBE⁵³ exchange correlation functional. We use 3x3 unit cell slabs to simulate adsorbate coverages of 0.11 ML to 0.33 ML and used 2x2 unit cell slabs to investigate adsorbate coverages of 0.25 ML. The Pd_{ML}Pt(111), Pt(111) and Pd(111) were simulated with five, six and four atomic layers, respectively. This choice was made based on convergence tests of adsorption energies with different number of layers. The k-point samplings for the 3x3 unit cell slabs were 6x6x1 for $Pd_{ML}Pt(111)$ and Pt(111) and 4x4x1 for the Pd(111); for the 2x2 unit cell slabs, 6x6x1 for Pd(111) and 4x4x1 for Pd_{ML}Pt(111) and Pt(111). The two bottommost layers were fixed at the calculated lattice constant of the bulk metal, 3.98 Å for Pt(111), also used for the Pd_{ML}Pt(111) slab, and 3.93 Å for Pd(111), and the remaining atomic layers were relaxed. The method of Methfessel-Paxton⁵⁴ to the second order was use to set the partial occupancies on each orbital and the smearing width was set to 0.2 eV for surfaces and adsorbed species. For the individual molecules $H_2(g)$, $H_2O(g)$, $CO_2(g)$, CO(g) a Gaussian smearing of 0.001 eV was used instead, and they were calculated in an asymmetric box of (15.0 x 15.1 x 15.3) Å at a k-point sampling of 1x1x1. The maximal forces on the atoms were converged to 0.02 eV Å⁻¹ for all simulations and the plane wave cutoff was set to 450 eV. A vacuum spacing of ~15.0 Å between metal slabs was set to simulate the surfaces of Pd_{ML}Pt(111), Pt(111), and Pd(111), and dipole corrections were also applied in the surface normal direction. The free energy of H₂O (g) was corrected to the free energy of H₂O (I) by adding -0.0887 eV to the TS term.⁵⁵ The formation free energies of adsorbed *H, *CO, *OCHO and *COOH were calculated from formic acid in solution, (HCOOH (aq)) for the formic acid oxidation reaction, and from carbon dioxide in gas-phase, (CO₂ (g)), electrons and protons in solution for the CO₂ reduction reaction. Gas-phase energy corrections for CO₂(g) and CO (g) are included,⁵⁶ and the CHE model 55 is used for the coupled proton and electron transfer. The exact details for calculating the free energies the different species from the DFT energies are outlined in the Appendix E.

6.7 References

- (1) Wieckowski, A. Fuel Cell Catalysis: A Surface Science Approach; Koper, M. T. M., Ed.; John Wiley & Sons, 2009.
- (2) Feliu, J.; Herrero, E.; Vielstich, W.; Gasteiger, H.; Lamm, A. Handbook of Fuel Cells. *Fundam. Appl.* **2003**, *2*, 625.

- (3) Aslam, N. M.; Masdar, M. S.; Kamarudin, S. K.; Daud, W. R. W. Overview on Direct Formic Acid Fuel Cells (DFAFCs) as an Energy Sources. *APCBEE Procedia* **2012**, *3*, 33-39.
- (4) Boronat-González, A.; Herrero, E.; Feliu, J. M. Heterogeneous Electrocatalysis of Formic Acid Oxidation on Platinum Single Crystal Electrodes. *Curr. Opin. Electrochem.* **2017**, *4* (1), 26-31.
- (5) Capon, A.; Parsons, R. The Oxidation of Formic Acid at Noble Metal Electrodes
 Part III. Intermediates and Mechanism on Platinum Electrodes. *J. Electroanal. Chem. Interfacial Electrochem.* **1973**, 45 (2), 205-231.
- (6) Miki, A.; Ye, S.; Osawa, M. Surface-Enhanced IR Absorption on Platinum Nanoparticles: An Application to Real-Time Monitoring of Electrocatalytic Reactions. *Chem. Commun.* **2002**, No. 14, 1500-1501.
- (7) Herrero, E.; Feliu, J. M. Understanding Formic Acid Oxidation Mechanism on Platinum Single Crystal Electrodes. *Curr. Opin. Electrochem.* **2018**, *9*, 145-150.
- (8) Grozovski, V.; Climent, V.; Herrero, E.; Feliu, J. M. Intrinsic Activity and Poisoning Rate for HCOOH Oxidation at Pt (100) and Vicinal Surfaces Containing Monoatomic (111) Steps. ChemPhysChem 2009, 10 (11), 1922-1926.
- (9) Koper, M. T. Structure Sensitivity and Nanoscale Effects in Electrocatalysis. *Nanoscale* **2011**, *3* (5), 2054-2073.
- (10) Baldauf, M.; Kolb, D. M. Formic Acid Oxidation on Ultrathin Pd Films on Au(Hkl) and Pt(Hkl) Electrodes. *J. Phys. Chem.* **1996**, *100* (27), 11375–11381.
- (11) Arenz, M.; Stamenkovic, V.; Schmidt, T. J.; Wandelt, K.; Ross, P. N.; Markovic, N. M. The Electro-Oxidation of Formic Acid on Pt-Pd Single Crystal Bimetallic Surfaces. *Phys. Chem. Chem. Phys.* **2003**, 5 (19), 4242-4251.
- (12) Jiang, K.; Zhang, H.-X.; Zou, S.; Cai, W.-B. Electrocatalysis of Formic Acid on Palladium and Platinum Surfaces: From Fundamental Mechanisms to Fuel Cell Applications. *Phys. Chem. Chem. Phys.* **2014**, *16* (38), 20360-20376.
- (13) Mazumder, V.; Chi, M.; Mankin, M. N.; Liu, Y.; Metin, Ö.; Sun, D.; More, K. L.; Sun, S. A Facile Synthesis of MPd (M = Co, Cu) Nanoparticles and Their Catalysis for Formic Acid Oxidation. *Nano Lett.* **2012**, *12* (2), 1102-1106.
- (14) Jin, M.; Zhang, H.; Xie, Z.; Xia, Y. Palladium Nanocrystals Enclosed by {100} and {111} Facets in Controlled Proportions and Their Catalytic Activities for Formic Acid Oxidation. *Energy Environ. Sci.* **2012**, *5* (4), 6352-6357.
- (15) Rizo, R.; Roldan Cuenya, B. Shape-Controlled Nanoparticles as Anodic Catalysts in Low-Temperature Fuel Cells. *ACS Energy Lett.* **2019**, *4* (6), 1484-1495.
- (16) Kibler, L. A.; El-Aziz, A. M.; Hoyer, R.; Kolb, D. M. Tuning Reaction Rates by Lateral Strain in a Palladium Monolayer. *Angew. Chem. Int. Ed.* **2005**, *44* (14), 2080-2084.

- (17) Llorca, M.; Feliu, J.; Aldaz, A.; Clavilier, J. Formic Acid Oxidation on Pd Ad+ Pt (100) and Pd Ad+ Pt (111) Electrodes. *J. Electroanal. Chem.* **1994**, 376 (1), 151-160.
- (18) Vidal-Iglesias, F.; Solla-Gullon, J.; Herrero, E.; Aldaz, A.; Feliu, J. Formic Acid Oxidation on Pd-Modified Pt (100) and Pt (111) Electrodes: A DEMS Study. J. Appl. Electrochem. **2006**, 36 (11), 1207-1214.
- (19) Arenz, M.; Stamenkovic, V.; Ross, P. N.; Markovic, N. M. Surface (Electro-)Chemistry on Pt(111) Modified by a Pseudomorphic Pd Monolayer. *Surf. Sci.* **2004**, *573* (1), 57-66.
- (20) Chen, X.; Koper, M. T. M. Mass-Transport-Limited Oxidation of Formic Acid on a PdMLPt(100) Electrode in Perchloric Acid. *Electrochem. Commun.* **2017**, *82*, 155-158.
- (21) Soriaga, M. P.; Stickney, J.; Bottomley, L. A.; Kim, Y.-G. *Thin Films: Preparation, Characterization, Applications*; Springer US, 2002.
- (22) Kortlever, R.; Balemans, C.; Kwon, Y.; Koper, M. T. M. Electrochemical CO2 Reduction to Formic Acid on a Pd-Based Formic Acid Oxidation Catalyst. *Catal. Today* **2015**, *244*, 58-62.
- (23) Min, X.; Kanan, M. W. Pd-Catalyzed Electrohydrogenation of Carbon Dioxide to Formate: High Mass Activity at Low Overpotential and Identification of the Deactivation Pathway. *J. Am. Chem. Soc.* **2015**, *137* (14), 4701–4708.
- (24) Chatterjee, S.; Griego, C.; Hart, J. L.; Li, Y.; Taheri, M. L.; Keith, J.; Snyder, J. D. Free Standing Nanoporous Palladium Alloys as CO Poisoning Tolerant Electrocatalysts for the Electrochemical Reduction of CO2 to Formate. *ACS Catal.* **2019**, *9* (6), 5290-5301.
- (25) Ryu, J.; Surendranath, Y. Polarization-Induced Local PH Swing Promotes Pd-Catalyzed CO2 Hydrogenation. *J. Am. Chem. Soc.* **2020**, *142* (31), 13384-13390.
- (26) Gao, D.; Zhou, H.; Cai, F.; Wang, J.; Wang, G.; Bao, X. Pd-Containing Nanostructures for Electrochemical CO2 Reduction Reaction. *ACS Catal.* **2018**, *8* (2), 1510-1519.
- (27) Koper, M. T. M. Thermodynamic Theory of Multi-Electron Transfer Reactions: Implications for Electrocatalysis. *J. Electroanal. Chem.* **2011**, 660 (2), 254–260.
- (28) Kortlever, R.; Peters, I.; Koper, S.; Koper, M. T. M. Electrochemical CO2 Reduction to Formic Acid at Low Overpotential and with High Faradaic Efficiency on Carbon-Supported Bimetallic Pd-Pt Nanoparticles. *ACS Catal.* **2015**, *5* (7), 3916–3923.
- (29) Koper, M. T. Blank Voltammetry of Hexagonal Surfaces of Pt-Group Metal Electrodes: Comparison to Density Functional Theory Calculations and Ultra-High Vacuum Experiments on Water Dissociation. *Electrochimica Acta* **2011**, *56* (28), 10645-10651.

- (30) Chen, X.; Granda-Marulanda, L. P.; McCrum, I. T.; Koper, M. T. M. Adsorption Processes on a Pd Monolayer-Modified Pt(111) Electrode. *Chem. Sci.* **2020**, *11* (6), 1703-1713.
- (31) Grozovski, V.; Vidal-Iglesias, F. J.; Herrero, E.; Feliu, J. M. Adsorption of Formate and Its Role as Intermediate in Formic Acid Oxidation on Platinum Electrodes. *ChemPhysChem* **2011**, *12* (9), 1641–1644.
- (32) Hoyer, R.; Kibler, L. A.; Kolb, D. M. The Initial Stages of Palladium Deposition onto Pt(1 1 1). *Electrochimica Acta* **2003**, *49* (1), 63–72.
- (33) López-Cudero, A.; Cuesta, A.; Gutiérrez, C. Potential Dependence of the Saturation CO Coverage of Pt Electrodes: The Origin of the Pre-Peak in CO-Stripping Voltammograms. Part 1: Pt(111). *J. Electroanal. Chem.* **2005**, *579* (1), 1-12.
- (34) Orts, J. M.; Fernández-Vega, A.; Feliu, J. M.; Aldaz, A.; Clavilier, J. Electrochemical Behaviour of CO Layers Formed by Solution Dosing at Open Circuit on Pt(111). Voltammetric Determination of CO Coverages at Full Hydrogen Adsorption Blocking in Various Acid Media. *J. Electroanal. Chem.* **1992**, *327* (1), 261-278.
- (35) Hara, M.; Linke, U.; Wandlowski, T. Preparation and Electrochemical Characterization of Palladium Single Crystal Electrodes in 0.1 M H2SO4 and HClO4: Part I. Low-Index Phases. *Electrochimica Acta* **2007**, *52* (18), 5733-5748.
- (36) Chen, Y. X.; Miki, A.; Ye, S.; Sakai, H.; Osawa, M. Formate, an Active Intermediate for Direct Oxidation of Methanol on Pt Electrode. *J. Am. Chem. Soc.* **2003**, *125* (13), 3680-3681.
- (37) Samjeské, G.; Miki, A.; Ye, S.; Osawa, M. Mechanistic Study of Electrocatalytic Oxidation of Formic Acid at Platinum in Acidic Solution by Time-Resolved Surface-Enhanced Infrared Absorption Spectroscopy. *J. Phys. Chem. B* **2006**, *110* (33), 16559-16566.
- (38) Pronkin, S.; Hara, M.; Wandlowski, T. Electrocatalytic Properties of Au(111)-Pd Quasi-Single-Crystal Film Electrodes as Probed by ATR-SEIRAS. *Russ. J. Electrochem.* **2006**, *42* (11), 1177–1192.
- (39) Miyake, H.; Okada, T.; Samjeské, G.; Osawa, M. Formic Acid Electrooxidation on Pd in Acidic Solutions Studied by Surface-Enhanced Infrared Absorption Spectroscopy. *Phys. Chem. Chem. Phys.* **2008**, *10* (25), 3662-3669.
- (40) Chen, Y. X.; Heinen, M.; Jusys, Z.; Behm, R. J. Kinetics and Mechanism of the Electrooxidation of Formic Acid–Spectroelectrochemical Studies in a Flow Cell. *Angew. Chem. Int. Ed.* **2006**, *45* (6), 981–985.
- (41) Xu, J.; Yuan, D.; Yang, F.; Mei, D.; Zhang, Z.; Chen, Y.-X. On the Mechanism of the Direct Pathway for Formic Acid Oxidation at a Pt(111) Electrode. *Phys. Chem. Chem. Phys.* **2013**, *15* (12), 4367-4376.

- (42) Rodes, A.; Pastor, E.; Iwasita, T. Structural Efects on CO2 Reduction at Pt Single-Crystal Electrodes: Part 2. Pt (111) and Vicinal Surfaces in the [011] Zone. *J. Electroanal. Chem.* **1994**, 373 (1-2), 167-175.
- (43) Hoshi, N.; Noma, M.; Suzuki, T.; Hori, Y. Structural Effect on the Rate of CO2 Reduction on Single Crystal Electrodes of Palladium. *J. Electroanal. Chem.* **1997**, *421* (1-2), 15-18.
- (44) Göttle, A. J.; Koper, M. T. M. Determinant Role of Electrogenerated Reactive Nucleophilic Species on Selectivity during Reduction of CO2 Catalyzed by Metalloporphyrins. *J. Am. Chem. Soc.* **2018**, *140* (14), 4826-4834.
- (45) Christmann, K.; Ertl, G.; Pignet, T. Adsorption of Hydrogen on a Pt(111) Surface. Surf. Sci. **1976**, 54 (2), 365-392.
- (46) Bohra, D.; Ledezma-Yanez, I.; Li, G.; de Jong, W.; Pidko, E. A.; Smith, W. A. Lateral Adsorbate Interactions Inhibit HCOO– While Promoting CO Selectivity for CO2 Electrocatalysis on Silver. *Angew. Chem. Int. Ed.* **2019**, *58* (5), 1345-1349.
- (47) Cuesta, A.; Escudero, M.; Lanova, B.; Baltruschat, H. Cyclic Voltammetry, FTIRS, and DEMS Study of the Electrooxidation of Carbon Monoxide, Formic Acid, and Methanol on Cyanide-Modified Pt (111) Electrodes. *Langmuir* **2009**, *25* (11), 6500-6507.
- (48) Clavilier, J.; Armand, D.; Sun, S. G.; Petit, M. Electrochemical Adsorption Behaviour of Platinum Stepped Surfaces in Sulphuric Acid Solutions. *J. Electroanal. Chem. Interfacial Electrochem.* **1986**, 205 (1), 267-277.
- (49) Álvarez, B.; Berná, A.; Rodes, A.; Feliu, J. M. Electrochemical Properties of Palladium Adlayers on Pt(100) Substrates. *Surf. Sci.* **2004**, *573* (1), 32-46.
- (50) Kwon, Y.; Koper, M. T. Combining Voltammetry with HPLC: Application to Electro-Oxidation of Glycerol. *Anal. Chem.* **2010**, *82* (13), 5420-5424.
- (51) Kresse, G.; Joubert, D. From Ultrasoft Pseudopotentials to the Projector Augmented-Wave Method. *Phys. Rev. B* **1999**, *59* (3), 1758-1775.
- (52) Kresse, G.; Furthmüller, J. Efficient Iterative Schemes for Ab Initio Total-Energy Calculations Using a Plane-Wave Basis Set. *Phys. Rev. B* **1996**, *54* (16), 11169-11186.
- (53) Perdew, J. P.; Burke, K.; Ernzerhof, M. Generalized Gradient Approximation Made Simple. *Phys. Rev. Lett.* **1996**, *77* (18), 3865-3868.
- (54) Methfessel, M.; Paxton, A. T. High-Precision Sampling for Brillouin-Zone Integration in Metals. *Phys. Rev. B* **1989**, *40* (6), 3616-3621.
- (55) Nørskov, J. K.; Rossmeisl, J.; Logadottir, A.; Lindqvist, L.; Kitchin, J. R.; Bligaard, T.; Jónsson, H. Origin of the Overpotential for Oxygen Reduction at a Fuel-Cell Cathode. *J. Phys. Chem. B* **2004**, *108* (46), 17886-17892.
- (56) Granda-Marulanda, L. P.; Rendón-Calle, A.; Builes, S.; Illas, F.; Koper, M. T. M.; Calle-Vallejo, F. A Semiempirical Method to Detect and Correct DFT-Based Gas-Phase Errors and Its Application in Electrocatalysis. ACS Catal. 2020, 10 (12), 6900-6907.





A: Supporting Information for Chapter 2

In Figure A1 we show that the PBE-calculated¹ d-band center of the Pt skin on the near-surface alloys studied here linearly correlates with the number of valence electrons of the metals along the 3d, 4d and 5d series. It was previously shown that valence electrons correlate linearly with the d-band centers of various transition metals.¹²

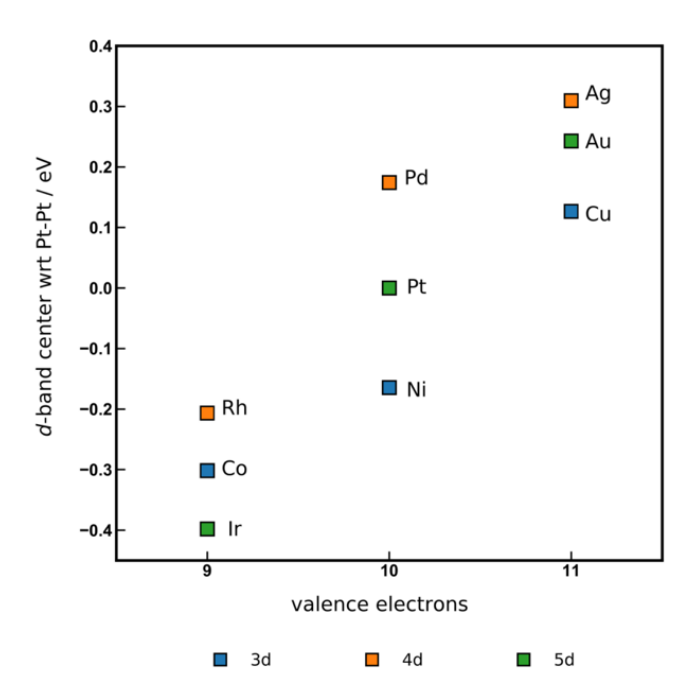


FIGURE A1

D-band center of the Pt skin on the NSAs with respect to the d-band center of the top layer of Pt(111) as a function of the valence electrons of the subsurface metals. A nearly linear correlation between the d-band center and the valence electrons for various metals along the 3d (Co, Ni, Cu), 4d (Rh, Pd, Ag), and 5d (Ir, Pt, Au) series is observed, in line with previous reports.^{1,3}

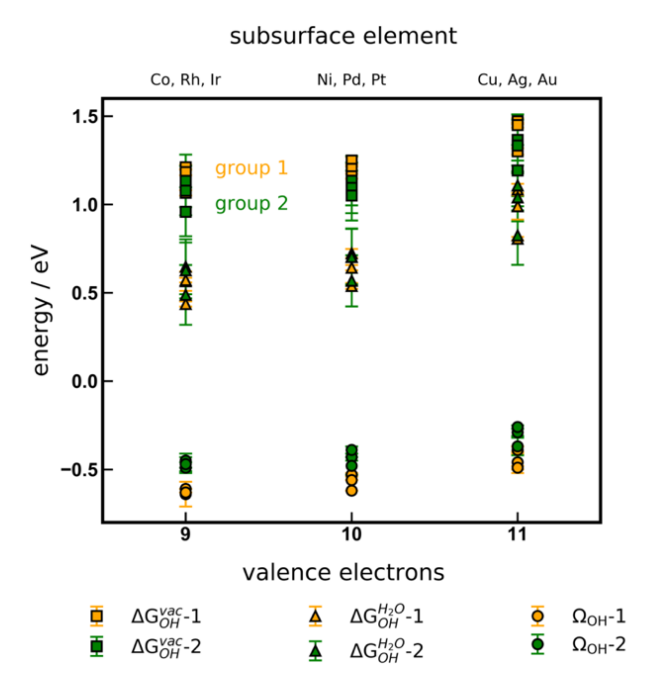


FIGURE A2

Adsorption energies of group 1 functionals (PBE/ PW91) in orange and group 2 functionals (RPBE, vdW and with dispersion corrections) in green as a function of the number of valence electrons of the subsurface metal atom in the Pt NSAs. For both groups, squares represent the energies of 1/3 ML *OH in vacuum (ΔG_{OH}^{vac}) triangles represent the energies of *OH within the water bilayer ($\Delta G_{OH}^{H_2O}$), and circles represent the solvation energy (Ω_{OH}). Solvation energies for group 2 (green) are generally less negative than those of group 1 (orange). The error bars cover the standard deviation of the respective groups of functionals. The correlation between the number of valence electrons and the d-band centers of the Pt skins is provided in Figure A1.

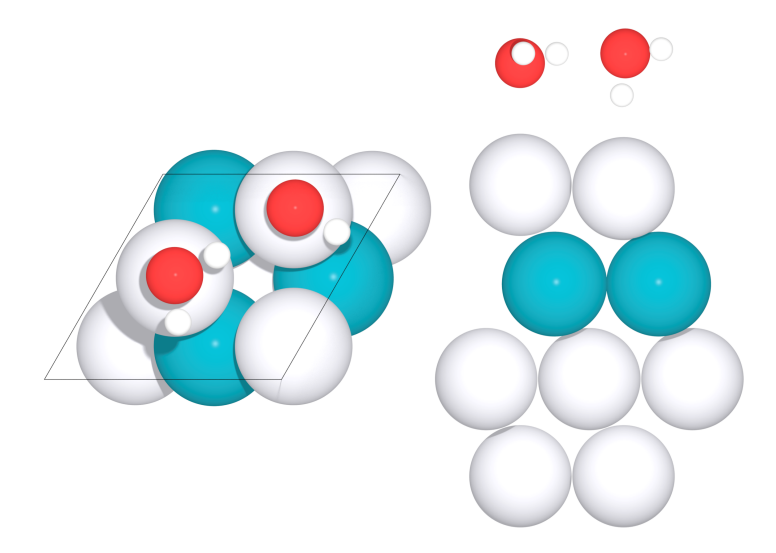


FIGURE A3

Top and side view of the water adlayer on a $\sqrt{3} \times \sqrt{3}$ R30° unit cell of Pt (111) NSA. The cell contains 3 metals per atom layer, and 2 water molecules per unit cell. The water molecules are on top of a Pt metal. One water molecule is on the flat configuration and the other one with one hydrogen pointing towards the surface as shown in the side view.

The water adlayer shown in Figure A3 is the ice-like water adlayer structure found to be computationally stable in closed-packed metal surfaces. ⁴⁻⁶ This water adlayer of 2/3 ML coverage can be adsorbed with one water molecule in the flat configuration while the other water molecule can be with one hydrogen pointing towards the surface (H-down) or away from it (H-up). The difference in energy between these two configurations is small, about 0.05 eV as reported in the literature based on DFT adsorption energies. ^{4,7} Our calculated free energies of adsorption of the water adlayer on Pt(111) show a difference of 0.01 eV between the H-up and H-down configuration being the H-down configuration more stable.

TABLE A1

Free energies of solvation (Ω_{OH}) in eV for 1/3 ML *OH coadsorbed with 1/3 ML *H₂O within a water bilayer using different functionals. Avg1 and avg2 are the averages of the solvation energies for group 1 functionals (PBE, PW91) and group 2 functionals (RPBE, vdW and dispersion corrections) across the same metal. Stdev1/2 are the corresponding standard deviations of avg1/avg2. Avg0 is the average of the solvation energies across the metals for all the functionals and stdev0 is its standard deviation. MAX and MIN are the maximal and minimal values in the dataset across the same functional. Range is the difference between MAX and MIN.^a

metal	PW91	PBE	RPBE	PBE- D3	RPBE- D3	Opt- PBE	BEEF- vdw	avg 0	avg 1	avg 2	stdev 0	stdev 1	stdev 2
Со	-0.60	-0.69	-0.50	-0.45	-	-0.52	-0.48	-0.54	-0.64	-0.49	0.09	0.07	0.03
Rh	-0.61	-0.61	-0.45	-0.47	-0.48	-0.47	-0.39	-0.50	-0.61	-0.45	0.08	0.00	0.04
Ir	-0.63	-0.63	-0.43	-0.50	-0.50	-0.49	-0.43	-0.52	-0.63	-0.47	0.08	0.00	0.04
Ni	-0.53	-0.52	-0.40	-0.43	-0.45	-0.43	-0.44	-0.46	-0.53	-0.43	0.05	0.01	0.02
Pd	-0.56	-0.56	-0.36	-0.40	-0.41	-0.40	-0.39	-0.44	-0.56	-0.39	0.08	0.00	0.02
Pt	-0.62	-0.62	-0.50	-0.45	-0.57	-0.45	-0.44	-0.52	-0.62	-0.48	0.08	0.00	0.05
Cu	-0.50	-0.42	-0.32	-0.31	-0.27	-0.29	-0.28	-0.34	-0.46	-0.29	0.09	0.06	0.02
Ag	-0.40	-0.38	-0.26	-0.25	-0.27	-0.25	-0.27	-0.30	-0.39	-0.26	0.06	0.02	0.01
Au	-0.49	-0.50	-0.35	-0.35	-0.46	-0.35	-0.33	-0.40	-0.49	-0.37	0.08	0.01	0.05
mean	-0.55	-0.55	-0.39	-0.40	-0.43	-0.41	-0.38						
stdev	0.08	0.10	0.08	0.08	0.11	0.09	0.07						
MAX	-0.40	-0.38	-0.26	-0.25	-0.27	-0.25	-0.27						
MIN	-0.63	-0.69	-0.50	-0.50	-0.57	-0.52	-0.48						
range	0.23	0.32	0.24	0.25	0.30	0.27	0.21						
LNDm	-0.08	-0.15	-0.10	-0.10	-0.14	-0.11	-0.10						
LPDm	0.15	0.17	0.14	0.16	0.16	0.16	0.11						
LPDPt	0.22	0.24	0.24	0.21	0.30	0.21	0.17						
LNDPt	-0.01	-0.07	0.00	-0.04	0.00	-0.06	-0.04						
AOM					-0.44			-					
Stdev AOM				0.07									

Stdev AOM	0.07
LND _{AOM}	-0.10
LPD _{AOM}	0.06
avg1 across functionals	-0.55
avg2 across functionals	-0.40
Diff avg1 - avg2 across functionals	0.15
Diff avg1 - avg2 across metals	0.14

[a] LNDm/LPDm: Largest negative/positive deviation from the mean LNDPt/LPDPt: Largest negative/positive deviation from Pt

AOM: Average of the means Standard deviation of AOM

 LND_{AOM}/LPD_{AOM} : Largest negative/positive deviation from the AOM

TABLE A2

Adsorption energies in eV of 1/3 ML *OH in vacuum (ΔG_{OH}^{vac}). avg1 and avg2 are the averages of the solvation energies for group 1 functionals (PBE, PW91) and group 2 functionals (RPBE, vdW and with dispersion corrections) across the same metal. Stdev1/2 are the corresponding standard deviations of avg1/avg2. Avg0 is the average of the solvation energies across the metals for all the functionals and stdev0 is its standard deviation.

metal	PW91	PBE	RPBE	PBE-D3	RPBE-D3	optPBE	BEEF-vdw	avg0	avg1	avg2	stdev0	stdev1	stdev2
Со	1.20	1.22	1.33	1.11	_	0.97	1.12	1.16	1.21	1.13	0.12	0.01	0.15
CO	1.20	1.22	1.55	1.11		0.77	1.12	1.10	1.21	1.13	0.12	0.01	0.13
Rh	1.17	1.19	1.31	1.03	1.02	0.94	1.10	1.11	1.18	1.08	0.13	0.02	0.14
Ir	1.05	1.08	1.19	0.91	0.89	0.82	0.98	0.99	1.07	0.96	0.12	0.02	0.14
Ni	1.23	1.26	1.36	1.08	1.08	0.99	1.15	1.17	1.25	1.13	0.13	0.02	0.14
Pd	1.19	1.21	1.33	1.04	1.04	0.96	1.11	1.12	1.20	1.09	0.13	0.01	0.14
Pt	1.15	1.17	1.28	0.99	0.99	0.91	1.07	1.08	1.16	1.05	0.13	0.01	0.14
Cu	1.44	1.46	1.57	1.28	1.24	1.20	1.37	1.37	1.45	1.33	0.13	0.01	0.15
Ag	1.46	1.48	1.60	1.31	1.29	1.23	1.40	1.40	1.47	1.37	0.13	0.02	0.14
Au	1.29	1.31	1.43	1.14	1.13	1.05	1.22	1.22	1.30	1.19	0.13	0.02	0.15

TABLE A3

Adsorption energies in eV of 1/3 ML *OH coadsorbed with 1/3ML *H2O ($\Delta G_{OH}^{H_2O}$). Avg1 and avg2 are the averages of the solvation energies for group 1 functionals (PBE, PW91) and group 2 functionals (RPBE, vdW and with dispersion corrections) across the same metal. Stdev1/2 are the corresponding standard deviations of avg1/avg2. Avg0 is the average of the solvation energies across the metals for all the functionals and stdev0 is its standard deviation.

metal	PW91	PBE	RPBE	PBE-D3	RPBE-D3	optPBE	BEEF-vdw	avg0	avg1	avg2	stdev0	stdev1	stdev2
Со	0.60	0.53	0.83	0.66	-	0.45	0.64	0.62	0.57	0.65	0.13	0.05	0.16
Rh	0.56	0.58	0.86	0.55	0.54	0.47	0.72	0.61	0.57	0.63	0.13	0.01	0.16
Ir	0.43	0.45	0.76	0.41	0.39	0.34	0.55	0.47	0.44	0.49	0.14	0.01	0.17
Ni	0.70	0.74	0.97	0.65	0.63	0.56	0.72	0.71	0.72	0.70	0.13	0.03	0.16
Pd	0.63	0.65	0.97	0.64	0.63	0.55	0.73	0.69	0.64	0.70	0.14	0.02	0.16
Pt	0.53	0.55	0.78	0.54	0.43	0.46	0.63	0.56	0.54	0.57	0.12	0.02	0.15
Cu	0.94	1.04	1.25	0.97	0.97	0.91	1.09	1.03	0.99	1.04	0.12	0.08	0.14
Ag	1.06	1.11	1.34	1.07	1.03	0.98	1.13	1.10	1.08	1.11	0.12	0.03	0.14
Au	0.80	0.81	1.08	0.79	0.66	0.70	0.89	0.82	0.81	0.82	0.14	0.01	0.17

TABLE A4Normalized adsorption energies in eV/H₂O molecule of 2/3 ML water adlayer on the Pt NSAs for the different functionals studied $(2*+2*H_2O(1) \rightarrow 2*H_2O, \Delta G_{H_2O})$.

metal	PW91	PBE	RPBE	PBE-D3	RPBE-D3	optPBE	BEEF-vdw
Со	0.07	0.15	0.24	-0.09	=	-0.01	0.11
Rh	0.10	0.12	0.23	-0.10	-0.01	-0.02	0.08
Ir	0.10	0.12	0.21	-0.10	-0.01	-0.02	0.09
Ni	0.08	0.10	0.23	-0.09	0.00	-0.01	0.13
Pd	0.10	0.13	0.21	-0.10	-0.02	-0.03	0.11
Pt	0.10	0.13	0.24	-0.11	-0.02	-0.03	0.11
Ag	0.09	0.10	0.22	-0.12	-0.02	-0.04	0.10
Au	0.09	0.12	0.23	-0.11	-0.02	-0.03	0.10
Cu	0.12	0.11	0.23	-0.10	-0.03	-0.03	0.09

TABLE A5Distances in Å between the oxygen of the water lying flat within the 2/3 ML water adlayer and the nearest Pt atom for the different functionals studied.

metal	PW91	PBE	RPBE	PBE-D3	RPBE-D3	optPBE	BEEF-vdw
Со	3.46	3.52	4.26	2.74	-	2.78	3.84
Rh	3.03	3.05	4.38	2.69	2.77	3.00	3.49
Ir	3.00	3.03	4.53	2.62	2.72	2.99	3.49
Ni	3.43	3.47	4.36	2.71	2.77	2.85	3.71
Pd	2.88	2.91	4.64	2.67	2.75	2.98	3.29
Pt	2.82	2.89	4.73	2.66	2.74	2.96	3.26
Ag	3.05	3.10	4.49	2.91	2.89	3.06	3.27
Au	2.97	3.02	4.46	2.79	2.81	2.98	3.21
Cu	3.31	3.32	4.46	2.87	2.85	3.13	3.74

TABLE A6 Distance in Å between the oxygen of the water lying flat in the 1/3 ML *OH coadsorbed with 1/3 ML $_2$ O and the nearest Pt atom.

metal	PW91	PBE	RPBE	PBE-D3	RPBE-D3	optPBE	BEEF-vdw
Со	2.27	2.27	2.32	2.25	-	2.29	2.34
Rh	2.25	2.25	2.31	2.25	2.28	2.28	2.33
Ir	2.23	2.23	2.28	2.23	2.26	2.26	2.30
Ni	2.27	2.27	2.33	2.27	2.30	2.30	2.35
Pd	2.25	2.26	2.32	2.25	2.29	2.28	2.33
Pt	2.23	2.23	2.28	2.22	2.27	2.25	2.30
Cu	2.34	2.33	2.43	2.32	2.37	2.37	2.46
Ag	2.34	2.35	2.49	2.33	2.40	2.39	2.48
Au	2.28	2.28	2.37	2.27	2.31	2.32	2.40

TABLE A7Zero point energies (ZPEs) in eV for molecules in the gas phase.

	-	-
PW91	0.269	0.568
PBE	0.268	0.568
RPBE	0.270	0.568
PBE-D3	0.268	0.568
RPBE-D3	0.270	0.567
optPBE	0.271	0.566
BEEF-vdw	0.277	0.577

TABLE A8Optimized lattice constants (a) in Å for bulk Pt.

Functional	a
PW91	3.99
PBE	3.98
RPBE	4.00
PBE-D3	3.93
RPBE-D3	3.95
optPBE	4.00
BEEF-vdw	4.00

References:

- (1) Calle-Vallejo, F.; Martínez, J. I.; García-Lastra, J. M.; Rossmeisl, J.; Koper, M. T. M. Physical and Chemical Nature of the Scaling Relations between Adsorption Energies of Atoms on Metal Surfaces. *Phys. Rev. Lett.* **2012**, *108* (11), 116103.
- (2) Su, H.-Y.; Sun, K.; Wang, W.-Q.; Zeng, Z.; Calle-Vallejo, F.; Li, W.-X. Establishing and Understanding Adsorption-Energy Scaling Relations with Negative Slopes. *J. Phys. Chem. Lett.* **2016**, *7* (24), 5302-5306.
- (3) He, Z.-D.; Hanselman, S.; Chen, Y.-X.; Koper, M. T. M.; Calle-Vallejo, F. Importance of Solvation for the Accurate Prediction of Oxygen Reduction Activities of Pt-Based Electrocatalysts. *J. Phys. Chem. Lett.* **2017**, *8* (10), 2243-2246.
- (4) Schnur, S.; Groß, A. Properties of Metal-Water Interfaces Studied from First Principles. *New J. Phys.* **2009**, *11* (12), 125003.
- (5) Ogasawara, H.; Brena, B.; Nordlund, D.; Nyberg, M.; Pelmenschikov, A.; Pettersson, L. G. M.; Nilsson, A. Structure and Bonding of Water on Pt(111). *Phys. Rev. Lett.* **2002**, *89* (27), 276102.
- (6) Michaelides, A.; Hu, P. Catalytic Water Formation on Platinum: A First-Principles Study. J. Am. Chem. Soc. **2001**, 123 (18), 4235-4242.
- (7) Michaelides, A.; Alavi, A.; King, D. A. Insight into H_2O -Ice Adsorption and Dissociation on Metal Surfaces from First-Principles Simulations. *Phys. Rev. B* **2004**, *69* (11), 113404.

B: Supporting Information for Chapter 3

TABLE B 1Calculated change in work function $\Delta \phi$, change in surface dipole $\Delta \mu$, distance between surface and adsorbates r, Bader partial charges |q|, and free energies of adsorption, of Cl, Br, I, SO_4 -sol/ SO_4 with and without solvation on Pt(111) and Au(111).

adsorbate	$\Delta\phi$ / eV		$\Delta \mu /\ e ext{\AA}$		r/ Å		q / e-		Gads/ eV	
	Pt	Au	Pt	Au	Pt	Au	Pt	Au	Pt	Au
Cl	-0.22	0.40	-0.07	0.13	2.52	2.71	-0.27	-0.39	0.55	0.92
Br	-0.45	0.23	-0.15	0.07	2.63	2.82	-0.12	-0.27	0.18	0.58
1	-0.81	-0.10	-0.27	-0.05	2.72	2.93	0.13	-0.09	-0.52	0.04
SO ₄	1.38	2.27	0.47	0.82	2.11	2.22	-0.85	-1.03	0.83	1.51
SO ₄ -sol	2.36	3.17	0.79	1.13	2.32	2.51	-0.97	-1.11	0.56	0.82

TABLE B 2

DFT simulated and experimentally measured adsorption potentials $^{1-3}$ in V vs SHE of I*, Br*, Cl*, and SO₄* on Pt(111) and Au(111) as well as OH* and the first and second monolayers of Ag* on Pt(111). The simulated adsorption potentials include dipole corrections and electrode-electrolyte interfacial field contribution using the experimental PZC of 0.3 and 0.51 V vs SHE for Pt(111) and Au(111). 4 SO₄* is solvated by displacing 2 water molecules from a 6 water adsorbed bilayer (leaving 4 water molecules with SO₄*) and OH* is solvated by removing a proton from a 3 water cluster (leaving 2 water molecules with OH*).

adsorbate	Pt(111)	Au	(111)
	DFT	Ехр	DFT	Ехр
Cl	0.55	0.30	0.92	0.44
Br	0.18	0.12	0.58	0.14
1	-0.52	-0.41	0.04	-0.26
SO ₄	0.83	0.48	1.51	0.74
SO ₄ -sol	0.56	0.48	0.82	0.74
OH-vac	1.15	0.60		
OH-sol	0.61	0.60		
Ag 1ML	0.99	1.22		
Ag 2ML	0.68	0.77		

TABLE B 3

DFT calculated adsorption potentials, U_{SHE} , with dipole corrections (μ corr) using the experimental PZC of Pt/Au (0.3/0.51 V) ⁴ and at PZC = 0 V vs SHE, and without dipole corrections (No μ corr). Diff 1 Pt/Au is the difference between the columns (No μ corr) and (μ corr / PZC Pt/Au, respectively. Diff 2 is the difference between the columns (No μ corr) and (μ corr / PZC=0 V).

Pt(111)

adsorbate	μ corr / PZC=0.3 V	μ corr/ PZC=0 V	No μ corr	Diff 1Pt	Diff2
Cl	0.55	0.54	0.55	0.01	0.01
Br	0.18	0.17	0.18	-0.01	0.01
1	-0.52	-0.54	-0.59	-0.07	-0.05
SO4	0.83	0.86	0.79	-0.04	-0.07
SO ₄ -sol	0.56	0.60	0.54	-0.03	-0.06
OH vac	1.15	1.15	1.14	-0.01	-0.01
OH-sol	0.61	0.59	0.63	0.02	0.04
Ag 1ML	0.99	0.99	0.97	-0.01	-0.01
Ag 2ML	0.68	0.68	0.68	0.00	0.00
		Au(111)			
	μ corr / PZC=0.51 V	μ corr / PZC=0 V	No μ corr	Diff 1Au	Diff2
Cl	0.92	0.94	0.90	-0.02	-0.04
Br	0.58	0.59	0.58	0.00	-0.01
I	0.04	0.03	0.03	-0.01	0.00
SO ₄	1.51	1.58	1.37	-0.14	-0.22
SO ₄ -sol	0.82	0.91	0.78	-0.05	-0.13

References:

- (1) Garcia-Araez, N.; Climent, V.; Herrero, E.; Feliu, J.; Lipkowski, J. Thermodynamic Studies of Bromide Adsorption at the Pt(111) Electrode Surface Perchloric Acid Solutions: Comparison with Other Anions. J. Electroanal. Chem. 2006, 591 (2), 149-158.
- (2) Lipkowski, J.; Shi, Z.; Chen, A.; Pettinger, B.; Bilger, C. Ionic Adsorption at the Au(111) Electrode. *Electrochimica Acta* **1998**, 43 (19), 2875–2888.
- (3) Hachiya, T.; Itaya, K. In Situ Scanning Tunneling Microscopy of Underpotential Deposition in Aqueous Solution III. Silver Adlayers on Au(111). *Ultramicroscopy* **1992**, *42-44*, 445-452.
- (4) Ojha, K.; Arulmozhi, N.; Aranzales, D.; Koper, M. T. M. Double Layer at the Pt(111)-Aqueous Electrolyte Interface: Potential of Zero Charge and Anomalous Gouy-Chapman Screening. *Angew. Chem. Int. Ed.* **2020**, *59* (2), 711-715.

C: Supporting Information for Chapter 4

C.1	P SLANE-WAVE CUTOFF CONVERGENCE TEST	142
C.2	PATA SET A	142
C.3	DATA SET B	144
	PINPOINTING ERRORS	
	.1 PBE	
•	C.4.1.1 -CH _x errors in PBE	
	C.4.1.2C=O- errors in PBE	
	C.4.1.3(C=O)O- ERRORS IN PBE	151
	C.4.1.4. –OH ERRORS IN PBE	
C.4	l.2. PW91	153
	C.4.2.1CH _x IN PW91	
	C.4.2.2C=O- IN PW91	
	C.4.2.3. –(C=O)O- ERRORS IN PW91	
	C.4.2.4. –OH ERRORS IN PW91	
C.4	l.3. RPBE	155
	C.4.3.1CH _x errors in RPBE	
	C.4.3.2. –C=O- ERRORS IN RPBE	155
	C.4.3.3. –(C=O)O- ERRORS IN RPBE	156
	C.4.3.4. –OH ERRORS IN RPBE	156
C.4	.4. BEEF-vdW	157
	C.4.4.1CH _x errors in BEEF-vdW	157
	C.4.4.2. –C=O- ERRORS IN BEEF-VDW	157
	C.4.4.3(C=O)O- ERRORS IN BEEF-VDW	158
	C.4.4.4. –OH ERRORS IN BEEF-VDW	159
	C.4.4.5. H ₂ errors in BEEF-vdW	159
C.5	ELECTROCATALYSIS-RELATED DATA	161
C.6	INTERLAYER COHESIVE ENERGY IN GRAPHITE	165
	ALTERNATIVE ANALYSIS USING TRAINING AND EXTRAPOLATION SETS	
	REFERENCES	
	, 	····· - / -

C.1 Plane-wave cutoff convergence test

Table C1 shows the results of a plane-wave cutoff test made to ensure that the results provided here do not strongly depend on the use of plane waves as a basis set and that 400 eV suffices to provide converged results.

TABLE C1

Plane-wave energy cutoff test (ENCUT, in eV) as for PBE, based on the free energy (ΔG_{DFT} , in eV) of $CO_2 + H_2 \rightarrow CO + H_2O$ from 300 eV to 1000 eV. The values under Diff (in eV) are the difference between successive higher and smaller plane-wave energy cutoffs.

ENCUT	ΔG_{DFT}	Diff
300	0.74	
350	0.73	-1.10×10 ⁻²
400	0.73	-2.46×10 ⁻³
500	0.74	1.17×10 ⁻²
600	0.74	-4.07×10 ⁻⁴
700	0.71	-3.18×10 ⁻²
800	0.72	1.69×10 ⁻²
900	0.71	-1.54×10 ⁻²
1000	0.70	-3.66×10 ⁻³

C.2 Data set A

In Table C2 we provide the calculated and experimental formation energies of the 27 compounds under study. The energies are calculated with respect to $H_2(g)$, $O_2(g)$, and C(s), modelled as graphene (see section 6). $O_2(g)$ energetics was corrected to obtain the values in Table C2, as its poor description by most xcfunctionals is well known.¹ The semiempirical approach is based on $H_2(g)$, $H_2O(1)$, and the energetics of $2H_2 + O_2 \rightarrow 2H_2O$, as described in previous works.^{1-42,3} For PBE, the gas-phase correction is -0.46 eV. If that correction is not applied, the average deviation in Data set A from experiments is 0.21 eV for PBE and all deviations are positive, corroborating previous observations on formation energies in which diatomic molecules are involved.⁴

TABLE C2

Standard free energies of formation (ΔG_{DFT}° , in eV) for 27 gas-phase molecules calculated with PBE, PW91, RPBE, and BEEF-vdW xc-functionals, together with the corresponding experimental values from thermodynamic tables.⁵⁻⁷

Compound	PBE	PW91	RPBE	BEEF-vdW	exp
СО	-1.18	-1.17	-1.50	-1.60	-1.42
CO_2	-4.27	-4.23	-4.55	-4.65	-4.09
CH2O (formaldehyde)	-1.13	-1.14	-1.27	-1.27	-1.06
CH_4 (methane)	-0.51	-0.55	-0.46	-0.27	-0.52
CH ₄ O (methanol)	-1.72	-1.75	-1.67	-1.59	-1.68
CH_2O_2 (formic acid)	-3.83	-3.82	-3.92	-3.98	-3.64
$C_2H_2O_2$ (glyoxal)	-2.13	-2.14	-2.39	-2.46	-1.97
$C_2H_4O_2$ (acetic acid)	-4.03	-4.05	-4.04	-4.02	-3.88
$C_2H_4O_2$ (methyl formate)	-3.31	-3.34	-3.34	-3.36	-3.11
C_2H_4 (ethylene)	0.75	0.69	0.68	0.88	0.71
C_2H_4O (ethylene oxide)	-0.31	-0.32	-0.34	-0.19	-0.13
C_2H_4O (acetaldehyde)	-1.46	-1.50	-1.53	-1.42	-1.38
C_2H_6 (ethane)	-0.29	-0.36	-0.21	0.08	-0.33
C_2H_6O (ethanol)	-1.74	-1.80	-1.63	-1.47	-1.74
C_2H_6O (dimethyl ether)	-1.21	-1.27	-1.10	-0.97	-1.17
C_2H_2 (acetylene)	2.29	2.25	2.06	2.21	2.18
C_3H_8 (propane)	-0.17	-0.26	-0.01	0.34	-0.24
C_3H_6O (acetone)	-1.65	-1.71	-1.64	-1.45	-1.58
C_3H_8O (isopropanol)	-1.73	-1.81	-1.52	-1.30	-1.80
C_3H_8O (propanol)	-1.61	-1.69	-1.41	-1.18	-1.66
C_3H_6O (propanal)	-1.36	-1.42	-1.35	-1.18	-1.28
C_3H_6O (propylene oxide)	-0.43	-0.46	-0.38	-0.16	-0.29
$C_3H_6O_2$ (methyl acetate)	-3.51	-3.56	-3.46	-3.40	-3.39
C_4H_8O (butanal)	-1.19	-1.27	-1.13	-0.88	-1.18
C_4H_{10} (butane)	-0.05	-0.16	0.18	0.59	-0.19
$C_4H_{10}O$ (butanol)	-1.48	-1.58	-1.22	-0.93	-1.56
C_5H_{12} (pentane)	0.09	-0.06	0.38	0.85	-0.09

C.3 Data set B

In the following tables we provide the reaction energies calculated for the formation of molecules in data set A from co₂ (Table C3) and CO (Table C4). in the free energies of reaction in Tables C3 and C4, we used gas-phase water, H₂O(g).

TABLE C3

Data set containing free energies of reaction (in eV) for the PBE, PW91, RPBE, BEEF-vdW xc-functionals together with the corresponding experimental values. The data set contains the free energies of reaction from $CO_2(g)$ and $H_2(g)$ and producing the specific substance in parentheses and $H_2O(g)$, when needed.

Reaction	PBE	PW91	RPBE	BEEF-vdW	Exp
$CO_2 + H_2 \rightarrow CO + H_2O$	0.73	0.69	0.68	0.68	0.30
$CO_2 + H_2 \rightarrow HCOOH$	0.45	0.41	0.63	0.67	0.45
$CO_2 + 2 H_2 \rightarrow CH_2O + H_2O$ (formaldehyde)	0.78	0.73	0.91	1.01	0.66
$CO_2 + 3 H_2 \rightarrow CH_3OH + H_2O $ (methanol)	0.18	0.11	0.51	0.69	0.04
$CO_2 + 4 H_2 \rightarrow CH_4 + 2 H_2O$ (methane)	-0.97	-1.05	-0.65	-0.36	-1.17
$2 CO_2 + 6 H_2 \rightarrow C_2H_4 + 4 H_2O$ (ethylene)	-0.18	-0.32	0.30	0.70	-0.59
$2 CO_2 + 3 H_2 \rightarrow C_2H_2O2 + 2 H_2O (glyoxal)$	1.68	1.59	1.97	2.10	1.47
$2 CO_2 + 4 H_2 \rightarrow C_2H_4O2 + 2 H_2O$ (acetic acid)	-0.22	-0.32	0.32	0.54	-0.44
$2 CO_2 + 4 H_2 \rightarrow C_2H_4O2 + 2 H_2O$ (methyl formate)	0.50	0.39	1.02	1.19	0.33
$2 CO_2 + 5 H_2 \rightarrow C_2H_4O + 3 H_2O$ (eth. oxide)	1.13	1.04	1.65	2.00	0.93
$2 CO_2 + 5 H_2 \rightarrow C_2H_4O + 3 H_2O$ (acetaldehyde)	-0.02	-0.14	0.46	0.77	-0.31
$2 CO_2 + 5 H_2 \rightarrow C_2H_2 + 4 H_2O$ (acetylene)	1.37	1.24	1.68	2.02	0.87
$2 CO_2 + 6 H_2 \rightarrow C_2 H_6 O + 3 H_2 O $ (ethanol)	-0.30	-0.44	0.36	0.72	-0.67
$2 CO_2 + 6 H_2 \rightarrow C_2H6O + 3 H_2O$ (dimethyl ether)	0.23	0.09	0.89	1.22	-0.10
$2 CO_2 + 7 H_2 \rightarrow C_2H_6 + 4 H_2O$ (ethane)	-1.22	-1.37	-0.58	-0.10	-1.63
$3 CO_2 + 8 H_2 \rightarrow C_3H_6O + 5 H_2O (acetone)$	-0.68	-0.86	0.16	0.65	-1.17
$3 CO_2 + 9 H_2 \rightarrow C_3H_8O + 5 H_2O $ (isopropanol)	-0.75	-0.96	0.29	0.80	-1.38
$3 CO_2 + 10 H_2 \rightarrow C_3H_8 + 6 H_2O$ (propane)	-1.56	-1.77	-0.58	0.07	-2.20
$3 CO_2 + 9 H_2 \rightarrow C_3H_8O + 5 H_2O (1-propanol)$	-0.63	-0.83	0.39	0.91	-1.24
$3 CO_2 + 8 H_2 \rightarrow C_3H_6O + 3 H_2O (propanal)$	-0.38	-0.56	0.45	0.92	-0.87
$3 CO_2 + 8 H_2 \rightarrow C_3H_6O + 5 H_2O$ (propylene oxide)	0.55	0.39	1.42	1.93	0.13
$3 CO_2 + 7 H_2 \rightarrow C_3H_6O2 + 4 H_2O$ (methyl acetate)	-0.17	-0.34	0.71	1.06	-0.60
$4 CO_2 + 11 H_2 \rightarrow C_4H_8O + 7 H_2O $ (butanal)	-0.67	-0.92	0.49	1.12	-1.42
$4 CO_2 + 13 H_2 \rightarrow C_4 H_{10} + 8 H_2 O (butane)$	-1.91	-2.18	-0.58	0.23	-2.79
$4 CO_2 + 12 H_2 \rightarrow C_4 H_{10}O + 7 H_2 O (1-but anol)$	-0.96	-1.23	0.39	1.07	-1.79
$5 CO_2 + 16 H_2 \rightarrow C_5 H_{12} + 10 H_2 O (pentane)$	-2.24	-2.58	-0.56	0.40	-3.34

Data set containing free energies of reaction (in eV) for the PBE, PW91, RPBE, BEEF-vdW xc-functionals together with the corresponding experimental values. The table contains free energies of reaction from CO(g) and $H_2(g)$ and producing the specific substance in parentheses and $H_2O(g)$, when needed. Only for formic acid, the product is obtained from CO(g) and $H_2O(g)$.

Reaction	PBE	PW91	RPBE	BEEF-vdW	Exp
$CO + H_2O \rightarrow CO_2 + H_2$	-0.73	-0.69	-0.68	-0.68	-0.30
$CO + H_2O \rightarrow HCOOH$ (formic acid)	-0.28	-0.28	-0.05	-0.01	0.15
$CO+ H_2 \rightarrow CH_2O$ (formaldehyde)	0.05	0.03	0.23	0.33	0.36
$CO + 2H_2 \rightarrow CH_3OH (methanol)$	-0.54	-0.58	-0.18	0.01	-0.26
$CO + 3H_2 \rightarrow CH_4 + H_2O $ (methane)	-1.70	-1.74	-1.33	-1.04	-1.47
$2 CO + 4 H_2 \rightarrow C_2H_4 + 2 H_2O$ (ethylene)	-1.63	-1.71	-1.07	-0.65	-1.19
$2 CO + H_2 \rightarrow C_2H_2O_2$ (glyoxal)	0.23	0.21	0.60	0.74	0.88
$2 CO + 2 H_2 \rightarrow C_2H_4O_2$ (acetic acid)	-1.67	-1.71	-1.05	-0.82	-1.03
$2 CO + 2 H_2 \rightarrow C_2H_4O_2$ (methyl formate)	-0.95	-1.00	-0.35	-0.16	-0.26
$2 CO + 3 H_2 \rightarrow C_2H_4O + H_2O$ (eth. oxide)	-0.32	-0.35	0.28	0.64	0.34
$2 CO + 3 H_2 \rightarrow C_2H_4O + H_2O$ (acetaldehyde)	-1.48	-1.53	-0.91	-0.59	-0.90
$2 CO + 3H_2 \rightarrow C_2H_2 + 2 H_2O$ (acetylene)	-0.09	-0.15	0.31	0.67	0.28
$2 CO + 4 H_2 \rightarrow C_2H_6O + H_2O$ (ethanol)	-1.75	-1.82	-1.01	-0.64	-1.27
$2 CO + 4 H_2 \rightarrow C_2H_6O + H_2O$ (dimethyl ether)	-1.22	-1.30	-0.48	-0.13	-0.69
$2 CO + 5 H_2 \rightarrow C_2 H_6 + 2 H_2 O$ (ethane)	-2.67	-2.75	-1.95	-1.46	-2.23
$3 CO + 5 H_2 \rightarrow C_3H_6O + 2 H_2O (acetone)$	-2.86	-2.94	-1.89	-1.39	-2.06
$3 CO + 6 H_2 \rightarrow C_3H_8O + 2 H_2O $ (isopropanol)	-2.93	-3.03	-1.77	-1.24	-2.27
$3 CO + 7 H_2 \rightarrow C_3H_8 + 3 H_2O $ (propane)	-3.74	-3.85	-2.63	-1.97	-3.08
$3 CO + 6 H_2 \rightarrow C_3H_8O + 2 H_2O (propanol)$	-2.81	-2.91	-1.66	-1.12	-2.16
$3 CO + 5 H_2 \rightarrow C_3H_6O + 2 H_2O (1-propanal)$	-2.56	-2.64	-1.60	-1.11	-1.77
$3 CO + 5 H_2 \rightarrow C_3H_6O + 2 H_2O$ (propylene oxide)	-1.63	-1.69	-0.63	-0.10	-1.01
$3 CO + 4 H_2 \rightarrow C_3H_6O_2 + H_2O$ (methyl acetate)	-2.35	-2.42	-1.34	-0.97	-1.49
$4 CO + 7 H_2 \rightarrow C_4 H_8 O + 3 H_2 O $ (butanal)	-3.58	-3.69	-2.25	-1.59	-2.60
$4 CO + 9 H_2 \rightarrow C_4 H_{10} + 4 H_2 O (butane)$	-4.81	-4.95	-3.31	-2.48	-3.98
$4 CO + 8 H_2 \rightarrow C_4 H_{10} O + 3 H_2 O (1-but anol)$	-3.87	-4.00	-2.34	-1.64	-2.98
$5 CO + 11 H_2 \rightarrow C_5 H_{12} + 5 H_2 O (pentane)$	-5.87	-6.05	-3.98	-2.99	-4.82

TABLE C5Applied corrections per functional for the molecules in data set A.

Compound	PBE	PW91	RPBE	BEEF-vdW
СО	CO	CO	CO	СО
CO_2	CO ₂	CO_2	CO ₂	CO ₂
CH ₂ O (formaldehyde)	-C=O-	-C=O-	-C=O-	-C=O-
CH ₄ (methane)	-CHx	-	-CHx	-CHx
CH_4O (methanol)	-CHx	-	-CHx	-CHx, OH
CH_2O_2 (formic acid)	CO ₂	-(C=O)O-	-(C=O)O-	-(C=O)O-
$C_2H_2O_2$ (glyoxal)	2 -C=O-	2 -C=O-	2 -C=O-	2 -C=O-
$C_2H_4O_2$ (acetic acid)	-CHx, CO ₂	-(C=O)O-	-CHx, -(C=O)O-	-CHx, -(C=O)O-
$C_2H_4O_2$ (methyl formate)	-CHx, CO ₂	-(C=O)O-	-CHx, -(C=O)O-	-CHx, -(C=O)O-
C_2H_4 (ethylene)	-	-	-	-
C_2H_4O (ethylene oxide)	-	-	-	-
C ₂ H ₄ O (acetaldehyde)	-CHx, -C=O-	-C=O-	-CHx, -C=O-	-CHx, -C=O-
C_2H_6 (ethane)	2 -CHx	-	2 -CHx	2 -CHx
C_2H_6O (ethanol)	2 -CHx	-	2 -CHx	2 -CHx, OH
C_2H_6O (dimethyl ether)	-	-	-	-
C_2H_2 (acetylene)	-	-	-	-
C_3H_8 (propane)	3-СНх	-	3-CHx	3-CHx
C_3H_6O (acetone)	2 -CHx, -C=O-	-C=O-	2 -CHx, -C=O-	2 -CHx, -C=O-
C_3H_8O (isopropanol)	3-СНх	-	3-CHx	3 -CHx, OH
C_3H_8O (propanol)	3-СНх	-	3-СНх	3 -CHx, OH
C ₃ H ₆ O (propanal)	2 -CHx, -C=O-	-C=O-	2 -CHx, -C=O-	2 -CHx, -C=O-
C ₃ H ₆ O (propylene oxide)	-СНх	-	-CHx	-CHx
$C_3H_6O_2$ (methyl acetate)	2 -CHx, CO ₂	-(C=O)O-	2 -CHx, -(C=O)O-	2 -CHx, -(C=O)O-
C_4H_8O (butanal)	3 -CHx, -C=O-	-C=O-	3 -CHx, -C=O-	3 -CHx, -C=O-
C_4H_{10} (butane)	4 -CHx	-	4 -CHx	4 -CHx
$C_4H_{10}O$ (butanol)	4 -CHx	-	4 -CHx	4 -CHx , OH
C_5H_{12} (pentane)	5 -CHx	-	5 -CHx	5 -CHx

C.4 Pinpointing errors

For all functionals, the errors in the energies of CO and CO_2 are determined by means of Eq. 4.2 in the main text. In the following, we summarize how the other errors in Table 1, besides \mathcal{E}_{CO} and \mathcal{E}_{CO_2} , were determined for each functional. The general procedure is shown in the workflow scheme 4.1 in the main text, and below.

1. Start with the simplest organic functional group in the data set. In this case, we start with alkanes, which are formed only by $-CH_x$ groups (see the column highlighted in red in Figure C1).

n_C		ΔG_{DFT}^{ullet}	ΔG_{EXP}°	$arepsilon_T$	ε_T/n_C
1	CH ₄	-0.51	-0.52	0.02	0.02
2	C ₂ H ₆	-0.29	-0.33	0.04	0.02
3	C ₃ H ₈	-0.17	-0.24	0.07	0.02
4	C ₄ H ₁₀	-0.05	-0.19	0.14	0.03
5	C ₅ H ₁₂	0.09	-0.09	0.17	0.03
				avg	0.03
				stdev	0.01

FIGURE C1

Pinpointing errors in data set A. Step 1: the alkanes in the set are gathered.

2. Calculate \mathcal{E}_T (Eq. 4.2 in the main text) and find common trends (is the error constant or increasing / decreasing by a relatively constant amount?). In this case for PBE, the error increases alongside the length of the carbon chain n_C (see the column highlighted in red in Figure C2).

n_C		ΔG_{DFT}°	ΔG_{EXP}°	$arepsilon_T$	ε_T/n_C
1	CH ₄	-0.51	-0.52	0.02	0.02
2	C_2H_6	-0.29	-0.33	0.04	0.02
3	C ₃ H ₈	-0.17	-0.24	0.07	0.02
4	C ₄ H ₁₀	-0.05	-0.19	0.14	0.03
5	C ₅ H ₁₂	0.09	-0.09	0.17	0.03
				avg	0.03
				stdev	0.01

Pinpointing errors in data set A. Step 2: the errors are calculated for each substance in the list.

3. To find an approximate \mathcal{E}_{CH_x} , normalize the separate errors by the number of -CH_x units (n_C) and calculate the average (see the column highlighted in red in Figure C3).

n_C		ΔG_{DFT}°	ΔG_{EXP}°	ε_T	ε_T/n_C
1	CH ₄	-0.51	-0.52	0.02	0.02
2	C ₂ H ₆	-0.29	-0.33	0.04	0.02
3	C ₃ H ₈	-0.17	-0.24	0.07	0.02
4	C ₄ H ₁₀	-0.05	-0.19	0.14	0.03
5	C5H12	0.09	-0.09	0.17	0.03
				avg	0.03
				stdev	0.01

FIGURE C3

Pinpointing errors in data set A. Step 3: the errors are normalized by the number of CH_x units in the compound. The $-CH_x$ error is the average of all the individual errors in the list.

4. For molecules with more than one functional group, first eliminate the error contribution of a known \mathcal{E}_i , then obtain the average value of the isolated error. For example, for aldehydes and ketones the carbonyl-group error is isolated by subtracting from the total error the contribution of the hydrocarbon error (see the column highlighted in red in Figure C4).

	ΔG_{DFT}°	ΔG_{EXP}°	$arepsilon_T$	$\varepsilon_T - n_C \cdot \varepsilon_{CH_x}$
CH ₂ O Formaldehyde	-1.13	-1.06	-0.06	-0.06
C ₂ H ₄ O Acetaldehyde	-1.46	-1.38	-0.09	-0.11
C ₃ H ₆ O Propanal	-1.36	-1.28	-0.08	-0.13
C ₄ H ₈ O Butanal	-1.19	-1.18	0.00	-0.08
C ₃ H ₆ O Acetone	-1.65	-1.58	-0.07	-0.12
			avg	-0.10
			stdev	0.03

FIGURE C4

Pinpointing errors in data set A. Step 4: the aldehydes in the data set are gathered, their errors calculated and the - CH_x errors subtracted to ultimately find the carbonyl-related error upon averaging.

To isolate the contributions of the groups to the overall errors, at least 2 molecules representative of the organic functional group are necessary. To illustrate that, the error in the carbonyl group -C=O- for PW91 was determined using 4 representative molecules out of 5, see Table C10.

C.4.1 PBE

C.4.1.1 -CH_x errors in PBE

To determine whether there is an error on this functional group we took the alkanes in data set A and compared their associated errors calculated with Eq. 4.2 in the main text. The errors are shown in Table C6.

The first observation is that the absolute value of ε_T increases alongside the length of the carbon chain. Thus, the error is normalized by the number of carbon atoms in the molecule, as shown in Table C6 in the column ε_T / n_C. The average of those values is the error attributed to -CH_x components. As this is a

cumulative error, it is particularly important to take it into account when correcting energies of molecules with large carbon chains.

TABLE C6

Calculated (PBE) and experimental standard free energies in eV for the alkanes in data set A. ε_T is the error with respect to experiments (Eq. 4.2 in the main text), ε_T /n_C is the error normalized by the number of -CH_x moieties (n_C) in the molecule. The average of ε_T /n_C is equivalent to ε_{CH_x} in Table 1 of the main text.

-CH _x		ΔG_{DFT}°	ΔG_{EXP}°	ε_T	ε_T / n_C
1	CH ₄	-0.51	-0.52	0.02	0.02
2	C ₂ H ₆	-0.29	-0.33	0.04	0.02
3	C ₃ H ₈	-0.17	-0.24	0.07	0.02
4	C ₄ H ₁₀	-0.05	-0.19	0.14	0.03
5	C_5H_{12}	0.09	-0.09	0.17	0.03
				avg	0.03
				stdev	0.01

C.4.1.2. -C=O- errors in PBE

-C=O- is the error of carbonyl groups, so it pertains to aldehydes and ketones. Some of the molecules in this group contain -CH_x moieties, so to determine the error that comes solely from the carbonyl group we subtract the -CH_x error from the total error, as shown in Table C7 under $\varepsilon_T - n_C \cdot \varepsilon_{CH_x}$. Acetaldehyde has one -CH_x moiety, propanal and acetone have two, and butanal has three. The average of the remainders ($\varepsilon_T - n_C \cdot \varepsilon_{CH_x}$) is the error for carbonyl groups, which is equal to -0.1 eV. To determine whether this error is significant and should be considered apart from the CO error, we took the difference between the calculated average error ($\varepsilon_{-C=0-}$) and ε_T^{CO} (0.24 eV). As the difference is on average -0.35 eV, we can safely classify the -C=O- error in a separate category and, thus, carbonyl groups are to be corrected by ~ -0.1 eV.

Calculated (PBE) and experimental standard free energies in eV for the molecules with carbonyl groups in data set A. $\mathcal{E}_T - n_C \cdot \mathcal{E}_{CH_x}$ is the difference between the respective error and the number of -CH_x components in the molecule. The average error corresponds to the -C=O- error in Table 1 of the main text.

Formaldehyde -1.13 -1.06 -0.06 -0.06	aldehydes/ketones		ΔG_{DFT}°	ΔG_{EXP}°	\mathcal{E}_T	$\varepsilon_T - n_C \cdot \varepsilon_{CH_x}$
		Formaldehyde	-1.13	-1.06	-0.06	-0.06
Acetaldehyde -1.46 -1.38 -0.09 -0.11		Acetaldehyde	-1.46	-1.38	-0.09	-0.11
Propanal -1.36 -1.28 -0.08 -0.13		Propanal	-1.36	-1.28	-0.08	-0.13
Butanal -1.19 -1.18 0.00 -0.08		Butanal	-1.19	-1.18	0.00	-0.08
Acetone -1.65 -1.58 -0.07 -0.12		Acetone	-1.65	-1.58	-0.07	-0.12
avg -0.10					avg	-0.10
stdev 0.03					stdev	0.03

C.4.1.3. -(C=O)O- errors in PBE

A similar analysis to that of -C=O- is followed for carboxylic acids and esters in data set A. First, we find that ε_T is nearly constant for all the molecules containing the -(C=O)O- moiety, then the error from $-CH_x$ is subtracted to finally obtain the tabulated error contribution for -(C=O)O- moieties of -0.19 eV. Furthermore, the difference in the calculated error and the CO_2 error is \sim -0.01 eV, indicating that the error in the energies of carboxyl-containing molecules might be corrected by the CO_2 error, depending on the desired level of accuracy.

Calculated (PBE) and experimental standard free energies in eV for carboxylic acids and esters in data set A. Avg is the average error associated to these compounds.

acids/esters		ΔG_{DFT}°	ΔG_{EXP}°	ε_T	$\mathcal{E}_T - n_C \cdot \mathcal{E}_{CH_x}$
	Formic Acid	-3.83	-3.64	-0.19	-0.19
	Acetic Acid	-4.03	-3.88	-0.15	-0.18
	Methyl formate	-3.31	-3.11	-0.20	-0.23
	Metyl Acetate	-3.51	-3.39	-0.13	-0.18
				avg	-0.19
				stdev	0.02

C.4.1.4. -OH errors in PBE

To determine whether alcohols need a correction, we deconvoluted the total error and the -CH $_{\rm x}$ error. The average error for -OH moieties is -0.04 eV. The MAE on the products from CO $_{\rm 2}$ and H $_{\rm 2}$ reactions, with and without correction -OH is 0.037 and 0.040 eV. For products from CO and H $_{\rm 2}$, the MAE with and without correction for -OH is 0.035 and 0.034 eV. Hence, we do not correct -OH, but note that this correction can enhance the reaction energetics particularly for short carbon chain alcohols, such as methanol and ethanol.

For example, the error for producing methanol within PBE based on the reaction $CO_2 + 3H_2 \rightarrow CH_3OH + H_2O$ is 0.14 eV, as seen from Table C3, data set B. After correcting the free energy of CO_2 on the reactants and -CH_x on the products (Eq. 4.6 in the main text: $\Delta G_{DFT}^{\circ} - \varepsilon_{CO_2} + \varepsilon_{CH_x}$) as (0.18 eV + (-0.19 eV) –(0.03 eV), the free energy becomes $\Delta G_{corr}^{\circ} =$ -0.04 eV and the error is -0.08 eV. Further correction by $\varepsilon_{OH} =$ -0.04 eV, reduces the error to -0.04 eV.

TABLE C9

Calculated (PBE) and standard free energies in eV for alcohols in data set A. Avg is the average error associated to these compounds.

alcohol		ΔG_{DFT}°	ΔG_{EXP}°	$arepsilon_T$	$\varepsilon_T - n_C \cdot \varepsilon_{CH_x}$
	Methanol	-1.72	-1.68	-0.04	-0.06
	Ethanol	-1.74	-1.74	0.00	-0.05
	Propanol	-1.61	-1.66	0.05	-0.03
	Butanol	-1.48	-1.56	0.09	-0.02
				avg	-0.04
				stdev	0.02

C.4.2. PW91

C.4.2.1. -CH_x in PW91

As shown in Table C10, -CH_x moieties in PW91 do not show significant errors. Therefore, PW91 calculated energies do not require this type of correction.

TABLE C10

Calculated (PW91) and experimental standard free energies in eV for the alkanes in data set A and an assessment of their associated errors.

$-CH_x$		ΔG_{DFT}°	ΔG_{EXP}°	$arepsilon_T$	ε_T/n_C
1	CH ₄	-0.55	-0.52	-0.02	-0.02
2	C_2H_6	-0.36	-0.33	-0.03	-0.01
3	C_3H_8	-0.26	-0.24	-0.02	-0.01
4	C_4H_{10}	-0.16	-0.19	0.03	0.01
5	C_5H_{12}	-0.06	-0.09	0.03	0.01
				avg	-0.01
				stdev	0.01

C.4.2.2. -C=O- in PW91

As there is practically no error associated to $-CH_x$ moieties for PW91, the errors for carbonyl groups are determined directly from the differences with respect to experiments.

TABLE C11

Calculated (PW91) and experimental standard free energies in eV for aldehydes and ketones in data set A, and an assessment of their average associated errors.

aldehydes/ketones		ΔG_{DFT}°	ΔG_{EXP}°	$arepsilon_T$
	Formaldehyde	-1.14	-1.06	-0.07
	Acetaldehyde	-1.50	-1.38	-0.12
	Propanal	-1.42	-1.30	-0.12
	Butanal	-1.27	-1.18	-0.09
			avg	-0.10
			stdev	0.02

C.4.2.3. -(C=O)O- errors in PW91

In line with PBE, the error for acids and esters in PW91 is similar to the CO_2 error. In fact, the average error of -0.19 eV differs from that of CO_2 (-0.15 eV) by 0.05 eV. In both cases, for the products obtained from CO_2 and H_2 , and CO and H_2 , the MAE is 0.041 and 0.037 eV correcting by -0.15 and -0.19 eV, respectively. Here we have decided to correct the -(C=O)O- moiety by the error found (-0.19 eV) but, in principle, one could correct CO_2 , carboxylic acids and esters using the CO_2 error, depending on the required degree of accuracy.

TABLE C12

Calculated (PW91) and experimental standard free energies of formation in eV for carboxylic acids and esters in data set A, and an assessment of their associated errors.

acids/esters		ΔG_{DFT}°	ΔG_{EXP}°	$arepsilon_T$
	Formic Acid	-3.82	-3.64	-0.18
	Acetic Acid	-4.05	-3.88	-0.17
	Methyl formate	-3.34	-3.11	-0.23
	Methyl Acetate	-3.56	-3.39	-0.18
			avg	-0.19
			stdev	0.03

C.4.2.4. -OH errors in PW91

Based on the error analysis in Table C10, this functional does not display sizable -CH $_{\rm x}$ errors. Therefore, the average -OH error can be straightforwardly calculated in Table C13 as -0.04 eV. As is the case for PBE (section C.4.1.4), correcting this error might be advisable for short carbon chain alcohols, depending on the required accuracy. The MAE for CO $_{\rm 2}$ and H $_{\rm 2}$ products and for CO and H $_{\rm 2}$ (some using CO and H $_{\rm 2}$ O) is 0.036 and 0.037 eV with and without -OH correction.

TABLE C13

Calculated (PW91) and experimental standard free energies in eV for alcohols in data set A, and an assessment of their associated errors.

alcohol		ΔG_{DFT}°	ΔG_{EXP}°	$arepsilon_T$
	Methanol	-1.75	-1.68	-0.07
	Ethanol	-1.80	-1.74	-0.06
	Propanol	-1.69	-1.68	-0.01
	Butanol	-1.58	-1.56	-0.02
			avg	-0.04
			stdev	0.03

C.4.3. RPBE

C.4.3.1. -CH_x errors in RPBE

The average contribution of - CH_x moieties to the total errors in the formation energies of alkanes is $0.08~eV/CH_x$. The total error is, thus, appreciably larger than that of PBE for large molecules.

TABLE C14

Calculated (RPBE) and experimental standard free energies in eV for the alkanes in data set A, and an assessment of their associated errors.

$-CH_x$		ΔG_{DFT}°	ΔG_{EXP}°	$arepsilon_T$	ε_T/n_C
1	CH ₄	-0.46	-0.52	0.07	0.07
2	C ₂ H ₆	-0.21	-0.33	0.13	0.06
3	C_3H_8	-0.01	-0.24	0.23	0.08
4	C_4H_{10}	0.18	-0.19	0.37	0.09
5	C_5H_{12}	0.38	-0.09	0.47	0.09
				avg	0.08
				stdev	0.01

C.4.3.2. -C=O- errors in RPBE

The average error obtained for aldehydes and ketones is -0.21 eV, see Table C15.

TABLE C15

Calculated (RPBE) and experimental standard free energies in eV for aldehydes and ketones, and an assessment of their associated errors.

Formaldehyde -1.27 -1.06 -0.21 -0.21 Acetaldehyde -1.53 -1.38 -0.15 -0.23	
Acetaldehyde -1.53 -1.38 -0.15 -0.23	
Propanal -1.35 -1.30 -0.06 -0.21	
Butanal -1.13 -1.18 0.05 -0.18	
Acetone -1.64 -1.58 -0.06 -0.22	
avg -0.21	
stdev 0.02	

C.4.3.3. –(C=O)O- errors in RPBE

The average error for acids and esters is -0.27 eV. Thus, correcting this moiety by the CO₂ error (-0.46 eV) is not advisable.

TABLE C16

Calculated (RPBE) and experimental standard free energies in eV for carboxylic acids and esters in data set A, and an assessment of their associated errors.

acids/esters		ΔG_{DFT}°	ΔG_{EXP}°	$arepsilon_T$	$\varepsilon_T - n_C \cdot \varepsilon_{CH_x}$
	Formic Acid	-3.92	-3.64	-0.28	-0.28
	Acetic Acid	-4.04	-3.88	-0.16	-0.24
	Methyl formate	-3.34	-3.11	-0.23	-0.31
	Methyl Acetate	-3.46	-3.39	-0.08	-0.23
				avg	-0.27
				stdev	0.04

C.4.3.4. –OH errors in RPBE

To determine whether alcohols need a correction, we deconvoluted the total error from that of -CH_x. As the values in the column $\varepsilon_T - n_C \cdot \varepsilon_{CH_x}$ in Table C17 show that the isolated error is not substantial (-0.01 eV), we conclude that simple alcohols do not need corrections in RPBE, but methanol and ethanol might benefit from specific corrections in specialized studies.

TABLE C17

Calculated (RPBE) and experimental standard free energies in eV for alcohols in data set A, and an assessment of their associated errors.

alcohol		ΔG_{DFT}°	ΔG_{EXP}°	ε_T	$\varepsilon_T - n_C \cdot \varepsilon_{CH_x}$
	Methanol	-1.67	-1.68	0.01	-0.07
	Ethanol	-1.63	-1.74	0.11	-0.05
	Propanol	-1.41	-1.68	0.27	0.04
	Butanol	-1.22	-1.56	0.34	0.02
				avg	-0.01
				stdev	0.05

C.4.4. BEEF-vdW

C.4.4.1. -CH_x errors in BEEF-vdW

As shown in Table C18, -CH $_{\rm x}$ errors are large for this xc-functional compared to the others: $0.21~{\rm eV/CH}_{\rm x}$.

TABLE C18

Calculated (BEEF-vdW) and experimental standard free energies in eV for the alkanes in data set A, and an assessment of their associated errors.

$-CH_x$		ΔG_{DFT}°	ΔG_{EXP}°	$arepsilon_T$	ε_T/n_C
1	CH ₄	-0.27	-0.52	0.25	0.25
2	C ₂ H ₆	0.08	-0.33	0.41	0.21
3	C_3H_8	0.34	-0.24	0.58	0.19
4	C ₄ H ₁₀	0.59	-0.19	0.78	0.20
5	C_5H_{12}	0.85	-0.09	0.94	0.19
				avg	0.21
				stdev	0.03

C.4.4.2. –C=O- errors in BEEF-vdW

The errors in aldehydes and ketones are on average -0.27 eV, obtained after subtracting the contributions of - CH_x moieties.

TABLE C19

Calculated (BEEF-vdW) and experimental standard free energies in eV for aldehydes and ketones in data set A, and an assessment of their associated errors.

aldehydes/ketones		ΔG_{DFT}°	ΔG_{EXP}°	ε_T	$\varepsilon_T - n_C \cdot \varepsilon_{CH_x}$
	Formaldehyd	-1.27	-1.06	-0.21	-0.21
	e				
	Acetaldehyde	-1.42	-1.38	-0.04	-0.25
	Propanal	-1.18	-1.30	0.12	-0.30
	Butanal	-0.88	-1.18	0.30	-0.33
	Acetone	-1.45	-1.58	0.13	-0.28
				avg	-0.27
				stdev	0.04

C.4.4.3. -(C=O)O- errors in BEEF-vdW

For BEEF-vdW this error is divided into 2 groups: that of carboxylic acids and that of esters (see Table 1). This is because the average calculated errors for the two groups differ by \sim 0.10 eV. In both cases the errors are different from that of CO_2 , see Tables S20-S21.

TABLE C20

Calculated (BEEF-vdW) and experimental standard free energies in eV for carboxylic acids in data set A, and an assessment of their associated errors.

carboxylic acids		ΔG_{DFT}°	ΔG_{EXP}°	$arepsilon_T$	$\varepsilon_T - n_C \cdot \varepsilon_{CH_x}$
	Formic Acid	-3.98	-3.64	-0.34	-0.34
	Acetic Acid	-4.02	-3.88	-0.14	-0.34
				avg	-0.34
				stdev	0.00

Calculated (BEEF-vdW) and experimental standard free energies in eV for esters in data set A, and an assessment of their associated errors.

esters		$\Delta G_{DFT}^{^{\circ}}$	$\Delta G_{EXP}^{^{\circ}}$	$arepsilon_T$	$\varepsilon_T - n_C \cdot \varepsilon_{CH_x}$
	Methyl formate	-3.36	-3.11	-0.25	-0.46
	Metyl Acetate	-3.40	-3.39	-0.01	-0.43
				avg	-0.44
				stdev	0.02

C.4.4.4. -OH errors in BEEF-vdW

We find that the average error attributable to this functional group is -0.14 eV, see Table C22.

TABLE C22

Calculated (BEEF-vdW) and experimental standard free energies in eV for alcohols in data set A, and an assessment of their associated errors.

alcohols		$\Delta G_{DFT}^{^{\circ}}$	ΔG_{EXP}°	\mathcal{E}_T	$\varepsilon_T - n_C \cdot \varepsilon_{CH_x}$
	Methanol	-1.59	-1.68	0.09	-0.11
	Ethanol	-1.47	-1.74	0.27	-0.14
	Propanol	-1.18	-1.68	0.50	-0.12
	Butanol	-0.93	-1.56	0.63	-0.20
				avg	-0.14
				stdev	0.04

C.4.4.5. H2 errors in BEEF-vdW

The framework shown here assumes that H₂ is reasonably well described, so we do not provide an H₂ correction by default. However, we verified that correcting the H₂ formation energy by 0.085 eV together with the correction of the other errors also lowers the MAE of data set A. Such value agrees well with the reported value of 0.09 eV. ^{8,9} Table C23 shows the corrections for the other types of errors when H₂ is corrected by 0.085 eV. We note that upon the H₂ correction, the values are rather similar to those of RPBE in Table 1.

Gas-phase errors for BEEF-vdW with a simultaneous $\rm H_2$ correction of 0.085 eV. The two values reported for -(C=O)O- are for carboxylic acids and esters (the latter in parentheses).

Error	BEEF-vdW
CO_2	-0.39
CO	-0.09
-C=O-	-0.21
$-CH_x$	0.08
-(C=O)O-	-0.24 (-0.30)
-OH	-0.08

Finally, we provide in Table C24 a compilation of data to show the progressive reduction in the errors as a result of the various corrections proposed in this study.

TABLE C24

Comparison of the initial mean absolute errors (MAE_{DFT}) for the CO₂ and CO reactions calculated with PBE, PW91, RPBE and BEEF-vdW, after applying corrections to the reactants ε_R (first correction, MAE_R), and after applying corrections to both the reactants ε_R and products ε_P (second correction, MAE_{RP}). %red_R = 100×(MAE_{DFT} - MAE_R) / MAE_{DFT}, and %red_{RP} = 100×(MAE_{DFT} - MAE_{RP}) / MAE_{DFT}.

CO ₂ –based reactions	PBE	PW91	RPBE	BEEF-vdW
MAE_{DFT} (eV)	0.43	0.30	1.14	1.53
MAE_{R} (eV)	0.10	0.09	0.18	0.31
MAE_{RP} (eV)	0.04	0.04	0.04	0.05
$\%$ red $_{ m R}$	77%	68%	84%	80%
$\%$ red $_{ ext{RP}}$	91%	87%	96%	97%

CO-based reactions	PBE	PW91	RPBE	BEEF-vdW
MAE_{DFT} (eV)	0.61	0.68	0.27	0.65
MAE_{R} (eV)	0.10	0.09	0.19	0.32
MAE_{RP} (eV)	0.04	0.04	0.04	0.05
$\%$ red $_{ m R}$	84%	87%	29%	50%
$\%$ red $_{RP}$	94%	95%	85%	92%

C.5 Electrocatalysis-related data

Figures C5 and C6 compare CO_2RR to CO on Au(100) and Au(110) single-crystal electrodes using PBE with (panel b) and without (panel a) gas-phase corrections applied to CO_2 and CO.

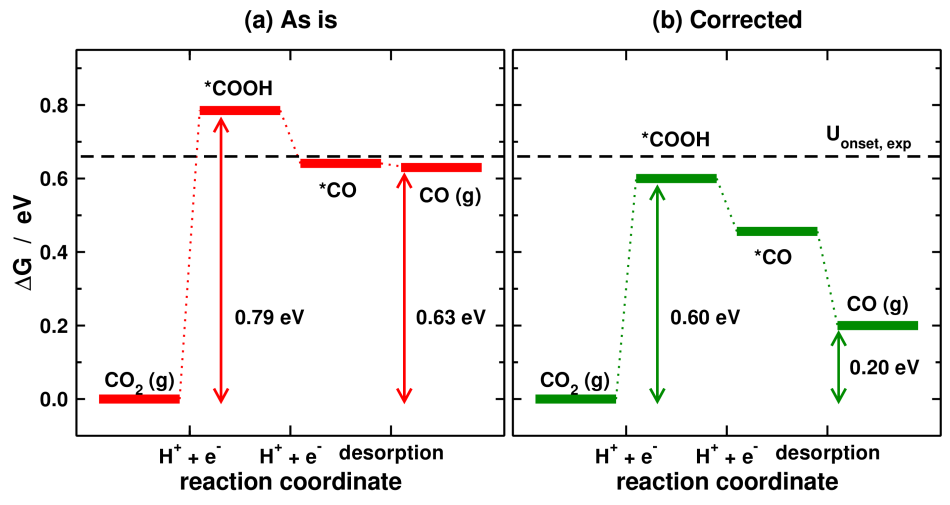
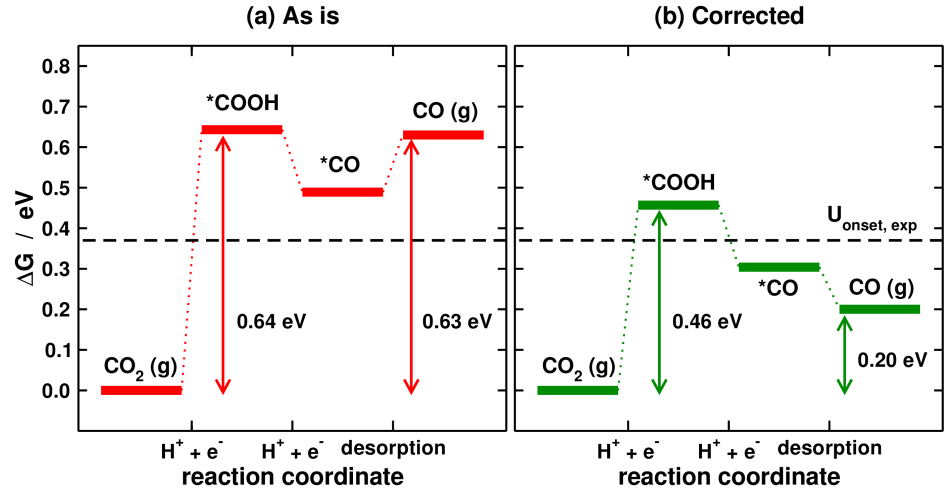


FIGURE C5

Free energy diagrams for CO_2 reduction to CO using Au(100) single-crystal electrodes. (a) Using DFT data as is, and (b) correcting CO_2 and CO for their gas-phase errors. The black dashed line at 0.66 eV marks the free energy corresponding to the experimental onset potential of -0.66 V vs RHE.¹⁰

Table C25 contains the experimental and computational data included in Figures 4.3 and 4.4 in the main text. Cu_{poly} and Ag_{poly} are simulated by missing-row reconstructed Cu(110) and Ag(110). Au_{poly} is represented by Au(211). For each electrode in Table C25 the corresponding slabs contained four layers: the bottommost two were fixed at the optimized bulk positions and the uppermost two and the adsorbates were completely free to relax.



Free energy diagrams for CO_2 reduction to CO using Au(110) single-crystal electrodes. (a) Using DFT data as is, and (b) correcting CO_2 and CO for their gas-phase errors. The black dashed line at 0.37 eV marks the free energy corresponding to the experimental onset potential of -0.37 V vs RHE.¹⁰

TABLE C25

Experimental, DFT calculated and semiempirically corrected onset potentials (in V vs RHE) for CO_2 electroreduction to CO on various metal electrodes.

Electrode	U_{DFT}	$U_{corrected}$	U_{exp}
Au(111)	-0.90	-0.71	-0.66 (ref. ¹⁰)
Au(110)	-0.64	-0.46	-0.37 (ref. ¹⁰)
Au(100)	-0.87	¹⁸ -0.69	-0.66 (ref. ¹⁰)
Au_{poly}	-0.53	-0.34	-0.26 (ref. ¹¹)
Ag(111)	-1.09	-0.90	-0.94 (ref. ¹²)
Ag_{poly}	-0.83	-0.65	-0.60 (ref. ¹³)
Cu_{poly}	-0.53	-0.34	-0.40 (ref. ¹¹)

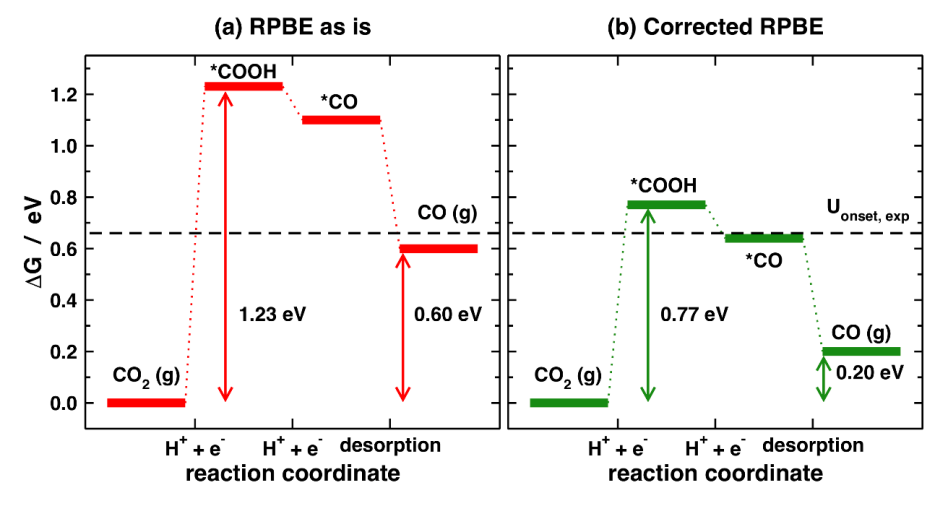
The ZPE, vibrational entropy and solvation corrections of *COOH and *CO can be found in Table C26. The solvation corrections were assessed from calculations in which water molecules were present/absent in the proximities¹⁴ of the adsorbates and are in line with previous reports.^{15,16}

TABLE C26

Zero-point, entropic and solvation contributions (in eV) to the free energies of *COOH and *CO on various metal electrodes.

Electrode	ZPE	TS_{vib}	$E_{solvation}$
COOH @ Au(111)	0.60	0.34	-0.42
CO @ Au(111)	0.17	0.15	0.00
COOH @ Au(110)	0.60	0.34	-0.42
CO @ Au(110)	0.17	0.15	0.00
COOH @ Au(100)	0.61	0.29	-0.42
CO @ Au(100)	0.19	0.16	0.00
COOH @ Au _{poly}	0.60	0.34	-0.42
$CO @ Au_{poly}$	0.17	0.15	0.00
COOH @ Ag(111)	0.59	0.26	-0.44
CO @ Ag(111)	0.16	0.25	0.00
COOH @ Ag _{poly}	0.59	0.28	-0.44
$CO @ Ag_{poly}$	0.16	0.25	0.00
COOH @ Cupoly	0.62	0.22	-0.28
$CO @ Cu_{poly}$	0.16	0.14	0.00

Finally, we modelled CO_2 electroreduction to CO on Au(111) and Au(100) with RPBE. The equilibrium potential is -0.30 V vs RHE before the corrections and -0.10 V vs RHE after the corrections (it is -0.10 V vs RHE in experiments). The ZPE, vibrational entropy and solvation corrections of *COOH (0.61, 0.29 eV) and *CO (0.17, 0.16 eV) are similar to those of PBE (see Table C26), and the solvation corrections are assumed to be the same. We compare in Figures C7-C8 the calculated onset potentials with the experimental ones in reference¹⁰, namely -0.66 V vs RHE for both facets. Without corrections, the onset potentials on Au(111) and Au(100) are -1.23 and -1.21 V vs RHE, giving errors of 0.57 and 0.55 V. Upon the corrections, the onset potentials are -0.77 and -0.75 V, giving errors of 0.11 and 0.09 V.



Free energy diagrams for CO_2 reduction to CO using Au(111) single-crystal electrodes. (a) Using DFT-RPBE data as is, and (b) correcting CO_2 and CO for their gas-phase errors. The black dashed line at 0.66 eV marks the free energy corresponding to the experimental onset potential of -0.66 V vs RHE.¹⁰

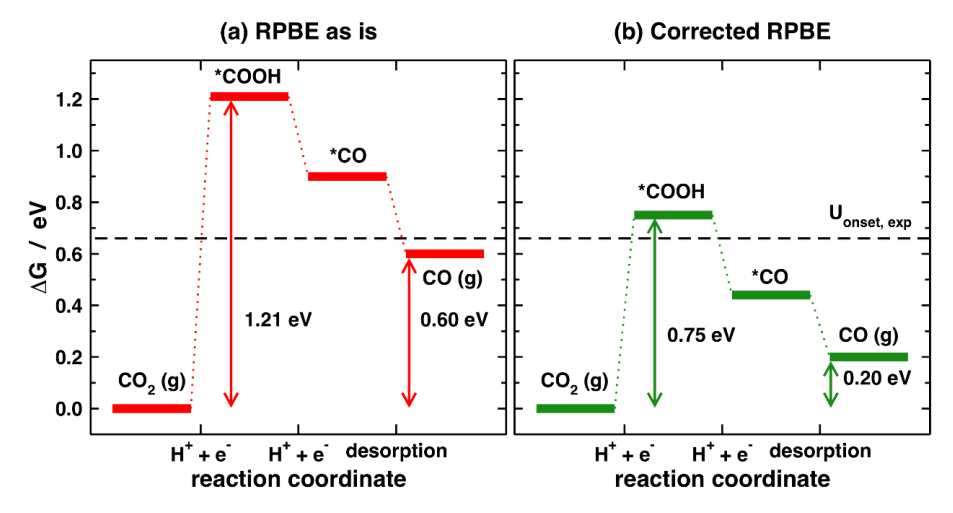


FIGURE C8

Free energy diagrams for CO_2 reduction to CO using Au(100) single-crystal electrodes. (a) Using DFT-RPBE data as is, and (b) correcting CO_2 and CO for their gas-phase errors. The black dashed line at 0.66 eV marks the free energy corresponding to the experimental onset potential of -0.66 V vs RHE. ¹⁰

C.6 Interlayer cohesive energy in graphite

Table C27 contains a literature survey on the experimental interlayer cohesive and/or binding energy of graphite, see Table R1. The values are in the range of 0.031 – 0.064 eV/atom, ^{17–22} and the average value is 0.046 eV/atom. This reflects the common notion that graphite layers are linked via weak van der Waals interactions and justifies the approximation of graphite by graphene for our current purposes.

TABLE C27

Experimental interlayer energy of interaction for graphite described by interlayer cohesive energies (CE) and interlayer binding energies (BE).

Energy (eV/atom)	Interlayer interaction	Source
0.064	CE	[17]
0.054	BE	[¹⁷]
0.043	CE	$[^{18}]$
0.052	CE	[¹⁹]
0.035	CE	$[^{20}]$
0.031	BE	[20]
0.055	BE	[21]
0.031	BE	[22]

C.7 Alternative analysis using training and extrapolation sets

We have also split the molecules in Data set A into a training set of 21 molecules and an extrapolation set of seven molecules (pentane, butanal, glyoxal, isopropanol, butanol, and methyl acetate) and added a new molecule (butanone). Note that the extrapolation set is formed by the largest molecules in every family of compounds (which helps in assessing the performance of the method as the molecules' size increases). The new errors were pinpointed in the training set exactly as described in section 4, Tables C6-C22. Table C28 shows that the errors are similar in the training set compared to the full set, being the average difference of only 0.01 eV. In general, we have observed that only one or two compounds are necessary to pinpoint a specific error, so the training set may easily be made smaller without compromising the accuracy of the method.

Comparison of the gas-phase corrections determined with the entire Data set A (in grey), and with a training set of 21 molecules (in white). All values are in eV.

Error	PI	BE	PV	V91	RP	BE	BEEF	-vdW
-CHx	0.02	0.03	-0.01	-0.01	0.07	0.08	0.21	0.21
-C=O-	-0.11	-0.10	-0.11	-0.10	-0.22	-0.21	-0.27	-0.27
-(C=O)O-	-0.20	-0.19	-0.19	-0.19	-0.27	-0.27	-0.34 (-0.44)	-0.34 (-0.47)
-ОН	-0.05	-0.04	-0.04	-0.04	-0.03	-0.01	-0.14	-0.14

Moreover, we extrapolated the corrections obtained in the training set to the extrapolation set for the formation energies, and the $\rm CO_2$ reduction and $\rm CO$ reduction energies. Tables C29-C31 show the free energies for the four functionals under study, the corrected free energies and the experimental values, providing in all cases the mean absolute errors (MAEs) with respect to experiments. From Tables C29-C31 we conclude that the MAEs are significantly decreased in the extrapolation set for the formation energies and those involved in $\rm CO_2$ and $\rm CO$ reduction reactions. Importantly, the final MAEs are comparable to those in Figures 4.1-4.2. Since the MAEs for a given functional are identical for the three corrected energies (see the bottom rows for the corrected functionals in Tables C29-C31), the errors do not appear to propagate in our method. Conversely, the errors grow rapidly among the uncorrected energies, particularly for RPBE and BEEF-vdW.

TABLE C29Formation energies of the compounds in the extrapolation set. All values are in eV.

Species	ΔG_{PBE}	ΔG_{PW91}	ΔG_{RPBE}	$\Delta G_{BEEF-vdW}$	ΔG_{PBE}^{corr}	ΔG_{PW91}^{corr}	ΔG_{RPBE}^{corr}	$\Delta G_{BEEF-vdW}^{corr}$	ΔG_{exp}
pentane	0.09	-0.06	0.38	0.85	-0.04	-0.02	0.01	-0.21	-0.09
butanal	-1.19	-1.27	-1.13	-0.88	-1.15	-1.14	-1.14	-1.25	-1.18
butanone	-1.54	-1.63	-1.45	-1.20	-1.51	-1.50	-1.46	-1.57	-1.52
glyoxal	-2.13	-2.14	-2.39	-2.46	-1.92	-1.93	-1.96	-1.92	-1.97
isopropanol	-1.73	-1.81	-1.52	-1.30	-1.76	-1.75	-1.71	-1.79	-1.80
butanol	-1.48	-1.58	-1.22	-0.93	-1.53	-1.51	-1.49	-1.64	-1.56
methyl acetate	-3.51	-3.56	-3.46	-3.40	-3.37	-3.35	-3.34	-3.38	-3.39
MAE	0.09	0.09	0.24	0.46	0.03	0.04	0.06	0.05	

Free energies for CO_2 reduction to the compounds in the extrapolation set. All values are in eV.

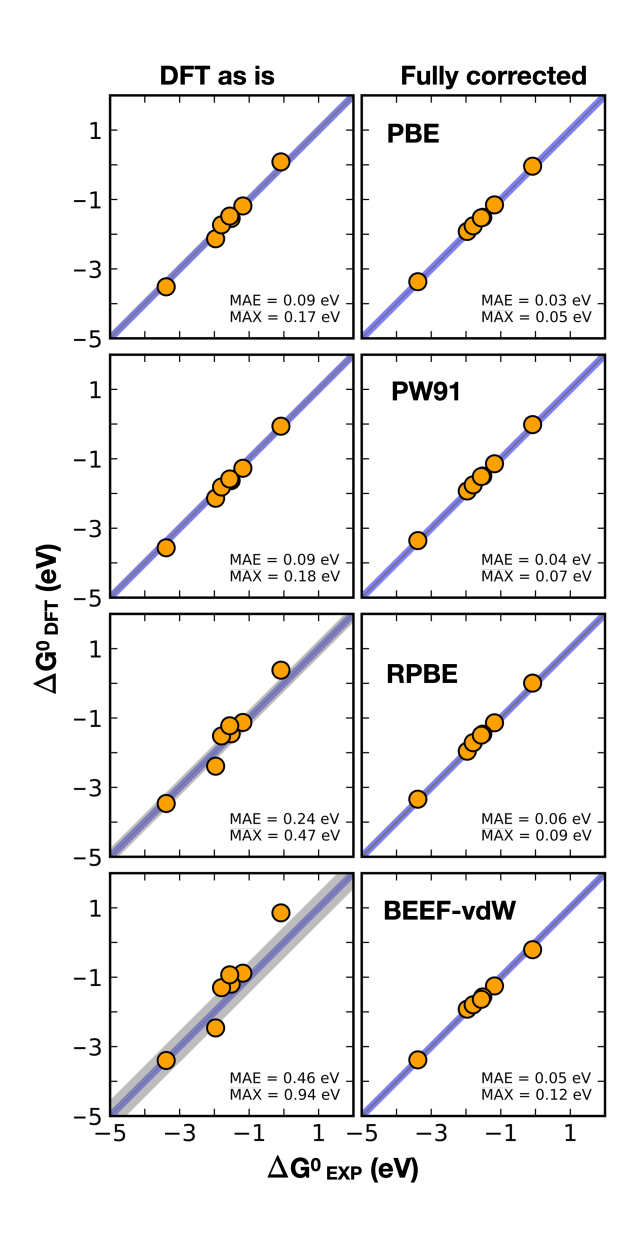
Species	ΔG_{PBE}	ΔG_{PW91}	ΔG_{RPBE}	$\Delta G_{BEEF-vdW}$	ΔG_{PBE}^{corr}	ΔG_{PW91}^{corr}	ΔG_{RPBE}^{corr}	$\Delta G_{BEEF-vdW}^{corr}$	ΔG_{exp}
pentane	-2.24	-2.58	-0.56	0.40	-3.29	-3.27	-3.25	-3.46	-3.34
butanal	-0.67	-0.92	0.49	1.12	-1.39	-1.38	-1.37	-1.49	-1.42
butanone	-1.03	-1.28	0.16	0.80	-1.75	-1.73	-1.70	-1.80	-1.75
glyoxal	1.68	1.59	1.97	2.10	1.52	1.51	1.48	1.52	1.47
isopropanol	-0.75	-0.96	0.29	0.80	-1.34	-1.33	-1.29	-1.38	-1.38
butanol	-0.96	-1.23	0.39	1.07	-1.76	-1.74	-1.73	-1.87	-1.79
methyl acetate	-0.17	-0.34	0.71	1.07	-0.58	-0.57	-0.55	-0.59	-0.60
MAE	0.67	0.44	1.75	2.31	0.03	0.04	0.06	0.05	-

TABLE C31

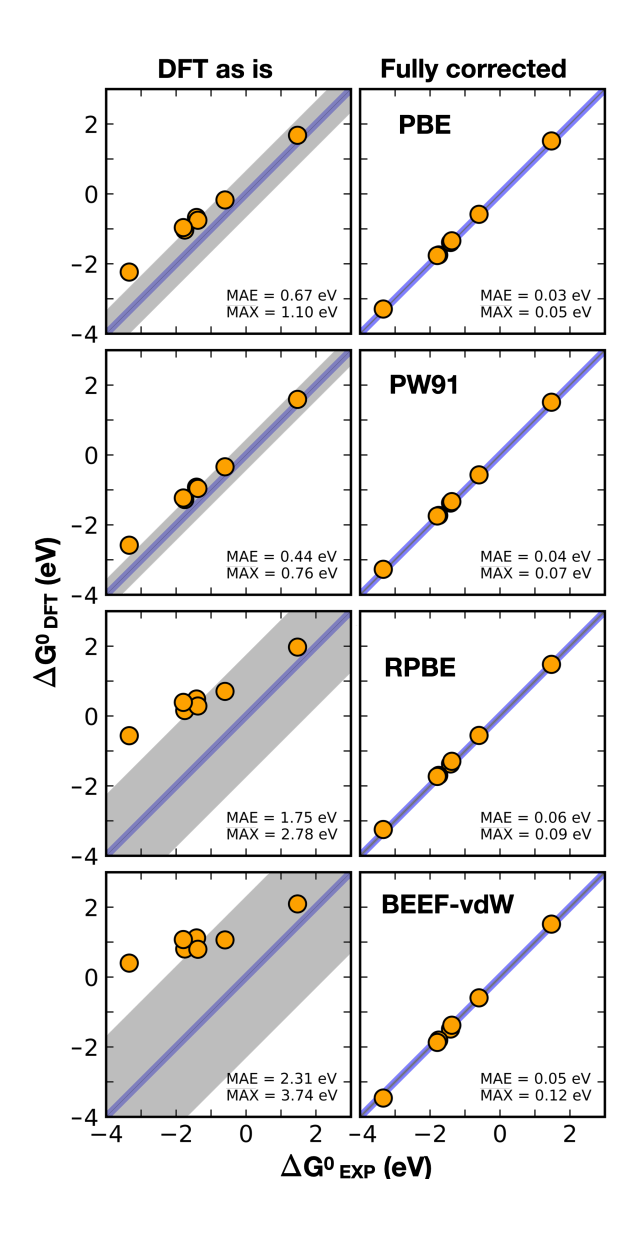
Free energies for CO reduction to the compounds in the extrapolation set. All values are in eV.

Species	ΔG_{PBE}	ΔG_{PW91}	ΔG_{RPBE}	$\Delta G_{BEEF-vdW}$	ΔG_{PBE}^{corr}	ΔG_{PW91}^{corr}	ΔG_{RPBE}^{corr}	$\Delta G_{BEEF-vdW}^{corr}$	ΔG_{exp}
pentane	-5.87	-6.05	-3.98	-2.99	-4.77	-4.75	-4.73	-4.94	-4.82
butanal	-3.58	-3.69	-2.25	-1.59	-2.57	-2.56	-2.56	-2.67	-2.60
butanone	-3.94	-4.05	-2.58	-1.91	-2.93	-2.92	-2.88	-2.99	-2.94
glyoxal	0.23	0.21	0.60	0.74	0.93	0.92	0.89	0.92	0.88
isopropanol	-2.93	-3.03	-1.77	-1.24	-2.23	-2.22	-2.18	-2.27	-2.27
butanol	-3.87	-4.00	-2.34	-1.64	-2.95	-2.93	-2.91	-3.06	-2.98
methyl	-2.35	-2.42	-1.34	-0.97	-1.47	-1.46	-1.44	-1.48	-1.49
acetate									
MAE	0.87	0.97	0.44	0.99	0.03	0.04	0.06	0.05	-

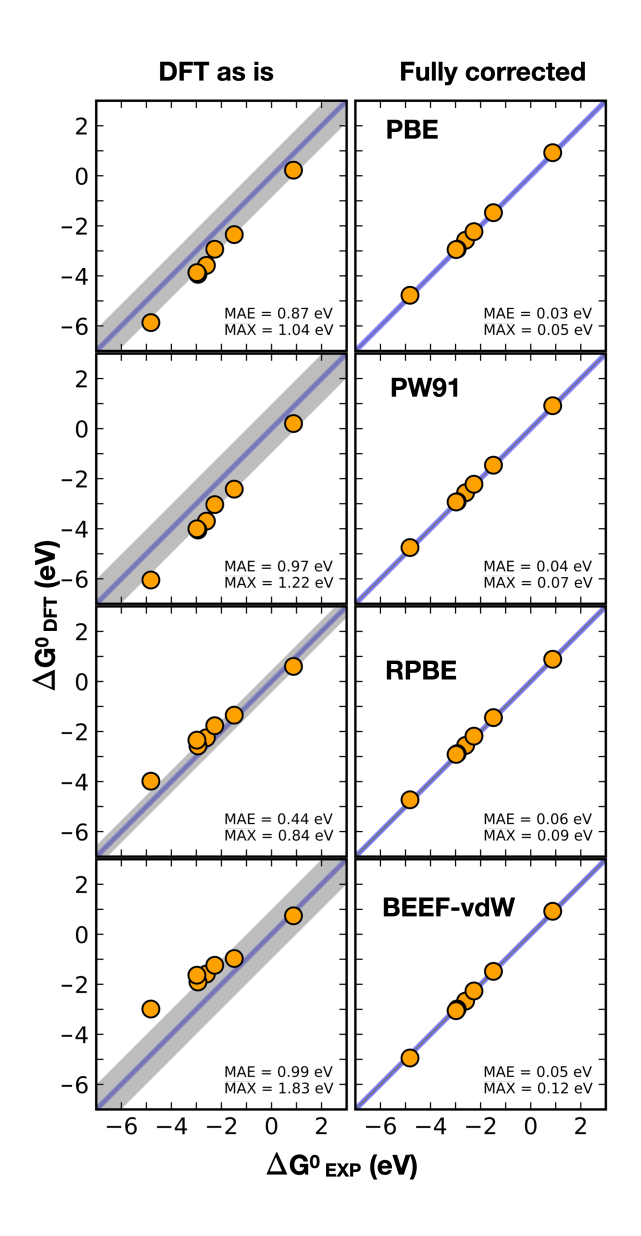
With the values in Tables C29-C31 we prepared Figures C9-C11. The figures display the data as parity plots comparing experimental and computational data without any corrections and applying all the corrections listed in Table C28. The plots illustrate that: (i) the errors are considerably decreased upon applying the corrections, (ii) the errors do not propagate in our method, (iii) the errors propagate quickly in as-is DFT as the molecules become larger (i.e. as ΔG gets increasingly negative in Figures C10-C11).



Parity plots for the experimental and DFT-calculated free energies of formation of the molecules in the extrapolation set using PBE, PW91, RPBE and BEEF-vdW. The left column shows the data calculated with DFT without any correction, the right column shows the data after correcting for all the errors detected in the training set. The mean and maximum absolute errors (MAE, MAX) are shown in each case. The grey area is \pm MAE in each case. The blue shaded area around the parity line covers an area of \pm 0.15 eV.



Parity plots for the experimental and DFT-calculated free energies for the production of the molecules in the extrapolation set from CO_2 and H_2 using PBE, PW91, RPBE and BEEF-vdW. The left column shows the data calculated with DFT without any correction. The right column shows the data after correcting for errors in CO_2 and the products. The mean and maximum absolute errors (MAE, MAX) are shown in each case. The grey area is \pm MAE in each case. The blue shaded area around the parity line covers an area of \pm 0.15 eV.



Parity plots for the experimental and DFT-calculated free energies for the production of the molecules in the extrapolation set from CO and H_2 using PBE, PW91, RPBE and BEEF-vdW. The left column shows the data calculated with DFT without any correction. The right column shows the data after correcting for errors in CO and the products. The mean and maximum absolute errors (MAE, MAX) are shown in each case. The grey area is \pm MAE in each case. The blue shaded area around the parity line covers an area of \pm 0.15 eV.

C.8 References

- (1) Kurth, S.; Perdew, J. P.; Blaha, P. Molecular and Solid-State Tests of Density Functional Approximations: LSD, GGAs, and Meta-GGAs. Int. J. Quantum Chem. 1999, 75, 889-909.
- (2) Calle-Vallejo, F.; Martínez, J. I.; García-Lastra, J. M.; Mogensen, M.; Rossmeisl, J. Trends in Stability of Perovskite Oxides. Angew. Chem. Int. Ed. 2010, 49, 7699-7701.
- (3) Martínez, J. I.; Hansen, H. A.; Rossmeisl, J.; Nørskov, J. K. Formation Energies of Rutile Metal Dioxides Using Density Functional Theory. Phys. Rev. B 2009, 79, 045120.
- (4) Bartel, C. J.; Weimer, A. W.; Lany, S.; Musgrave, C. B.; Holder, A. M. The Role of Decomposition Reactions in Assessing First-Principles Predictions of Solid Stability. Npj Comput. Mater. 2019, 5, 1-9.
- (5) Lide, D. R. CRC Handbook of Chemistry and Physics, 85th Edition; CRC Press, 2004.
- (6) M. W. Chase; C. A. Davies; J. R. Downey; D. J. Frurip; R. A. MacDonald; A. N. Syverud. NIST-JANAF Thermochemical Tables. J. Phys. Chem. Ref. Data 1985, Suppl. 1 to Vol. 14, 1856.
- (7) Informatics, N. O. of D. and. NIST Chemistry WebBook https://webbook.nist.gov/chemistry/ (accessed Oct 18, 2019).
- (8) Studt, F.; Behrens, M.; Kunkes, E. L.; Thomas, N.; Zander, S.; Tarasov, A.; Schumann, J.; Frei, E.; Varley, J. B.; Abild-Pedersen, F.; Nørskov, J. K.; Schlögl, R. The Mechanism of CO and CO₂ Hydrogenation to Methanol over Cu-Based Catalysts. ChemCatChem 2015, 7, 1105–1111.
- (9) Studt, F.; Abild-Pedersen, F.; Varley, J. B.; Nørskov, J. K. CO and CO₂ Hydrogenation to Methanol Calculated Using the BEEF-VdW Functional. Catal. Lett. 2013, 143, 71–73.
- (10) Todoroki, N.; Tei, H.; Tsurumaki, H.; Miyakawa, T.; Inoue, T.; Wadayama, T. Surface Atomic Arrangement Dependence of Electrochemical CO₂ Reduction on Gold: Online Electrochemical Mass Spectrometric Study on Low-Index Au(Hkl) Surfaces. ACS Catal. 2019, 9, 1383–1388.
- (11) Kuhl, K. P.; Hatsukade, T.; Cave, E. R.; Abram, D. N.; Kibsgaard, J.; Jaramillo, T. F. Electrocatalytic Conversion of Carbon Dioxide to Methane and Methanol on Transition Metal Surfaces. J. Am. Chem. Soc. 2014, 136, 14107-14113.
- (12) Hoshi, N.; Kato, M.; Hori, Y. Electrochemical Reduction of CO₂ on Single Crystal Electrodes of Silver Ag(111), Ag(100) and Ag(110). J. Electroanal. Chem. 1997, 440, 283-286.
- (13) Ma, M.; Trześniewski, B. J.; Xie, J.; Smith, W. A. Selective and Efficient Reduction of Carbon Dioxide to Carbon Monoxide on Oxide-Derived Nanostructured Silver Electrocatalysts. Angew. Chem. Int. Ed. 2016, 55, 9748-9752.
- (14) Calle-Vallejo, F.; F. de Morais, R.; Illas, F.; Loffreda, D.; Sautet, P. Affordable Estimation of Solvation Contributions to the Adsorption Energies of Oxygenates on Metal Nanoparticles. J. Phys. Chem. C 2019, 123, 5578-5582.

- (15) Peterson, A. A.; Abild-Pedersen, F.; Studt, F.; Rossmeisl, J.; Nørskov, J. K. How Copper Catalyzes the Electroreduction of Carbon Dioxide into Hydrocarbon Fuels. Energy Environ. Sci. 2010, 3, 1311-1315.
- (16) Calle-Vallejo, F.; Koper, M. T. M. Theoretical Considerations on the Electroreduction of CO to C2 Species on Cu(100) Electrodes. Angew. Chem. Int. Ed. 2013, 52, 7282-7285.
- (17) Wang, W.; Dai, S.; Li, X.; Yang, J.; Srolovitz, D. J.; Zheng, Q. Measurement of the Cleavage Energy of Graphite. Nat. Commun. 2015, 6, 1-7.
- (18) Girifalco, L. A.; Lad, R. A. Energy of Cohesion, Compressibility, and the Potential Energy Functions of the Graphite System. J. Chem. Phys. 1956, 25, 693-697.
- (19) Zacharia, R.; Ulbricht, H.; Hertel, T. Interlayer Cohesive Energy of Graphite from Thermal Desorption of Polyaromatic Hydrocarbons. Phys. Rev. B 2004, 69, 155406.
- (20) Benedict, L. X.; Chopra, N. G.; Cohen, M. L.; Zettl, A.; Louie, S. G.; Crespi, V. H. Microscopic Determination of the Interlayer Binding Energy in Graphite. Chem. Phys. Lett. 1998, 286, 490-496.
- (21) Xia, M.; Liang, C.; Cheng, Z.; Hu, R.; Liu, S. The Adhesion Energy Measured by a Stress Accumulation-Peeling Mechanism in the Exfoliation of Graphite. Phys. Chem. Chem. Phys. 2019, 21, 1217-1223.
- (22) Liu, Z.; Liu, J. Z.; Cheng, Y.; Li, Z.; Wang, L.; Zheng, Q. Interlayer Binding Energy of Graphite: A Mesoscopic Determination from Deformation. Phys. Rev. B 2012, 85, 205418.

D: Supporting Information for Chapter 5

D1 Experimental

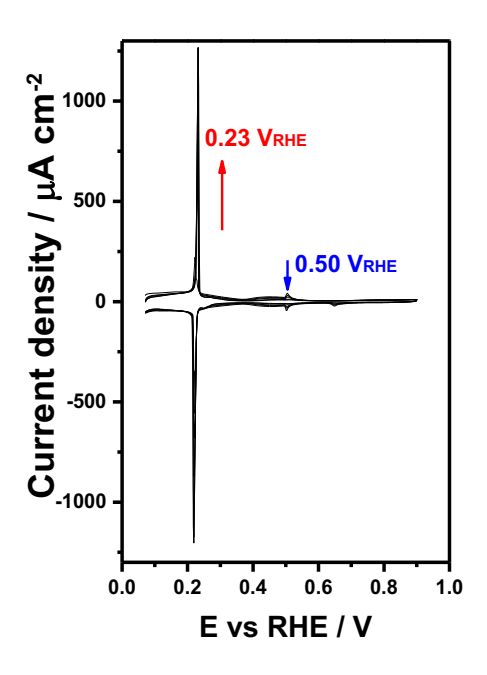


FIGURE D1

Electrochemical deposition of a palladium monolayer on Pt(111) electrode from 0.1 M $H_2SO_4 + 0.1$ mM PdSO₄. Scan rate: 50 mV s⁻¹. Arrows indicate the evolution with time.

Figure D1 shows the effect of the progressive accumulation of palladium on the Pt(111) electrode surface on the voltammetric profile of the electrode during the electrochemical deposition of a palladium monolayer. Initially, the presence of palladium on the surface is reflected by the growth of a sharp adsorption state at 0.23 V_{RHE} , concomitant with the progressive decrease of the characteristic adsorption states of Pt(111) in 0.1 M $H_2\mathrm{SO_4}$. In addition, the presence of the characteristic spike of Pt(111) at 0.50 V_{RHE} strongly suggests the existence of wide Pt(111) domains. With increasing deposition cycles the last contributions from the Pt(111) domains around 0.50 V_{RHE} disappear. Previous studies using scanning tunnelling microscopy (STM) showed that a complete pseudomorphic monolayer of Pd is formed prior to bulk deposition during electrochemical deposition of Pd on Pt(111). The voltammetric charge of (bi)sulfate adsorption at 0.23 V_{RHE} can be related in a quantitative way to the palladium coverage and corresponds to a charge of 320 μ C cm⁻² for Pd_{ML}Pt(111).

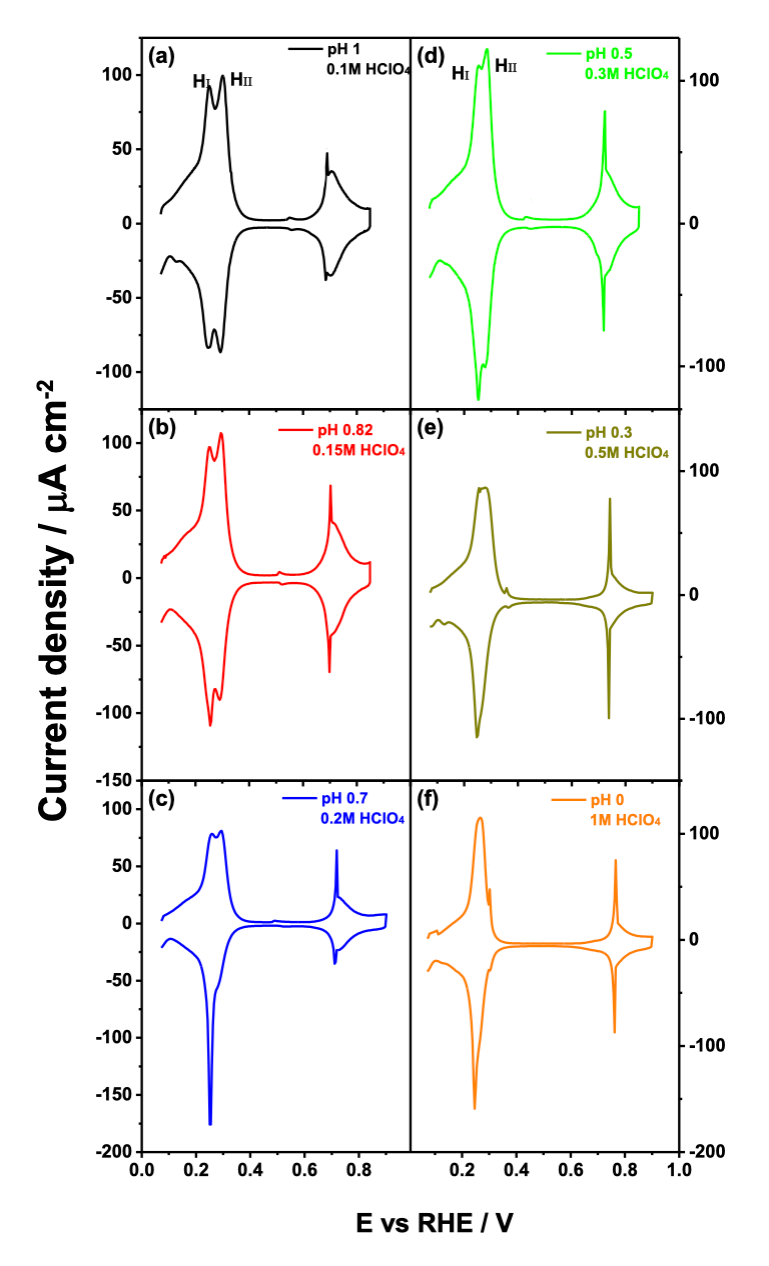


FIGURE D2

Cyclic voltammogram of $Pd_{ML}Pt(111)$ electrode recorded in (a) 0.1 M HClO₄ (pH = 1), (b) 0.15 M HClO₄ (pH = 0.82), (c) 0.2 M HClO₄ (pH = 0.7), (d) 0.3 M HClO₄ (pH = 0.5), (e) 0.5 M HClO₄ (pH = 0.3) and (f) 1 M HClO₄ (pH = 0). Scan rate: 50 mV s⁻¹.

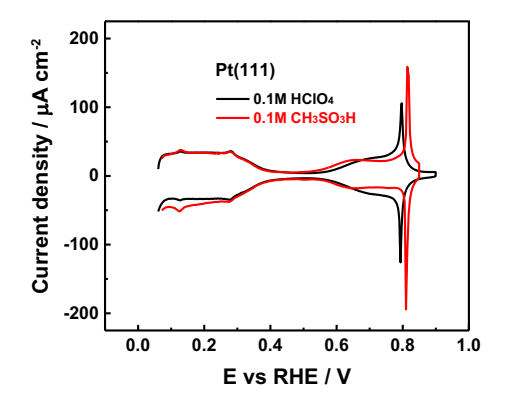


FIGURE D3

Cyclic voltammogram of Pt(111) in 0.1 M HClO₄ and 0.1 M CH₃SO₃H. Scan rate: 50 mV s^{-1} .

Figure D3 compares the cyclic voltammograms of a Pt(111) electrode recorded in 0.1 M HClO₄ and 0.1 M CH₃SO₃H. At potentials lower than 0.55 $V_{\rm RHE}$, where the hydrogen adsorption/desorption and the double-layer regions take place, there is an almost perfect coincidence between the curves. However, at higher potentials, when the adsorption of oxygen-containing species occurs, visible differences between the CVs appear. At potentials in the range of 0.55 to 0.90 $V_{\rm RHE}$, where adsorption of hydroxyl from water dissociation is expected, OH adsorption starts at slightly lower potentials in CH₃SO₃H than in HClO₄ and this could suggest weak specific adsorption. In contrast, the following sharp peak, the spike of the so-called "butterfly" feature, is slightly shifted to higher potentials in 0.1 M CH₃SO₃H.

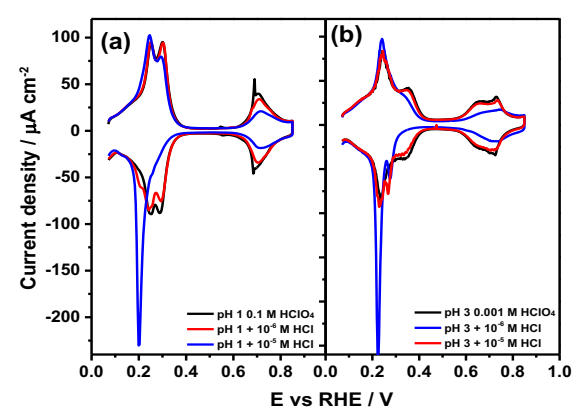


FIGURE D4

Cyclic voltammogram of $Pd_{ML}Pt(111)$ electrode recorded in (a) 0.1 M $HClO_4$ (pH = 1) and (b) 0.001 M $HClO_4$ (pH = 3), without and with different concentrations of Cl⁻. Scan rate: 50 mV s⁻¹.

Figure D4 shows the cyclic voltammograms of the $Pd_{ML}Pt(111)$ electrode recorded in (a) 0.1 M HClO₄ (pH = 1) and (b) 0.001 M HClO₄ (pH = 3) with small concentrations (10^{-6} and 10^{-5} M) of Cl⁻. The change caused by Cl⁻ is the same as reported by Markovic et al³: the observed H_I and H_{II} peaks exhibit asymmetry, in contrast to the symmetric peaks observed in solutions containing only HClO₄. Therefore, chloride is in competition with H_{upd} as well as with OH_{ads} .

D2 Computational methods

All of the calculations were performed using the Vienna Ab initio Simulation Package (VASP)⁴ with the Generalized-Gradient-Approximation (GGA) PBE exchange-correlation functional⁵ and the projector-augmented wave (PAW) method.⁶ The plane-wave energy cut-off was 450 eV. Pt(111) and Pd_{ML}Pt(111) surfaces were modeled using a slab consisting of a (3×3) unit cell. After verifying energy convergence with respect to atomic layers we decided to use 6 atomic layers for Pd_{ML}Pt(111) and Pt(111), in this way providing a convergence criterion of adsorption energies to \leq 0.05 eV. The k-point sampling grids used for both surfaces were (6×6×1) generated using the Monkhorst-Pack approach. [4-6][4-6]7

To account for bulk effects in a finite slab, the first two atomic layers were kept fixed at the PBE optimized lattice constant of Pt (3.98 Å) while the remaining atomic layers were relaxed. We included empirical van der Waals (vdW) corrections through the DFT-D3(BJ)^{8,9} method on PBE, here denoted as PBED3, to the calculations for a comparison of the energetics of the water-water and water-metal interactions. The relaxations to find the ground-state configurations were made using the quasi-Newton algorithm. Site analysis and geometry optimizations were performed until the forces were smaller than 0.02 eV Å-1. To prevent spurious interactions between the slabs along the z axis, a vacuum of ~15.0 Å was set for all cases and dipole corrections were also applied by adding the tags LDIPOL= .TRUE. and IDIPOL = 3. The slab was positioned at the bottom of the cell, in this way assuring convergence when using the dipole moment corrections. Several attempts with the cell positioned in the center plus dipole corrections failed to converge.

For the surfaces and adsorbed species, the method of Methfessel-Paxton¹⁰ to the second order was used to set the partial occupancies on each orbital and the smearing width was set to 0.2 eV. For the individual molecules, a Gaussian smearing with a width of 0.001 eV was used instead. The gas-phase molecules, $H_2O(g)$, $H_2(g)$, $ClO_2(g)$, $F_2(g)$ and $SO_2(g)$ were simulated in an asymmetric box of $(15.0 \times 15.1 \times 15.3)$ Å³ at the gamma point $(1 \times 1 \times 1)$.

D3 Gibbs Free Energy of Adsorption

The changes in free energies of adsorption were calculated using the hypothetical chemical reaction 1, following Eq. D.2. A(g) is a gas-phase molecule, * is the surface and *A is the adsorbed species on the surface.

$$A_{(g)} + * \rightarrow * A$$
 D.1

$$\Delta G_{ads}^{*A} = G^{*A} - G_{(g)}^{A} - G^{*}$$
 D.2

Where,

$$G^{*A} = E_{DFT}^{*A} + ZPE^{*A} - TS_{vib}^{*A}$$
 D.3

$$G_{(g)}^{A} = E_{DFT(g)}^{A} + ZPE_{(g)}^{A} - TS_{trans, rot, vib(g)}^{A}$$
 D.4

$$G^* = E_{DFT}^*$$
 D.5

where E_{DFT}^{x} is the relative energy from the optimization extrapolated to 0 K (sigma \rightarrow 0) where x refers to either *A, A(g) or (*), ZPE is the zero-point energy and TS is the entropy contribution at 298.15 K. For the gas-phase molecules, the entropy includes all contributions, and was obtained from standard thermodynamic tables. For the adsorbed species, the entropy includes only the vibrational contributions and was calculated using statistical mechanics equations within the harmonic oscillator approximation. These contributions were obtained by performing a vibrational analysis within the VASP code using several displacements around the ground state. Within this method only the adsorbed species are displaced in all directions while the slab is kept fixed. To obtain the solution-phase free energy of water from DFT-calculated gas-phase

water, we corrected the energy by adding -0.087 eV to the TS term.¹³ This represents the difference between the free energy of formation of gas-phase water and liquid-phase water at 298.15 K.

The potential dependence of all the proton-coupled electron transfer reactions was calculated using the computational hydrogen electrode (CHE) model, 13 where at equilibrium and standard conditions (0 V and a pressure of 1 atm), the protons in solution and the electrons in the electrode (H⁺(aq), e⁻) are in equilibrium with H₂(g), as shown in the following chemical equation:

$$\frac{1}{2}H_{2(g)} \rightleftarrows H^{+}_{aq} + e^{-}$$
 D.6

With this thermodynamic convention we can overcome the computational difficulty of calculating the energy of protons and electrons in DFT and instead calculate the ground-state free energy of a $H_2(g)$ molecule. Half of that energy will then represent the free energy of the coupled proton and electron as shown in Eq D.6. 13,14

The solution-phase free energies of perchlorate, sulfate and bisulfate anions were calculated via a thermodynamic cycle combining DFT free energies and tabulated experimental standard redox chemical potentials at standard conditions (298.15 K and 1 atm), as a direct calculation of these anion free energies would be difficult with DFT due to the long length and time scales of the solvation energetics. Using an electrochemical thermodynamic cycle allows us to calculate the solution-phase free energy of an anion from a neutral, typically gas-phase, species, such that its energy can be accurately determined with DFT as G = ZPE - TS + PV. This is analogous to the computational hydrogen electrode method, except it requires experimentally measured equilibrium potentials, whereas in the computational hydrogen electrode method, the equilibrium potential between hydrogen gas and aqueous protons at standard conditions is defined to be exactly 0 V, i.e., $Ge = -n |e| U^{\circ} = 0$

As an example, the solution-phase free energy of $\mathrm{ClO}_{4(aq)}^-$ is discussed below. Using the following redox equations at standard conditions, we can use the calculated free energy of $\mathrm{ClO}_{2(g)}$ to calculate the free energy of aqueous perchlorate.

$$ClO_{3(aq)}^{-} + 2H^{+} + e^{-} \leftrightharpoons ClO_{2(g)} + H_{2}O_{(aq)}E^{\circ} = 1.18V$$
 D.7

$$ClO_{4\ (aq)}^{-} + 2H^{+} + 2e^{-} \leftrightharpoons ClO_{3\ (aq)}^{-} + H_{2}O_{(aq)}E^{\circ} = 1.2V$$
 D.8

From Eq. D.7, $ClO_{3(aq)}^{-}$ free energy can be determined which can then be used in Eq. D.8 to determine the solution-phase free energy of $ClO_{4(aq)}^{-}$. Note that the free energy of the electron is, $G^{e^{-}} = -n|e|U^{\circ}$ and the total free energy is, $\Delta G = \Delta G^{\circ} - k_b ln(10) pH$, where the second term of the equation is 0 at pH = 0 and at equilibrium $\Delta G = 0$. Therefore, the free energy of Eq. D.7 is

$$\Delta G = G_{(g)}^{ClO_2} + G_{(aq)}^{H_2O} - G_{(aq)}^{ClO_3} - G_{(g)}^{H_2} - G^{e^-}$$
 D.9

Substituting $G^{e^-} = -n|e|U^{\circ}$, and $E^{\circ} = U^{\circ}$:

$$G_{(aq)}^{ClO_3^-} = G_{(g)}^{ClO_2} \ + \ G_{(aq)}^{H_2O} \ - \ G_{(g)}^{H_2} \ - \ (-n|e|U^\circ) \label{eq:closed}$$
 D.10

$$G_{(aq)}^{clo_3^-} = G_{(g)}^{clo_2} + G_{(aq)}^{H_20} - G_{(g)}^{H_2} + 1.18 \text{ eV}$$
 D.11

Similarly,

$$G_{(aq)}^{clO_4^-} = G_{(aq)}^{clO_3^-} + G_{(aq)}^{H_2O} - G_{(g)}^{H_2} + 2.4 \text{ eV}$$
 D.12

Now, the calculated free energy of the proton in solution is obtained following the definition that the standard hydrogen electron redox potential is set to 0 V on the SHE scale.

Given the previous definitions:

$$\frac{1}{2}H_{2(g)} \rightleftharpoons H^{+}_{aq} + e^{-}E^{\circ} = 0V$$
 D.13

$$\Delta G = G_{(aq)}^{H^+} - n|e|U - \frac{1}{2}G_{(g)}^{H_2}$$
 D.14

Then,

$$0 = G_{(aq)}^{H^+} - 1x e(0V) - \frac{1}{2}G_{(g)}^{H_2}$$
 D.15

$$\frac{1}{2}G_{(g)}^{H_2} = G_{(aq)}^{H^+}$$
 D.16

Then, the adsorption energy of perchlorate on the surface is calculated as follows: Given the following reaction, where we used an adsorbed water adlayer as the reference state *6 H₂O then,

$$*6H_2O + ClO_{4(aq)}^- \rightarrow *ClO_4 - H_2O + 5H_2O_{(aq)} + e^-$$
 D.17

represents the adsorbed perchlorate co-adsorbed with one water molecule. Then, we can determine the change in free energy of adsorption of adsorbed solvated perchlorate as shown below in Eq. D18.

$$\Delta G_{ads}^{*ClO_4-H_2O} = G^{*ClO_4-H_2O} + 5G_{(aq)}^{H_2O} - G^{*~6H_2O} - G_{(aq)}^{ClO_4^-} - n|e|U \quad \text{D.18}$$

which represents the energy of adsorption of a perchlorate ion on a surface covered with 2/3 ML water molecules, perturbing the water adlayer and displacing water molecules after its adsorption. In our case, the adsorbed perchlorate is solvated with one water molecule.

D4 Adsorption free energies of *OH, *H and *O

D4.1 Adsorption of hydroxyl and water adlayer

The adsorption energy of *OH was calculated within a explicit water bilayer. In this study we used a single water bilayer with a total water species coverage of 2/3 ML, and varied the hydroxyl (*OH + *H₂O) coverage by removing hydrogen from the adlayer. The water bilayer structure of $\sqrt{3} \times \sqrt{3}$ $R30^{\circ}$ has been found to be stable on closed-packed metal surfaces. Furthermore, the good match between the lattice constant of metals and the water layer makes this model attractive for computational electrocatalysis as a good aproximation to account for solvation effects, 13,18-21 especially those coming from the first solvation shell.

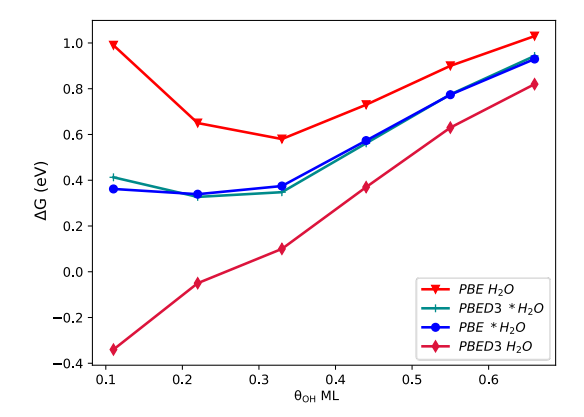


FIGURE D5

Hydroxyl (*OH) free energy of adsorption as a function of coverage on $Pd_{ML}Pt(111)$ calculated at the PBE and PBED3 levels of theory. The plotted adsorption energy is calculated with two different reference states: from the adsorbed water bilayer (*H₂O) and from solution-phase water (H₂O).

We can calculate the adsorption energy of *OH in two ways: (i) by using the adsorbed water bilayer as the reference state^{18,22} (i.e. using Eq. D.19), and (ii) by using solution-phase water as the reference state (i.e. using Eq. D.20).

*
$$H_2O \rightarrow * nOH - (x - n)H_2O + n(H^+ + e^-)$$
 D.19

* +
$$x H_2 O_{(aq)} \longrightarrow * n OH - (x - n)H_2 O + n(H^+ + e^-)$$
 D.20

In both cases x = 6. Figure D5 shows the adsorption energy of *OH as a function of *OH coverage calculated from either solution phase water (H_2O (aq)) or an adsorbed water bilayer (H_2O) as reference state and with and without dispersion corrections for both cases. We observe that:

- 1) When referencing with respect to adsorbed water, for PBE and PBED3 the adsorption energies are basically the same and do not differ by more than $0.05~(\pm~0.02)~eV$, see Table D1 OH (b) and Figure D5 cyan (PBED3) and blue lines (PBE).
- 2) When referencing with respect to solution-phase water with PBE, the energies are less favorable (red triangles) than those calculated with PBED3 (velvet diamonds). The difference between these two at the lowest coverage is ~ 1.32 eV.
- 3) As the *OH coverage increases, the energies tend to converge and do not differ by more than ~0.2 eV, independent of the reference state.

Since the water-metal interactions are most affected by vdW interactions, 23,24 the strong promotion of the adsorption of *OH + *H₂O at low *OH coverage, and

weaker promotion at high *OH coverage (relative to that calculated without vdW corrections) is simply proportional to the amount of water present in the *OH + *H_2O bilayer. This effect is roughly canceled when using an adsorbed water as the reference state.

Similarly to case 1, the adsorption thermodynamics of the water adlayer on Pt(111) relative to that on $Pd_{\text{ML}}Pt(111)$ with vdW corrections does not significantly differ from that obtained without the vdW corrections. In fact, the difference in binding strength with vs. without vdW corrections between the two surfaces is $\sim\!0.03$ eV, with stronger adsorption on $Pd_{\text{ML}}Pt(111)$. This is because the stabilization incorporated by the vdW corrections for both surfaces is of the same magnitude, $\sim\!0.24$ eV. Thus, the effect of including vdW corrections is also canceled when using adsorbed water as a reference state in the calculation of our adsorption potentials. In this way, the impact of vdW corrections is minimal as shown in Figure D5 on $Pd_{\text{ML}}Pt(111)$. In either case, an appropriate representation of water adsorption is necessary for obtaining accurate DFT adsorption potentials.

TABLE D1

Free energies of adsorption in eV for 1/3 ML coverage of *H, *O and 1/3*OH-1/3 *H2O (PBE and PBED3). Using (a) solution-phase water and (b) adsorbed water bilayer as the reference state.

PBE		PBED3		
	Pd _{ML} Pt(111)	Pt(111)	Pd _{ML} Pt(111)	Pt(111)
*H	-0.35	-0.29	-0.45	-0.39
*OH (a)	0.66	0.71	0.10	0.20
*ОН (b)	0.37	0.43	0.35	0.39
*0	1.25	1.46	1.11	1.31

D4.2 Adsorption of hydrogen and oxygen

The free energies of adsorption of *H, *O were calculated at different coverages using the same 3×3 unit cell by the following equations:

$$n(H^+ + e^-) + * \rightarrow * nH$$
 D.21

$$\Delta G_{ads}^{*H} = \frac{G^{(*nH)} - \frac{n}{2}G_{(g)}^{H_2} - G^*}{n}$$
 D.22

$$n H_2 O_{(aq)} + * \rightarrow * nO + 2n(H^+ + e^-)$$
 D.23

$$\Delta G_{ads}^{*0} = \frac{G^{*n0} + 2n\frac{1}{2}G_{(g)}^{H_2} - nG_{(aq)}^{H_2O} + G^*}{n}$$
 D.24

where (*) is the surface , *H and *O are adsorbed species, n equals the number of adsorbed species per unit cell, and G(*) is the free energy of the isolated slab. The adsorption of *H and *O were calculated at their most stable sites (fcc) in both cases, and without explicit solvation following Eqs. D.22 and D.24.

D5 Free energies vs. coverage diagrams

D5.1 Pd_{ML}Pt(111) Phase Diagrams

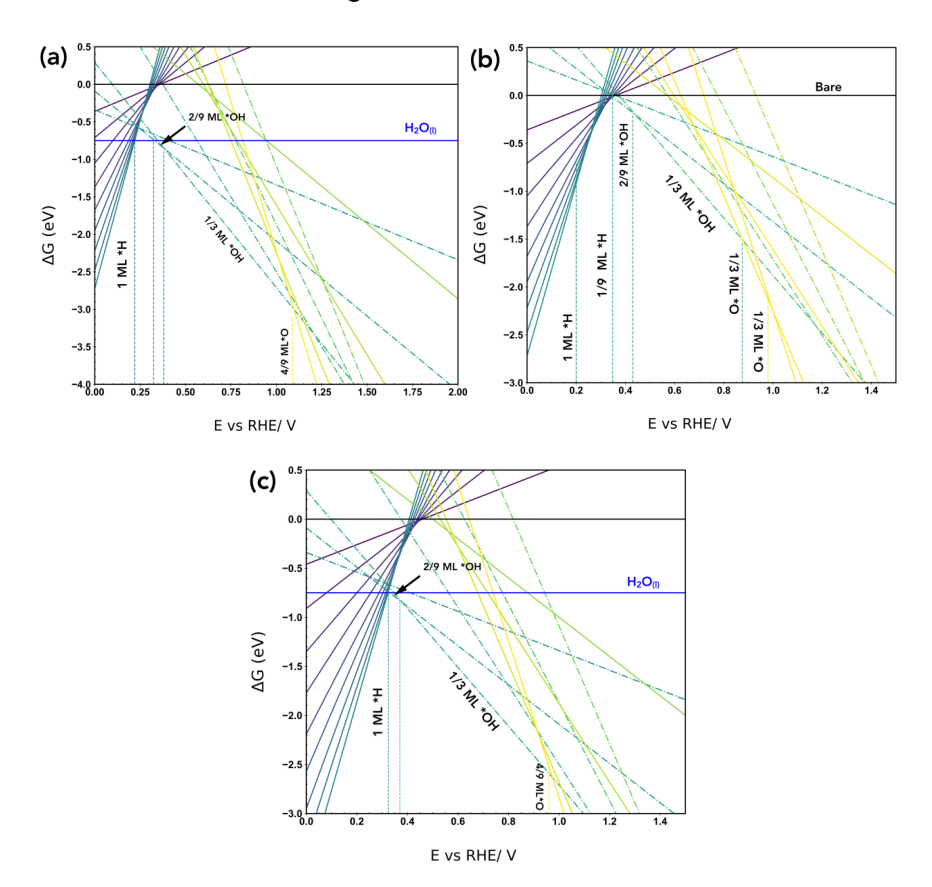


FIGURE D6

Calculated free energies of adsorption for $Pd_{ML}Pt(111)$ as a function of potential vs RHE using three different methods. Method 1, shown in (a), where the adsorption potentials of hydroxyl are calculated from solution phase water with PBED3, as shown in Eq. D.20, while the adsorption potentials of hydrogen and oxygen are calculated with PBE. Method 2, shown in (b), the adsorption potentials are calculated with PBE and the reference state for *OH adsorption is the adsorbed water adlayer, as shown in Eq. D.19. Method 3, shown in (c), the adsorption potentials are calculated with PBED3 and solution phase water is used as the refence state, as shown in Eq. D.20.

D5.2 Pt(111) Phase Diagrams

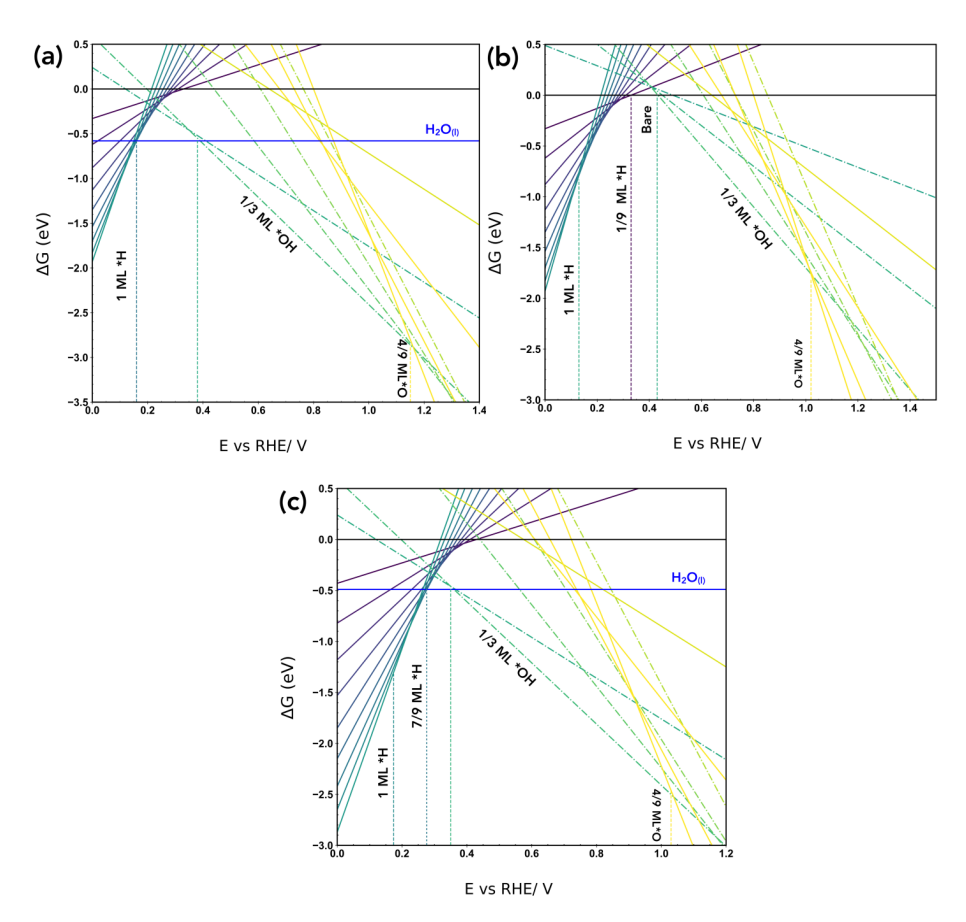


FIGURE D7

Calculated free energies of adsorption for Pt(111) as a function of potential vs RHE using three different methods. Method 1, shown in (a), where the adsorption potentials of hydroxyl are calculated from solution phase water with PBED3, as shown in Eq. D.20, while the adsorption potentials of hydrogen and oxygen are calculated with PBE. Method 2, shown in (b), the adsorption potentials are calculated with PBE and the reference state for *OH adsorption is the adsorbed water adlayer, as shown in Eq. D.19. Method 3, shown in (c), the adsorption potentials are calculated with PBED3 and solution phase water is used as the refence state, as shown in equation 20.

D6 References

- (1) Hoyer, R.; Kibler, L. A.; Kolb, D. M. The Initial Stages of Palladium Deposition onto Pt(1 1 1). *Electrochim. Acta* **2003**, *49* (1), 63-72.
- (2) Thin Films: Preparation, Characterization, Applications; Soriaga, M. P., Stickney, J., Bottomley, L. A., Kim, Y.-G., Eds.; Springer US, 2002.
- (3) Arenz, M.; Stamenkovic, V.; Schmidt, T. J.; Wandelt, K.; Ross, P. N.; Markovic, N. M. The Effect of Specific Chloride Adsorption on the Electrochemical Behavior of Ultrathin Pd Films Deposited on Pt(111) in Acid Solution. *Surf. Sci.* **2003**, *523* (1), 199–209.
- (4) Kresse, G.; Furthmüller, J. Efficient Iterative Schemes for Ab Initio Total-Energy Calculations Using a Plane-Wave Basis Set. *Phys. Rev. B* **1996**, *54* (16), 11169-11186.
- (5) Perdew, J. P.; Burke, K.; Ernzerhof, M. Generalized Gradient Approximation Made Simple. *Phys. Rev. Lett.* **1996**, *77* (18), 3865-3868.
- (6) Kresse, G.; Joubert, D. From Ultrasoft Pseudopotentials to the Projector Augmented-Wave Method. *Phys. Rev. B* **1999**, *59* (3), 1758–1775.
- (7) Monkhorst, H. J.; Pack, J. D. Special Points for Brillouin-Zone Integrations. *Phys. Rev. B* **1976**, *13* (12), 5188-5192.
- (8) Grimme, S.; Antony, J.; Ehrlich, S.; Krieg, H. A Consistent and Accurate Ab Initio Parametrization of Density Functional Dispersion Correction (DFT-D) for the 94 Elements H-Pu. *J. Chem. Phys.* **2010**, *132* (15), 154104.
- (9) Grimme, S.; Ehrlich, S.; Goerigk, L. Effect of the Damping Function in Dispersion Corrected Density Functional Theory. *J. Comput. Chem.* **2011**, *32* (7), 1456-1465.
- (10) Methfessel, M.; Paxton, A. T. High-Precision Sampling for Brillouin-Zone Integration in Metals. *Phys. Rev. B* **1989**, *40* (6), 3616–3621.
- (11) Chase, Jr., M. W.; Davies, C. A.; Downey, Jr., J. R.; Frurip, D. J.; MacDonald, R. A.; Syverud, A. N. NIST-JANAF Thermochemical Tables. *J. Phys. Chem. Ref. Data* **1985**, *Suppl. 1 to Vol. 14*, 1856.
- (12) Fultz, B. Vibrational Thermodynamics of Materials. *Prog. Mater. Sci.* **2010**, 55, 247–352.
- (13) Nørskov, J. K.; Rossmeisl, J.; Logadottir, A.; Lindqvist, L.; Kitchin, J. R.; Bligaard, T.; Jónsson, H. Origin of the Overpotential for Oxygen Reduction at a Fuel-Cell Cathode. *J. Phys. Chem. B* **2004**, *108* (46), 17886-17892.
- (14) Calle-Vallejo, F.; Koper, M. T. M. First-Principles Computational Electrochemistry: Achievements and Challenges. *Electrochim. Acta* **2012**, *84* (Supplement C), 3-11.
- (15) Ogasawara, H.; Brena, B.; Nordlund, D.; Nyberg, M.; Pelmenschikov, A.; Pettersson, L. G. M.; Nilsson, A. Structure and Bonding of Water on Pt(111). *Phys. Rev. Lett.* **2002**, *89* (27), 276102.
- (16) Schnur, S.; Groß, A. Properties of Metal-Water Interfaces Studied from First Principles. *New J. Phys.* **2009**, *11* (12), 125003.
- (17) Michaelides, A.; Hu, P. Catalytic Water Formation on Platinum: A First-Principles Study. J. Am. Chem. Soc. **2001**, 123 (18), 4235-4242.

- (18) He, Z.-D.; Hanselman, S.; Chen, Y.-X.; Koper, M. T. M.; Calle-Vallejo, F. Importance of Solvation for the Accurate Prediction of Oxygen Reduction Activities of Pt-Based Electrocatalysts. *J. Phys. Chem. Lett.* **2017**, *8* (10), 2243–2246.
- (19) McCrum, I. T.; Janik, M. J. PH and Alkali Cation Effects on the Pt Cyclic Voltammogram Explained Using Density Functional Theory. *J. Phys. Chem. C* **2016**, *120* (1), 457-471.
- (20) Roman, T.; Groß, A. Structure of Water Layers on Hydrogen-Covered Pt Electrodes. *Catal. Today* **2013**, *202* (Supplement C), 183–190.
- (21) Granda-Marulanda, L. P.; Builes, S.; Koper, M. T. M.; Calle-Vallejo, F. Influence of Van Der Waals Interactions on the Solvation Energies of Adsorbates at Pt-Based Electrocatalysts. *ChemPhysChem* **2019**, *0* (0).
- (22) McCrum, I. T.; Hickner, M. A.; Janik, M. J. First-Principles Calculation of Pt Surface Energies in an Electrochemical Environment: Thermodynamic Driving Forces for Surface Faceting and Nanoparticle Reconstruction. *Langmuir* **2017**, *33* (28), 7043–7052.
- (23) Forster-Tonigold, K.; Groß, A. Dispersion Corrected RPBE Studies of Liquid Water. *J. Chem. Phys.* **2014**, *141* (6), 064501.
- (24) Carrasco, J.; Klimeš, J.; Michaelides, A. The Role of van Der Waals Forces in Water Adsorption on Metals. *J. Chem. Phys.* **2013**, *138* (2), 024708.

E: Supporting Information for Chapter 6

E1 Experimental Details

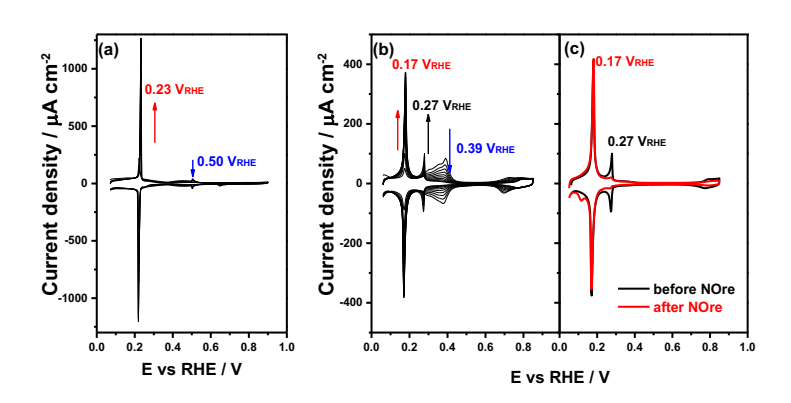


FIGURE E1

Cyclic voltammograms for (a) Pt(111) and (b) Pt(100) in 0.1 M $H_2SO_4 + 0.1$ mM PdSO₄, recorded in successive stages during Pd deposition experiment. Scan rate: 50 mV s⁻¹. Arrows indicate the evolution with time. (c) Stable cyclic voltammograms of Pd/Pt(100) electrode in 0.1 M H_2SO_4 before NO adsorption and reductive stripping (black line) and the same Pd/Pt(100) electrode in 0.1 M H_2SO_4 after NO adsorption and reductive stripping (red line).

Figure E1a shows the effect of the progressive accumulation of palladium on the voltammetric profile of Pt(111) electrode during the electrochemical deposition of palladium monolayer. At the shortest deposition times, the presence of palladium on the surface is reflected in the growth of a sharp adsorption state at 0.23 V_{RHE} , simultaneously with the progressive decrease of the characteristic adsorption states of Pt(111) in 0.1 M H₂SO₄. In addition, the presence of the characteristic spike of Pt(111) at 0.50 V_{RHE} strongly suggests the existence of wide Pt(111) domains. Increasing deposition cycles lead to the contributions from the Pt(111) domains around 0.50 V_{RHE} to become blocked progressively. A previous study using in situ scanning tunnelling microscopy (STM) showed an complete pseudomorphic monolayer of Pd is formed prior to bulk deposition during electrochemical deposition of Pd on Pt(111).¹ The voltammetric charge of (bi)sulfate adsorption at 0.23 V_{RHE} can be related in a quantitative way to the palladium coverage and increases to a charge value of 320 μ C cm⁻² for Pd_{ML}Pt(111).^{2,3}

Figure E1b shows the characteristic adsorption peak of Pt(100) electrode at 0.39 V_{RHE} progressively diminishes whereas a new sharp adsorption state appears at 0.17 V_{RHE} . The experimental result is interpreted as the progressive blocking of the Pt(100) substrate sites by a first monolayer of palladium atoms directly deposited on the Pt(100) substrate. As the deposition continues a new feature appears at 0.27 V_{RHE} while the peak at 0.39 V_{RHE} corresponding to the remaining Pt(100) unblocked sites has not been completely suppressed. The appearance of a second adsorption state at 0.27 V_{RHE} for palladium deposited on Pt(100) substrates is associated to the growth of palladium in second, third and further layers. The easiest way to obtain a Pt(100) electrode fully covered by a single palladium monolayer is to deposit palladium until all the Pt(100) sites are blocked and then remove the excess by the NO treatment described above:⁴

 $Pt(100) + Pd_{further layers}/Pd_{first layer}/Pt(100) + NO \rightarrow Pd_{first layer}/Pt(100)-NO + Pd_{sol}$ in which $Pd_{first layer}$ means palladium adatoms in the first monolayer, $Pd_{further layers}$ is the second and multilayers, and Pd_{sol} represents stable palladium species in solution.

Figure E1c shows the final voltammogram in $0.1\,\mathrm{M}$ H₂SO₄ (red line): a characteristic peak at $0.17\,\mathrm{V}_{\mathrm{RHE}}$ related to the (bi)sulfate anion adsorption on Pd monolayer is observed, the contributions assigned to the second stage of Pd deposition at $0.27\,\mathrm{V}_{\mathrm{RHE}}$ and uncovered Pt(100) electrode domain at $0.39\,\mathrm{V}_{\mathrm{RHE}}$ have been eliminated. The voltammogram of Pd_{ML}Pt(100) is stable upon successive cycles, suggesting that the monolayer does not undergo further modification.

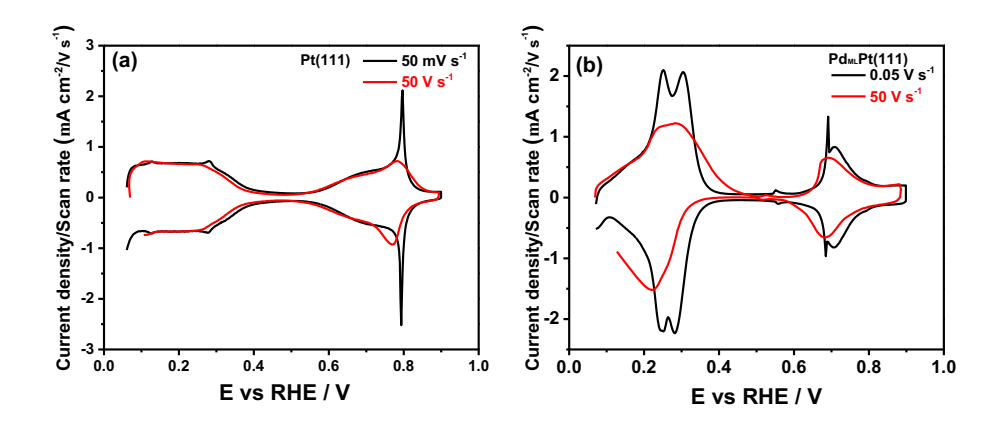


FIGURE E2 Voltammograms of (a) Pt(111) and (b) Pd_{ML}Pt(111) electrode in 0.1 M HClO₄ recorded at $0.05~V~s^{-1}$ (black line) and $50~V~s^{-1}$ (red line), resp.

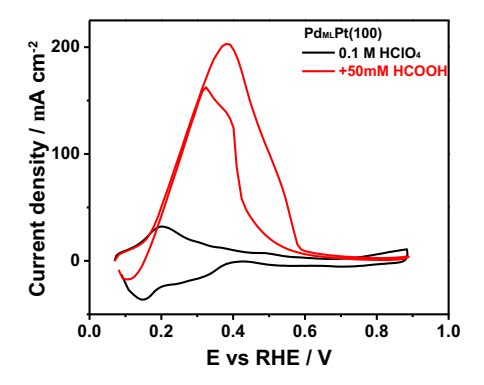


FIGURE E3

Voltammograms of $Pd_{ML}Pt(100)$ electrode in 0.1 M HClO₄ (black line) and 0.1 M HClO₄ + 50 mM HCOOH, recorded at 50 V s⁻¹.

Figure E4 shows the oxidation of formic acid on $Pd_{ML}Pt(100)$ electrode in 0.1 M HClO₄ + 50 mM HCOOH at a high scan rate of 50 V s⁻¹. The current corresponding to the oxidation of formic acid process is much larger than the current corresponding to the reversible formate adsorption/desorption so that this latter contribution cannot be separated from the voltammogram. The results suggest a much faster kinetics of formic acid oxidation reaction on $Pd_{ML}Pt(100)$ than that on $Pd_{ML}Pt(111)$ electrode.

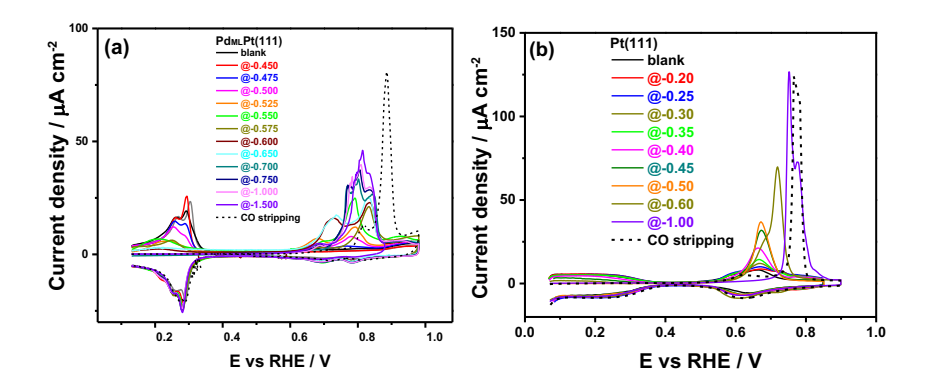


FIGURE E4

Voltammograms for the oxidative stripping of CO adlayer produced on (a) $Pd_{ML}Pt(111)$ and (b) Pt(111) electrode after doing CO_2 reduction at different vertex potentials in pH=3.0 (0.001M $HClO_4/0.099M$ $KClO_4$) solution saturated with CO_2 , recorded at 10 mV s⁻¹. A CO stripping experiment result (dashed line) of a saturated CO adlayer is performed under identical condition for comparison.

Figure E5 shows the voltammograms for the oxidative stripping of CO adlayer produced during CO₂ reduction on the Pd_{ML}Pt(111) and Pt(111) electrode, resp. Figure E5a shows anodic peaks between 0.650 and 0.900 V_{RHE} are observed when doing CO₂ reduction on the Pd_{ML}Pt(111) electrode by increasing the vertex potential in steps of 0.025 V from -0.475 V_{RHE}. These anodic peaks correspond to the oxidation of adsorbed CO formed during CO₂ reduction. It is reasonable to assume that there is no CO formation from CO₂ reduction on $Pd_{ML}Pt(111)$ surface at lower overpotentials than that of $-0.475V_{RHE}$. In Figure E4a, the production of the CO is shown to increase with increasing the overpotential for CO₂ reduction: for the overpotential of -0.475, -0.500, -0.525, -0.550, -0.575, -0.600, -0.650, -0.700 and $-0.750 \text{ V}_{\text{RHE}}$, the coverage of CO adlayer is 0.13, 0.19, 0.22, 0.29, 0.31, 0.52, 0.58, 0.71 and 0.72 ML, resp. As can be seen from Figure E4a, the onset potential and shape of CO adlayer oxidation peak on the Pd_{ML}Pt(111) electrode strongly depends on its coverage. The full CO adlayer is stripped off at 0.90 V_{RHE} (dashed line); such a high coverage is noy obtained during CO₂ reduction. The subsequent scan indicates the entire CO adlayer on Pd_{ML}Pt(111) electrode was stripped in a single positive-going sweep and retains the welldefined hydrogen adsorption and anion desorption features in the low-potential region. In the case of the Pt(111) electrode, reducing CO₂ to adsorbed CO starts at -0.25 V_{RHE} and the surface is poisoned when the negative vertex potential reaches -0.60 V_{RHE}. Figure E4b shows that with increasing overpotential for CO₂ reduction on Pt(111), the formation of the CO increases: for the overpotential of -0.25, -0.30, -0.35, -0.40, -0.50, -0.60 and $-1.0 V_{RHE}$, the coverage of CO adlayer is 0.23, 0.37, 0.37, 0.47, 0.59, 0.63 and 0.66 ML, resp. The subsequent scan shows the recovery of the Pt(111) surface after the CO adlayer oxidation.

E2 Computational Details

E2.1 Free energies calculations

The formation free energies of adsorbed *H, *CO, *OCHO and *COOH were calculated from formic acid in solution, (HCOOH (aq)) for the formic acid oxidation reaction, and from carbon dioxide in gas-phase, (CO_2 (g)), protons and electrons, for the CO_2 reduction reaction. Below we show how the free energies are calculated in both cases.

F2.2 Formic Acid oxidation

The following chemical equations show how the formation free energies of the different adsorbates are calculated for formic acid oxidation.

$$HCOOH(aq) + * \rightarrow * H + CO_2(q) + H^+ + e^-$$

$$HCOOH(aq) + * \rightarrow * OCHO + H^+ + e^-$$
 E2

$$HCOOH(aq) + *\rightarrow *COOH + H^+ + e^-$$
 E3

$$HCOOH(aq) +*\rightarrow *CO + H_2O(l)$$
 E4

where, * represents the adsorption site. The free energies of adsorption are then calculated as shown below

$$G_{*H}^{ads} = G_{*H} + G_{CO_2(g)} + \frac{1}{2}G_{H_2(g)} - G_{HCOOH(aq)} - G_*$$
 E5

$$G_{*OCHO}^{ads} = \; G_{*OCHO} \; + \frac{1}{2} G_{H_2(g)} - G_{HCOOH(aq)} - G_* \label{eq:Gads}$$
 E6

$$G_{*COOH}^{ads} = G_{*COOH} + \frac{1}{2}G_{H_2(g)} - G_{HCOOH(aq)} - G_*$$
 E7

$$G_{*CO}^{ads} = G_{*CO} + G_{H_2O(l)} - G_{HCOOH(aq)} - G_*$$
 E8

Each free energy is calculated as G = EDFT + ZPE + TS, where EDFT is the energy obtained from the DFT calculation at 0K, ZPE is the zero-point energy determined from the vibrational frequencies obtained using the harmonic-oscillator approximation. The TS is the temperature at T = 298.15 K times the entropy (S) term containing i) all the contributions (translational, rotational and vibrational) for the free energies of species in the gas phase and is taken from standard thermodynamic tables⁵ and ii) for the free energies of adsorbed species containing vibrational contributions. The free energy of the surface, G_* , is the energy from DFT at 0 K. The free energies of $CO_2(g)$ and CO(g) are corrected by -0.19 and 0.24 eV, these corrections come from the difference between the experimental standard free energy of formation ΔG_{Exp}° and the DFT formation energy ΔG_{DFT}° , as PBE does not describe well their formation energies.⁶⁻⁸

E2.3 Free energy of solution phase HCOOH (aq)

The solution phase free energy of HCOOH (aq) was calculated using the SHE equilibrium redox potential of CO_2 (g) + 2H⁺ + 2e⁻ \rightarrow HCOOH (aq), E° = -0.11 V vs SHE, where the free energy of CO_2 (g) is calculated within DFT. This was used to solve for the standard free energy of formic acid in solution phase, $\Delta G^{\circ}_{HCOOH}(aq)$ and ultimately to solve for the aqueous free energy at the experimental conditions, see below.

$$\Delta G_{HCOOH}^{\circ}(aq) = G_{CO_2(q)}^{\circ} + 2G_{H^+}^{\circ} - 2|e|U$$
 E9

where $U = E^{\circ} = -0.11 \text{ V,}^{9}$ and $G^{\circ}_{H^{+}} = \frac{1}{2} G_{H_{2}(g)}$ at 0 V in the SHE scale.

The standard solution phase free energy, $\Delta G^{\circ}_{HCOOH}(aq)$, was then used to obtained the free energy of formic acid, ΔG_{HCOOH} , at the experimental conditions of 0.1M HClO₄ and 50 mM HCOOH, following the Nernst equation.

$$\Delta G_{HCOOH} = \Delta G_{HCOOH}^{\circ}(aq) + k_b T ln(Cf)$$
 E10

Cf is the actual concentration of HCOOH and is obtained using the pKa of formic acid, 3.94 and the starting concentrations of HClO₄ and HCOOH.

The free energies of the protons and electrons as expressed in the adsorption reactions, equations 1 to 4, were calculated using the computational hydrogen electrode (CHE) model.¹⁰

E2.4 Formate coadsorption with *H, *CO and *COOH

To investigate the effect of formate coverage on the free energy of formation of adsorbed of *H, *CO and *COOH we calculated the energies from HCOOH (aq) and n molecules of formate *OCHO adsorbed on the surface. For example, the adsorption of *COOH at different formate coverages is calculated using the following chemical reaction

$$HCOOH(aq) +* nOCHO \rightarrow * [COOH - nOCHO] + H^+ + e^-$$
 E11

and its free energy of adsorption

$$G_{*[COOH-nOCHO]}^{ads} = G_{*[COOH-nOCHO]} + \frac{1}{2}G_{H_2(g)} - G_{HCOOH(aq)} - G_{*nOCHO} \label{eq:Gads}$$
 E12

with n=1-3 using the 3x3 unit cell representing coverages of 0.11ML to 0.33 ML and with n=1 using the 2x2 unit cell to represent coverages of 0.25 ML. *[COOH-nOCHO] means both COOH and n OCHO are adsorbed in the same unit cell.

E2.5 CO₂ Reduction

Similarly, the adsorption energetics were calculated for the reduction reaction, i.e. the production of formic acid from CO_2 . This time the reference state is based on CO_2 (g), protons, and electrons. All the gas-phase corrections for $CO_2(g)$ and CO (g) are included as discussed above, and the CHE model is used for the coupled proton and electron transfer.

$$H^+ + e^- + * \rightarrow * H$$

$$CO_2(g) + H^+ + e^- + * \rightarrow * OCHO$$

$$CO_2(g) + H^+ + e^- + * \rightarrow *COOH$$
 E15

$$CO_2(g) + 2H^+ + 2e^- + * \rightarrow *CO + H_2O(l)$$
 E16

The free energies of adsorption are then calculated as shown below.

$$G_{*H}^{ads} = G_{*H} - \frac{1}{2}G_{H_2(g)} - G_*$$
 E17

$$G_{*OCHO}^{ads} = G_{*OCHO} - G_{CO_2(g)} - \frac{1}{2}G_{H_2(g)} - G_*$$
 E18

$$G_{*COOH}^{ads} = G_{*COOH} - G_{CO_2(g)} - \frac{1}{2}G_{H_2(g)} - G_*$$
 E19

$$G_{*CO}^{ads} = G_{*CO} + G_{H_2O(l)} - G_{CO_2(g)} - G_{H_2(g)} - G_*$$
 E20

The limiting potentials for the first protonation step during CO_2 reduction reaction to *COOH are calculated at the potential when the $G_{*COOH}^{ads} = 0$ as show in Eq.E23

$$CO_2 + (H^+ + e^-) + * \rightarrow * COOH$$
 E21

$$G_{*COOH}^{ads} = G_{*COOH} - G_{CO_2(g)} - \frac{1}{2}G_{H_2(g)} - G_* + |e|U$$
 E22

$$U = \frac{G(CO_2 g) + \frac{1}{2}G(H_2(g)) + G * COOH + G(*)}{1|e|}$$
 E23

Table E1 shows the free energies adsorption for *COOH , the precursor of *CO, with H-up and H-down (see Figure E6), calculated from HCOOH (aq), Eq. E7, and from CO_2 (g), Eq. E19, at 1/9 ML coverage on $Pd_{ML}Pt(111)$, Pt(111) and Pd(111).

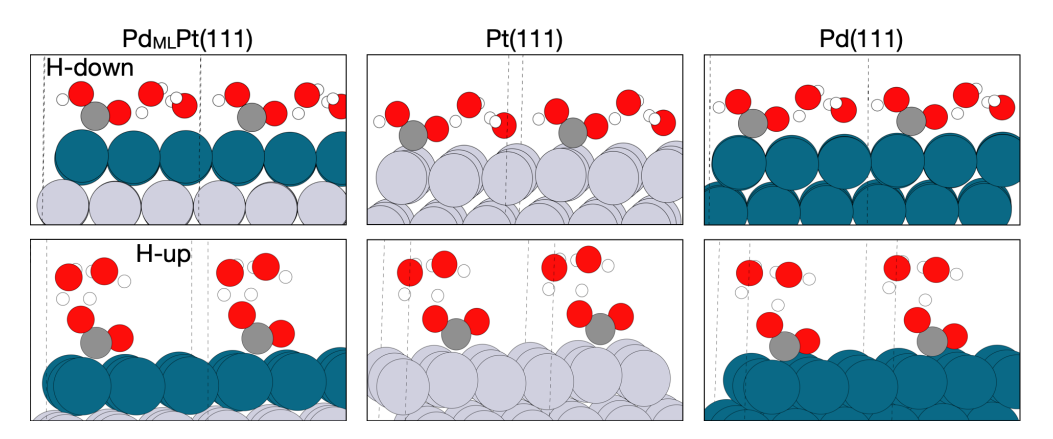


FIGURE E5:

Illustration of *COOH solvated with two explicit water molecules with hydrogen down (H-down) and hydrogen up (H-up) configuration on the $Pd_{ML}Pt(111)$, Pt(111), and Pd(111) surfaces. The boundary of the unit cell is delineated by the vertical dashed line, and each Figure Ehows two-unit cells of 3x3.

TABLE E1

Free energies of adsorption for solvated *COOH with H-up and H-down configuration at 1/9 ML coverage calculated for formic acid oxidation reaction, and for CO_2 reduction reaction, where HCOOH (aq) or CO_2 (g) are the reference state respectively. Energies are in eV.

	$Pd_{ML}Pt(1111)$	Pt(111)	Pd(111)
COOHup-sol from HCOOH (aq)	-0.15	-0.48	-0.10
COOHdown-sol from HCOOH (aq)	-0.37	-0.63	-0.29
COOHup-sol from $CO_2(g)$	-0.003	-0.34	0.04
COOHdown-sol from CO₂(g)	-0.23	-0.49	-0.15

E2.6 Effect of hydrogen coverage on the free energy of *COOH

We investigated the influence of the hydrogen coverage on the adsorption energy of *COOH-sol, the precursor of *CO formation, on the three different surfaces. The energy of *COOH-sol is described further below in the solvation effects section. Basically, the

solvation energy is added to the free energies of the systems in vacuum. The free energies were calculated following the equations below, *nH represents the surface with n number of adsorbed hydrogens per unit cell. The hydrogen coverages investigated were 1/3 ML and 1ML.

From Figure E6 we can see that the effect of hydrogen coverage on the adsorption energy of *COOH-sol is a decrease in its binding energy, as expected due to repulsion interactions, but comparing between the three surfaces *COOH-sol adsorbs on Pt(111) stronger.

$$CO_2 + *nH + H^+ + e^- \rightarrow *[COOH - nH]$$
 E24

$$G_{*[COOH-nH]}^{ads} = G_{*[COOH-nH]} - G_{CO_2} - G_{*nH} - \frac{1}{2}G_{H_2(g)}$$
 E25

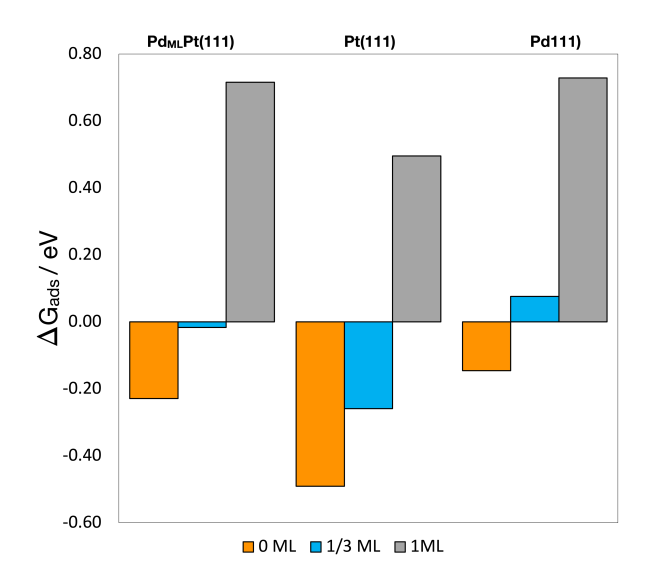


FIGURE E6

Free energy of formation of adsorbed *COOH in the absence (orange) and presence of different coverages of coadsorbed hydrogen at 1/3 ML (blue) and 1 ML (grey) on $Pd_{ML}Pt(111)$, Pt(111) and Pd(111) at 0 V vs RHE, the solvation energy is added to *COOH in all cases as explained in the solvation effects section.

E2.7 Solvation effects

E2.7.1 Solvation effect on *COOH

We consider the effect of solvation on the adsorption of *COOH by solvating *COOH with 2 explicit water molecules, named as *COOH-sol. Adsorbed water bilayer and solution-phase formic acid were used as the reference states, see Eq. E26 for formic acid oxidation, while for the reduction reaction we use adsorbed water, CO₂ (g), and protons and electrons, Eq. E27 The adsorbed water reference state is the adsorbed water in the ice-like structure in a 3x3 unit cell, while in 2x2 unit cell we used a reference state of 4 adsorbed hydrogen bonded water molecules. The following equations correspond to n=6 in the 3x3 unit cell and n=4 in the 2x2 unit cell.

$$HCOOH(aq) + n * H_2O \rightarrow * [COOH - 2H_2O] + (n-2)H_2O(l) + H^+ + e^-$$
 E26

$$CO_2(g) + n * H_2O + H^+ + e^- \rightarrow * [COOH - 2H_2O] + (n-2)H_2O(l)$$
 E27

The solvation energy of adsorbed *COOH, Ω_{*COOH} , is the difference between the non-solvated and solvated free energies of *COOH. That difference gives Eq. E28 and the solvation energy is Eq. E29

$$*COOH + n * H_2O \rightarrow * [COOH - 2H_2O] + (n-2)H_2O(l) + *$$
 E28

$$\Omega_{*COOH} = G_{*[COOH-2H_2O]} + (n-2)G_{H_2O(l)} + G_* - G_{*COOH} - n G_{*H_2O}$$
E29

The solvation energy, $\Omega_{^*COOH}$, calculated here is an estimate to capture the effect of solvation of coabsorbed *COOH with *OCHO, that is *[COOH-nOCHO], and to capture the effect of coadsorbed *COOH with hydrogen *[COOH-nH]. To account for such solvation effects, the solvation energy is added to the final free energy as, $G^{ads}_{*[COOH-nOCHO]} + \Omega_{*COOH}$, and $G^{ads}_{*[COOH-nH]} + \Omega_{*COOH}$ and represents an upper bound estimate of the solvation effect.

Table E2 shows the solvation energies determined for *COOH with H-up and H-down configuration at both 1/9 ML and 1/4 ML coverages on $Pd_{ML}Pt(111)$, Pt(111) and Pd(111) surfaces. We determine 3 different solvation energies following Eq. E29. For example, H-down vac to Hup-sol, means that the reference state (*COOH) is adsorbed *COOH with hydrogen down configuration in vacuum (H-down vac), and the solvated *COOH is with hydrogen in the up configuration (Hup-sol). At high coverages 1/4 ML *COOH, higher stabilization (more negative solvation energies) is achieved for the *COOH with H up

configuration, while at low coverages higher stabilization is achieved for H down-vac to H down-sol. The reason for this might be more predominant repulsive interactions than solvation stabilization at higher coverages than at low coverages.

TABLE E2

Calculated solvation energies for *COOH adsorbate on $Pd_{ML}Pt(111)$, Pt(111), Pd(111), at 1/9 ML and 1/4 ML coverages following Eq. E29. The solvation energies where calculated following different positions of the hydrogen on *COOH, where the H of the OH group could be on the H-down position or up.

3x3-111 (1/9 ML)	$Pd_{ML}Pt(111)$	Pt(111)	Pd(111)
H down vac to H up-sol	-0.30	-0.47	-0.35
H up vac to H up-sol	-0.38	-0.59	-0.46
H down vac to H down-sol	-0.53	-0.62	-0.54
2x2-111 (1/4 ML)	Pd _{ML} Pt(111))	Pt(111)	Pd(111)
2x2-111 (1/4 ML) H down vac to H up-sol	Pd _{ML} Pt(111)) -0.17	Pt(111) -0.20	Pd(111) -0.28

In summary, *COOH is preferably adsorbed with a H-down type configuration at least up to 0.25 ML coverage of formate. Once the coverage of formate is increased to 0.33ML, *COOH with H-up configuration is more favorable. Therefore, in the coadsorbed system, where *COOH is co-adsorbed with 0.33 ML of *OCHO, we corrected for solvation with the solvation energy determined for the *COOH with H-up configuration.

*COOH coadsorbed with 1ML of hydrogen prefers to adsorb with H down configuration. For Pd and $Pd_{ML}Pt(111)$ it is ~0.2 eV more favorable than H-down, while for Pt (111) is more favorable by ~0.04 eV. Therefore, we corrected the energy of the coadsorbed system with the solvation energy determined for *COOH with H-down configuration.

Again, these solvation corrections are an upper bound estimation of the solvation effect on *COOH.

E2.7.2 Solvation on *OCHO

Formate retains partial negative charge upon adsorption; to assess whether or not adsorbed formate might benefit from solvation, we determine its solvation energy with 1, 2, and 3 explicit water molecules following the assessment described in ref ¹¹. Briefly, the adsorbate in question can benefit from solvation via hydrogen bonding if the

difference between solvation energy with (n) number of water molecules and (n-1) is more negative than the water-self solvation energy on that surface, $\Omega^{n}-\Omega^{n-1} \leq \Omega$ H₂O, (where, Ω , refers to solvation energy). The water-self solvation energy was calculated as the difference in free energy between one water molecule at 1/9 ML and a water molecule within the water bilayer at 2/3 ML coverage. For Pt(111) that difference is -0.29 eV, for Pd_{ML}Pt(111) it is -0.18 eV and for Pd it is -0.14 eV. From column Δ 2 w-1w in Table E3, the difference in solvation energies of formate with two and one water molecules is higher than the water self-solvation, on all surfaces respectively, suggesting that solvation with one water molecule is enough. This solvation energy is an upper bound estimation of the solvation effect on formate.

The reference state to calculate the solvation energy is the adsorbed water bilayer in the 3x3 (111) unit cell, at 2/3 ML coverage, Eq. E30, and the solvation energy is the difference between the free energy of the solvated formate and the non-solvated formate, $\Omega_{^{*}\text{OCHO}}$, Eq. E31.

* OCHO + 6 *
$$H_2O \rightarrow * [OCHO - 1H_2O] + 5 H_2O(l) + *$$
 E30

$$\Omega_{*OCHO} = G_{*[OCHO-1H_2O]} + 5G_{H_2O(l)} + G_* - G_{*OCHO} - 6G_{*H_2O}$$
 E31

TABLE E3:

Calculated solvation energies for adsorbed formate at 1/9 ML with 1, 2, and 3 water molecules. Last two columns show the difference between, $2\,H_2O$ molecules (2w) and $1\,H_2O$ molecules, and between $3\,H_2O$ (3w) and $2\,H_2O$ molecules.

Surface	1 H ₂ O	2 H ₂ O	3 H ₂ O	∆ 2 w-1w	∆ 3 w-2w
Pd _{ML} Pt (111)	-0.50	-0.27	-0.24	0.23	0.03
Pt (111)	-0.39	-0.23		0.16	
Pd (111)	-0.51	-0.25	-0.24	0.26	0.01

E2.8 Dipole moments and Bader partial charges

Bader partial charge analysis was performed with the Atoms in Molecules, AIM, Bader analysis, 12,13 using the Bader program from Henkelman's group. 14

TABLE E4

Dipole moments and Bader partial charges for various adsorbates on $Pd_{ML}Pt(111)$, Pt(111) and Pd(111) at 1/9 ML coverage unless specified otherwise. [a] Total partial Bader charge of hydrogens adsorbed on the surface on the fcc sites, and [b] partial Bader charge of only *COOH.

	4	Δµ/e*Å			$ q /e^{-}$	
adsorbate	Pd _{ML} Pt(111)	Pt(111)	Pd(111)	Pd _{ML} Pt(111)	Pt(111)	Pd(111)
H-fcc	0.02	-0.01	0.01	-0.09	-0.03	-0.08
H-top	0.03	-0.03	0.02	0.00	0.04	0.00
СО	0.18	-0.03	0.17	-0.23	-0.01	-0.22
ОСНО	-0.06	-0.23	-0.07	-0.50	-0.40	-0.48
СООН- Н ир	-0.24	-0.16	-0.25	-0.22	-0.16	-0.19
COOH- H down	0.06	0.21	0.06	-0.14	0.01	-0.10
COOH-Hup sol	-0.23	-0.18	-0.29	-0.20	-0.12	-0.17
COOH-Hdown sol	0.06	-0.35	-0.17	-0.15	-0.08	-0.11
OCHO-sol	-0.25	-0.41	-0.24	-0.58	-0.39	-0.39
1/3 ML Hads-fcc	0.06	-0.03	0.04	-0.25	-0.06	-0.21
1 ML Hads-fcc	0.09	-0.17	0.06	-0.56	-0.07	-0.51
°1/3 ML *H in *COOH	0.12	0.18	0.15	-0.19	-0.05	-0.19
^a 1 ML *H in *COOH	0.24	0.05	0.20	-0.61	-0.05	-0.48
^b *COOH in 1/3 ML *H				-0.08	-0.01	-0.04
^b *COOH in 1 ML *H				0.03	0.02	0.07

E2.9 Work functions

Work functions, Φ , were determined as, $\Phi=V-E_{Fermi}$, the difference between the Fermi energy and the one electron potential in vacuum.

TABLE E5

Calculated work function for the bare surfaces, $Pd_{ML}Pt(111)$, Pt(111) and Pd(111), and at different hydrogen coverages.

Φ / eV					
	Pd _{ML} Pt(111)	Pt (111)	Pd (111)		
Bare	5.14	5.74	5.29		
1/9 ML	5.20	5.71	5.32		
1/3 ML	5.33	5.64	5.37		
1ML	5.45	5.20	5.42		

E3 References

- Wakisaka, M., Asizawa, S., Uchida, H. & Watanabe, M. In situ STM observation of morphological changes of the Pt(111) electrode surface during potential cycling in 10 mM HF solution. *Phys. Chem. Chem. Phys.* 12, 4184-4190 (2010).
- 2. Álvarez, B., Climent, V., Rodes, A. & Feliu, J. M. Anion adsorption on Pd-Pt(111) electrodes in sulphuric acid solution. *J. Electroanal. Chem.* **497**, 125-138 (2001).
- 3. Soriaga, M., Stickney, J., Bottomley, L. & Kim, Y. *Thin Films: Preparation, Characterization, Applications.* (Springer US, 2002).
- 4. Álvarez, B., Berná, A., Rodes, A. & Feliu, J. M. Electrochemical properties of palladium adlayers on Pt(100) substrates. *Surf. Sci.* **573**, 32-46 (2004).
- 5. Chase, Jr., M. W. et al. NIST-JANAF Thermochemical Tables. J. Phys. Chem. Ref. Data Suppl. 1 to Vol. 14, 1856 (1985).
- 6. Peterson, A. A., Abild-Pedersen, F., Studt, F., Rossmeisl, J. & Nørskov, J. K. How copper catalyzes the electroreduction of carbon dioxide into hydrocarbon fuels. *Energy Environ. Sci.* **3**, 1311-1315 (2010).
- 7. Christensen, R., Hansen, H. A. & Vegge, T. Identifying systematic DFT errors in catalytic reactions. *Catal. Sci. Technol.* **5**, 4946–4949 (2015).
- 8. Granda-Marulanda, L. P. *et al.* A Semiempirical Method to Detect and Correct DFT-Based Gas-Phase Errors and Its Application in Electrocatalysis. *ACS Catal.* **10**, 6900-6907 (2020).
- 9. Bratsch, S. G. Standard Electrode Potentials and Temperature Coefficients in Water at 298.15 K. J. Phys. Chem. Ref. Data 18, 1-21 (1989).
- 10.Nørskov, J. K. *et al.* Origin of the Overpotential for Oxygen Reduction at a Fuel-Cell Cathode. *J. Phys. Chem. B* **108**, 17886-17892 (2004).
- 11.Rendón-Calle, A., Builes, S. & Calle-Vallejo, F. Substantial improvement of electrocatalytic predictions by systematic assessment of solvent effects on adsorption energies. *Appl. Catal. B Environ.* **276**, 119147 (2020).
- 12.Bader, R. F. W. Atoms in molecules: a quantum theory. (Clarendon Press, 1994).
- 13.Bader, R. F. W. Atoms in molecules. Acc. Chem. Res. 18, 9-15 (1985).
- 14.Henkelman, G., Arnaldsson, A. & Jónsson, H. A fast and robust algorithm for Bader decomposition of charge density. *Comput. Mater. Sci.* **36**, 354-360 (2006).



SUMMARY & FUTURE PERSPECTIVES

This dissertation focused on computational methods based on first principles calculations using the Density Functional Theory (DFT) framework. Emphasis was laid on affordable methods that can provide a tradeoff between computational expense and accuracy. Specifically, we investigated solvation effects near the surface of the electrode, used thermodynamic cycles to compute solution-phase energies and also proposed a workflow to detect gas-phase errors on the free energies of target molecules. We used these simple methods to study complex adsorption processes at the Pd_{ML}Pt(111) electrode surface. DFT and experimental studies were crucial to guide the investigation forward

Summary

Chapter 2 was dedicated to understanding the role of different DFT functionals with and without van der Waals (vdW) interactions, on the solvation energy of *OH adsorbed on near-surface alloys (NSAs) of Pt-M-Pt (111), where M = Co, Rh, Ir, Ni, Pd, Pt, Cu, Ag, Au. From this study, we obtained a dataset of solvation energies per functional, and found that (i) adsorbate stabilization due to water solvation is weaker when including vdW interactions, (ii) extrapolating solvation energies within functionals that include vdW interactions is safe, and (iii) while extrapolating solvation energies obtained with PW91 to PBE and vice versa is OK, it is not advisable to extrapolate from RPBE to neither PBE nor PW91. We concluded that it is important to assess solvation energy specifically for the system under study, and that it is safe to use solvation energies calculated with other functional as long as it belongs to the same group.

Accurate and affordable methods are necessary to describe ions both in the bulk solution (far away from the electrode surface) and at the metal-electrode interface, to predict catalytic activities, influenced by not only the reaction intermediates but also by their interaction with the adsorbed ions from the electrolyte. In *Chapter 3*, we presented a simple-to-use method to determine solution-phase free energies of any ion in solution using simple electrochemical thermodynamic cycles. This solution-phase reference method does not require intensive computational models of solvation to obtain the free energy of the solvated ion, avoids periodic calculations of charged species by linking neutral gas-phase or solid-state species to the charged ones through experimentally measured equilibrium potentials, and offers solution-phase energies of the ions that lie at the same potential scale. This allows for comparisons across different ions/adsorbates. We examined the adsorption potentials of various ions on Pt(111) and Au(111), and were able to reproduce the trend between the ions measured experimentally.

DFT methods based on the generalized gradient approximation (GGA) provide accurate energetics and describe well the electronic and geometric structures of

bulk metals. However, gas-phase molecules require more sophisticated and expensive calculations, often based on hybrid functionals. A clear problem is that hybrid functionals are not suitable for metals, and GGA functionals are not particularly accurate for molecules. Therefore, Chapter 4 was dedicated to providing an inexpensive solution for this dilemma, where we can model adsorption processes when a metal surface is in contact with gas-phase species, as it is the case in electro(catalysis). We presented a systematic, semiempirical method to correct errors in the gas-phase energies of four GGA functionals commonly used in catalysis, namely PBE, PW91, RPBE and BEEF-vdW. This method was applied to a dataset of 27 gases and we found that it lowers the maximum and mean absolute errors by one order of magnitude. We identified an intrinsic limitation of DFT for the description of CO and CO₂ across all studied functionals, as the energy difference between the formation energies of these species is constant, and implementation of this method significantly decreased the errors of the calculated onset potentials when used to model electrocatalytic CO₂ reduction on Au, Ag and Cu electrodes. Therefore, with this method we can identify and correct errors in gas-phase molecules leading to predictive electrocatalysis models.

The simple and affordable DFT methods proposed in *Chapters 2-4* were implemented in the remaining chapters of this thesis, where we investigated the adsorption processes on the $Pd_{ML}Pt(111)$ surface, one of the most active catalysts for the oxidation of formic acid and the carbon dioxide reduction reaction, in a comparative fashion with Pt(111).

To elucidate the mechanisms of reactions catalyzed by Pd_{MI}Pt(111) during electrochemical conditions, under applied potentials, it is important to study the adsorption processes happening at the electrode surface. In *Chapter 5* we combined experimental measurements with density functional simulations to investigate the adsorption processes corresponding to various peaks in the blank cyclic voltammogram of Pd_{MI}Pt(111) in perchloric acid, and compared with Pt(111) at the same conditions. We found that the peak named H_I is significantly influenced by cations while the peak H_{II} is greatly influenced by anions. We ascribed the peaks in the region between 0.05 to 0.35 V vs RHE to be first the replacement of adsorbed hydrogen with adsorbed hydroxyl, that is the peak at 0.25 V vs RHE, and second the exchange of the H/OH adlayer to adsorbed perchlorate at 0.306 V vs RHE. The peak at later potentials between 0.60 and 0.90 V vs RHE was ascribed to a perchlorate/ hydroxide adlayer or the replacement of perchlorate with a higher coverage of adsorbed hydroxide, and this peak is suppressed by strong binding anions. The detailed information gained in this chapter is important to understand the catalytic properties of palladium-based electrodes.

There has been some debate on whether adsorbed formate plays a role as an active intermediate or spectator species during the formic acid oxidation reaction. Although recent works agree on the role of adsorbed formate being that of spectator and not an intermediate, its role as spectator remains elusive. Furthermore, during carbon dioxide reduction, the $Pd_{ML}Pt(111)$ catalyst produces formate at a low overpotential while Pt(111) is passivated with CO. *Chapter 6* was devoted to gaining knowledge on the particular question of how $Pd_{ML}Pt(111)$ prevents CO poisoning during CO_2 reduction and HCOOH oxidation by combining experiments on well-defined single-crystal electrodes of $Pd_{ML}Pt(111)$ and Pt(111), and density functional theory calculations. We found that the coverage at which formate adsorbs during the oxidation reaction dictates

whether or not CO forms, high coverages of 1/3 ML prevent CO formation on $Pd_{ML}Pt(111)$ by blocking the sites necessary for COOH (CO precursor), while coverages of 1/4 ML on Pt(111) allows COOH formation and subsequent electrode poisoning. During the reduction reaction the nature of the adsorbed hydrogen on the surface plays an important role on the mechanism of formation of formic acid from carbon dioxide. We find that this hydrogen on $Pd_{ML}Pt(111)$ is more negatively charged than that on Pt(111), and suggest that the reaction proceeds via nucleophilic attack. The knowledge gained in this study can help in catalyst design where CO poisoning is to be avoided.

Future Perspectives

From the work conducted in this thesis various other questions emerged or were left unanswered, and those questions could be the beginning of future projects.

- Chapter 2: Similar to the investigation conducted in this chapter, we were curious to know how solvation energies varied for the *OOH adsorbate on the same surface alloys studied and to verify if the trend found for *OH is similar or not to *OOH. For example, the unanswered question here is whether the solvation energies for the *OOH are significantly different when calculated with the different DFT functionals with and without van der Waals (vdW) interactions? Since *OOH is similar to *OH we could expect similar trends.
- Chapter 3: The investigation from this chapter can be extended through a screening investigation of adsorption energies of various anions on various transition metals (TM), but to follow the line of the work in this thesis, the investigation would be for palladium overlayers on different TM surface (Pd_{ML}(hkl)/TM(hkl), and one could investigate the effect of adsorbing anions on the electronicstructure properties, like d-band centers and work functions.
- Chapter 4: Future work from this chapter is the implementation of a machine-learning algorithm that can follow the proposed workflow, and be able to run calculations, get the free energies, pinpoint the errors in formation energies of gas-phase molecules and produce error corrections. This can have great potential in scientific software automation and development.
- Chapters 5 and 6: There are still various questions that emerged from this work. One of them was to know whether a clean monolayer of palladium is formed on the Pt(111) surface, to know whether defects form during the experiments, or whether the surface contained segregated Pt atoms. We conducted preliminary DFT investigations at very early stages of this project where we calculated the adsorption energies of *OH on intermetallic Pt₁Pd₂(111)/Pt(111), that is 1/3 ML of Pt on Pd. Although we found the energetics of the *OH to be favorable, we believed that it would be kinetically forbidden to have such exchange of atoms. Further research would be of great interest to understanding Pd/Pt alloy behavior. From Chapter 6, one interesting question that appeared and is left unanswered is to obtain an electronic-structure explanation as to why *COOH binds more strongly on Pt(111). The hypothesis proposed is that *COOH forms a

more covalent interaction with the Pt(111) surface than with Pd(111). If that is true, stronger overlap between the orbitals of the metal and the adsorbate should be observed on Pt(111) than on Pd(111).

SAMENVATTING & TOEKOMSTPERSPECTIEVEN

Dit proefschrift focust zich op computationele methoden gebaseerd op "first principles" berekeningen gebruik makend van een Density Functional Theory (DFT) kader. Nadruk is gelegd op betaalbare methodes die kunnen voorzien in een compromis tussen computationele kosten en nauwkeurigheid. Wij hebben in het bijzonder onderzoek gedaan naar de effecten van solvatatie dichtbij het oppervlak van de elektrode, gebruik makend van thermodynamische cycli om de solvatatie energieën uit te rekenen. Daarbij hebben we ook een workflow voorgesteld om fouten in de vrije energie van de moleculen in gas fase te detecteren. We hebben gebruik gemaakt van simpele methodes om complexe adsorptie processen op het oppervlak van een $Pd_{ML}Pt(111)$ elektrode te bestuderen. Zowel DFT als experimentele studies waren cruciaal om het onderzoek vooruit te brengen.

Samenvatting

Hoofdstuk 2 is gewijd aan het begrijpen van de rol van verschillende DFT functionalen met en zonder van der Waals (vdW) interacties, op de solvatatie-energie van *OH geadsorbeerd op oppervlakte legeringen (zogenaamde nearsurface alloys NSAs) van Pt-M-Pt (111), waar M = Co, Rh, Ir, Ni, Pd, Pt, Cu, Ag, Au. Uit deze studie hebben we een dataset van solvatatie-energieën per functionaal gekregen en gevonden dat (i) adsorbaten een stabiliserende werking hebben doordat water solvatatie zwakker is wanneer vdW interacties worden meegenomen, (ii) het aanvaardbaar is om solvatatie-energieën binnen een functionaal met vDW interacties te extrapoleren, en (iii) hoewel het correct is om solvatatie-energieën verkregen met PW91 te extrapoleren naar PBE en vice versa, is het niet te adviseren om te extrapoleren van RPBE naar PBE of PW91. We concluderen dat het belangrijk is om de solvatatie-energie van het specifiek te onderzoeken systeem in te schatten, en dat het veilig is om gebruik te maken van solvatatie-energieën berekend met andere functionalen, zolang deze tot dezelfde groep behoren.

Nauwkeurige en betaalbare methoden zijn noodzakelijk om zowel ionen in de bulk oplossing (ver van de elektrode) als bij het metaal-elektrode oppervlak te beschrijven en katalytische activiteiten te voorspellen die niet alleen worden beïnvloed door de reactie intermediairen, maar ook door de interactie met geadsorbeerde ionen uit het elektrolyt. In *Hoofdstuk 3* presenteren wij een simpele methode om de vrije energie van een willekeurig ion in de oplossing te bepalen via simpele elektrochemische thermodynamische cycli. Deze oplossingsfase-referentiemethode vereist geen intensieve rekenkundige modellen van solvatatie om de vrije energie van het gesolvateerde ion te verkrijgen,

voorkomt periodieke berekeningen van geladen deeltjes door middel van het linken van neutrale deeltjes in de gas of vaste fase met geladen deeltjes via experimenteel gemeten evenwichtspotentialen, en verschaft oplossingsfaseenergieën van ionen die in dezelfde potentiaalschaal liggen. Dit staat vergelijkingen tussen verschillende ionen/adsorbaten toe. We hebben de adsorptie potentiaal van verschillende ionen op Pt(111) en Au(111) onderzocht, en zijn in staat om de experimenteel gemeten trend tussen deze ionen te reproduceren.

DFT methodes gebaseerd op gegeneraliseerde gradiënt benadering (GGA) bieden accurate energetica en beschrijven de elektronische en geometrische structuren van bulk metalen goed. Gasfasemoleculen vereisen echter meer geavanceerdere en duurdere berekeningen, vaak gebaseerd op hybride functionalen. Een duidelijk probleem is dat hybride functionalen niet geschikt zijn voor metalen, en GGA functionalen niet erg accuraat zijn voor moleculen. Daarom is *Hoofdstuk 4* gewijd aan het leveren van een betaalbare oplossing voor dit dilemma, waar we adsorptie processen, waarbij een metaal oppervlak in contact is met gasfase deeltjes, net als in (elektro)katalyse, kunnen modeleren. We presenteren een systematische, semi-empirische methode om fouten in de gasfase-energieën te corrigeren voor vier, vaak in katalyse gebruikte, GGA functionalen, namelijk PBE, PW91, RPBE en BEEF-vdW. Deze methode is toegepast op een dataset van 27 gassen en we hebben gevonden dat deze de maximale en gemiddelde absolute fout verkleint met een orde van grootte. We identificeren een intrinsieke limitatie van DFT voor het beschrijven van CO en CO₂ bij alle bestudeerde functionalen, aangezien de energie verschillen tussen formatie-energieën van deze deeltjes constant is, en implementatie van deze methode vermindert de fouten van de berekenende evenwichtspotentialen significant wanneer deze gebruikt wordt om elektrochemische CO₂ reductie op Au, Ag en Cu elektrodes te modeleren. Daarom kunnen we met deze methode fouten in gasfasemoleculen vaststellen en verbeteren, wat leidt tot voorspellende elektrochemische modellen. De simpele en betaalbare DFT methodes voorgesteld in Hoofdstuk 2-4 zijn geïmplementeerd in de overige hoofdstukken van deze thesis, waar we de adsorptie processen op een Pd_{MI} Pt(111) oppervlak, één van de meest actieve katalysatoren voor oxidatie van mierenzuur en de reductie van koolstofdioxide, hebben onderzocht en vergeleken met Pt(111).

Om de mechanismes van reacties gekatalyseerd door Pd_{ML}Pt(111) onder elektrochemische omstandigheden op te helderen, is het belangrijk om de adsorptie processen aan het oppervlak van de elektrode te bestuderen. In *Hoofdstuk 5* combineren we experimentele resultaten met DFT berekeningen om de adsorptie processen die corresponderen met verscheidene pieken in het blanco cyclisch voltammogram van Pd_{ML}Pt(111) in perchloorzuur te bestuderen, en vergelijken deze met Pt(111) onder dezelfde condities. We hebben gevonden dat de piek genaamd H_I significant wordt beïnvloed door kationen terwijl de piek H_{II} sterk wordt beïnvloed door anionen. We schrijven de pieken in de regio tussen 0.05 en 0.35 V vs RHE toe aan de substitutie van geadsorbeerd waterstof met geadsorbeerde hydroxide, dat is de piek op 0.25 V vs RHE, en de tweede piek bij 0.306 V vs RHE aan de uitwisseling van de geadsorbeerde H/OH laag met perchloraat. De piek bij latere potentialen tussen 0.60 en 0.90 V vs RHE wordt toegeschreven aan een geadsorbeerde perchloraat / hydroxide laag of de substitutie van perchloraat met een hogere bedekking van geadsorbeerde hydroxide, en deze piek wordt onderdrukt door sterk bindende anionen. De

gedetailleerde informatie die wordt verkregen in dit hoofdstuk is belangrijk om het katalytisch proces van op palladium gebaseerde elektrodes te begrijpen.

Er is discussie in de literatuur of geadsorbeerd formiaat een rol speelt als actief intermediair of als toeschouwer tijdens de mierenzuur oxidatie reactie. Hoewel recent werk het er over eens is dat geadsorbeerd formiaat een toeschouwer is en geen intermediair, blijft de exacte rol als toeschouwer onduidelijk. Verder produceert de Pd_MPt(111) katalysator formiaat bij lage overpotentialen tijdens koolstofdioxidereductie, terwijl Pt(111) gepassiveerd wordt met CO. Hoofdstuk 6 is gewijd aan het verkrijgen van kennis over de specifieke vraag hoe Pd_{MI} Pt(111) CO vergiftiging tijdens CO₂ reductie en HCOOH oxidatie voorkomt, door het combineren van experimenten op goed gedefinieerde eenkristalelektrodes van Pd_{MI}Pt(111) en Pt(111) en DFT berekeningen. We hebben gevonden dat de bedekking bij welke formiaat adsorbeert tijdens de oxidatie reactie bepaalt of CO wordt gevormd of niet. Een hoge bedekking van 1/3 ML voorkomt CO vorming op Pd_{ML}Pt(111) door het blokkeren van plaatsen noodzakelijk voor COOH (voorloper van CO), terwijl de bedekking van 1/4 ML op Pt(111) COOH vorming en de daaropvolgende vergiftiging toelaat. Gedurende de reductiereactie speelt de aard van het geadsorbeerde waterstof op het oppervlak een belangrijke rol in het mechanisme van de vorming van mierenzuur uit koolstofdioxide. We hebben gevonden dat waterstof op Pd_{ML}Pt(111) negatiever geladen is dan op Pt(111), en dit suggereert dat de reactie plaatsvindt via een nucleofiele aanval. De kennis verkregen in deze studie kan helpen in het ontwerpen van katalysatoren waarbij CO vergiftiging kan worden vermeden.

Toekomstperspectieven

Uit het werk gedaan in dit proefschrift zijn verschillende andere vragen opgekomen of onbeantwoord gelaten, en deze vragen kunnen het begin zijn van toekomstige projecten.

- Hoofdstuk 2: Vergelijkbaar met de studie gedaan in dit hoofdstuk, zijn we geïnteresseerd om te weten hoe solvatatie-energieën variëren voor het *OOH adsorbaat op dezelfde legeringsoppervlakken en om te verifiëren of de trend gevonden voor *OH gelijk is of niet aan *OOH. Bijvoorbeeld, de onbeantwoorde vraag is of de solvatatie-energieën voor *OOH significant verschillen wanneer deze berekend worden met DFT functionalen met of zonder van der Waals (vdW) interacties.
- *Hoofdstuk 3*: Het onderzoek uit dit hoofdstuk kan worden uitgebreid door een studie van adsorptie-energieën van verschillende anionen op verschillende overgangsmetalen (TM), maar om de lijn te volgen uit het proefschrift zou men palladium bovenlagen op verscheidene TM oppervlakken (Pd_{ML}(hkl)/TM(hkl)) en het effect van geadsorbeerde anionen op de elektronen structuur, zoals de d-band centra en werk functies, kunnen onderzoeken.
- Hoofdstuk 4: Toekomstig werk voortkomend uit dit hoofdstuk is de implementatie van machine-learning algoritmes die de voorgestelde workflow kunnen volgen, en in staat zijn berekeningen te maken, vrije

- energieën te verkrijgen, fouten in formatie-energieën van gasfasemoleculen vast te stellen, en foutcorrecties te produceren. Dit kan een groot potentieel hebben in wetenschappelijke softwareautomatisering en -ontwikkeling.
- Hoofdstuk 5 en 6: Er zijn nog verscheidene vragen die voortkomen uit dit werk. Eén daarvan is om te weten of een exacte monolaag van palladium wordt gevormd op het Pt(111) oppervlak, om te weten of zich defecten vormen tijden de experimenten, of dat het oppervlak gesegregeerde Pt atomen bevat. We hebben inleidende DFT studies gedaan in de allereerste fases van dit onderzoek waar we de adsorptieenergieën van *OH op intermetallische Pt₁Pd₂(111)/Pt(111), dat is 1/3 ML van Pt op Pd, hebben berekend. Hoewel we hebben gevonden dat de energetica van de *OH gunstig is, geloven we dat het kinetisch ongunstig is om zo'n uitwisseling van atomen te hebben. Vervolgonderzoek zou van groot belang zijn om het gedrag van de Pd/Pt legering te begrijpen. Eén van de interessante vragen die voortkwam uit Hoofdstuk 6 en onbeantwoord is gebleven, is om een elektronische-structuur motivering te verkrijgen die uitlegt waarom *COOH sterker bindt aan Pt(111) dan aan Pd_{ML}/Pt(111). De voorgestelde hypothese is dat *COOH een meer covalente interactie vormt met het Pt(111) oppervlak dan met Pd(111). Als dit klopt, dan zou op Pt(111) een sterkere overlap tussen de orbitalen van het metaal en het adsorbaat moeten worden waargenomen dan op Pd(111).

LIST OF PUBLICATIONS, CONFERENCES AND AWARDS

Publications

Chapter 2

Granda-Marulanda, L. P., Builes, S., Koper, M. T. M. & Calle-Vallejo, F. Influence of Van der Waals Interactions on the Solvation Energies of Adsorbates at Pt-Based Electrocatalysts. *ChemPhysChem* **20**, 2968–2972 (2019).

Chapter 3

Granda-Marulanda, L. P., McCrum, I. T. & Koper, M. T. M. A simple method to calculate solution-phase free energies of charged species in computational electrocatalysis. *J. Phys.: Condens. Matter* **33**, 204001 (2021).

Chapter 4

Granda-Marulanda, L. P., Builes, S., Koper, M. T. M., Illas, F. & Calle-Vallejo, F. A Semiempirical Method to Detect and Correct DFT-Based Gas-Phase Errors and Its Application in Electrocatalysis. *ACS Catal.* **10**, 6900–6907 (2020).

Chapter 5

Chen, X., **Granda-Marulanda**, L. P., McCrum, I. T. & Koper, M. T. M. Adsorption processes on a Pd monolayer-modified Pt(111) electrode. *Chem. Sci.* 11, 1703–1713 (2020).

Chapter 6

Chen, X., Granda-Marulanda, L. P., McCrum, I. T. & Koper, M. T. M.

How Palladium prohibits CO poisoning during electrocatalytic formic acid oxidation and carbon dioxide reduction. (2021). *Submitted*

Conferences

69th Annual Meeting of the International Society of Electrochemistry Electrochemistry from Knowledge to Innovation, 2 to 7 September 2018. Bologna, Italy Laura Granda Marulanda, Xiaoting Chen, Ian McCrum, Federico Calle-Vallejo, Marc Koper. Insights into HCOOH Oxidation and HCOOH Production from CO₂ on Pd_{ML}/Pt-based Electrocatalysts from Theoretical and Experimental Studies. [poster]

Awards

HPC-Europa3 Transnational Access programme -2019

A scholarship to promote collaborations within the theoretical/computational scientific community within Europe. Awarded with computing time in the MareNostrum super computer in Barcelona. Hosted by Dr. Federico Calle-Vallejo of the Institute of Theoretical and Computational Chemistry of the Universitat de Barcelona (IQTCUB)

ISE poster prize -2018

Poster prize at the 69th Annual Meeting of the International Society of Electrochemistry in Bologna, Italy.



ACKNOWLEDGEMENTS

I remember very well the sunny day in September 2016 when I came to Leiden for my interview. I had missed the bus stop to the university and ended up a few blocks away. I was panicking because I got lost, but I finally made it to the interview. Finishing my PhD is just the beginning of a new chapter, but it is also the closure of a 12-year chapter of my life. It started when I enrolled the graduate program at Texas A&M back in 2009, then I took a longer path, but that allowed me to see the other side of the world (literally), a world I never imagined I will live in. This opportunity made me grew on a personal and professional level and allowed me to finish my graduate studies.

In that respect I would like to thank first my supervisor, *Marc Koper* for giving me the opportunity to pursue the doctorate degree in the CASC group, and most importantly for your personal and professional support, for your understanding, for being open and available for discussions and for the freedom to do research. Also, thank you for encouraging me to attend the summer school in Denmark, one of the most enriching experiences during my PhD. Thank you for bringing up the questions- the puzzles, which helped me tremendously to stay focused and on the right track within my noisy mind.

I am honored to have pursued graduate studies and research at Leiden University and for the emerged collaborations, friendship and support from all past and present collogues. Isis, the first person I met from the CASC group, thank you for agreeing to meet me before all this started, for answering all my questions related to life in Leiden and for encouraging me to pursue my PhD journey. Federico Calle-Vallejo, thank you for your guidance during the first year of my journey, where I was very lost in space and time, ©, thank you for helping me prioritize my goals. But mostly I am enormously grateful for encouraging me to apply to the HPC3 program, and for the fruitful collaboration it led to. There I got momentum, and confidence to continue this journey and I strongly believed that without that opportunity I would not be where I am now. From you I've learned that DFT and modelling in electrocatalysis is very complex, but still, it can be simple and fun. I learned the importance of testing and how to discern data. Thank you for all the time helping me improving and correcting my manuscripts and chapters of my thesis and for the very insightful "consejos de vida" (life tips). Ian McCrum, thanks for sharing your contagious passion and excitement for science, for the many fun discussions and for supporting my dreams of opening a company, and even if it does not materialize, I am grateful for the inspirational chats we had regarding to that. For your availability to discuss science, for teaching me computational electrocatalysis, DFT and the analysis of experimental data from a practical lens. For helping me improve my presentations and manuscripts and for your cheerful famous quotes; "you can do whatever you want" and "I have faith in you". Xiaoting Chen, thank you for all your hard work and research that led to beautiful science and collaboration, thank you for your patience in waiting for my DFT results ©, and for our chats and discussions over lunch. Selwyn, thank you for teaching me the statistical thermodynamics needed for my scripts, and for helping me during the first months of my PhD to set up my computer and have it ready to go. Thank you for the work discussions and for being always available to help. Miss. José, thank you a lot for all the personal and technical support you offered me, I am so grateful for your help in finding a temporal place to stay in Leiden and for sharing your knowledge and passion about plants. A very huge thanks to my A-leaf friends from the CASC group, Thomas and Amanda for sharing special moments in our A-leaf meetings and for making those enjoyable, thanks for your support and friendship.

To all my previous mentors: *Nelson Granda, José Cortés-Figueroa, Phill Bhüllman, Manuel Soriaga, James Bateas*, and *Igor Pašti*. I am deeply grateful for the learning and research opportunities I had with you, for your mentorship and guidance before I started the PhD. Those opportunities were turning points that led me to this stage.

To all the CASC past and present members, postdocs, fellows, students and technical staff that I have met since my start: *Adrien, Akansha, Alisson, Amanda, Arthur, Asad, Cássia, Charlotte, Christoph, Chunmiao, Dajo, Damien, Davide, Diana, Diyu, Elena, Eli, Federico, Francesc, Giulia, Ian, Jan, Jess, José, Kasinath, Katharina, Koen, Leon, Mahesh, Sabine W., Marcel, Mariana, Marta, Matías, Matthijs, Mehdi, Nakkiran, Rafaël, Richard, Sabine A., Selwyn, Silvia, Stefan, Steven, Thom, Thomas, Vlad, Wentian, Xiaoting, Xin, Yohan, Yuvraj and Zhiqin. Thank you all for all the work discussion, chats over lunch, cake breaks, coffee breaks, beers at the science club or the mathematics building, for the Potluck dinners, for the group outings and for priceless experiences like the summer and winter schools and conferences we attended together. Thank you for making the CASC group a very pleasant working environment and for making my PhD more enjoyable in the Netherlands.*

Special thanks to my colleagues and friends *Diana*, *Jess*, *Stefan*, *Giulia*, *Matías*, *Amanda*, *and Ian*. Thank you for all the shared moments and memories we built together also outside the working hours. Some of you from the start and some of you at the end of my journey. Thank you for your generous friendship. For those long walks in the city center and around the lakes of Leiden, for the sushi dinners and the movie nights. I learned from you about life and research. *Diana* and *Jess*, first thanks for the analytical chemistry conversations, and python code fixes, but most importantly thank you for being there during my darkest and happiest moments during this journey and for the constant encouragement to keep moving forward and not give up.

To my friends outside university: *Monique* and *Lilian*, my soul sisters, thank you for spicing up my life in The Netherlands, for understanding me and for being there in the good and bad. You have taught me to balance PhD life with life. I am grateful for all the laughs and tears we shared, the wines and tequilas and deep conversations about life.

To all my caring and supportive friends: Alexis, Melissa, Tatiana, Linda, Kethura, Mavreen, Milagros, Hecgli, Leslie, Andrea, Natalia, Nancy, Lina, Marianne, Ceci, Leda, Desi, Kristhell, Sarahí, and Đorđe, thank you for teaching me so many things about life and myself, I would need a new chapter to write all our memories but I want to let you know that I am thankful for the support provided at all different stages of this journey.

To my beloved partner in crime: *Ivica Milovanović*, out of the 12 years of this journey, we did 11. Thank you for all your support, love and care- even on your hardest and difficult moments. Thank you for encouraging me to pursue computational chemistry, for all the chemistry discussions and for teaching me some fancy functional programming for my scripts. Thank you for always pushing me to keep becoming a better person, to "follow my heart", and most importantly, for overcoming many obstacles together, and accompanying me in The Netherlands.

A mi querida familia, mis padres y mis hermanos a los que adoro mucho. *Mami* y *papi*, gracias por darme todas las herramientas necesarias para poder construir mis alas y volar. A pesar de todo el esfuerzo que requiere emigrar de Colombia y hacer la maestría en un nuevo país y además con dos hijos, nunca me faltó su apoyo y cariño. Gracias por enseñarme a ser persistente y precavida y sobre todo por apoyarme a lograr y perseguir mis metas. Les dedico esta tesis con todo mi corazón, mis logros son sus logros. Hermanos queridos: *Nelson* y *Sebastián*, estoy totalmente agradecida por su amor y cariño y porque a pesar de la distancia nos seguimos apoyando, los quiero mucho.

Mojoj srpskoj porodici - Ljiljani, Draganu i Blesi - hvala vam za vašu ljubav i brigu tokom svih ovih godina. *Ljiljana*, hvala ti na pordšci i ohrabrenju. Od tebe sam naučila da sve ima rešenje i pokušavam da tu mudrost primenim u svakodnevnom životu. *Dragane*, od tebe sam naučila da stvari držim na svom mestu. Ili bar pokušavam. ⊚ -Mnogo vas volim.

CURRICULUM VITAE

Laura Patricia Granda Marulanda was born on 9th June 1988 in Cali, Colombia. At the age of 6 she moved to Puerto Rico where she completed her high school and bachelor education. She enrolled the Chemistry program from the university of Puerto Rico at Mayagüez graduating in 2009. During this period, she did an internship at the university of Minnesota in the USA under the LANDO program and worked on the project "Design of a solid-contact ion selective electrode for the detection of perfluoroalkyl acids". From 2009 to 2011 she enrolled graduate studies and worked as a teacher assistant in the Chemistry department at Texas A&M. There, her preliminary research involved fundamental studies of silicate minerals using the Atomic Force Microscope. Later, fascinated by the world of computational chemistry, she redirected her research interests and enrolled the faculty of Physical Chemistry at the University of Belgrade in Serbia, where she completed her master's degree in 2013 on the project: "Theoretical study of the interaction of PtTM dimers (TM = Ru, Rh, Pd, Ir and Pt) with MgO(001) surface - adsorption, mobility and electronic structure".

In January 2017, Laura started her PhD in the CASC group, Leiden University, The Netherlands under the supervision of prof. dr. M. T. M. Koper. The main results obtained during this graduate research are described in this thesis, presented at international conferences and published in scientific journals.

Besides science, Laura enjoys long walks, dancing salsa and bachata, doing Zumba®, pole fitness, and loves to gaze at the horizon. She used to play the oboe, and now she is learning the ukulele. She also enjoys listening to informative podcasts and reading.